PDF modelling
and particle-turbulence interaction
of turbulent spray flames

Nijso Arie Beishuizen

PDF modelling and particle-turbulence interaction of turbulent spray flames

Proefschrift

ter verkrijging van de graad van doctor
aan de Technische Universiteit Delft,
op gezag van de Rector Magnificus prof. dr. ir. J. T. Fokkema,
voorzitter van het College voor Promoties,
in het openbaar te verdedigen op maandag 25 februari 2008 om 10:00 uur

door

Nijso Arie BEISHUIZEN

Ingenieur Luchtvaart- en Ruimtevaarttechniek
Technische Universiteit Delft

geboren te Assen

Dit proefschrift is goedgekeurd door de promotor:
Prof. dr. D.J.E.M. Roekaerts

Samenstelling promotiecomissie:

Rector Magnificus	voorzitter
Prof. dr. D. J. E. M. Roekaerts	Technische Universiteit Delft, promotor
Prof. dr. ir. Th. H. van der Meer	Universiteit Twente
Prof. dr. R. F. Mudde	Technische Universiteit Delft
Prof. dr. ir. G. Ooms	Technische Universiteit Delft
Prof. dr. ir. R. S. G. Baert	Technische Universiteit Eindhoven
Prof. dr. E. Gutheil	Universiteit Heidelberg
Dr. B. Naud	CIEMAT

This work was financially supported by the technology foundation STW.

Printed by PrintPartners Ipskamp B.V.

ISBN 978-90-9022750-4

Voor mijn moeder

SUMMARY

PDF modelling and particle-turbulence interaction of turbulent spray flames

Turbulent spray flames can be found in many applications, such as Diesel engines, rocket engines and power plants. The many practical applications are a motivation to investigate the physical phenomena occurring in turbulent spray flames in detail in order to be able to understand, predict and optimise them.

Turbulent spray flames are a two-phase flow system consisting of a turbulent reacting continuum phase and a dispersed liquid phase contained in the continuum phase. In this thesis the interaction between these two phases is being studied, and specifically the effects of vaporisation and the effects of the presence of droplets on the turbulence characteristics of the continuum phase (the two-way coupling effect). The main goal of the research described in this thesis is to develop and evaluate stochastic Lagrangian models for turbulent spray flames that are characterised by significant or dominant two-way coupling effects.

In the first part of the thesis, isolated droplet vaporisation models are studied and several models are evaluated. The problem of droplet interaction is briefly explained using some simple simulations and general theoretical ideas and the concept of group combustion is introduced.

In the second part of the thesis the hybrid Lagrangian-Lagrangian method is presented. The continuum phase is described by the transport equation for the joint mass density function (MDF) of velocity and composition, which is solved indirectly using a Monte Carlo particle method where Langevin type equations are solved. This method is augmented by a finite volume method where the mean Eulerian transport equations for momentum, Reynolds stresses and turbulence dissipation are solved, making it a hybrid approach for the continuum phase. The dispersed phase is described solely by the droplet MDF which is also solved using a Monte Carlo method.

A novel modification of the turbulence model for the pressure rate of strain in the Eulerian transport equation for the Reynolds stresses is presented that takes into account the effect of the presence of particles and the effect of mass transfer.

The models in the Langevin equation in the Lagrangian formulation are then modified in order to be consistent with the pressure rate of strain model in the Eulerian formulation. The modification of the diffusion term in the Langevin equation implies a modification of Kolmogorov's hypothesis regarding the first order Lagrangian structure function.

An investigation of the transport equation for the scalar dissipation rate shows that Lagrangian mixing models are affected by liquid particle vaporisation. Other theoretical developments are the extension of the Generalised Gradient diffusion

model and the Daly Harlow model for the triple correlations and an exact expression for the effect of mass transfer on the turbulence dissipation.

In the third part of this thesis the results of numerical simulations of two test cases are presented. In the first test case an Eulerian-Lagrangian approach was used and the influence of the modification of the model for the pressure rate of strain by the presence of particles is investigated for an axially symmetric non-burning turbulent dispersed spray and compared with experimental data. Small improvements in turbulence quantities over the conventional turbulence and two-way coupling model are noticed when the novel modification of the pressure rate of strain is being used.

In the second test case, simulations of an axially symmetric turbulent spray flame are performed to illustrate the performance of the complete hybrid method proposed in this thesis. A good agreement with experimental data was found using the hybrid method. In the mass transfer controlled spray flame studied in this thesis, taking into account the reduction of the drag coefficient and the heat and mass transfer coefficient due to mass transfer turned out to be crucial to the performance of the method.

SAMENVATTING

PDF modellering en deeltjes-turbulentie interactie van turbulente spray vlammen

Turbulente spray vlammen komen voor in veel toepassingen, zoals Diesel motoren, raket motoren en energiecentrales. De vele praktische toepassingen zijn een motivatie om de fysische fenomenen die voorkomen in turbulente spray vlammen nader te onderzoeken met als doel om ze beter te kunnen begrijpen, voorspellen en optimaliseren.

Een turbulente spray vlam is een twee-fasen systeem bestaande uit een turbulent reagerende gasfase en een vloeibare gedispergeerde (druppeltjes) fase. In dit proefschrift wordt de interactie tussen deze twee fases bestudeerd, en met name de effecten van verdamping en de effecten van de aanwezigheid van druppeltjes op de turbulentie van de gasfase (het two-way coupling effect). Het hoofddoel van het onderzoek is het ontwikkelen en valideren van stochastische Lagrangiaanse modellen voor turbulente spray vlammen die gekarakteriseerd worden door significante of dominante two-way coupling effecten.

In het eerste deel van dit proefschrift worden verdampingsmodellen voor geisoleerde druppeltjes bestudeerd en gevalideerd. Het probleem van druppeltjes interactie wordt kort behandeld door middel van enkele simpele modellen en een theoretisch kader wordt geschetst van het begrip groepsverbranding ('group combustion').

In het tweede deel van dit proefschrift wordt de hybride Lagrangiaans- Lagrangiaanse methode gepresenteerd. De gasfase en de druppeltjesfase worden beschreven door een transportvergelijking voor de massa dichtheidsfunctie (de MDF). Deze vergelijking wordt indirect opgelost door middel van het oplossen van Langevin vergelijkingen in een Monte Carlo deeltjesmethode. De gasfase Monte Carlo methode wordt aangevuld met een eindige volume methode waarmee de gemiddelde Euleriaanse transportvergelijkingen voor impuls, Reynolds spanningen en turbulentie dissipatie worden opgelost. In dit proefschrift wordt speciale aandacht geschonken aan de consistentie van deze twee methoden. Een innovatieve aanpassing van het turbulentiemodel voor de *pressure rate of strain* in de Euleriaanse transportvergelijking voor de Reynolds spanningen wordt beschreven waarin het effect van de aanwezigheid van druppels en het effect van verdamping wordt meegenomen. Het Langevin model in de Lagrangiaanse formulering wordt op zodanige wijze aangepast dat het Langevin model zo consistent mogelijk is met het Euleriaanse model. De aanpassingen van de diffusieterm in de Langevin vergelijking impliceert een modificatie van de hypothese van Kolmogorov voor de eerste orde Lagrangiaanse structuurfunctie.

Een nadere beschouwing van de transport vergelijking voor de scalaire dissipatie snelheid laat zien dat ook Lagrangiaanse mengmodellen beinvloed worden

door de verdamping van aanwezige druppeltjes. Andere theoretische ontwikkelingen die beschreven worden zijn de uitbreiding van het gegeneralizeerde gradient diffusie model en het model van Daly-Harlow, die de derde orde correlaties beschrijven. Ook wordt een exacte uitdrukking gegeven voor het effect van verdamping op de turbulentie dissipatie.

In het derde deel van dit proefschrift worden numerieke resultaten van twee testgevallen gepresenteerd. In het eerste testgeval wordt een Euleriaanse methode voor de gasfase en een Lagrangiaanse methode voor de gedispergeerde fase gebruikt om de invloed van de aanpassingen in het turbulentie model te onderzoeken. Een axiaal-symmetrische niet isotherme spray wordt onderzocht en de numerieke resultaten worden vergeleken met experimentele data. Geconstateerd wordt dat kleine verbeteringen in de voorspellingen van de Reynolds spanningen optreden wanneer het aangepaste model gebruikt wordt. In het tweede testgeval zijn simulaties van een axiaal-symmetrische turbulente spray vlam uitgevoerd om de prestaties van het complete hybride model te illustreren. In deze door massaoverdracht gedomineerde spray is het vooral de reductie van de weerstandscoefficient en de warmte- en massaoverdrachtscoefficient door massaoverdracht die cruciaal blijkt te zijn om goede overeeenkomsten met de experimenteel verkregen waarden te verkrijgen.

CONTENTS

CHAPTER 1

Introduction

1.1 Background and Motivation

The evaporation and combustion of droplets and sprays has been studied extensively (experimentally as well as numerically) because of their numerous important applications, including spark-ignition engines, diesel engines, aircraft propulsion systems, liquid rocket engines, liquid fuelled furnaces, etc. However, the major focus has always been the experimental and numerical study of either a single, isolated vaporising or burning droplet [149, 150] or the experimental investigation of atomisation and burning of fuel sprays [16, 49, 50, 51]. Whereas the experimental and numerical studies of isolated droplets were performed under idealised conditions (no turbulence, fast chemistry), the (mainly experimental) studies on spray combustion focused on a wide range of complex phenomena like primary and secondary break-up, ignition, dispersion and gas-droplet interaction. Although this has led to a lot of insights and knowledge about spray combustion, numerical simulations of spray flames have long been limited to simple locally homogeneous flow (where gas and droplet velocity are the same) and $k-\epsilon$ type flow simulations with simple chemistry. More complex numerical simulations of practical sprays that were studied experimentally have been computationally too expensive until very recently.

1.2 PDF methods

Probability Density Function (PDF) methods maintain a high level of physical detail, while still remaining computationally attractive. Since their introduction in the beginning of the 1980s [127, 128, 130], PDF methods have become standard methods to compute reacting gas flows. In PDF methods, the problem of turbulent reacting flows is attacked from a statistical point of view and a model transport equation of the probability density function (PDF) of composition and/or velocity is being solved [117, 180]. This high dimensional transport equation is computationally unattractive to solve by direct integration. It has long been known that there is a direct relationship between this transport equation of the PDF (which is a Fokker-Planck type equation) and stochastic equations of motion, also known as Langevin equations [56, 120, 136]. The general form of the Langevin equation for velocity is:

$$dU_i(t) = G_{ij}(U_i(t) - \widetilde{U}_i(t))dt + B_{ij}dW_i(t), \tag{1.1}$$

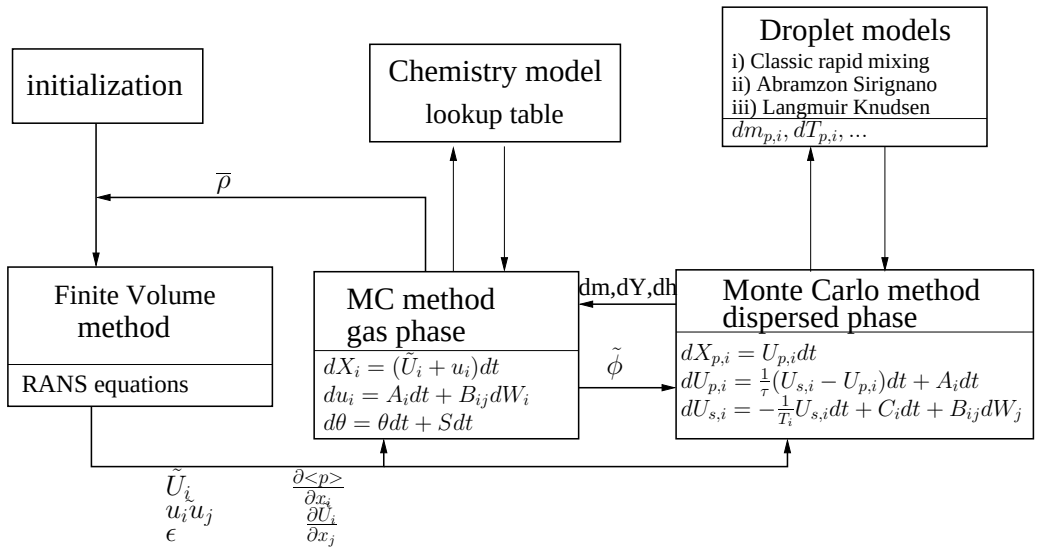

Figure 1.1: Sketch of the hybrid Finite Volume - Monte Carlo modelling approach.

where $G_{ij}(x,t)$ and $B_{ij}(x,t)$ are constants that depend only on the local values of the mean Reynolds stresses, turbulence dissipation and the mean velocity gradients. $dW_i(t)$ is a Wiener process [56, 136]. Solving the transport equation of the PDF indirectly by solving Langevin equations for stochastic particles is called a Monte Carlo (MC) method. Since the solution of (stochastic) Lagrangian equations of motion like equation (1.1) is computationally more attractive than solving a high-dimensional transport equation for the PDF, and since it can be easily implemented, solving the transport equations indirectly by means of a Monte Carlo method is the preferable approach. There is a big advantage of PDF methods over Reynolds Averaged Navier Stokes (RANS) methods, in which only transport equations for the first and second moments of velocity are solved. In PDF methods the reaction source term appears in closed form, which makes it especially appealing for solving reacting flow problems [72].

Using a Monte Carlo method also has a drawback. The velocities of the computational particles present in a finite volume cell in the solution domain are used to compute the mean velocity in this cell. When the number of computational particles is low, there will be a statistical error in the mean velocity. This mean velocity is then used in the Langevin equation (1.1) to compute the evolution of the individual computational particles. This feed-back mechanism leads to a *bias* error, which is a deterministic error, but with a statistical cause [183, 184]. A solution to this problem is to calculate the mean velocities and mean Reynolds stresses using a Finite Volume (FV) method, with which the Reynolds Averaged Navier Stokes equations are being solved. Only a Langevin equation for the *fluctuating* velocity is solved with the Monte Carlo method. This hybrid FV-MC method can lead to possible inconsistencies between the second moments of velocity computed in the

Finite Volume method and those computed using the Langevin equations in the Monte Carlo method. The relationships between second moment closures and the Lagrangian equations of turbulence have been investigated in detail in the past for single phase flows [129]. However, these relationships have not been extended for multiphase flow problems. In multiphase flows, more than one phase is present in the flow. In polydispersed two-phase flows, which will be the focus of this thesis, liquid droplets (the dispersed phase) of varying diameter are transported by the turbulent carrier fluid (the gas phase). In a hot or reacting environment, these droplets will vaporise and the droplet diameter will change. The dispersion -or spreading- of solid or liquid particles in a turbulent flow depends on the particle diameter. Extensive research about Lagrangian models for polydispersed two-phase flows can be found in the literature [60, 89, 109, 110, 117, 122]. Because Lagrangian equations of motion are used for both simulations of the gas phase and the dispersed phase we denote our approach as a 'Lagrangian-Lagrangian' approach, different from the more standard Eulerian-Lagrangian approach. In this thesis some time will be spent on examining a specific dispersion model. However, the major part of the thesis will focus on the interaction between the dispersed phase and the gas phase.

1.3 Gas-particle interaction

In dispersed two phase flows, the presence of liquid or solid particles will disturb the flow of the gas phase. When the particle mass loading, which is the ratio of the total particle mass over the total mass of the gas phase, in a small finite volume is high, the disturbances may not be negligible anymore. Extra source terms that take into account momentum transfer, interphase mass transfer and transfer of transported scalars (e.g. heat), appear in the transport equation of the PDF as well as in the RANS equations [39, 58, 60, 89]. When the mass loading increases further, some assumptions may need to be re-evaluated to ascertain their validity in dispersed two-phase flows. In sprays, droplets may not be considered to be isolated anymore; neighboring droplets will compete for oxygen (or for heat, in the case of vaporisation), their vaporisation rate will be changed, as well as their drag, heat transfer, etc. Droplet-vaporisation interaction effects, which is an important feature of *group combustion*, may become a dominant feature of the spray flame.

The mixing of the fuel vapour with the air as well as the dispersion of liquid particles is mostly governed by the turbulence characteristics of the gas phase. A better understanding of the interaction between particles and turbulence, and of the vaporisation modulation of particles due to turbulence and interaction with other particles will not only be of academic importance, but will also be of use in the industry, where complex flow solvers are used to design and develop multiphase flow and combustion devices.

It is therefore interesting to identify the main interaction mechanisms and to as-

sess their importance in turbulent spray flames. The main interaction mechanisms identified and studied in this thesis are:

- The influence of the gas on the particle phase (one-way coupling);
- The momentum interaction between the gas and the particles (two-way coupling);
- The interaction between particle vaporisation and transported scalars like heat and fuel vapour (two-way coupling, group combustion).

1.4 Objectives of the research

In hybrid Lagrangian-Lagrangian simulations of turbulent spray flames, the interaction between droplets and the gas phase is extremely important. The main objective of this study is to develop a Lagrangian turbulence model that takes into account the effect of the presence of vaporising particles on the carrier phase, and to establish the relationship between Eulerian second moment closures and Lagrangian turbulence and mixing models. Knowing these relationships will lead to a consistent hybrid model for the continuum phase.

Once these relationships are established, it is important to compare simulation results of this approach with experimental data to establish its performance and to compare simulation results with different models with each other to establish the importance of the model improvements. A second objective is therefore to assess the model performance of the turbulence and mixing models in turbulent spray flames.

1.5 Outline of this thesis

This thesis consists of 8 chapters and 1 appendix. The first chapter is this introduction and in the last chapter, conclusions and perspectives are given. In chapter 2, we will consider the heating, vaporisation and burning of a single isolated particle. A review of currently used models is given. We will also discuss the vaporisation modulation of a pair of droplets and a cloud of droplets, known as group combustion.

Chapter 3 treats the (Eulerian) Reynolds averaged transport equations. Special attention is paid to the effect of the presence of particles on the gas phase: the two-way coupling effect. Chapter 4 treats the Lagrangian approach of the gas phase. The Langevin model is chosen in such a way that it is consistent with the Eulerian transport equations, specifically the model for the pressure rate of strain. Chapter 5 introduces the Lagrangian modelling approach for the dispersed phase and discusses in detail the Lagrangian dispersion model. In Chapter 6, the effect

of the modifications of the turbulence model is shown using a polydispersed non-evaporating spray. In chapter 7, the simulation results of a methanol spray flame are used to establish the performance of the hybrid PDF method to turbulent spray flames. In Chapter 8 the main conclusions, which were already given at the end of each chapter, are briefly discussed and recommendations for future research are given. Finally, in the appendix the stochastic integration method that was used to integrate the system of stochastic equations of motion describing the dispersed phase is given in appendix A.

CHAPTER 2

Isolated and interacting fuel droplet vaporisation and combustion

The evaporation and combustion of an isolated droplet is considered in this chapter. Several vaporisation models are presented and compared under different circumstances. The single droplet evaporation models are sensitive to the way thermodynamic properties are evaluated, and a lot of freedom exists in the evaluation method. This aspect of the model is investigated. A brief literature review of vaporisation modulation due to neighboring droplets is given and the concept of droplet interaction in sprays and 'group combustion' is presented.

2.1 Introduction

Since a spray flame contains droplets, a first step towards modelling a complete spray is to be able to model a single, isolated vaporising or burning fuel droplet. Many single droplet model studies can be found in the literature, experimental [25, 93, 119, 179] as well as numerical [3, 108, 145, 149, 150, 167]. In this chapter some standard single droplet vaporisation and heat transfer models are given

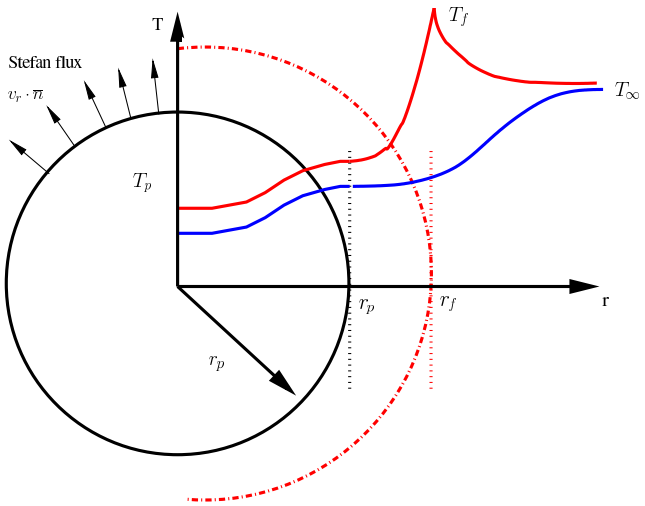

Figure 2.1: Temperature profiles for an isolated vaporising droplet and a burning droplet.

and their performances are compared with each other as well as with experimental data. The detailed explanation about the derivation of the single droplet mass vaporisation rate in section (2.2) will aid in the understanding of the problems occurring in vaporisation modulation of interacting droplets. The numerical simulations were performed for two specific fuels, namely n-decane and methanol. N-decane fuel droplet vaporisation is interesting to study from a practical point of view since it is a main component of gasoline. Its chemistry can however be quite complex and in academic studies of spray flames, chemically simple fuels are sometimes used to reduce the complexity and to isolate and study a specific phenomenon. This is why methanol fuel vaporisation and burning is also studied here. Another advantage of using methanol fuel, which is closely related to its simple chemistry, is that hardly any soot formation occurs. The spray flames studied later in this thesis both use methanol as a fuel, so the single droplet model performance of the methanol droplet simulations can give insights into the performance of the spray flame simulations.

Although studies of isolated droplets can give us valuable information that can be used to analyse the performance of spray flame simulations, droplets cannot always be considered isolated in sprays [3, 15, 150, 167]. Apart from the occurrence of particle collisions, fuel vapour from neighboring droplets and local flame structures will invalidate the assumptions made in the single droplet vaporisation models. A review of vaporisation interaction of two droplets at small separation distances and the interaction of droplet clouds is given in the second part of this chapter.

2.2 Detailed droplet evolution equations

In this section we will consider a spherically symmetric droplet which is evaporating or burning in a stagnant hot gas without convection, see Figure (2.1). The flow around the droplet is caused only by the Stefan flux $\rho_{\mathrm{g}} v_{\mathrm{g}}$ (the mass flux at the droplet interface in the direction of the outward normal) due to evaporation. Oxygen diffuses to the surface and fuel diffuses to the environment. Heat radiation is neglected for now. The heat released from the flame zone is transferred on one side of the flame sheet located at r_{flame} to the droplet and on the other side to the environment.

Gaseous phase The governing equations of continuity, energy (temperature) and species concentration can be simplified to a one-dimensional system of partial dif-

ferential equations and can be written in spherical coordinates as:

$$\begin{aligned}
\frac{\partial \rho_{\mathrm{g}}}{\partial t} + \frac{1}{r^2}\frac{\partial}{\partial r}(r^2 \rho_{\mathrm{g}} v_{\mathrm{g}}) &= 0 \\
\rho_{\mathrm{g}}\frac{\partial Y_{\mathrm{g},i}}{\partial t} + \rho_{\mathrm{g}} v_{\mathrm{g}}\frac{\partial Y_{\mathrm{g},i}}{\partial r} &= -\frac{1}{r^2}\frac{\partial}{\partial r}(r^2 \rho_{\mathrm{g}} Y_{\mathrm{g},i} V_{r,i}) + \omega_{\mathrm{g},i} \\
\rho_{\mathrm{g}} C_{p_{\mathrm{g}}}\frac{\partial T_{\mathrm{g}}}{\partial t} + \rho_{\mathrm{g}} C_{p_{\mathrm{g}}} v_{\mathrm{g}}\frac{\partial T_{\mathrm{g}}}{\partial r} &= +\frac{1}{r^2}\frac{\partial}{\partial r}(r^2 \lambda_{\mathrm{g}}\frac{\partial T_{\mathrm{g}}}{\partial r}) - \rho_{\mathrm{g}}\sum_{i=1}^{n}(Y_{\mathrm{g},i} V_{r,i} C_{p_{\mathrm{g},i}})\frac{\partial T_{\mathrm{g}}}{\partial r} - \sum_{i=1}^{n}\omega_{\mathrm{g},i} H_{\mathrm{g},i}
\end{aligned} \tag{2.1}$$

In these equations, t is time and r is the radial distance from the centre of the droplet. $\rho_{\mathrm{g}}, T_{\mathrm{g}}, C_{p_{\mathrm{g}}}, v_{\mathrm{g}}$ and λ_{g} are the density, temperature, heat capacity (at constant pressure), fluid velocity in radial direction and the thermal conductivity of the gas at (t, r). $Y_{\mathrm{g},i}, V_{r,i}, \omega_{\mathrm{g},i}, C_{p_{\mathrm{g},i}}$ and $H_{\mathrm{g},i}$ are the mass fraction, diffusion velocity, gas phase mass production rate, heat capacity (at constant pressure) and enthalpy (of combustion) of the gaseous i^{th} species of a total of n species that are being considered. These equations are augmented by two algebraic equations. The first is the equation of state:

$$\rho_{\mathrm{g}}\sum_{i=1}^{n}\frac{Y_{\mathrm{g},i}}{W_i} = \frac{\mathrm{p}}{RT_{\mathrm{g}}}, \tag{2.2}$$

with p pressure, R the universal gas constant $R = 8.314 J\cdot K^{-1}\cdot \mathrm{mole}^{-1}$ and W_i the molar weight of species i. The second algebraic equation is a general form of Ficks law for the diffusion velocity $V_{r,i}$:

$$V_{r,j} = \frac{-1}{X_{\mathrm{g},i}\overline{W}}\frac{\sum_{j\neq i}^{n} X_{\mathrm{g},j} W_j}{\sum_{j\neq i}^{n}\frac{X_{\mathrm{g},j}}{\Delta_{ji}}}\frac{\partial X_{\mathrm{g},i}}{\partial r} - \frac{I\!D^{T}_{\mathrm{g},i}}{\rho_{\mathrm{g}} Y_{\mathrm{g},i}}\frac{1}{T_{\mathrm{g}}}\frac{\partial T_{\mathrm{g}}}{\partial r}, \tag{2.3}$$

where $X_{\mathrm{g},i}$ is the mole fraction and W_i is the molecular weight of the i^{th} species. $\overline{W}$ is the average molecular weight of the mixture and $I\!D^{T}_{\mathrm{g},i}$ is the thermal diffusion coefficient of the i^{th} species. Δ_{ji} is the binary diffusion coefficient of Hirschfelder. Mole fractions and mass fractions are related by:

$$Y_i = \frac{X_i W_i}{\sum_{i=1}^{n} X_i W_i}, X_i = \frac{Y_i/W_i}{\sum_{i=1}^{n} Y_i/W_i}. \tag{2.4}$$

The evaluation of the thermodynamic properties are not discussed here, but standard methods can be found in e.g. [126] or [78, 79, 80].

Liquid phase The governing equations of mass, species and energy conservation for the liquid phase are given by:

$$\begin{aligned}
\frac{\partial \rho_l}{\partial t} + \frac{1}{r^2}\frac{\partial}{\partial r}(r^2 \rho_l v_l) &= 0 \\
\rho_l \frac{\partial Y_{l,i}}{\partial t} + \rho_l v_l \frac{\partial Y_{l,i}}{\partial r} &= \frac{1}{r^2}\frac{\partial}{\partial r}(r^2 \rho_l \mathbb{D}_l \frac{\partial Y_{l,i}}{\partial r}) \\
\rho_l C_{p_l} \frac{\partial T_l}{\partial t} + \rho_l C_{p_l} v_l \frac{\partial T_l}{\partial r} &= \frac{1}{r^2}\frac{\partial}{\partial r}(r^2 \lambda_l \frac{\partial T_l}{\partial r}),
\end{aligned} \tag{2.5}$$

where it is assumed that no reactions occur in the liquid phase. For a multicomponent droplet, the different components are assumed to be perfectly mixed with equal diffusivities and the liquid thermodynamic properties can be described by the mixture values of the liquid density ρ_l, the diffusion coefficient $\mathbb{D}_l$ and the liquid heat capacity C_{p_l}.

Boundary conditions Neumann (symmetry) boundary conditions at $r = 0$ and Dirichlet boundary conditions at $r = \infty$ are applied:

$$\left.\frac{\partial Y_{l,i}}{\partial r}\right|_{r=0} = 0 \quad , \quad \left.\frac{\partial T_l}{\partial r}\right|_{r=0} = 0 \tag{2.6}$$

$$Y_{\mathrm{g},i}(\infty, t) = Y_{\mathrm{g},i_\infty} \quad , \quad T_{\mathrm{g}}(\infty, t) = T_{\mathrm{g}_\infty} \tag{2.7}$$

At the interface $r = r_{\mathrm{p}}$, the gas and liquid temperature are assumed equal to each other ($T_{\mathrm{g}} = T_l$) and the droplet radius decrease, temperature gradient and species gradients at the interface are given by:

$$\frac{dr_{\mathrm{p}}}{dt} = \left.\left(v_l - (v_{\mathrm{g}} - v_l)\frac{\rho_{\mathrm{g}}}{\rho_l}\right)\right|_{r=r_{\mathrm{p}}} \tag{2.8}$$

$$V_{r,i} = v_{\mathrm{g}}(\epsilon_i - Y_{\mathrm{g},i}) \tag{2.9}$$

$$\rho_l \mathbb{D}_l \frac{\partial Y_{l,i}}{\partial r} - (v_{\mathrm{g}} - v_l)\rho_{\mathrm{g}}(Y_{l,i} - \epsilon_i) = 0 \tag{2.10}$$

$$\lambda_l \frac{\partial T_l}{\partial r} - \lambda_{\mathrm{g}} \frac{\partial T_{\mathrm{g}}}{\partial r} - \rho_{\mathrm{g}}(v_{\mathrm{g}} - v_l)L = 0, \tag{2.11}$$

where r_{p} is the interface location (i.e. the droplet radius) and L is the total latent heat of vaporisation of the mixture:

$$L = \sum_{i=1}^{n} \epsilon_i L_i, \tag{2.12}$$

with ϵ_i is the fractional gasification rate of the i^{th} species, which is defined as:

$$\epsilon_i = \frac{\dot{m}_{\mathrm{p}_i}}{\sum_{i=1}^{n} \dot{m}_{\mathrm{p}_i}}. \tag{2.13}$$

By definition, the fractional gasification rate is zero for species which do not condense into the liquid phase. A negative fractional gasification rate indicates that there is an inward flux from the gas phase into the liquid phase over the interface for that species. This condensation occurs for instance in the burning of methanol droplets where water, which is formed as a combustion product, is absorbed by the methanol droplet [97, 187]. The fractional gasification rate is found using

$$\rho_{\mathrm{g}} v_{\mathrm{g}} \epsilon_i = \rho_{\mathrm{g}} v_{\mathrm{g}} Y_{\mathrm{g},i} - \rho_{\mathrm{g}} I\!D_{\mathrm{g}} \frac{\partial Y_{\mathrm{g},i}}{\partial r}. \tag{2.14}$$

The first interface condition equation (2.8) describes the balance of the interface location r_{p} by momentum on the liquid phase side and momentum on the gas phase side. The second condition (2.9) implies that the diffusion velocity of each of the species at the interface is the balance between the fraction of the radial velocity of the gas phase due to gasification and the local gas phase mass fraction of the species. The third condition (2.10) describes a similar balance saying that the interface concentration gradient is due to the balance between local concentration and gasification. The last equation (2.11) describes the heat balance at the interface, which is given by the difference in conductive fluxes and the heat required for vaporisation. In this equation, L_i is the latent heat of vaporisation of the i^{th} species, evaluated at temperature T_{p}. Gas phase equilibrium at the interface is assumed to obey the Clausius-Clapeyron equation:

$$X_{\mathrm{eq}}^{(I)} = \frac{p_{\mathrm{sat}}}{p_{\mathrm{atm}}} = \exp\left(\frac{L}{R/W_V}\left(\frac{1}{T_{\mathrm{boil}}} - \frac{1}{T_l^{(I)}}\right)\right), \tag{2.15}$$

where W_V is the molecular weight of the fuel vapour, T_{boil} is the boiling temperature of the liquid and $T_l^{(I)}$ is the particle temperature at the interface I located at r_{p}. When the internal liquid particle temperature is uniform, ($T_l(t,r) \rightarrow T_l(t)$), we will use the notation $T_l^{(I)} = T_{\mathrm{p}}$. The accuracy of expression (2.15) has been questioned by Bellan and Summerfield [5, 8] for droplet temperatures close to the boiling point and for very small droplet diameters, but is generally accepted to be valid throughout the droplet lifetime, e.g. in [150].

This already simplified one-dimensional system of differential equations (2.2)-(2.5) can be solved numerically and single droplet simulations can be found in the literature [25, 34, 77, 97]. The spatial resolution that is needed to accurately capture the numerical solution of these equations however is too large to be of practical use in spray combustion simulations. A more simplified approach is needed.

2.2.1 Derivation of the burning rate formula, or "d^2"-law

We will now consider a single component liquid fuel droplet with uniform (but not constant) temperature $T_{\rm p}(t)$ that is vaporising or burning in stagnant air. The classical derivation of the equation for the mass vaporisation rate was first reported by Spalding and Godsave and is detailed in standard works like Williams [178], Kuo [85], and others. The continuity equation can be written as

$$\frac{dm_{\rm p}}{dt} = 4\pi r^2 \rho_{\rm p} v_{\rm g} = \text{Constant}, \tag{2.16}$$

In a quasi-steady approach, the temperature and species equations are simplified to

$$\rho_{\rm g} v_{\rm g} C_{p_{\rm g}} \frac{dT_{\rm g}}{dr} = \frac{1}{r^2}\frac{d}{dr}(r^2 \lambda_{\rm g} \frac{dT_{\rm g}}{dr}) - \omega_T, \tag{2.17}$$

$$\rho_{\rm g} v_{\rm g} \frac{dY_{{\rm g},i}}{dr} = \frac{1}{r^2}\frac{d}{dr}(r^2 \rho_{\rm g} \mathbb{D}_{\rm g} \frac{dY_{{\rm g},i}}{dr}) + \omega_{{\rm g},i}. \tag{2.18}$$

Here, $\omega_T = \sum_{i=1}^{n} \omega_{{\rm g},i} H_{{\rm g},i}$. The only species considered are Fuel (F), Oxidiser (O), Products (P) and inert gas (N, usually Nitrogen) and we assume that reactions can be described by the one step reaction

$$\nu_F {\rm F} + \nu_O {\rm O} \rightarrow \nu_P {\rm P}. \tag{2.19}$$

Furthermore, all species are assumed to diffuse in the same way, having the same diffusion constant $\mathbb{D}_{\rm g}$. If we multiply the species and temperature equations by $4\pi r^2$ and use the continuity equation, we obtain:

$$\frac{d\dot{m}_{\rm p} C_{p_{\rm g}} T_{\rm g}}{dr} = \frac{d}{dr}(4\pi r^2 \lambda_{\rm g} \frac{dT_{\rm g}}{dr}) - 4\pi r^2 \omega_T, \tag{2.20}$$

$$\frac{d\dot{m}_{\rm p} Y_{{\rm g},i}}{dr} = \frac{d}{dr}(4\pi r^2 \mathbb{D}_{\rm g} \rho_{\rm g} \frac{dY_{{\rm g},i}}{dr}) + 4\pi r^2 \omega_i. \tag{2.21}$$

Since the mass fractions of the individual components sum to one, the nitrogen mass fraction can be found with the algebraic relationship $Y_N = 1 - Y_F - Y_O - Y_P$. The 8 boundary equations for the 4 remaining second order differential equations are determined by the ambient temperature and species concentration at $r = \infty$ and by the heat and mass flux at the droplet boundary. The energy boundary condition at the droplet boundary is given by the difference of conductive fluxes and the energy required for vaporising the liquid at the surface:

$$4\pi r_{\rm p}^2 \lambda_{\rm g} \frac{dT_{\rm g}}{dr}\bigg|_{r=r_{\rm p}^+} = \dot{q}_l - \frac{dm}{dt} L = \frac{dm}{dt} L_{\rm eff}, \tag{2.22}$$

with $\dot{q}_l = 4\pi \lambda_l r_{\rm p}^2 \frac{\partial T_l}{\partial r}\big|_{r=r_{\rm p}^-}$ the liquid phase conductive heat flux at the droplet surface approached from the liquid phase. At the liquid droplet surface, the sum

of Stefan convection and diffusion on the gas side is equal to the convection on the liquid side:

$$\frac{dm}{dt}Y_{\mathrm{g},i}^{(I)} - \rho_{\mathrm{g}}\mathbb{D}_{\mathrm{g}}4\pi r_{\mathrm{p}}^2\frac{dY_{\mathrm{g},i}}{dr}\bigg|_I = \frac{dm_{\mathrm{p}}}{dt}\delta_{iF}, \tag{2.23}$$

where the index $i = F, O, N, P$. Finally, the boundary equations at $r = \infty$ are prescribed Dirichlet boundary conditions. When all fuel vapour comes from the droplet then:

$$\begin{aligned} T_{\mathrm{g}}(\infty, t) &= T_\infty \\ Y_{\mathrm{g},F}(\infty, t) &= 0 \\ Y_{\mathrm{g},P}(\infty, t) &= 0 \\ Y_{\mathrm{g},O}(\infty, t) &= Y_{O,\infty} \\ Y_{\mathrm{g},N}(\infty, t) &= Y_{N,\infty} \end{aligned} \tag{2.24}$$

After integration of eq. (2.21) and using the boundary conditions at the interface, this leads to:

$$\frac{dm_{\mathrm{p}}}{dt}[C_{p_{\mathrm{g}}}(T_{\mathrm{g}_\infty} - T_{\mathrm{p}}) + L_{\mathrm{eff}}] = 4\pi r^2\lambda_{\mathrm{g}}\frac{dT_{\mathrm{g}}}{dr} + \int_{r_{\mathrm{p}}}^{r} 4\pi r^2\omega_T dr. \tag{2.25}$$

Integrating again, we obtain the final form of the equation for the vaporisation rate:

$$\frac{dm_{\mathrm{p}}}{dt} = \frac{1}{\int_{r_{\mathrm{p}}}^{\infty}(4\pi r^2\rho_{\mathrm{g}}\mathbb{D}_{\mathrm{g}})^{-1}dr}\ln\left[1 + \frac{\sum_{i=1}^{n}(\int_{T_{\mathrm{f}}^{(I)}}^{T_{\mathrm{g}\infty}} C_{p_{\mathrm{g},i}}dT) + \nu(Y_{\mathrm{g},O_\infty} - Y_{\mathrm{g},O}^{(I)})H_{\mathrm{g},F}}{L + \nu Y_{\mathrm{g},O}^{(I)}\Delta h_{\mathrm{g},F}}\right]. \tag{2.26}$$

If we now assume that $\frac{\lambda_{\mathrm{g}}}{C_{pg}} = \rho_{\mathrm{g}}\mathbb{D}_{\mathrm{g}} =$ constant, then we can evaluate the integrals in equation (2.26) from r_{p} to ∞ to obtain $\frac{dm_{\mathrm{p}}}{dt}$:

$$\frac{dm_{\mathrm{p}}}{dt} = 4\pi r_{\mathrm{p}}\frac{\lambda_{\mathrm{g}}}{C_{p_g}}\ln(1 + \frac{c_{\mathrm{p}}(T_{\mathrm{g}} - T_s)}{L_{\mathrm{eff}}}) = 4\pi r_{\mathrm{p}}\frac{\lambda_{\mathrm{g}}}{C_{p_{\mathrm{g}}}}\ln(1 + B_T), \tag{2.27}$$

$$\frac{dm_{\mathrm{p}}}{dt} = 4\pi r_{\mathrm{p}}\rho_{\mathrm{g}}\mathbb{D}_{\mathrm{g}}\ln(1 + \frac{Y_{F,I}}{1 - Y_{F,I}}) = 4\pi r_{\mathrm{p}}\rho_{\mathrm{g}}\mathbb{D}_{\mathrm{g}}\ln(1 + B_M). \tag{2.28}$$

In equation (2.28), the Spalding mass transfer coefficient B_M and the Spalding heat transfer coefficient B_T are defined as

$$B_M = \frac{Y_{\mathrm{g},F}^{(I)} - Y_{\mathrm{g},F_\infty}}{Y_{\mathrm{g},F_0} - Y_{\mathrm{g},F}^{(I)}}, \tag{2.29}$$

$$B_T = \frac{C_{p_\mathrm{g}}(T_{\mathrm{g}\infty} - T_\mathrm{g}^{(I)})}{L_\mathrm{eff}}, \tag{2.30}$$

where Y_{g,F_0} is the mass fraction of fuel in the interior of the droplet (which, in the case of a single component fuel, is equal to one). Here, λ_g is the thermal conductivity of the gas. The specific enthalpy of species i is $h_i = \int_{T_0}^{T} C_{p_{\mathrm{g},i}} dT + H_{\mathrm{g},i}$, with $H_{\mathrm{g},i}$ the specific formation enthalpy of species i.

This equation can be rewritten as the well-known d^2 law by using

$$\frac{d\dot{m}_\mathrm{p}}{dt} = 4\pi r_\mathrm{p}^2 \rho_l \frac{dr_\mathrm{p}}{dt} = \frac{\pi r_\mathrm{p}}{2} \rho_l \frac{d(d_\mathrm{p}^2)}{dt}, \tag{2.31}$$

where $d_\mathrm{p} = 2r_\mathrm{p}$. If we now define the burning rate constant as $K = \frac{d(d_\mathrm{p}^2)}{dt}$, the vaporisation law can be rewritten as

$$d_\mathrm{p}^2(t) = d_\mathrm{p}^2(0) - Kt. \tag{2.32}$$

The constant K can be calculated from equation (2.28) as

$$K = 8\frac{\rho_\mathrm{g}}{\rho_l} I\!D_\mathrm{g} \ln(1 + B_M), \tag{2.33}$$

and an estimation of the droplet lifetime is then simply $t_\mathrm{p} = d_\mathrm{p}^2(0)/K$.

If the droplet is vaporising in a gaseous environment the thermodynamic properties of the surroundings will in principle be spatially varying. Then, the integral expression in the detailed burning rate equation (2.26) cannot be simply reduced to a constant. This is an important observation. It shows that the vaporisation rate depends on the volume integrated properties of the gas phase. The volume integration can be represented by a single value for the thermodynamic properties. Determining the temperature at which the thermodynamic properties need to be evaluated is important to realise a good performance of the vaporisation model. Several models for the temperature seen have been proposed in the literature [108, 149, 186]. Droplets with low boiling points in high temperature environments will quickly reach their wet-bulb temperature. When diffusion to the environment is slow, the droplet is assumed to be immersed in its own fuel gas having a temperature T_wb or T_boil and the temperature used to evaluate the thermodynamic properties is either the wet-bulb or boiling temperature. Yuen and Chen on the other hand suggest a $\frac{1}{3}$ rule to evaluate this temperature. The vapour mass fraction and temperature $(Y_\mathrm{m}, T_\mathrm{m})$ at which the gas phase properties will be evaluated are determined using:

$$T_\mathrm{m} = T_\mathrm{p} + \frac{1}{3}(T_\mathrm{s} - T_\mathrm{p}) \quad \text{and} \quad Y_\mathrm{m} = Y_\mathrm{surf} + \frac{1}{3}(Y_\mathrm{s} - Y_\mathrm{surf}), \tag{2.34}$$

where T_s and Y_s are the gas phase temperature and gas phase mass fraction of the environment 'seen' by the droplet. Yuen and Chen [186] also advocate the use

of a '1/3' rule to calculate the dynamic viscosity used to determine the droplet Reynolds number (defined below):

$$\mu_{\mathrm{m}} = \mu_{\mathrm{surf}} + \frac{1}{3}\left(\mu_{\mathrm{s}} - \mu_{\mathrm{surf}}\right). \tag{2.35}$$

In turbulent evaporating spray simulations without combustion it was shown that the mean vaporisation rate will not be affected much when temperature variations in the surrounding gas are taken into account, although individual droplet evolution (of variance or diameter) may be significantly affected by temperature variations [13].

2.3 Empirical correlation based models for convective droplet heating

2.3.1 Infinite conductivity model for droplet temperature evolution

The droplet temperature evolution is determined by a balance between conductive heating and evaporative cooling. When the liquid thermal conductivity is infinitely fast, the temperature of the droplet can be considered uniform, but time-varying. Models of this type are called infinite conductivity or rapid mixing models. Using Newtons law for the convective heat transfer to the droplet, the temperature evolution of the droplet is given by:

$$m_{\mathrm{p}} C_{p_l} \frac{dT_{\mathrm{p}}}{dt} = \mathrm{Nu}\pi\lambda_{\mathrm{g}}(T_{\mathrm{s}} - T_{\mathrm{p}}) - L\dot{m}_{\mathrm{p}}. \tag{2.36}$$

In this equation, C_{p_l} is the liquid heat capacity, λ_{g} is the thermal conductivity of the gas phase and Nu is the Nusselt number. The Nusselt number is the nondimensional heat transfer coefficient and tells about the relative importance of convection over heat diffusion. It can be determined with the Ranz-Marshall correlation:

$$\mathrm{Nu} = 2 + 0.552\mathrm{Re}_{\mathrm{p}}^{1/2}\mathrm{Pr}_{\mathrm{g}}^{1/3}, \tag{2.37}$$

where the Prandtl number is defined as

$$\mathrm{Pr}_{\mathrm{g}} = \frac{\mu_{\mathrm{g}} C_{p_{\mathrm{g}}}}{\lambda_{\mathrm{g}}}. \tag{2.38}$$

A different way of writing the evolution equation of temperature to take into account different model assumptions can be found in Miller *et al*. [108]:

$$\frac{dT_{\mathrm{p}}}{dt} = \frac{f_2 \mathrm{Nu}}{3Pr_{\mathrm{g}}} \frac{C_{p_{\mathrm{g}}}}{C_{p_l}} \frac{(T_\infty - T_{\mathrm{p}})}{\tau_{\mathrm{p}}^{\mathrm{St}}} - \frac{\dot{m}_{\mathrm{p}}}{m_{\mathrm{p}}} \frac{L(T_{\mathrm{p}})}{C_{p_l}}, \tag{2.39}$$

with $\tau_{\mathrm{p}}^{\mathrm{St}}$ the particle characteristic time scale in Stokes flow:

$$\tau_{\mathrm{p}}^{\mathrm{St}} = \frac{\rho_{\mathrm{p}} d_{\mathrm{p}}^2}{18\mu_{\mathrm{g}}}. \tag{2.40}$$

Due to the balance between heating and cooling, liquid droplets usually do not reach the boiling point of the liquid when they are heated. Instead, the temperature evolves towards the wet-bulb temperature. An estimation of the wet-bulb temperature can be obtained by setting the left-hand side of equation (2.39) to zero [31]. When droplets are placed in a very hot carrier gas, they will reach the wet-bulb temperature quickly. The wet-bulb temperature can then be used instead of the evolution equation of the droplet temperature. When the carrier gas is hot and the boiling point of the liquid is low, the wet-bulb temperature will be close to the boiling temperature of the liquid.

The standard d^2 law together with an infinite conductivity model for the droplet temperature typically overpredicts the vaporisation rate, leading to shorter droplet lifetimes. Some corrections have been proposed in the literature [1, 108, 145]. We will consider two of them, the model of Abramzon and Sirignano [1] and the model of Miller, Harstad and Bellan [108].

2.3.2 Forced convection

When a droplet is exposed to forced convection, fuel vapour surrounding the droplet will convect away and the vaporisation rate is enhanced. The effect of forced convection can be implemented using the Nusselt number. Assuming a stagnant film with radius r_1 surrounding the droplet and assuming a balance between heat conduction in the film and heat convection in the surroundings, then

$$Q = \pi d_{\mathrm{p}}^2 h(T - T_s) = \pi \frac{d_1 d_{\mathrm{p}} \lambda}{r_1 - r_{\mathrm{p}}}(T - T_s). \tag{2.41}$$

The radius r_1 of the stagnant film surrounding the droplet is a function of Nu,

$$r_1 = r_{\mathrm{p}} \frac{\mathrm{Nu}}{\mathrm{Nu} - 2}, \tag{2.42}$$

where Nu is given by equation (2.37). Instead of using $r = \infty$ as the upper boundary of the integral in equation (2.26), we can use $r = r_1$ as the upper boundary and the evaporation rate can now be written as:

$$\frac{dm_{\mathrm{p}}}{dt} = \pi d_{\mathrm{p}} \frac{\lambda_{\mathrm{g}}}{C_{p_l}} \mathrm{Nu} \ln(1 + B_T). \tag{2.43}$$

The d^2 law can now be obtained by using the definition of the evaporation rate:

$$\frac{dm_{\mathrm{p}}}{dt} = 4\pi r_{\mathrm{p}}^2 \rho_l \frac{dr_{\mathrm{p}}}{dt} = \frac{\pi r_{\mathrm{p}}}{2} \rho_l \frac{d(d_{\mathrm{p}}^2)}{dt}. \tag{2.44}$$

We can now write the mass vaporisation rate as a d^2 law including the Nusselt number as:

$$\frac{d(d_{\mathrm{p}}^2)}{dt} = 4\mathrm{Nu}\frac{\lambda_{\mathrm{g}}}{\rho_l C_{p_{\mathrm{g}}}}\ln(1+B_T) \tag{2.45}$$

$$d_{\mathrm{p}}^2(t) = d_{\mathrm{p}}^2(0) - 4\mathrm{Nu}\frac{\lambda_{\mathrm{g}}}{\rho_l C_{p_{\mathrm{g}}}}\ln(1+B_T)\cdot t, \tag{2.46}$$

or equivalently:

$$d_{\mathrm{p}}^2(t) = d_{\mathrm{p}}^2(0) - 4\mathrm{Nu}\frac{\rho_{\mathrm{g}}}{\rho_l}\mathbb{D}_{\mathrm{g}}\ln(1+B_M)\cdot t. \tag{2.47}$$

Unfortunately, the vaporisation rate is very sensitive to the way the thermodynamic properties in equations (2.46,2.47) are evaluated. In droplet vaporisation modelling, the thermodynamic properties are functions of temperature T and composition(mass fraction) Y. The question is at which temperature T and composition Y the thermodynamic properties should be evaluated, since (T,Y) can vary between the values at the droplet surface and the values of the undisturbed fluid flow. Often, the '1/3' rule [186] is used:

$$T = T_{\mathrm{p}} + \frac{1}{3}(T_\infty - T_{\mathrm{p}}), \tag{2.48}$$

$$Y = Y_I + \frac{1}{3}(Y_\infty - Y_I). \tag{2.49}$$

$$\tag{2.50}$$

This approach is also adopted here, although we will also compare numerical results using different assumptions.

Several detailed studies of the effects of convective heat transfer of a liquid droplet on the Nusselt number, Sherwood number and drag coefficient can be found in the literature [1, 14, 52, 150].

2.4 The effect of Stefan flow

Abramzon and Sirignano [1] revised the infinite conductivity model to incorporate the effects of Stefan flow on heat and mass transfer. This approach is based on the so-called 'thin-film' theory where it is assumed that the resistance to heat or mass exchange between a surface and a gas flow may be modelled by introducing the concept of gas films of constant thickness around the droplet. The occurrence of Stefan flow will lead to a boundary layer thickening.

The Nusselt and Sherwood numbers are modified to take this into account and are calculated as

$$\mathrm{Sh}^{\star} = 2 + \frac{\mathrm{Sh} - 2}{F_M} \quad , \quad F_M = \frac{(1 + B_M)^{0.7}}{B_M} \ln(1 + B_M) \tag{2.51}$$

$$\mathrm{Nu}^{\star} = 2 + \frac{\mathrm{Nu} - 2}{F_T} \quad , \quad F_T = \frac{(1 + B'_T)^{0.7}}{B_T} \ln(1 + B'_T) \tag{2.52}$$

with

$$B'_T = (1 + B_M)^{\phi}, \phi = \frac{C_{p_v}}{C_{p_g}} \frac{\mathrm{Sh}^{\star}}{\mathrm{Nu}^{\star}} \frac{1}{Le}, \tag{2.53}$$

with C_{p_v} the specific heat of the vapour and C_{p_g} the specific heat of the gas (air) determined using the 1/3 rule for temperature and mass fraction. Equations (2.52), (2.53) are solved iteratively by first determining the $Le = \frac{\lambda_g}{\rho_g D_g C_{p_g}}$, F_M and Sh, and then using an initial guess for B_T (e.g. $B_T = B_M$) to subsequently determine F_T, Nu, ϕ and B_T. When $|B_{T_{\mathrm{old}}} - B_{T_{\mathrm{new}}}| > \epsilon$ with ϵ a small value, we replace the initial guess for B_T with our new B_T and continue until B_T has converged. B_T is then used in the temperature equation as:

$$m_p C_{p_l} \frac{dT_p}{dt} = \frac{C_{p_v}(T_s - T_p)\dot{m}_p}{B_T} - L\dot{m}_p. \tag{2.54}$$

Rewriting this equation as in equation (2.39) yields for f_2:

$$f_2 = \frac{\dot{m}_p}{m_p B'_T} \frac{3\mathrm{Pr}\tau_p}{\mathrm{Nu}} \tag{2.55}$$

A comparative analysis of the performance of the model of Abramzon and Sirignano with other, similar models for fuel droplet heating can be found in Sazhin *et al*. [145].

2.5 Non-equilibrium effects

Miller *et al*. [108] report that non-equilibrium effects will become important for droplets with small initial diameter. The non-equilibrium Langmuir-Knudsen law [5] is incorporated through the definition of the vapour mole fraction at the droplet surface:

$$X^{(I)}_{\mathrm{neq}} = X^{(I)}_{\mathrm{eq}} - \frac{L_K}{r_p}\beta, \tag{2.56}$$

with $X^{(I)}_{\mathrm{eq}}$ the equilibrium mole fraction of fuel vapour at the surface given by equation (2.15). L_K is the Knudsen layer thickness, given by

$$L_K = \frac{\mu_g \sqrt{2\pi T_p \frac{R}{W_F}}}{\alpha_e \mathrm{Sc}_p}. \tag{2.57}$$

α_e is the molecular accommodation coefficient representing the fraction of molecules that vaporise and enter the gas phase at the surface (here, we assume as was done in Miller *et al*. that all molecules participate in the evaporation process and $\alpha_e = 1$) and β is the nondimensional evaporation parameter:

$$\beta = -\frac{3}{2}\mathrm{Pr}\tau_\mathrm{p}\frac{\dot{m}_\mathrm{p}}{m_\mathrm{p}}. \tag{2.58}$$

The nonequilibrium mole fraction is then used in the calculation of the Spalding mass transfer number B_M in equation (2.29). More important is the correction to the heat equation proposed by Miller *et al*. . The evaporation correction to the heat balance f_2 in equation (2.39) is given by the expression

$$f_2 = \frac{\beta}{e^\beta - 1}. \tag{2.59}$$

The thermodynamic non-equilibrium effects incorporated by equation (2.56) are important only for initial droplet diameters $< 50\mu\mathrm{m}$ [108]. The results in [108] show that the vaporisation rate slightly decreases and slightly longer droplet lifetimes are predicted when incorporating the non-equilibrium thermodynamic effects. The main improvement in the predictions comes from the expression f_2, which is not due to the non-equilibrium analysis. However, we will keep using the term 'non-equilibrium model' or 'Langmuir Knudsen model' to refer to the model of Miller *et al*. because this term has already been adopted in the literature.

2.6 Single droplet simulation results and comparison with experimental data

The performance of the different droplet vaporisation and heating models described in the previous section should be evaluated using single droplet experiments. To this purpose, some experiments found in literature were chosen where small hydrocarbon droplets vaporise in a high temperature convective gaseous environment. However, experimental data on single droplet vaporisation seems to be limited to rather large droplets, ranging mainly from $100\mu\mathrm{m}$ up to 5 mm.

Model	f_1
Classic rapid mixing	0
Abramzon-Sirignano	$\frac{\dot{m}_\mathrm{p}}{m_\mathrm{p}B_T'}\frac{3\mathrm{Pr}\tau_\mathrm{p}}{\mathrm{Nu}}$
Miller, Harstad and Bellan	$\frac{\beta}{e^\beta-1}$

Table 2.1: Different infinite conductivity droplet models used to simulate single droplet vaporisation.

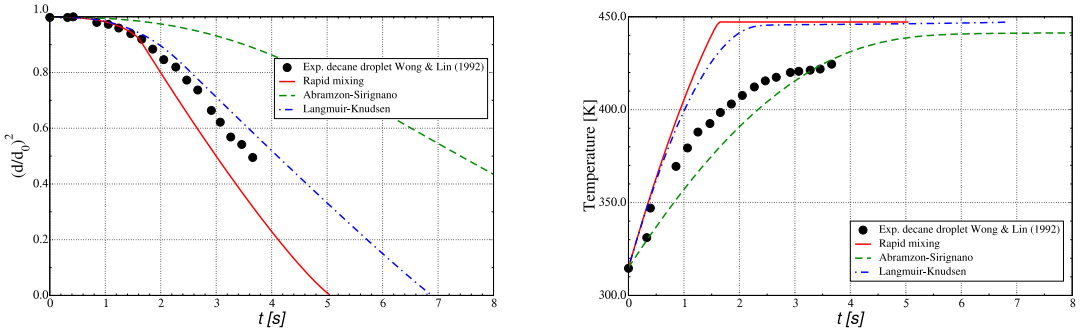

(a) (b)

Figure 2.2: Temporal evolution of the droplet diameter squared and the droplet temperature for decane. Experimental results from Wong and Lin. Reference conditions are far field conditions at decane boiling temperature ($T_b = 447.7K$).

The smallest droplet range measured experimentally are the largest droplets commonly found in spray combustors. There are two reasons that explain the diameter range chosen by experimentalists. First of all, small droplets vaporise faster than large droplets, so the spatial resolution as well as the frequency of the high speed camera used in the experiment needs to be high. Secondly, the droplets are usually fixed using a small needle or cross-wire quartz fibres. When the droplets are small, the relative disturbance of the positioning fibres will be larger. Micrometer size fibres are needed to ensure that only small disturbances to the droplet deformation and small heat transfer through the fibres occurs.

We start our comparison with the experimental data of Wong and Lin [179], which was also used in the paper by Miller *et al*. [108]. Measurements of droplet size and internal temperature distributions under conditions of relatively high evaporation rate are available. Their experiments consist of a droplet of decane with initial diameter $d_{\mathrm{p}}(0) = 2.0$ mm and liquid temperature $T_{\mathrm{p}}(0) = 315K$ placed in a high temperature ($T_\infty = 1000K$) convective environment with an initial Reynolds number of $Re(0) = 17$. Multiple experiments were performed under identical conditions. Only the position of the thermocouple was changed in order to obtain spatial information of the internal liquid temperature. This allowed the experimentalists to obtain the spatial as well as the temporal temperature distribution inside the droplet. In the experimental results shown for droplet temperature, the measured temperature at $r/r_{\mathrm{p}} = 0.6$ was taken.

Figure (2.2) shows a comparison between the experimental and numerical results for the diameter squared (2.2(a)) and temperature (2.2(b)). As a reference temperature, the liquid boiling temperature was used to evaluate the thermodynamic properties of the fuel vapour. The standard infinite conductivity model (also called rapid mixing model) is still able to predict the correct diameter evolution,

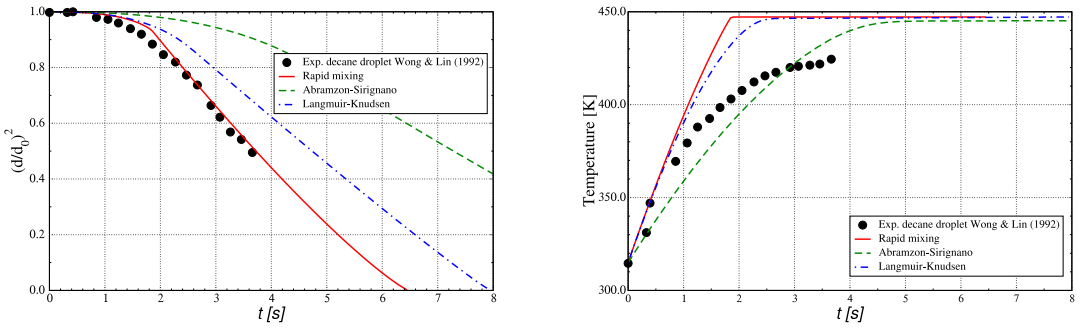

(a) (b)

Figure 2.3: Temporal evolution of the droplet diameter squared and the droplet temperature for decane. Experimental results from Wong and Lin. Reference conditions are far field conditions evaluated at the wet bulb temperature.

although it fails to obtain a correct heat balance, resulting in too fast heating of the droplet. Furthermore, the rapid mixing model does not converge towards the liquid boiling point as shown in Figure (2.2(b)) and the model needs to be augmented by the condition $T_{\mathrm{p}} < T_{\mathrm{boil}}$. This behaviour for the rapid mixing model was also found in [108].

The non-equilibrium Langmuir Knudsen model compares well with the experimentally obtained results, but the Abramzon-Sirignano model overpredicts the droplet diameter. The bad performance of the Abramzon-Sirignano model is due to the fact that we have not taken average values of the thermodynamic properties and we have not used the '1/3' law as proposed in the original model [1]. Both models predict a temperature evolution towards the liquid boiling point and do not need an auxiliary cut-off requirement.

These numerical results were obtained with the reference conditions of the gas phase taken at the boiling temperature ($T_{\mathrm{boil}} = 447.7K$) of decane and the gas phase conditions occurring in the far field region of the droplet were taken. Since the droplet temperature does not evolve towards the liquid boiling point T_{boil} but towards the wet-bulb temperature T_{wb} (which can be close to the boiling point however, depending on the saturation conditions of the gas phase), it might be better to use T_{wb} as the temperature seen by the particle. The numerical results for these simulations are shown in Figure (2.3).

The simulation results when the $'1/3'$ rule is used for the temperature as well as the mass fraction seen are shown in Figure (2.4). The thermodynamic properties are then evaluated using these reference conditions. A mixing rule is used to determine the thermodynamic properties seen, e.g.

$$\overline{\lambda} = Y_{\mathrm{m}}\lambda_F + (1 - Y_{\mathrm{m}})\lambda_{\mathrm{g}}, \tag{2.60}$$

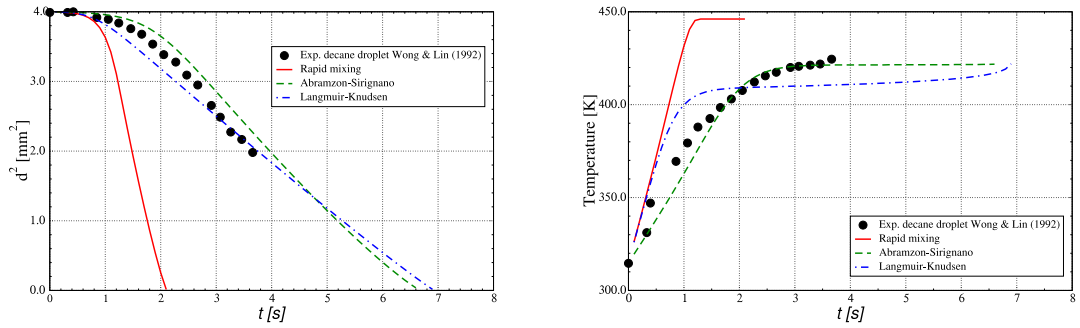

(a) (b)

Figure 2.4: Temporal evolution of the droplet diameter squared and the droplet temperature for decane. Experimental results from Wong and Lin. Reference conditions are $'1/3'$ rule for mass fraction and temperature.

where subscript F indicates a property of the fuel vapour. These reference and mixing conditions were used in the original paper of Abramzon and Sirignano [1].

The droplet diameter as well as the droplet temperature are predicted correctly by the model of Abramzon and Sirignano and the Langmuir-Knudsen model. The model of Abramzon and Sirignano also correctly predicts the nonlinear deviation from the d^2 law shown by the experimental results in (2.4(a)). During the first half of the evaporation time, the Langmuir-Knudsen model underpredicts the droplet diameter and the Abramzon-Sirignano model overpredicts the droplet diameter. During the second part of the lifetime, the Langmuir Knudsen model predicts a higher droplet diameter than the Abramzon-Sirignano model. These observations are directly related to the evolution of droplet temperature shown in Figure (2.4(b)). Similar simulations were performed where equation (2.35) was used to evaluate the viscosity instead of a mixture rule based on mass fraction. A remark of Yuen and Chen [186] where they say that the far field gas density ρ_g should be used to evaluate the Reynolds number was also tested. Both model changes led to a slight increase in the droplet lifetime and no real improvements were observed.

The conclusion from this comparison is that the Langmuir-Knudsen law performs the best when used with far field thermodynamic conditions, whereas the model of Abramzon and Sirignano performs the best when used with the $\frac{1}{3}$-law. The Langmuir-Knudsen model is also found to be the least sensitive to the choice of reference conditions, which is a desirable property.

Since the spray flame simulations discussed later in this thesis in chapter 7 use methanol as liquid fuel, a single droplet simulation using methanol can be of value. Law *et al*. [93] have done experiments on droplet vaporisation in humid air at room temperature ($T_\infty = 298K$) and with droplet diameters of $d_p(0) = 1.60$ mm. No experimental data on methanol vaporisation at higher temperatures were

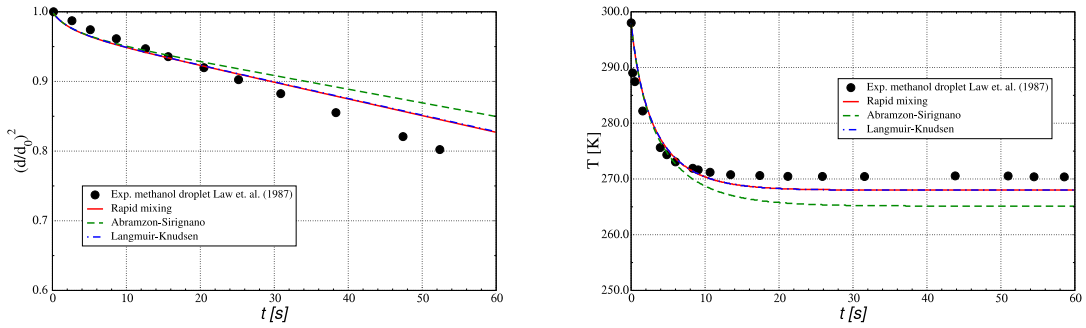

(a) (b)

Figure 2.5: Temporal evolution of the droplet diameter squared and the droplet temperature for methanol vaporisation in dry air. Experimental results from Law *et al*.

found in the literature, but an abundance of data on burning methanol droplets is available. The simulation of burning methanol droplets will be discussed in a later section. Figure (2.5) shows the diameter squared and temperature evolution of a 1.60 mm diameter methanol droplet vaporising in dry (zero water content) air with temperature $T_\infty = 298$ K. Because of the low gas temperature, the droplet cools down due to evaporation. The temperature reaches a steady state value of around 270 K. The numerical simulations slightly underpredict the steady state temperature by 2 K for the rapid mixing and the Langmuir Knudsen model. The model of Abramzon and Sirignano underpredicts the temperature by 5 K, which is the reason that it shows a slightly slower vaporisation rate in figure (2.5(b)). The diameter squared is almost linear in time, but because the droplet temperature is slightly underpredicted by all three models, the droplet evaporates a little too slow and the droplet diameter is slightly overpredicted. This is in agreement with the numerical results from Law *et al*. , although our approach is less complex than the method discussed in [93], where gas and liquid phase are spatially resolved.

2.7 Finite conductivity models

In the previous section infinite conductivity models were discussed. The droplet was considered to be a point, and its thermodynamic properties were only dependent on time, i.e. $T_\mathrm{p}(t)$. The emphasis was on the model description in the gas phase. In this section, we will discuss finite conductivity models, where the liquid phase is described in more detail. Thermodynamic properties are spatially varying and are not considered to be uniform throughout the droplet anymore, i.e. we consider $T_\mathrm{p}(t, r)$.

2.7.1 Conduction limit model

In this section, the conduction limit model describing the internal temperature distribution of a liquid droplet will be discussed for a single isolated droplet [91]. The heat diffusion equation describing the temperature $T(r,t)$ of a spherically symmetric liquid droplet is given by [150]:

$$\frac{\partial T_l}{\partial t} = \alpha_l \left(\frac{\partial^2 T_l}{\partial r^2} + \frac{2}{r}\frac{\partial T_l}{\partial r} \right), \tag{2.61}$$

which is the temperature equation (2.5) with $\alpha_l = \frac{\lambda_l}{\rho_l C_{p_l}}$ and $v_l \approx 0$. The zero-dimensional infinite conductivity model is obtained by letting $\alpha_l \to \infty$. The symmetry condition at r=0 is given by

$$\left.\frac{\partial T}{\partial r}\right|_{r=0} = 0, \tag{2.62}$$

and the initial droplet temperature is assumed to be uniform:

$$T(r,0) = T_0. \tag{2.63}$$

The boundary condition at the droplet surface is more complicated, but can be found to be [150]:

$$\begin{aligned} \left.\frac{\partial T_l}{\partial r}\right|_I &= \frac{\lambda_\mathrm{g}}{\lambda_l}\frac{\partial T}{\partial r}_I - \frac{\dot{m}_\mathrm{p} L}{4\pi r_\mathrm{p}^2 \lambda_l} \\ &= \frac{\lambda_\mathrm{g}}{\lambda_l}\frac{\mathrm{Nu}}{2}\frac{T_\mathrm{s} - T_\mathrm{p} + \frac{\nu Q Y_{O\infty}}{C_{p_\mathrm{g}}}}{r_\mathrm{p}} - \frac{\dot{m}_\mathrm{p} L}{4\pi r_\mathrm{p}^2 \lambda_l} \end{aligned} \tag{2.64}$$

2.7.2 Effective conductivity model

The heat transfer in a liquid droplet is usually not only governed by conduction but also by convection (see Figure (2.6(a))). Internal circulation caused by surface friction plays can play an important role in droplet vaporisation [149]. Taking convection into account means solving two-dimensional differential equations (usually the vorticity-stream function equations [14, 52]), and to avoid this we instead modify the thermal conductivity and use an effective conductivity derived from detailed numerical results. The thermal diffusivity is now replaced by an effective thermal diffusivity $\alpha_{\text{eff}} = \chi \alpha_l$ [1, 150], with

$$\chi = 1.86 + 0.86\tanh(2.225\log(Pe_l/30)), \tag{2.65}$$

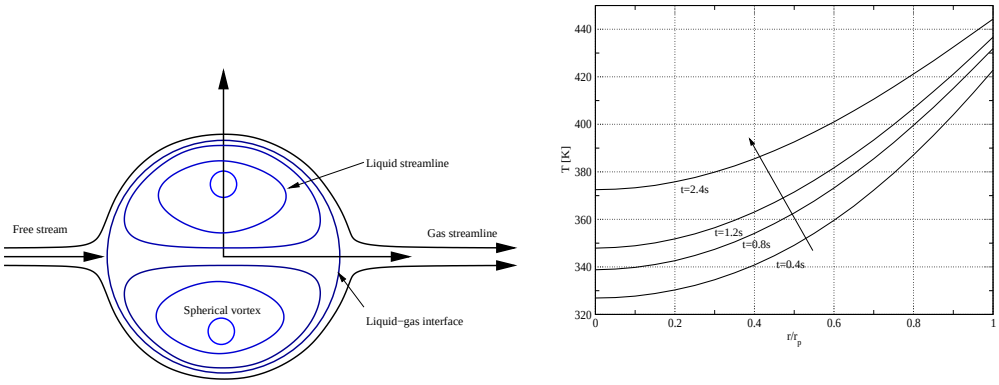

(a) (b)

Figure 2.6: Sketch of a liquid droplet with internal circulation (2.6(a)) and numerical results of the temperature $T_l(t, r)$ inside a decane droplet obtained with the effective conductivity model.

with the liquid Peclet number defined as :

$$
\begin{aligned}
Pe_l &= \frac{2U_{\max} r_{\mathrm{p}} \rho_l C_{p,l}}{\lambda_l}, \\
U_{\max} &= \frac{1}{6\pi} \frac{\mu_{\mathrm{g}}}{\mu_l} C_F \mathrm{Re}_{\mathrm{p}} \left| \boldsymbol{U}_{\mathrm{s}} - \boldsymbol{U}_{\mathrm{p}} \right| \\
C_F &= \frac{12.69 \mathrm{Re}_{\mathrm{p}}^{-2/3}}{1 + B_M}
\end{aligned}
\tag{2.66}
$$

The effective conductivity model will correct for internal circulation in the sense that internal circulation will speed up the internal droplet heating through convection. By assuming faster conduction, this faster heating is mimicked.

2.7.3 Non-dimensional form

When using the conduction limit model or the effective conductivity model, the heat diffusion equation describing the internal droplet temperature, eq. (2.61), has to be solved numerically. After each time step, an amount of liquid fuel has been vaporised and the droplet diameter decreases. The surface regression of the droplet complicates the numerical calculations, since discrete points near the liquid/gas boundary can be located outside the new computational domain at the next timestep. To overcome this problem and the need for interpolation, it is best to perform a transformation of coordinates and rewrite the heat conduction equation in non-dimensional form [150]. The heat conduction equation can be cast into

a non-dimensional form to obtain a fixed boundary problem as follows. We define:

$$\xi = \frac{r}{r_{\rm p}(t)} \quad , \quad \tau = \frac{\alpha_l t}{r_{\rm p}^2(0)},\ r_s(\tau) = \frac{r_{\rm p}(t)}{r_{\rm p}(0)}$$
$$z = \frac{T_l(t,r) - T_l(0,r)}{T_l(0,r)} \quad , \quad \beta = \frac{1}{2}\frac{dr_s^2}{d\tau}, \tag{2.67}$$

with $T_l(0,r)$ the initial (uniform) temperature of the liquid, ξ is the normalised radius, τ is the transformed time, r_s is the ratio of droplet diameter with respect to the initial droplet diameter, z is the nondimensionalised temperature and β is the d^2 rate of change with time τ. We can now write the heat diffusion equation as:

$$r_s^2\frac{\partial z}{\partial \tau} - \beta\xi\frac{\partial z}{\partial \xi} = \frac{\chi}{\xi^2}\frac{\partial}{\partial \xi}(\xi^2\frac{\partial z}{\partial \xi}) \tag{2.68}$$

The boundary equation transforms to:

$$\frac{\partial z}{\partial \xi}(1,\tau) = \frac{\lambda_{\rm g}}{\lambda_l}\frac{T_\infty - T_s}{2T_{l,0}}{\rm Nu} - \frac{\dot{m}_{\rm p}L}{4\pi r_{\rm p}\lambda_l T_{l,0}}. \tag{2.69}$$

Equation (2.69) can now easily be solved by the Crank-Nicolson method, which is an implicit method with second order accuracy in space and time and unconditionally stable. These qualities make it the preferred method for solving heat equations [1].

The numerical results for the internal droplet temperature for the conditions of the experiment of Wong and Lin are shown in Figure (2.6(b)).

The liquid temperature $T_l(t,r)$ at four moments in time is shown. The centre of the droplet is always the coldest, but the temperature difference between the droplet centre and the droplet interface decreases. The effect of finite conductivity is therefore mainly important in the transient heating phase. Note that in a real droplet, due to the internal vortex structure, the minimum temperature is not in the centre of the droplet. The effective conductivity model is therefore not qualitatively correct in the sense that it cannot predict an off-centre temperature minimum [1].

Numerical results for the classical rapid mixing infinite conductivity model, the conduction limit model and the effective conductivity model, together with the experimental results from Wong and Lin [179] are shown in figure (2.7). The thermodynamic properties of the gas phase are all evaluated at the interface temperature $T_{\rm p}$. The number of internal gridpoints was set to $N = 20$, which was sufficient to guarantee a grid-independent solution.

The effect of taking into account the finiteness of the conductivity is very large. The droplet diameter is now severely overpredicted by the conduction limit model. Forced convection creates internal circulation in the droplet, and the correction to

[1] exact solutions also exist. See for instance [143].

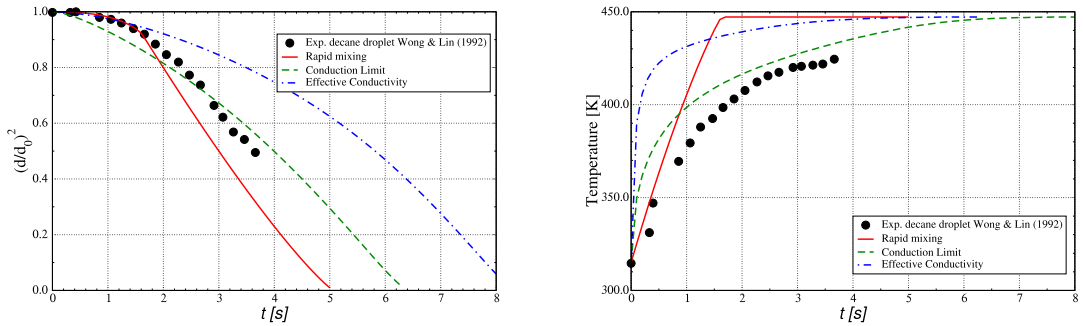

(a) (b)

Figure 2.7: Temporal evolution of the droplet diameter squared and the droplet temperature for decane. Experimental results from Wong and Lin (1992).

the conductivity implemented in the effective conductivity model improves the predictions. The effective conductivity model predicts a slightly higher temperature at the start of the vaporisation process, and the droplet diameter is slightly underpredicted.

From this analysis the following conclusions can be drawn. Resolving the internal droplet temperature does not systematically improve the predictions of the droplet diameter evolution or the temperature evolution. The extra computational effort of solving the conduction equation (2.61) is much higher than for the infinite conductivity model. Although there are cases where the internal droplet temperature distribution can be important (large droplets with low conductivity in a low temperature environment), for spray flame simulations the infinite conductivity models will suffice.

2.8 Burning droplet modelling

In turbulent spray flames two limit cases of droplet burning can be distinguished. In the first case the droplet vaporises in a hot (burning) environment. The fuel vapour mixing with the environment is fast and no local flame structures influence the droplet vaporisation process. In the other limit, the fuel vapour diffusing from the droplet forms a diffusion flame surrounding the droplet and a local flame structure will influence the droplet burning characteristics. Although the case of single droplet burning will not frequently happen in turbulent spray flames, local flame structures can appear that partially surround a single droplet or a droplet cluster. It is for this reason that single droplet burning behaviour is more than an academic test case.

We assume in our droplet-burning analysis that the fuel and oxygen depletion

are related in stoichiometric proportions (see also Kuo [85] or Williams [178]):

$$\begin{aligned} \dot{\omega}_F &= \dot{\omega}_O \left(\frac{F}{O}\right)_{st} \\ \dot{\omega}_F h_{r,F} &= \dot{\omega}_O h_{r,F} \left(\frac{F}{O}\right)_{st} = -\dot{Q}, \end{aligned} \tag{2.70}$$

where $\left(\frac{F}{O}\right)_{st}$ is the stoichiometric fuel to oxidiser mass ratio. The spalding mass transfer number for combustion becomes:

$$B_M = \frac{Y_{F,\infty} - Y_{F_s} + Y_{O_s} - Y_{O_\infty}\left(\frac{F}{O}\right)_{st}}{(Y_{F_s} - 1) + \left(\frac{F}{O}\right)_{st} Y_{O_s}} = \frac{\left(\frac{F}{O}\right)_{st} Y_{O_{st}} + Y_{F_s}}{1 - Y_{F_s}}. \tag{2.71}$$

and the Spalding heat transfer number becomes:

$$\begin{aligned} B_{O,T} &= \frac{C_{p_g}(T_\infty - T_s) + (Y_{O_\infty} - Y_{O_s})\left(\frac{F}{O}\right)_{st} h_{r,F}}{h_v + Y_{O_s}\left(\frac{F}{O}\right)_{st} h_{r,F}} \\ &= \frac{C_{p_g}(T_\infty - T_s) + Y_{O_\infty}\left(\frac{F}{O}\right)_{st} h_{r,F}}{h_{v,F}}. \end{aligned} \tag{2.72}$$

For a general hydrocarbon fuel F, the heat of reaction (heat of combustion) $h_{r,F}$ can be determined using the formation enthalpies for the stoichiometric reaction $\nu_1^{'} F + \nu_2^{'} O_2 \rightarrow \nu_1^{''} CO_2 + \nu_2^{''} H_2O$.

Many experiments on single droplet combustion can be found in the literature, most of them performed under zero-gravity conditions [41, 97, 182] to avoid natural convection (gravity) effects. We will discuss here simulation results under conditions similar to the experimental conditions described in Xu *et al*. [182], who describes experiments on n-decane droplets at gaseous temperatures between $T = 298K$ and $T = 1093K$. Detailed numerical simulations have been performed by Cuoci *et al*. [34]. A droplet can be ignited by using a spark ignition when the gas temperature is low, or by auto-ignition in a hot temperature field where $T_{\mathrm{g}} > T_{\mathrm{p,ignition}}$. The choice of reference temperature is now important, because in the auto-ignition and in the spark-ignited cases the droplet will see different temperature fields. When using the standard $\frac{1}{3}$-rule, the flame temperature is not taken into account. In the case of spark ignition, the far field temperature is low, $T_\infty = 298K$ and the droplet will see a low temperature. After ignition, a flame will develop surrounding the liquid particle, as depicted in Figure (2.1). The effects of the presence of a flame, located at a certain flame standoff distance r_f, needs to be taken into account. The flame standoff distance r_f/r_{p} can be calculated using [178]:

$$\frac{r_f}{r_{\mathrm{p}}} = \frac{\ln(1 + B_M)}{\ln(1 + \frac{\nu_F W_F}{\nu_O W_O} Y_{F,\infty})}, \tag{2.73}$$

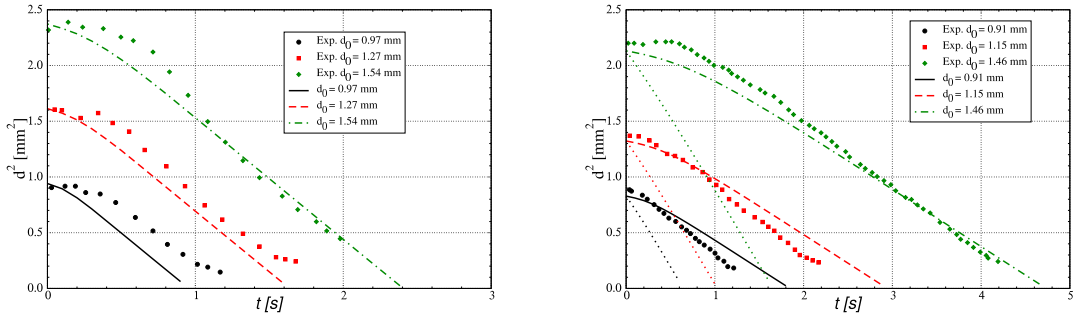

(a) (b)

Figure 2.8: $d^2(t)$ of n-decane droplets for different initial diameters during (2.8(a)) auto ignition ($T_\infty = 1093K$) and (2.8(b)) spark ignition ($T_\infty = 298K$). Dots: Experimental results from [182]. Lines: simulation using $1/3$ rule. Dotted lines in (2.8(b)): simulation using wet-bulb temperature.

although other estimations can be found in the literature, e.g. [166]. For spark ignition, the flame standoff distance is smaller compared to the auto-ignition case, and the temperature gradient between the droplet and the flame will be larger. In other words, the near-field temperature will be larger and the droplet sees a larger temperature. The thermodynamic properties should be evaluated at the wet-bulb temperature. In the case of autoignition, the flame standoff distance will be larger. The integral effect of the surrounding temperature field will be larger and the thermodynamic properties can best be evaluated with a $'1/3'$ averaging rule. The effect of this modification of the temperature at which droplet properties are evaluated is demonstrated in Figure (2.8). The numerical simulations were performed using the Langmuir-Knudsen model and the $'1/3'$ rule was used to determine the saturation mass fraction and thermodynamic properties. The importance of the choice of temperature seen is illustrated in figure (2.8(b)). Using the $'1/3'$ rule for the spark ignited case leads to severe overprediction of the vaporisation rate, resulting in an underestimation of the droplet life time. Simulations using the wet-bulb temperature now perform much better. These simulations illustrate that information about the spatial structure of the flame can be of importance. In zero-dimensional single droplet calculations, this information is compressed into a single property: the temperature at which the thermodynamic properties should be evaluated.

The method proposed by Ulzama and Specht [166], where diffusion of fuel vapour between the droplet and the flame is assumed to be in a quasi-steady state and the diffusion of oxygen is assumed to be in an unsteady state, might improve the burning rate predictions. In turbulent flows however, the spherically symmetric nature of the diffusion flame will be lost and more detailed simulations are needed to correctly predict the burning rate [157].

2.8.1 Methanol combustion

Several single droplet experiments as well as spray experiments were performed using methanol as liquid fuel. The advantage of using methanol in experiments and numerical simulations is that its chemistry is simpler than that of heavier fuels like kerosene or gasoline, and that there is almost no soot formation. A disadvantage of using methanol as a liquid fuel is that it absorbs water from the environment. Since water is an important byproduct of methanol combustion, a methanol droplet will tend to absorb the water formed by its own combustion. Water absorption during evaporation has been investigated by Law *et al*. [93], and water absorption during combustion by Marchese and Dwyer [97], using the experimental results of Cho *et al*. [25]. They find that the liquid Peclet number:

$$\mathrm{Pe}_l = \frac{1}{8}\frac{\left|\frac{d(d_\mathrm{p}^2)}{dt}\right|}{I\!D_l}, \tag{2.74}$$

with $I\!D_l$ the liquid diffusivity, is the governing parameter that determines the rate of absorption: A low Peclet number will lead to more and faster water absorption than a high Peclet number. Zhang and Williams [187] found that the Lewis number of water is a governing parameter and for Lewis numbers close to unity, the water absorption rate is maximised. Experiments with large ($d_\mathrm{p}(0) > 1000\mu\mathrm{m}$) methanol droplets combusting in a water containing environment show that extinction can occur long before the droplet has completely evaporated, due to the high water mass fraction in the droplet. However, experiments [188] show that the water mass fraction absorbed by methanol droplets drops to zero very fast for droplets with an initial diameter smaller than $d_\mathrm{p}(0) = 1000\mu\mathrm{m}$. This suggests that water absorption is less important for the small droplets found in spray flames, which are typically smaller than $d_\mathrm{p}(0) = 100\mu\mathrm{m}$. The effect of water absorption is therefore neglected in this work.

Figure (2.9) shows the results of a numerical simulation of a burning methanol droplet and a comparison with the experimental data of Cho *et al*. [25]. The initial droplet diameter was $d_\mathrm{p}(0) = 1000\mu\mathrm{m}$ and the temperature of the air $T_\infty = 298K$. The numerical results where the boiling point of the liquid was taken as the reference temperature compares most favourably with the experimental data. The temperature evolution shows that there is no balance between heating and evaporation. The temperature quickly rises to the liquid boiling point and is then fixed at $T_\mathrm{p}(t) = T_\mathrm{boil}$.

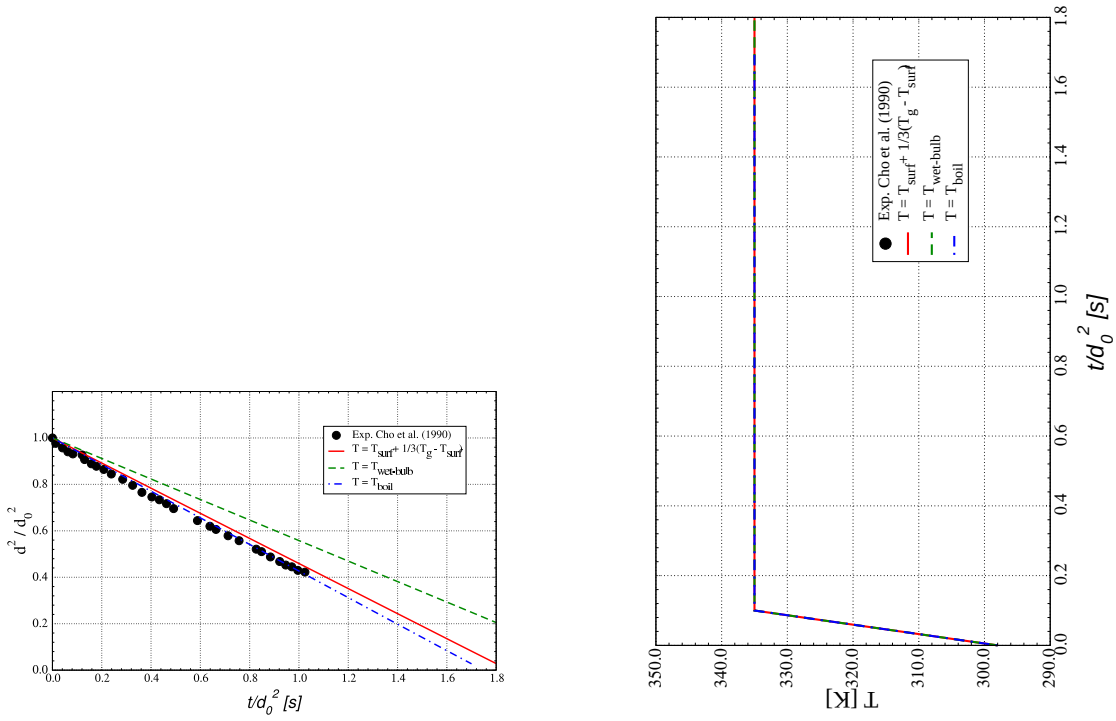

(a) (b)

Figure 2.9: Droplet diameter squared and temperature evolution for a $1000\mu\mathrm{m}$ diameter burning methanol droplet in air at 1 atm and $T_\infty = 298K$. Classic rapid mixing model with three different reference temperatures for evaluating physical properties.

2.9 Vaporisation modulation of interacting droplets

The equation for the droplet vaporisation rate (2.44) was derived under the assumption that the droplet is an isolated droplet vaporising and burning in a one-dimensional gaseous environment (thermodynamic properties are a function of the distance to the centre of the droplet). This allowed us to explicitly evaluate the integral in eq. (2.25). But when the temperature and mass fraction fields are disturbed by the presence of other vaporising droplets, this integral expression cannot be easily evaluated. In spray combustion devices where the spray can be considered dilute, the isolated droplet vaporisation rate is still a reasonable assumption when the mean interdroplet spacing $\frac{l}{d_\mathrm{p}}$ is large, say $\frac{l}{d_\mathrm{p}} > 10$. However, when the interdroplet spacing is small, vaporisation modulation will occur due to droplet-droplet interaction. This is similar to hydrodynamic interaction between particles where the assumption of isolated particles in an undisturbed one-dimensional flowfield is also violated. Interactive problems are dealt with primarily by four methods:

1. Bispherical coordinates, suitable for two drop arrays;
2. The method of images, suitable for small arrays of less than 20 drops;
3. The point source method, suitable for arrays of up to 1000 droplets;
4. The continuum method, suitable for clouds;

The vaporisation modulation of two interacting vaporising droplets is the first step towards understanding the interaction of a group of droplets. The interaction between two burning droplets has been investigated analytically by Umemura *et al*. [168, 169] and by Labowski [86]. Umemura introduces bipolar coordinates

$$\sigma = \frac{c \sin \eta}{\cosh \xi - \cos \eta}, z = \frac{c \sinh \xi}{\cosh \xi - \cos \eta}, -\infty < \xi < \infty, 0 < \eta < \pi, \tag{2.75}$$

and assumes that the mass flux can be derived from a scalar potential ϕ:

$$\rho v_i = \frac{\partial \phi}{\partial x_i}, \tag{2.76}$$

and ϕ must satisfy the Laplace condition $\frac{\partial^2 \phi}{\partial x_i^2} = 0$. In the end, Umemura finds that the vaporisation modulation of either of the two droplets can be written as

$$\frac{dm_\mathrm{p}}{dt} = C \left. \frac{dm_\mathrm{p}}{dt} \right|_0, \tag{2.77}$$

with the modulation factor

$$C = \sinh(\xi^\star) \sum_{n=0}^{\infty} (1 - \tanh(n + \frac{1}{2})\xi^\star), \tag{2.78}$$

Type of array	modulation
triangular (2D)	$g = \frac{r_\mathrm{p}(\phi_s-\phi_\infty)}{1+2\frac{r_\mathrm{p}}{l}}$
tetrahedral (3D)	$g = \frac{r_\mathrm{p}(\phi_s-\phi_\infty)}{1+3\frac{r_\mathrm{p}}{l}}$
square (2D)	$g = \frac{r_\mathrm{p}(\phi_s-\phi_\infty)}{1+(2+\frac{1}{2}\sqrt{2})\frac{r_\mathrm{p}}{l}}$
cubical (3D)	$g = \frac{r_\mathrm{p}(\phi_s-\phi_\infty)}{1+(3+\frac{3}{2}\sqrt{2}+\frac{1}{3}\sqrt{3})\frac{r_\mathrm{p}}{l}}$

Table 2.2: Modulation factor g for different geometries according to the analysis of Marberry *et al*. .

where $\xi^\star$ is the position of the droplet surface in the coordinate system (ξ, η). The analytical results show that the vaporisation of each of the droplets decreases from $\frac{dm_\mathrm{p}}{dt} = \frac{dm_\mathrm{p}}{dt}\Big|_0$ for large separation distances to approximately $\frac{dm_\mathrm{p}}{dt} = 0.7\,\frac{dm_\mathrm{p}}{dt}\Big|_0$ for two vaporising droplets touching each other.

Labowski [86] uses the method of imaging to obtain similar conclusions for modest groups of droplets ($N = 9$).

Marberry *et al*. [87, 96] uses a method closely resembling panel methods to solve the potential field around geometrically arranged droplet arrays. In this study, they obtain approximate vaporisation modulations of the form

$$\frac{dm_\mathrm{p}}{dt} = \frac{dm_\mathrm{p}}{dt}\bigg|_0 \frac{g r_\mathrm{p}}{3(\phi_s - \phi_\infty)} \sum_{i=1}^{N} \frac{e_{1,i}}{r_{1,i}}, \tag{2.79}$$

with

$$e_{1,i} = |x_1 - x_i| + |y_1 - y_i| + |z_1 - z_i|\,, \tag{2.80}$$
$$r_{1,i}^2 = (x_1 - x_i)^2 + (y_1 - y_i)^2 + (z_1 - z_i)^2, \tag{2.81}$$

and

$$e_{1,1} = 3r_\mathrm{p}, \qquad r_{1,1} = r_\mathrm{p}. \tag{2.82}$$

The expression of the vaporisation modulation g for some configurations are given in table (2.2).

The vaporisation modulation for a particle pair could not be described by equation (2.79) but is given by:

$$\frac{dm_\mathrm{p}}{dt} = \frac{dm_\mathrm{p}}{dt}\bigg|_0 \left[\frac{C_1}{r_{\mathrm{p},1}} + \frac{C_2}{6r_{\mathrm{p},1}}\left(\frac{1}{(P_1-1)^2} + \frac{1}{(P_1+1)^2} + \frac{4}{(P_1^2+1)^{\frac{3}{2}}}\right)\right], \tag{2.83}$$

with

$$C_1 = r_{\mathrm{p},1}\frac{P_1 - \frac{r_{\mathrm{p},2}}{r_{\mathrm{p},1}}}{P_1 - \frac{1}{P_2}}, \qquad C_2 = r_{\mathrm{p},2}\frac{P_2 - \frac{r_{\mathrm{p},1}}{r_{\mathrm{p},2}}}{P_2 - \frac{1}{P_1}}. \tag{2.84}$$

and $P_1 = \frac{l}{r_{\mathrm{p},1}}$ and $P_2 = \frac{l}{r_{\mathrm{p},2}}$.

More recently, Imaoka and Sirignano [70, 71] have developed a method which is also based on the solution of the Laplace equation for the mass flux. Simulations for droplet arrays of up to 1000 droplets in several configurations indicate that the vaporisation rate of symmetric droplet arrays with monosized droplets and uniform spacing correlates well with a similarity parameter ξ given by

$$\xi = \frac{l}{r_{\mathrm{p}}} \frac{1}{N_{\mathrm{p}}^{0.72}} \tag{2.85}$$

The array vaporisation rate

$$\eta = \frac{\frac{dm_{\mathrm{p}}}{dt}}{\left.\frac{dm_{\mathrm{p}}}{dt}\right|_0} \tag{2.86}$$

can be described in terms of the similarity parameter ξ and was found to be

$$\eta = 1 - \frac{1}{1 + 0.725671\xi^{0.91716}} \tag{2.87}$$

An interesting result from their studies is that the vaporisation rate of a droplet array is maximised at a specific droplet number density. This is in correspondence with the group combustion theory that will be discussed in the next section.

2.9.1 Comparison with experimental data for a pair of droplets

Since the droplet pair interaction models all predict approximately the same vaporisation rates, only the predictions using Marberry's correlations will be given here. Figure (2.10) shows the experimentally measured values of diameter squared in time for a burning pair of methanol droplets at different separation distances [119]. The initial droplet size was 900μm and the gas phase conditions for the experiments shown here are air at one atmosphere ambient pressure and room temperature.

The experimental data show an almost linear decrease of the diameter squared over the entire droplet lifetime, except near the end of the burning period, where extinction (possibly due to water absorption) occurs. The experimental data for the isolated droplet case matches well with the numerical solution, where as a reference temperature a '1/3' rule was used with the flame temperature instead of the ambient temperature: $T_{\mathrm{av}} = T_{\mathrm{p}} + \frac{1}{3}(T_{\mathrm{flame}} - T_{\mathrm{p}})$. As a reference fuel mass fraction the classical '1/3' law was used and thermodynamic properties were evaluated using a mixture of fuel and air at these reference conditions. It is immediately clear from Figure (2.10) that the correction factor for the droplet pair vaporisation is too small to capture the large vaporisation modulation that occurred in the experiments. Even the theoretical correction factor of 0.69 from Marberry for two

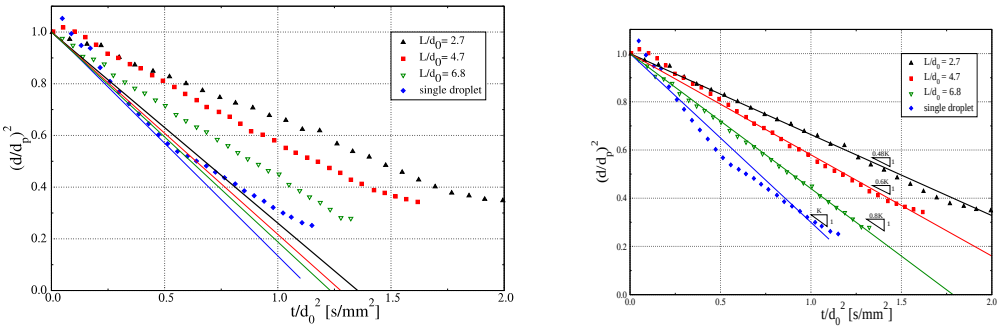

(a) (b)

Figure 2.10: Droplet diameter squared as a function of time for a burning droplet pair at different separation distances. Experiments are from Okai *et al*. [119]. Figure (2.10(a)) shows the correction of Marberry *et al*. , Figure (2.10(b)) shows the actual slopes of $r_{\mathrm{p}}^2(t)$.

touching droplets is not enough to capture the vaporisation rate of the droplet pair, even when they are almost five droplet diameters apart. Other processes that were not taken into account in the analysis of Marberry play a role here. The unsteadyness of the near field region might be of importance [124, 166]. The experimental results in Mikami *et al*. [107] were also compared with the quasi steady theory, but they found that the liquid phase unsteadyness plays an important role. Reasonably matching results were obtained for droplet pairs with not too small separation distances for the experimental results of Miyasaka *et al*. [111] and Xiong *et al*. [181].

2.10 Combustion of droplet clouds

When the interdroplet spacing of droplets in a droplet cloud or spray becomes smaller and smaller, droplets will start to interact with each other. For droplet coalescence and droplet breakup, the droplets actually have to touch each other. A burning droplet on the other hand can influence other droplets over large distances due to the heating of the surrounding gas, the presence of combustion products and the presence of a flame zone located at several droplet diameters from the droplet centre. Chiu and others [22, 23, 30, 190] have developed group combustion models where a spherically symmetric droplet cloud of radius r_c is completely or partially surrounded by a diffusion flame at radius r_f. When $r_f < r_c$, all droplets located outside the flame burn individually, whereas all droplets located at $r < r_f$ share the diffusion flame at r_f. In the limit where the cloud radius goes to the droplet radius, the group combustion model reduces to a single droplet burning model where all droplet in the cloud burn individually. The group combus-

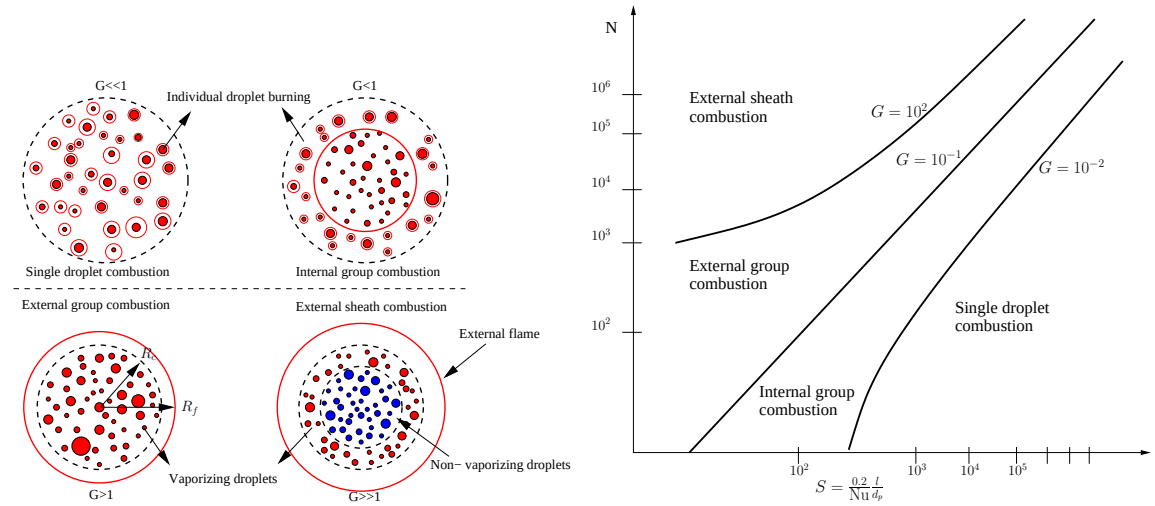

(a) (b)

Figure 2.11: The four combustion modes defined by Chiu [22].

tion model knows 4 different burning modes depending on the group combustion number G, defined here as[2]

$$G = \frac{3}{4}\mathrm{LeSh}N_{\mathrm{p}}^{\frac{2}{3}}\frac{d_{\mathrm{p}}}{l}, \tag{2.88}$$

where Le is the Lewis number, Sh the Sherwood number, N_{p} the total number of droplets in the cloud and l the mean droplet separation distance.

A graphical representation of the burning modes is shown in Figure (2.11(a)). In single droplet combustion all droplets burn individually with a surrounding flame. The group combustion number G is much smaller than one in this case. When the group combustion number increases to unity, a flame sheet enclosing a group of droplets will appear in the centre of the cloud. All droplets in the interior vaporise and all droplets in the exterior burn individually. This is called internal group combustion. When the group combustion number increases even more, the flame sheet will eventually reach the boundary of the droplet cloud and a flame stand off distance between the vaporising droplet cloud and the flame sheet appears, which is known as external group combustion. When the flame standoff distance increases, the droplets near the centre of the cloud will not be heated enough to evaporate. This combustion mode where a non-vaporising inner core exists is called external sheet combustion. As this core grows larger, less fuel vapour will enter the gas phase and at a certain point, not enough fuel will enter the gas phase to sustain a stable flame and extinction will occur.

The hypothesis is made that the same equations used to calculate the vaporisation and burning of a single droplet can be used for the vaporisation and burning

[2]Other definitions can be found in the literature, e.g. in [23].

δ_{if}	1	$i = O$
	-1	$i = F$
δ_f	1	$r \leq R_c$
	0	$r \geq R_c$

$r = 0$	$u = 0$, $\frac{\partial \alpha_j}{\partial r} = 0$	symmetry conditions
$r = R_c$	$\alpha\big\vert_{R_c^+} = \alpha\big\vert_{R_c^-}$	
	$\frac{\partial \alpha}{\partial r}\big\vert_{R_c^+} = \frac{\partial \alpha}{\partial r}\big\vert_{R_c^-}$	continuity conditions
$r = \infty$	$\alpha_j = \alpha_\infty$	
$t = t_0 = 0$	$\rho = \rho(r)$, $\alpha_j(r) = \alpha_j$, $u = 0$, $r_l = r_l(t_0)$	initial conditions

of a spherically symmetric droplet cloud of radius R_c containing n droplets:

$$\frac{\partial \rho_{\rm g}}{\partial t} + \frac{1}{r}\frac{\partial \rho r^2 u}{\partial r} = n\frac{dm_{\rm p}}{dt}\dot{\delta}_s \tag{2.89}$$

$$\frac{\partial \rho_{\rm g} Y_i}{\partial t} + \rho_{\rm g} v \frac{\partial Y_i}{\partial r} - \frac{1}{r^2}\frac{\partial}{\partial r}(r^2 \rho_{\rm g} I\!D_{\rm g} \frac{\partial Y_i}{\partial r}) = n\frac{dm_{\rm p}}{dt}\delta_{if} + \dot{\omega}_i \delta_f \tag{2.90}$$

$$\frac{\partial \rho_{\rm g} T_{\rm g}}{\partial t} + \rho_{\rm g} v C_{p_{\rm g}} \frac{\partial T_{\rm g}}{\partial r} - \frac{1}{r^2}\frac{\partial}{\partial r}(r^2 \lambda_{\rm g} \frac{\partial T_{\rm g}}{\partial r}) = -n\frac{dm_{\rm p}}{dt} L + \dot{\omega}_T \delta_f \tag{2.91}$$

$$\tag{2.92}$$

with boundary conditions given in Table (2.10) and the definition of δ_{if}, δ_f given in Table (2.10). After making these equations non-dimensional by introducing the dimensionless variables $\alpha_i = \frac{Y_i}{W_i \nu_i}$, $\alpha_T = \frac{C_{p_{\rm g}}(T_{\rm s} - T_{\rm p})}{q}$, $\overline{v} = v/v_c$ and $\eta = \frac{r}{R_c}$, we get the result:

$$\frac{d\rho_{\rm g} I\!D_{\rm g} \frac{v R_b}{v_c R_c}}{d\eta} = n\frac{dm_{\rm p}}{dt}\frac{I\!D_{\rm g} R_b}{v_c R_c} \tag{2.93}$$

$$\rho_{\rm g} I\!D_{\rm g} \overline{v}\frac{R_b}{R_c}\frac{d\alpha_i}{d\eta} - \frac{d}{d\eta}(\eta^2 \overline{I\!D} \rho_{\rm g} I\!D_{\rm g} \frac{d\alpha_i}{d\eta}) = \frac{1}{W_i \nu_i}(\overline{I\!D} G \frac{r_{\rm p}}{r_{p_0}} \ln(1 + B_f)\delta_{if}\delta_s + \dot{\omega}_i \delta_f) \tag{2.94}$$

$$\rho_{\rm g} I\!D_{\rm g} \overline{v}\frac{d\alpha_T}{d\eta} - \frac{d}{d\eta}(\eta^2 \overline{I\!D}\frac{\lambda}{c_{\rm p}}\frac{d\alpha_T}{d\eta}) = \overline{I\!D} G \frac{r_{\rm p}}{r_{p_0}}\frac{L}{q}\ln(1 + B_f)\delta_s + \dot{\omega}_T \delta_f \tag{2.95}$$

with $\overline{I\!D} = \frac{D_{\rm g}}{R_c v_c}$ and the group combustion number

$$G = \frac{2\pi r_{l_0} \lambda_{\rm g} \eta {\rm Sh} R_b^2}{\rho_{\rm g} I\!D_{\rm g} C_{p_{\rm g}}} \tag{2.96}$$

Chiu and Liu among others [23] report that the group burning rate of a cloud of droplets with large group combustion number G (such that we are in the external group combustion regime) is similar to the burning rate of a single droplet

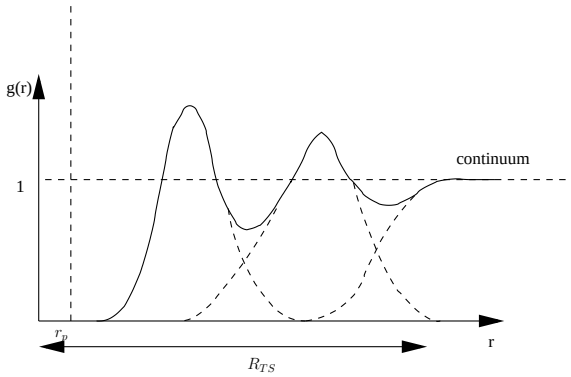

Figure 2.12: Typical shape of a pair distribution function (solid line). The dashed line represents the underlying single droplet factor.

with a radius equal to the cloud radius r_c. It is difficult however to extend these analyses to spray combustion phenomena, where the cloud radius is not defined anymore. Chiu [18] tried to extend first the analysis of the vaporisation rate of a single isolated droplet in a diffusion controlled gaseous environment to that of a general flow governed by the complete Navier-Stokes equations using renormalisation theory [17, 18, 20, 21]. This leads however to an extremely complicated volume integration over the space where the droplet resides and it requires detailed knowledge about the exact state of the surrounding gas phase. It is therefore mainly suited for studies in Direct Numerical Simulations. The model however reduces to the rapid mixing law (2.32) in the limit of a spherically symmetric stationary droplet in a uniform environment, which is convenient when droplet clouds are being studied.

For the determination of the vaporisation rate as well as the aerodynamic drag of a droplet in a droplet cloud, a similar approach is used [19, 24]. In this approach, Chiu assumes that the droplet under consideration only cares about the droplets located in the direct vicinity of this droplet. The far field region is seen as a continuum where the exact location of droplets is not important anymore. The droplets in the near-field region are assumed to be distributed according to a pair distribution function g (also known as the pair correlation function in statistical physics [158]), which is the joint probability density of finding the test droplet and a neighboring droplet (in the near field region) at a particular separation distance. In general, for g we have that

$$g(r) \geq 0 \qquad \lim_{r\to\infty} g(r) = 1. \tag{2.97}$$

Figure (2.12) shows a pair distribution typical for random distributions of spherical particles. The vaporisation modulation of a droplet in a dispersed two-phase flow

can be written as [24]:

$$\frac{dm_{\rm p}}{dt} = \frac{\left.\frac{dm_{\rm p}}{dt}\right|_0}{1 + (4\pi \frac{r_l}{1-\frac{r_l}{r_{ts}}}) \int_{r_l}^{r_{ts}} \frac{dr}{r^2} \int_V ng\mu_{\rm g}(1 + \frac{\alpha_T}{\alpha_T+\gamma})dV} \tag{2.98}$$

where $\left.\frac{dm_{\rm p}}{dt}\right|_0$ is the vaporisation rate of an isolated droplet, determined according to the analysis of Chiu, or by using the Godsave-Spalding (classic rapid mixing) law (2.28). The results of numerical simulations of Chiu show that:

1. Vaporisation rate decreases with decreasing separation distance
2. For higher temperatures, interaction effects will be smaller
3. For higher Reynolds numbers, interaction effects will be weaker [3]. The effects of temperature on the vaporisation rate is less pronounced for higher Reynolds numbers
4. Droplet drag decreases with decreasing separation distance
5. The effect of temperature on the drag is negligible for all but the smallest separation distances

From the analysis and numerical results of Chiu we may conclude that in spray flames, where the temperature and Reynolds number is high, the vaporisation corrections to the isolated mass vaporisation rate may be small.

A different analysis of spray flames was proposed by Borghi [11]. Borghi proposes a categorisation that includes the characteristic flame time τ_f, a flame thickness δ_f and an evaporation delay time τ_v, analogous to the 'Borghi' diagram for turbulent premixed gas flames. When $\tau_V \ll \tau_f$ the droplets vaporise before they reach the reaction zone and a premixed flame develops. If the characteristic flame length is larger than the droplet separation distance l, droplets are immersed into the reaction zone, leading to a thick flame zone. Other regions can be identified depending on the ratio of the droplet separation distance over the characteristic flame length. If this ratio is small, flames between droplets will be suppressed due to the high fuel/oxygen ratio. This is similar to the external group combustion regime of Chiu. As this ratio increases, flames may be formed between droplet groups and percolation occurs. Eventually, pockets of droplets with surrounding flames may be formed. This is similar to internal group combustion, where only part of the droplets have a shared diffusion flame. Réveillon and Vervisch [135] propose a slightly more complex categorisation than Borghi, based on direct numerical simulations of laminar and weakly turbulent spray flames. In their analysis, the liquid

[3] This is not apparent in the figures shown in [24], but the Re dependence is clear in the correction factors given in the paper.

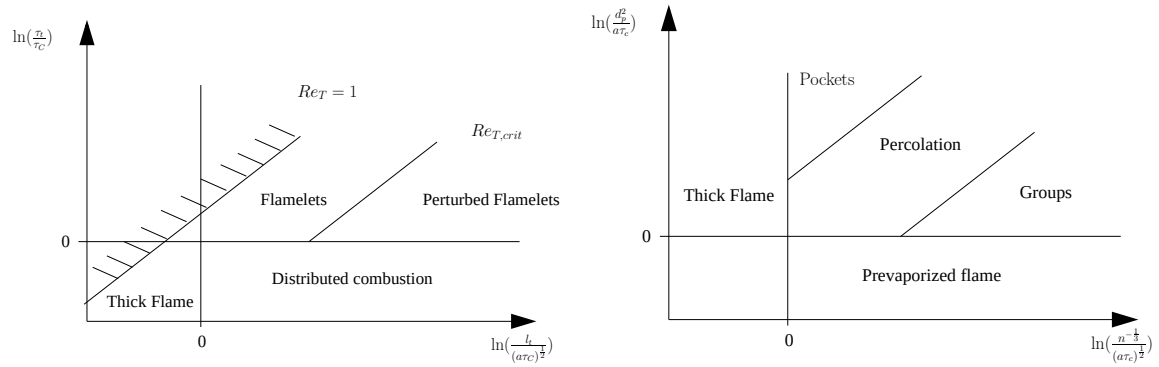

Figure 2.13: The Borghi diagram for gas flames and spray flames.

fuel over air mass ratio is taken into account. Other studies of droplet arrays or droplet groups can be found in the literature, e.g. [5, 6, 7, 40, 115, 139, 144, 165] and [3, 167] and the references therein.

2.11 Conclusions

In this chapter the performance of several droplet vaporisation models was investigated under different circumstances. First, some isolated droplet vaporisation models were investigated. The main conclusion from this analysis is that all droplet vaporisation models studied here are very sensitive to the way the thermodynamic properties are evaluated, and that there is a preferred evaluation method for each of the models: the classical rapid mixing model tends to predict too fast vaporisation and the thermodynamic properties are best evaluated at the wet-bulb temperature. The model of Abramzon and Sirignano was tuned to perform optimally using the '1/3' law and the Langmuir-Knudsen model of Miller *et al*. performs the best when the thermodynamic properties are evaluated at the boiling temperature of the liquid. When the evolution of droplet temperature as well as droplet diameter are considered, it seems that the model of Abramzon and Sirignano performs marginally better than the model of Miller. The classic rapid mixing model always fails to predict a correct temperature evolution.

Resolving the internal droplet temperature increases the computational time significantly because a differential equation needs to be solved for the liquid temperature. However, this does not lead to better predictions of the droplet diameter or the droplet temperature for the case investigated here.

When burning droplets are considered, it is much more difficult to correctly predict the diameter evolution of the droplet because the surrounding temperature field increases in complexity. The droplet diameter could not be predicted correctly for both the auto-ignited and the spark-ignited droplet using the same method. This interesting observation certainly deserves more attention in future work on the development of single droplet burning models.

The interaction of two or more vaporising and burning droplets has been a research topic for some decades. In the past, a good correspondence was found between experimental data and numerical predictions of the droplet evolution of a burning droplet pair. However, the numerical predictions of droplet diameter evolution of a burning droplet pair did not correspond with the experimental results presented in this chapter. The vaporisation rate for the burning droplet pair was found to be much smaller (the droplet interaction was stronger) than the numerical results predicted.

In the last section of this chapter different concepts of droplet group combustion were presented. The main difficulty according to the analysis of Chiu is that for each droplet the volume integration of the temperature field surrounding the droplets is needed to evaluate the vaporisation rate in a spray flame. The analysis of Borghi and also of Réveillon and Vervisch shows that in spray flames, different regions exist where the flame structure is fundamentally different and therefore the droplet vaporisation rate also differs in each region.

CHAPTER 3

Turbulence modelling in dispersed two-phase flows: I

Second Moment Closure modelling in momentum and scalar transport

A modified Reynolds stress turbulence model for the pressure rate of strain tensor Π_{ij} can be derived for dispersed two-phase flows taking into account two way coupling between the continuous phase and the dispersed phase. The transport equations for the Reynolds stresses as well as the equation for the fluctuating pressure can be derived starting from the multiphase Navier Stokes equations. The unknown pressure rate of strain correlation in the Reynolds stress equations is then modelled by considering the multiphase equation for the fluctuating pressure. This leads to a multiphase pressure rate of strain model. The extra particle interaction source terms occurring in the model for the pressure rate of strain can be constructed easily, with no noticeable extra computational cost. The modified turbulence model for Π_{ij} predicts a faster return to isotropy in dispersed two phase flows. Lagrangian mixing models, which are related to the transport equation for the scalar dissipation rate, are shown to be affected by the mass transfer between the phases through the model for the scalar dissipation rate. The often used algebraic gradient diffusion models for the Reynolds stress, the triple correlations as well as the Reynolds flux are extended to multiphase flows.

3.1 Introduction

Second moment closures (SMC) have become a standard method of solving turbulence problems. The starting point are the Eulerian Navier Stokes equations which are decomposed into a mean and a fluctuating part using the (Reynolds) decomposition $U = \langle U \rangle + u'$ and $p = \langle p \rangle + p'$. The Reynolds stresses $\widetilde{u_i'' u_j''}$ then appear as unknowns in the transport equation for momentum. These Reynolds stresses are then obtained by solving a transport equation for them.

The modelling of the pressure rate of strain term appearing in the transport equations for the Reynolds stresses has been given the most attention over the years [26, 90, 95, 116, 138, 155], but also algebraic closures of the second and third order correlations have been developed [35, 64, 129].

The modeled Reynolds stress equation can also be obtained by starting with the Navier Stokes equations in Lagrangian form and using a Reynolds decomposition. The Lagrangian evolution can then be modeled using a Langevin equation for the

velocity U_i of a computational gas particle [127] $dU_i = G_{ij}(U_j - \widetilde{U_j})dt + B_{ij}dW_j(t)$, where models for the drift tensor G_{ij} and diffusion tensor B_{ij} need to be found. Equations for the mean momentum, the Reynolds stresses, turbulence dissipation et cetera can then be derived from this stochastic Lagrangian model [65, 127, 128, 129, 130]. Both approaches lead to an almost identical form of the Reynolds stress equation. The relationship between these two approaches for single phase flows was investigated in [129]. This will be treated in detail in chapter 4. First, in this chapter, the Eulerian SMC modelling approach will be treated.

When considering multiphase flows, additional source terms appear in the Navier Stokes equations [42, 76, 117]. There can be momentum exchange, mass transfer due to vaporisation or condensation, heat transfer or, more general, transfer of a scalar through the interface between the phases. These effects also show up in the Reynolds stress equations leading to new closure problems compared to the case of single phase flow. In particular, the closure of the pressure rate of strain has to be reconsidered. Simulation results of a polydispersed particle laden jet where the modification of the (Eulerian) model for the pressure rate of strain has been investigated numerically were already reported in [4].

In section 3.2, the instantaneous transport equations describing a two-phase flow are presented and in section 3.3 the mean transport equations are derived. In section 3.4, the Reynolds stress transport equation is introduced to close the mean momentum equation, and model closures are presented. In section 3.5, the modelling of the pressure rate of strain, occurring in the transport equation for the Reynolds stresses, is described and an extension to multiphase flow turbulence is proposed. In section 3.6, the modelling of scalar transport is presented and a transport equation for the scalar dissipation rate (used in a later chapter in the model for Lagrangian mixing) is derived. We end with some general remarks and conclusions in section 3.7.

3.2 Instantaneous equations

Our starting point is the multiphase Navier Stokes equation derived previously by Drew [42] and Kataoka [76] and more recently revisited by Naud [117]. We will consider here dispersed two phase flows, where the continuous phase is a gaseous phase and the dispersed phase is assumed to be present in the form of liquid particles (droplets) or solid particles. In a conservative formulation the properties of a continuous phase, namely the instantaneous velocity $\mathbf{U}_{\mathrm{f}} = U_{\mathrm{f},i}$ and the pressure field p, together with a transported scalar ϕ, are given by the solution of the transport equations:

$$\frac{\partial}{\partial t}\left(\rho\mathcal{X}\right) + \frac{\partial}{\partial x_j}\left(\rho U_j\mathcal{X}\right) = \mathcal{S}_m^{(I)}, \tag{3.1}$$

$$\frac{\partial}{\partial t}\left(\rho U_i \mathcal{X}\right) + \frac{\partial}{\partial x_j}\left(\rho U_i U_j \mathcal{X}\right) = -\frac{\partial\left(p\mathcal{X}\right)}{\partial x_i} + \frac{\partial\left(\tau_{ij}\mathcal{X}\right)}{\partial x_j} + \left(\rho\mathcal{X}\right) g_i + \mathcal{S}_{U_i}^{(I)} + U_{I,i}\mathcal{S}_m^{(I)}, \tag{3.2}$$

$$\frac{\partial}{\partial t}\left(\rho\phi\mathcal{X}\right) + \frac{\partial}{\partial x_j}\left(\rho\phi U_j \mathcal{X}\right) = -\frac{\partial}{\partial x_j}\left(J_j\mathcal{X}\right) + \left(\rho\mathcal{X}\right)\mathcal{S} + \mathcal{S}_\phi^{(I)} + \phi_I\mathcal{S}_m^{(I)}, \tag{3.3}$$

where ρ is the density of the carrier fluid and g_i is the gravity vector. $\mathcal{X}(\boldsymbol{x}, t)$ is the indicator function of the continuous phase: equal to one when the continuous phase is present at $(\boldsymbol{x}, t)$ and equal to zero otherwise.

Any continuous phase property Q is a priori only defined when $\mathcal{X} = 1$. Thus, rather than discontinuous fields Q, we will consider the associated generalised functions [117]

$$Q\mathcal{X}. \tag{3.4}$$

$\mathcal{S}_{U_i}^{(I)}$ is the two-way coupling source term: the source of momentum due to stress at the interface (surface forces). The source term $\mathcal{S}_\phi^{(I)}$ is the two way coupling source term due to the scalar flux at the interface and $\mathcal{S}$ is the source term due to chemical reactions in the carrier fluid. Finally, $\mathcal{S}_m^{(I)}$ is the source term taking into account mass transfer from the dispersed phase to the carrier phase due to evaporation. In the momentum equation, it is premultiplied by the fluid velocity at the interface: $U_{I,i}$. The vaporised mass is assumed to enter the gas phase with the instantaneous particle velocity $U_{\mathrm{p},i}$, and therefore $U_{I,i} = U_{\mathrm{p},i}$. In the scalar equation, the source term for mass transfer is premultiplied by the scalar value at the interface ϕ_I. The value of ϕ_I is in general determined by thermodynamic equilibrium. The Newtonian stress tensor τ_{ij} in the continuous phase reads:

$$\tau_{ij}\mathcal{X} = \mu\mathcal{X}\left[\left(\frac{\partial U_i\mathcal{X}}{\partial x_j} + \frac{\partial U_j\mathcal{X}}{\partial x_i}\right) - \frac{2}{3}\frac{\partial U_k\mathcal{X}}{\partial x_k}\delta_{ij}\right], \tag{3.5}$$

with μ the dynamic viscosity of the fluid. For the molecular flux J appearing in equation (3.3) we assume a gradient diffusion such that:

$$J_j\mathcal{X} = -\Gamma\mathcal{X}\frac{\partial\phi\mathcal{X}}{\partial x_j} = -\rho\mathcal{X}\mathbb{D}\frac{\partial\phi\mathcal{X}}{\partial x_j}. \tag{3.6}$$

In equation (3.6), $\Gamma \equiv \rho\mathbb{D}$ is the molecular diffusivity and $\mathbb{D}$ is the diffusion coefficient.

3.3 Mean continuity and momentum equation

The mean continuity and mean momentum equations are obtained by Reynolds averaging and taking the expected value $\langle\ \rangle$ of equations (3.1) and (3.2):

$$\frac{\partial\overline{\rho}}{\partial t}+\frac{\partial\overline{\rho}\widetilde{U}_j}{\partial x_j}=\langle\mathcal{S}_m^{(I)}\rangle, \tag{3.7}$$

$$\begin{aligned}\frac{\partial\overline{\rho}\widetilde{U}_i}{\partial t}+\frac{\partial\overline{\rho}\widetilde{U}_j\widetilde{U}_i}{\partial x_j} \;=\; &-\frac{\partial\overline{p}}{\partial x_i}-\frac{\partial\overline{\rho}\widetilde{u_i''u_j''}}{\partial x_j}+\frac{\partial\overline{\tau_{ij}}}{\partial x_j}\\ &+\overline{\rho}g_i+\left\langle\mathcal{S}_{U_i}^{(I)}\right\rangle+\langle U_{I,i}\mathcal{S}_m^{(I)}\rangle,\end{aligned} \tag{3.8}$$

$$\begin{aligned}\frac{\partial}{\partial t}\left(\overline{\rho}\widetilde{\phi}\right)+\frac{\partial}{\partial x_j}\left(\overline{\rho}\widetilde{\phi}\widetilde{U}_j\right)=&-\frac{\partial\overline{J_j}}{\partial x_j}-\frac{\partial\overline{\rho}\widetilde{u_j''\phi''}}{\partial x_j}+\overline{\rho}\widetilde{\mathcal{S}}\\ &+\left\langle\mathcal{S}_\phi^{(I)}\right\rangle+\langle\phi_I\mathcal{S}_m^{(I)}\rangle,\end{aligned} \tag{3.9}$$

where the following notations have been introduced:

$$\overline{Q}=\alpha\langle Q\rangle_{|\mathrm{f}}=\langle Q_\mathrm{f}\mathcal{X}\rangle,\qquad \widetilde{Q}=\widetilde{Q}_{|\mathrm{f}}=\frac{\langle\rho_\mathrm{f}Q_\mathrm{f}\mathcal{X}\rangle}{\langle\rho_\mathrm{f}\mathcal{X}\rangle}, \tag{3.10}$$

To be more precise, the notation $\langle\ \rangle$ refers to the expected value of volume averages over small volumes. The fluctuations are defined as

$$\begin{aligned}q'\mathcal{X}&=Q\mathcal{X}-\langle Q\rangle_{|\mathrm{f}}\mathcal{X}, &\qquad q_I'a_I&=Q_Ia_I-\langle Q\rangle_{|\mathrm{f}}a_I,\\ q''\mathcal{X}&=Q\mathcal{X}-\widetilde{Q}\mathcal{X}, &\qquad q_I''a_I&=Q_Ia_I-\widetilde{Q}a_I,\end{aligned} \tag{3.11}$$

which will be used later in the derivation. In equation (3.11), a_I is the interfacial area concentration, which can be defined as

$$a_{I_\mathrm{k}}(\boldsymbol{x},t)=|\boldsymbol{\nabla}\varphi_\mathrm{k}|\,\delta(\varphi_\mathrm{k}(\boldsymbol{x},t))\,. \tag{3.12}$$

δ is the Dirac delta function and φ_k is the interface function, given by

$$\begin{aligned}&\varphi_\mathrm{k}(\boldsymbol{x},t)>0 \quad \text{within phase } k,\\ &\varphi_\mathrm{k}(\boldsymbol{x},t)<0 \quad \text{within any other phase than phase } k,\\ &\varphi_\mathrm{k}(\boldsymbol{x},t)=0 \quad \text{at the interface of phase } k.\end{aligned} \tag{3.13}$$

Two way coupling Considering that the integral of the forces exerted on a particle surface are equal to the drag force, the expected value of the source term $\left\langle \mathcal{S}_{U_i}^{(I)} \right\rangle$ describing momentum transfer at the particle interface is obtained as a sum over the particles present in a small domain Ω of volume $\mathcal{V}_\Omega$:

$$\left\langle \mathcal{S}_{U_i}^{(I)} \right\rangle = -\frac{1}{\mathcal{V}_\Omega} \left\langle \sum_\Omega m_\mathrm{p} \left(\frac{dU_{\mathrm{p},i}}{dt} - \frac{1}{\rho_\mathrm{p}} \frac{\partial \overline{p}}{\partial x_i} - g_i \right) \right\rangle. \tag{3.14}$$

The particle force $F_\mathrm{p} = m_\mathrm{p} \frac{dU_{\mathrm{p},i}}{dt}$ exerted on the carrier fluid can be obtained from the equation of motion of a particle in a turbulent fluid, which is given by the Maxey-Riley equation [99] discussed in chapter 5. In subsequent sections, we will work with the general source term $\mathcal{S}_{U_i}^{(I)}$ instead of substituting the specific form appearing at the right-hand side of (3.14). This makes the procedure described in this paper independent of the form of the source term and therefore more generally applicable. Similarly, the mean source term for mass transfer $\left\langle \mathcal{S}_m^{(I)} \right\rangle$ is obtained as the sum of the vaporisation rate of the individual droplets in the considered volume $\mathcal{V}_\Omega$:

$$\left\langle \mathcal{S}_m^{(I)} \right\rangle = -\frac{1}{\mathcal{V}_\Omega} \left\langle \sum_\Omega \dot{m}_\mathrm{p} \right\rangle. \tag{3.15}$$

Models to determine $\dot{m}_\mathrm{p}$ were discussed in chapter 2. Note that the notations introduced in (3.10) imply that the mean density and pressure appearing in equations (3.7) and (3.8) are averaged over the whole two-phase flow. For instance, in case of a constant density ρ_f:

$$\overline{\rho} = \langle \mathcal{X} \rangle \rho_\mathrm{f}, \tag{3.16}$$

where $\langle \mathcal{X} \rangle$ is the probability of presence of the continuous phase (i.e. the volume fraction of the continuous phase since we consider volume averages). The mean continuity equation can be substituted into the mean momentum equation to yield the non conservative form of the mean momentum equation

$$\begin{aligned} \overline{\rho} \frac{\partial \widetilde{U}_i}{\partial t} + \overline{\rho} \widetilde{U}_j \frac{\partial \widetilde{U}_i}{\partial x_j} \;=\; & -\frac{\partial \overline{p}}{\partial x_i} - \frac{\partial \overline{\rho} \widetilde{u_i'' u_j''}}{\partial x_j} + \frac{\partial \overline{\tau_{ij}}}{\partial x_j} \\ & + \overline{\rho} g_i + \left\langle \mathcal{S}_{U_i}^{(I)} \right\rangle + \left\langle U_{I,i} \mathcal{S}_m^{(I)} \right\rangle - \widetilde{U}_{\mathrm{f},i} \left\langle \mathcal{S}_m^{(I)} \right\rangle. \end{aligned} \tag{3.17}$$

In this non conservative formulation, the source term for mass transfer will disappear from equation (3.17) only if the velocity at the interface is taken to be the mean fluid velocity. It is important to realise that in the instantaneous nonconservative formulation the source term due to mass transfer disappears whereas for the mean nonconservative formulation not resolving the flow around the droplets leads to the appearance of a source term.

3.4 Reynolds stress transport equation

The mean momentum equation contains an extra term that was not present in the instantaneous momentum equation: the transport term of the second moment correlations $\widetilde{u_i'' u_j''}$. Due to these second moment correlations, also called the Reynolds stresses, the system of equations (3.7-3.8) is not closed. Although many models have been proposed in the literature (see e.g. [130, 176]) we will restrict ourselves here to a closure based on the modelling of the exact transport equation for the Reynolds stresses. This approach is known as *Second Moment Closure* (SMC). The fluctuating velocity transport equation can be obtained from the Navier Stokes equations and is given by:

$$\begin{aligned}
&\frac{\partial}{\partial t}\left(\rho u_i''\mathcal{X}\right) + \frac{\partial}{\partial x_k}\left(\rho u_i''\widetilde{U}_k\mathcal{X}\right) + \rho u_k''\mathcal{X}\frac{\partial \widetilde{U}_i}{\partial x_k} \\
&\quad = -\frac{\partial p\mathcal{X}}{\partial x_i} + \frac{\partial \tau_{ik}\mathcal{X}}{\partial x_k} - \frac{\partial}{\partial x_k}\left(\rho u_i'' u_k''\mathcal{X}\right) + \mathcal{S}_{U_i}^{(I)} + u_{I,i}''\mathcal{S}_m^{(I)} \\
&\qquad - \rho\mathcal{X}\left[\frac{\partial \widetilde{U}_i}{\partial t} + \widetilde{U}_k\frac{\partial \widetilde{U}_i}{\partial x_k} - g_i\right].
\end{aligned} \tag{3.18}$$

Multiplying equation (3.18) by $u_j''\mathcal{X}_\mathrm{k}$ we obtain an equation (E_{ij}). $\langle (E_{ij}) + (E_{ji})\rangle$ then gives the exact transport equation for the Reynolds stress:

$$\begin{aligned}
&\frac{\partial}{\partial t}\left(\overline{\rho}\widetilde{u_i'' u_j''}\right) + \frac{\partial}{\partial x_k}\left(\overline{\rho}\widetilde{u_i'' u_j''}\widetilde{U}_k\right) + \overline{\rho}\widetilde{u_i'' u_k''}\frac{\partial \widetilde{U}_j}{\partial x_k} + \overline{\rho}\widetilde{u_j'' u_k''}\frac{\partial \widetilde{U}_i}{\partial x_k} \\
&\quad = -\left[\overline{u_i''\frac{\partial p}{\partial x_j}} + \overline{u_j''\frac{\partial p}{\partial x_i}}\right] + \left[\overline{u_i''\frac{\partial \tau_{jk}}{\partial x_k}} + \overline{u_j''\frac{\partial \tau_{ik}}{\partial x_k}}\right] \\
&\qquad - \frac{\partial}{\partial x_k}\left[\overline{\rho}\widetilde{u_i'' u_j'' u_k''}\right] \\
&\qquad + \left\langle \mathcal{S}_{u_i u_j}^{(I)} \right\rangle \\
&\qquad + 2\left\langle u_{I,i}'' u_{I,j}'' \mathcal{S}_m^{(I)}\right\rangle - \widetilde{u_i'' u_j''}\left\langle \mathcal{S}_m^{(I)}\right\rangle,
\end{aligned} \tag{3.19}$$

with the two way coupling source term $\mathcal{S}_{u_i u_j}^{(I)}$ due to momentum transfer between the phases defined as:

$$\left\langle \mathcal{S}_{u_i u_j}^{(I)} \right\rangle \equiv \left\langle u_{I,i}'' \mathcal{S}_{U_j}^{(I)} \right\rangle + \left\langle u_{I,j}'' \mathcal{S}_{U_i}^{(I)} \right\rangle, \tag{3.20}$$

where $\boldsymbol{u}_I'' \equiv \boldsymbol{U}_I - \widetilde{U}_\mathrm{f}$ is the velocity fluctuation at the interface.

The interface source terms $\left\langle \mathcal{S}_{u_i u_j}^{(I)} \right\rangle$ and $2\left\langle u_{I,i}'' u_{I,j}'' \mathcal{S}_m^{(I)} \right\rangle - \widetilde{u_i'' u_j''}\left\langle \mathcal{S}_m^{(I)} \right\rangle$ reflect the modulation of turbulence due to interface momentum transfer and mass transfer. $\left\langle \mathcal{S}_{u_i u_j}^{(I)} \right\rangle$ accounts for the effects of surface forces (mainly due to the drag in case

of particles in a gas). The contribution to the modulation of the Reynolds stresses due to mass transfer can be decomposed into two terms. First of all, $\left\langle u''_{I,i}u''_{I,j}\mathcal{S}_m^{(I)}\right\rangle$ accounts for the effect of mass transfer (the effect of extra mass appearing in the gas in the case of droplet evaporation) entering the gas phase with the Reynolds stress $\widetilde{u''_{I,i}u''_{I,j}}$. The source term $\left\langle u''_{I,i}u''_{I,j}\mathcal{S}_m^{(I)}\right\rangle - \widetilde{u''_iu''_j}\left\langle \mathcal{S}_m^{(I)}\right\rangle$ accounts for fluctuations in the (local) vaporisation rate and arises from the continuity equation. This term is zero when the source term for mass transfer knows no local fluctuations: $\mathcal{S}_m'^{(I)} = \mathcal{S}_m^{(I)} - \left\langle \mathcal{S}_m^{(I)}\right\rangle = 0$. Introducing the dissipation ϵ:

$$\epsilon \equiv \frac{1}{2}\epsilon_{kk} \qquad \text{with} \qquad \overline{\rho}\epsilon_{ij} \equiv 2\left\langle \mu\mathcal{X}\frac{\partial u''_i\mathcal{X}}{\partial x_k}\frac{\partial u''_j\mathcal{X}}{\partial x_k}\right\rangle, \tag{3.21}$$

and neglecting the terms $\langle u''_i\mathcal{X}\rangle$ (in the decomposition of the velocity-pressure gradient tensor) and the molecular diffusion terms, equation (3.19) can be written as:

$$\begin{aligned}\frac{\partial}{\partial t}\left(\overline{\rho}\widetilde{u''_iu''_j}\right) + \frac{\partial}{\partial x_k}\left(\overline{\rho}\widetilde{u''_iu''_j}\widetilde{U}_k\right) \\ = P_{ij} + \mathcal{T}_{ij} + \Pi_{ij} - \frac{2}{3}\overline{\rho}\epsilon\delta_{ij} \\ + \left\langle \mathcal{S}^{(I)}_{u_iu_j}\right\rangle + 2\langle u''_{I,i}u''_{I,j}\mathcal{S}_m^{(I)}\rangle - \langle u''_{I,i}u''_{I,j}\rangle\langle\mathcal{S}_m^{(I)}\rangle,\end{aligned} \tag{3.22}$$

where the production P_{ij},

$$P_{ij} \equiv -\overline{\rho}\widetilde{u''_iu''_k}\frac{\partial\widetilde{U}_j}{\partial x_k} - \overline{\rho}\widetilde{u''_ju''_k}\frac{\partial\widetilde{U}_i}{\partial x_k}, \tag{3.23}$$

is closed and needs no modelling. The tensor $\mathcal{T}_{ij}$ contains the third order correlations together with the pressure fluctuations:

$$\mathcal{T}_{ij} \equiv -\frac{\partial}{\partial x_k}\left[\overline{\rho}\widetilde{u''_iu''_ju''_k} - \overline{p'u''_i}\delta_{jk} - \overline{p'u''_j}\delta_{ik}\right], \tag{3.24}$$

where the pressure-velocity fluctuation correlations come from the decomposition of the velocity-pressure gradient tensor. The tensor Π_{ij} is defined by

$$\Pi_{ij} \equiv \left\langle p'\mathcal{X}\left(\frac{\partial u''_i\mathcal{X}}{\partial x_j} + \frac{\partial u''_j\mathcal{X}}{\partial x_i}\right)\right\rangle - \overline{\rho}\left(\epsilon_{ij} - \frac{1}{3}\epsilon_{kk}\delta_{ij}\right). \tag{3.25}$$

Under the assumption of local isotropy, the last term in equation (3.25) cancels, and Π_{ij} is the pressure rate of strain. Except for the production term, all terms on the right hand side of equation (3.23) are unclosed and need to be modeled.

3.4.1 Assumptions on the velocity at the interface $U_{I,i}$

The velocity at the interface between the phases is known in Direct Numerical Simulations (DNS), where the flow at the interface is resolved. In our Reynolds Averaged approach however, an assumption for the velocity at the interface needs to be adopted. Several approaches exist in the literature for determining the velocity $U_{I,i}$ and the velocity fluctuations at the interface $u''_{I,i}$ [2, 31, 32, 60, 89].

The approach termed 'standard' approach assumes that in expressions which have to be Reynolds averaged the velocity at the interface is the fluid phase velocity: $U_{I,i} = U_{\mathrm{f},i}$. The source term $\left\langle u''_{I,i}\mathcal{S}^{(I)}_{U_j}\right\rangle$ is then modeled as:

$$\left\langle u''_{I,i}\mathcal{S}^{(I)}_{U_j}\right\rangle = \left\langle U_{\mathrm{f},i}\mathcal{S}^{(I)}_{U_j}\right\rangle - \langle U_{\mathrm{f},i}\rangle\left\langle \mathcal{S}^{(I)}_{U_j}\right\rangle. \tag{3.26}$$

The second approach was proposed by Crowe [32] and is based on an energy balance (i.e. the first law of thermodynamics). A no-slip condition is imposed on the particle surface, implying that the velocity at the interface is equal to the particle velocity: $U_{I,i} = U_{\mathrm{p},i}$. The velocity fluctuation at the interface is written as (see eq. (3.11))

$$\begin{aligned} u''_{I,i} &= U_{I,i} - \widetilde{U}_{\mathrm{f},i} \\ &= U_{\mathrm{p},i} - \widetilde{U}_{\mathrm{f},i} \end{aligned} \tag{3.27}$$

and the source terms appearing in (3.20) can be written as

$$\left\langle u''_{I,i}\mathcal{S}^{(I)}_{U_j}\right\rangle = \left\langle U_{\mathrm{p},i}\mathcal{S}^{(I)}_{U_j}\right\rangle - \widetilde{U}_{\mathrm{f},i}\left\langle \mathcal{S}^{(I)}_{U_j}\right\rangle. \tag{3.28}$$

Note that the mean of the fluctuations at the interface does not equal zero because we have used the zero-slip assumption to determine the instantaneous velocity at the interface. In general, the mean particle velocity is not equal to the mean fluid velocity. Equation (3.28) can be written out into the following form for the source term appearing in the equation for the turbulent kinetic energy:

$$\mathcal{S}_k = \frac{1}{\tau_{\mathrm{p}}}\frac{\widetilde{\rho}_{\mathrm{p}}}{\widetilde{\rho}_{\mathrm{f}}}\left[\left|\langle U_{\mathrm{p},i}\rangle - \langle U_{\mathrm{f},i}\rangle\right|^2 + \left(\left\langle u''_{\mathrm{p},i}u''_{\mathrm{p},i}\right\rangle - \left\langle u''_{\mathrm{f},i}u''_{\mathrm{f},i}\right\rangle\right)\right] \tag{3.29}$$

The interpretation of the first term on the right hand side of equation (3.29) is that it describes the wake induced turbulence; it reflects the conversion of mechanical energy by the drag force into turbulent kinetic energy. The second term functions as a redistribution of the turbulent kinetic energy of the particles to that of the carrier fluid.

Ahmadi *et al*. [2, 27] go a step further by considering a thermodynamically consistent modelling approach involving the Clausius-Duhem inequality. After a lengthy analysis, they find an expression for the source term appearing in the

equation for the Reynolds stresses. In their analyses, the Reynolds stress equations are contracted to yield an expression for the turbulent kinetic energy. The expression can be written down in several ways, but a comparison with the expression of Crowe is possible by writing it in the following form:

$$\mathcal{S}_{u_i u_j} = \beta \underbrace{\left\langle u''_{I,i} \mathcal{S}^{(I)}_{U_j} \right\rangle}_{\text{Crowe}} + \underbrace{\left\langle u''_{\mathrm{f},j} \mathcal{S}^{(I)}_{U_i} \right\rangle}_{\text{standard term}}, \tag{3.30}$$

with

$$\beta = \alpha' + \frac{(1-\alpha')\left(\left\langle U_{\mathrm{p},i} \mathcal{S}^{(I)}_{U_i} \right\rangle - \langle U_{\mathrm{p},i} \rangle \left\langle \mathcal{S}^{(I)}_{U_i} \right\rangle\right)}{\left\langle u''_{I,i} \mathcal{S}^{(I)}_{U_i} \right\rangle}. \tag{3.31}$$

β is interpreted as a model coefficient that needs to be determined. In the calculations presented in Chrigiu *et al*. [27], a value of $\beta = 0.5$ has been used. Effectively, the model of Ahmadi *et al*. is an interpolation between the classical two-way coupling term (3.26) and the two way coupling term of Crowe (3.28).

Expression (3.30) reduces to the source term proposed by Crowe when the fluid velocity fluctuations at the interface are zero and when $\beta = 1$.

In the approach used in this thesis, the velocity at the interface is modelled according to the model of Crowe, as was done in [89].

3.4.2 Turbulent kinetic energy equation

We can construct the transport equation for the turbulent kinetic energy from the Reynolds stress equation by using $k = \frac{1}{2} u''_i u''_i$, $\widetilde{k} = \frac{1}{2} \widetilde{u''_i u''_i}$. Taking the trace of equation (3.23) gives:

$$\begin{aligned} &\frac{\partial \overline{\rho} \widetilde{k}}{\partial t} + \frac{\partial}{\partial x_k}\left(\overline{\rho} \widetilde{U}_k \widetilde{k}\right) \\ &\quad = P_{ii} + \mathcal{T}_{ii} + \Pi_{ii} - \overline{\rho}\epsilon \\ &\quad + \frac{1}{2}\left\langle \mathcal{S}^{(I)}_{u_i u_i} \right\rangle + 2\left\langle k_I \mathcal{S}^{(I)}_m \right\rangle - \langle k_I \rangle \left\langle \mathcal{S}^{(I)}_m \right\rangle, \end{aligned} \tag{3.32}$$

where $k_I = \frac{1}{2} u''_{I,i} u''_{I,i}$. In flows where mass transfer occurs, the trace of the pressure rate of strain is not exactly zero, since the continuity condition contains a source term for mass transfer. The trace of the pressure rate of strain in case of mass transfer is

$$\Pi_{ii} = 2\langle p'_I \mathcal{S}'_m \rangle. \tag{3.33}$$

Note that in this case, the pressure rate of strain Π_{ij} is not an 'ideal' redistribution term for the Reynolds stress anymore since the trace is not zero.

Constant	C_s^ϵ	$C_{\epsilon 1}$	$C_{\epsilon 2}$	$C_{\epsilon 3}$
Value	0.18	1.44	1.92	1.8

Table 3.1: Model constants in the equation for turbulence dissipation.

3.4.3 Dissipation equation

The exact equation for the dissipation ϵ can be derived starting from the transport equation for the velocity fluctuations and taking the gradient of this expression. However, it is more usual to work with a model dissipation equation [130]. Adding the exact two way coupling terms for interface momentum and mass transfer to a standard form of the modeled single phase dissipation equation, one obtains

$$\frac{\partial \overline{\rho}\epsilon}{\partial t} + \frac{\partial \overline{\rho}\widetilde{U}_j\epsilon}{\partial x_j} = \frac{\partial}{\partial x_j}\left[\left(\overline{\mu}\delta_{jk} + \frac{C_s^\epsilon}{\omega}\overline{\rho}\widetilde{u_j''u_k''}\right)\frac{\partial \epsilon}{\partial x_k}\right] + \omega\left(C_{\epsilon 1}\frac{1}{2}P_{kk} - C_{\epsilon 2}\overline{\rho}\epsilon\right) + \left\langle \mathcal{S}_\epsilon^{(I)}\right\rangle + \left\langle \mathcal{S}_{\epsilon_m}^{(I)}\right\rangle. \tag{3.34}$$

In equation (3.35), the turbulence frequency is defined as $\omega \equiv \frac{\epsilon}{\widetilde{k}}$.

The two way coupling source term

$$\left\langle \mathcal{S}_\epsilon^{(I)}\right\rangle \equiv 2\left\langle \frac{\mu}{\rho}\mathcal{X}\frac{\partial u_i''\mathcal{X}}{\partial x_j}\frac{\partial \mathcal{S}_{U_i}^{(I)}}{\partial x_j}\right\rangle \tag{3.35}$$

is usually modelled as [60, 89]

$$\left\langle \mathcal{S}_\epsilon^{(I)}\right\rangle = C_{\epsilon_3}\frac{\epsilon}{\widetilde{u_k''u_k''}}\left\langle \mathcal{S}_{u_ku_k}^{(I)}\right\rangle, \tag{3.36}$$

where the value of the constant $C_{\epsilon_3} = 1.8$ is taken from [89]. The values of the other constant are taken from standard literature [130] and are given in table (3.4.3). Note that the two-way coupling source term $\langle \mathcal{S}_\epsilon\rangle$ given by equation (3.36) is different from the source term used in the analysis of Mashayek and Taulbee [98]. They find for homogeneous flows the expression

$$\mathcal{S}_\epsilon^{(I)} = \frac{\epsilon}{\widetilde{k}}\frac{\lambda\alpha_{\mathrm{p}}}{\tau_{\mathrm{p}}}(2\widetilde{k} - C_{\epsilon_3}u_{\mathrm{f},k}''u_{\mathrm{p},k}''), \tag{3.37}$$

with $\lambda \equiv \rho_{\mathrm{p}}\rho_{\mathrm{f}}$ and a constant $C_{\epsilon_3} = 0.8$.

The exact form of the mass transfer source term following from the derivation of the equation for dissipation is given by

$$\left\langle \mathcal{S}_{\epsilon_m}^{(I)}\right\rangle = 2\left\langle \frac{\mu}{\rho}\mathcal{X}\frac{\partial u_i''\mathcal{X}}{\partial x_j}\frac{\partial u_i''\mathcal{X}}{\partial x_j}\mathcal{S}_m^{(I)}\right\rangle. \tag{3.38}$$

When the instantaneous dissipation and the source term for mass transfer are uncorrelated, this source term can be written as

$$\left\langle \mathcal{S}_{\epsilon_m}^{(I)} \right\rangle = \epsilon \left\langle \mathcal{S}_m^{(I)} \right\rangle. \tag{3.39}$$

A model similar to equation (3.36) can be used to model (3.38) as suggested in Berlemont *et al*. [9]. However, the advantage of the approach given here is that there is no need to introduce an extra model constant. Model (3.39) implies that the direct effect of vaporisation (in which case the source term $\mathcal{S}_m$ will be positive) is that it always causes an *increase* of the turbulence dissipation.

3.5 Modelling the pressure rate of strain tensor

In the transport equation for the Reynolds stresses, the unknown pressure rate of strain tensor Π_{ij} appears. The modelling of this term is of crucial importance to correctly determine the Reynolds stresses. Much attention has been given to the modelling of the pressure rate of strain tensor over the past several decades [26, 64, 90, 95, 116, 138, 155]. Models for the pressure rate of strain tensor Π_{ij} can be constructed by examining the equation for the fluctuating pressure, which can be derived from the Navier Stokes equation. The Poisson equation for the fluctuating pressure p' can be obtained by subtracting the divergence of the mean momentum equation (3.8) from the divergence of the transport equation for the fluctuating velocity (3.18) (in conservative form). We then obtain:

$$\begin{aligned} -\frac{\partial^2 p' \mathcal{X}}{\partial x_i^2} &= \underbrace{2\frac{\partial \overline{\rho}\widetilde{U}_i}{\partial x_j}\frac{\partial u_j'' \mathcal{X}}{\partial x_i}}_{\text{Rapid part}} + \underbrace{\frac{\partial}{\partial x_i}\left[\frac{\partial \rho \mathcal{X} u_i'' u_k'' - \overline{\rho}\widetilde{u_i'' u_k''}}{\partial x_k}\right]}_{\text{Slow part}} \\ &+ \underbrace{\frac{\partial}{\partial x_i}\left[\mathcal{S}_{U_i}^{(I)} - \left\langle \mathcal{S}_{U_i}^{(I)} \right\rangle\right]}_{\text{Particle contribution to slow part}} + \underbrace{\frac{\partial}{\partial x_i}\left[U_{I,i}\mathcal{S}_m^{(I)} - \left\langle U_{I,i}\mathcal{S}_m^{(I)} \right\rangle\right]}_{\text{Vaporisation contribution to slow part}}. \end{aligned} \tag{3.40}$$

In this work, surface contributions (wall effects) will be neglected and therefore do not appear in equation (3.40).

We see that the presence of particles as well as the occurrence of mass transfer give a contribution to the slow part consisting of respectively the fluctuations in the two way coupling source term for momentum transfer and the fluctuations in the two way coupling source term for mass transfer.

In the work of Chou [26], it is shown that the solution of the equation for the fluctuating pressure in single phase flows can be written in terms of Green's functions. The equation for the fluctuating pressure can be written as a Poisson equation. The solution of a Poisson equation with a general right hand side $f(x)$,

$$\frac{\partial^2 p'}{\partial x_i^2} = f(x) \tag{3.41}$$

and boundary conditions $p' = 0$ (we neglect the surface contribution) is given by the volume integration over the Green's function $\frac{1}{|\mathbf{y}-\mathbf{x}|}$,

$$p' = -\frac{1}{4\pi}\int_V \frac{f(y)}{|\mathbf{y}-\mathbf{x}|}dV. \tag{3.42}$$

In equation (3.42), $\mathbf{x}$ denotes the location at which p' is evaluated and $\mathbf{y}$ is the location in the flow domain over which the integration is taken. V is the volume of the flow domain bounded by surface S. Since the Poisson equation is linear, the solution of each of the inhomogeneous terms at the right hand side of equation (3.40) can be calculated separately and then added to obtain the final solution. The pressure strain correlation[1] $\Pi_{ij} = \left\langle p'\mathcal{X}(\frac{\partial u_i''\mathcal{X}}{\partial x_j}+\frac{\partial u_j''\mathcal{X}}{\partial x_i})\right\rangle$ is obtained by multiplying the solution by the fluctuating strain rate $s_{ij}''=\frac{\partial u_i''\mathcal{X}}{\partial x_j}+\frac{\partial u_j''\mathcal{X}}{\partial x_i}$ and taking the expected value of the result. The pressure-velocity gradient correlation can now be written in terms of second and fourth order tensors [151, 164] as follows:

$$\Pi_{ij} = \underbrace{A_{ij} + M_{ijkl}\frac{\partial\overline{\rho}\widetilde{U_k}}{\partial x_l}}_{\Pi_{ij}^{(\mathrm{f})}} + \Pi_{ij}^{(\mathrm{fp})} + \Pi_{ij}^{(m)}. \tag{3.43}$$

Single phase flow The slow term of the pressure rate of strain tensor $\Pi_{ij}^{(1)} = A_{ij}$ is given by

$$A_{ij} = \frac{1}{4\pi}\int_V \left\langle (\frac{\partial u_i''\mathcal{X}}{\partial x_j} + \frac{\partial u_j''\mathcal{X}}{\partial x_i})\frac{\partial^2\rho u_k''u_l''\mathcal{X}}{\partial x_k\partial x_l}\right\rangle \frac{dV}{|\mathbf{y}-\mathbf{x}|}, \tag{3.44}$$

and $\Pi_{ij}^{(2)} = M_{ijkl}\frac{\partial\overline{\rho}\widetilde{U_k}}{\partial x_l}$ is the rapid term, where the fourth order tensor M_{ijkl} is given by:

$$M_{ijkl} = \frac{1}{2\pi}\int_V \left\langle (\frac{\partial u_i''\mathcal{X}}{\partial x_j} + \frac{\partial u_j''\mathcal{X}}{\partial x_i})\frac{\partial u_l''\mathcal{X}}{\partial x_k}\right\rangle \frac{dV}{|\mathbf{y}-\mathbf{x}|}. \tag{3.45}$$

Tensors A_{ij} and M_{ijkl} satisfy the constraints of

- symmetry : $A_{ij} = A_{ji}$, $M_{ijkl} = M_{jikl} = M_{ijlk}$,
- continuity : $A_{ii} = 0$, $M_{ijkk} = M_{iikl} = 0$,
- normalisation : $M_{ijkk} = 2\overline{\rho}\widetilde{u_i''u_j''}$.

[1] Note that in the literature, the pressure rate of strain correlation is usually defined to contain $\frac{p'}{\rho}$ instead of simply p'.

These constraints were already recognised by Rotta [138].

The modelling assumption that we make is that the tensors A_{ij} and M_{ijkl} can be written as algebraic tensors depending only on the history of the Reynolds stress tensor and dissipation rate (See for details on the single phase turbulence model the paper of Speziale *et al*. [155]):

$$\begin{aligned} A_{ij} &= \epsilon \mathcal{A}_{ij}(\mathbf{b}), \\ M_{ijkl} &= \widetilde{k} \mathcal{M}_{ijkl}(\mathbf{b}), \end{aligned} \tag{3.46}$$

with $\mathbf{b}$ the normalised anisotropy tensor:

$$b_{ij} = \frac{\widetilde{u_i'' u_j''}}{\widetilde{u_k'' u_k''}} - \frac{1}{3}\delta_{ij}. \tag{3.47}$$

The mean velocity gradient tensor can be decomposed into a symmetric and an antisymmetric part:

$$\frac{\partial \widetilde{U}_i}{\partial x_j} = S_{ij} + \Omega_{ij}, \tag{3.48}$$

with the mean strain rate tensor S_{ij} and the mean vorticity tensor Ω_{ij} defined as:

$$S_{ij} = \frac{1}{2}\frac{\widetilde{k}}{\epsilon}\left(\frac{\partial \widetilde{U}_i}{\partial x_j} + \frac{\partial \widetilde{U}_j}{\partial x_i}\right) \qquad \text{and} \qquad \Omega_{ij} = \frac{1}{2}\frac{\widetilde{k}}{\epsilon}\left(\frac{\partial \widetilde{U}_i}{\partial x_j} - \frac{\partial \widetilde{U}_j}{\partial x_i}\right). \tag{3.49}$$

The model for the pressure strain correlation can be written in the equivalent form:

$$\Pi_{ij} = \epsilon f_{ij}^L(\mathbf{b}, \mathbf{S}, \mathbf{\Omega}) \tag{3.50}$$

Here, f_{ij}^L is the part of the tensor function f_{ij} that is linear in the mean velocity gradients and traceless. Form invariance under a change of coordinates requires f_{ij}^L to transform as:

$$\mathbf{Q} f(\mathbf{b}, \mathbf{S}, \mathbf{\Omega}) \mathbf{Q}^T = f(\mathbf{Q}\mathbf{b}\mathbf{Q}^T, \mathbf{Q}\mathbf{S}\mathbf{Q}^T, \mathbf{Q}\mathbf{\Omega}\mathbf{Q}^T), \tag{3.51}$$

where $\mathbf{Q}$ is the rotation tensor. This relationship implies that f_{ij}^L be an isotropic tensor function of its arguments. The most general form of the pressure strain correlation for the single phase terms $\Pi_{ij} = A_{ij} + M_{ijkl}\frac{\langle U_k \rangle}{\partial x_l}$ is [151]:

$$\begin{aligned} \Pi_{ij}^{(f)} &= \beta_1 \overline{\rho}\epsilon b_{ij} + \beta_2 \overline{\rho}\epsilon (b_{ij}^2 - \frac{1}{3} b_{kk}^2 \delta_{ij}) + \beta_3 \overline{\rho}\epsilon S_{ij} \\ &+ \beta_4 \overline{\rho}\epsilon (b_{kj} S_{ik} + b_{ik} S_{kj} - \frac{2}{3} b_{lk} S_{kl} \delta_{ij}) + \beta_5 \overline{\rho}\epsilon (b_{kj}^2 S_{ik} + b_{ik}^2 S_{kj} - \frac{2}{3} b_{lk}^2 S_{kl} \delta_{ij}) \\ &+ \beta_6 \overline{\rho}\epsilon (b_{ik}\Omega_{kj} + b_{kj}\Omega_{ik}) + \beta_7 \overline{\rho}\epsilon (b_{kj}^2 \Omega_{ik} + b_{ik}^2 \Omega_{kj}). \end{aligned} \tag{3.52}$$

Model	C_1	C_2	C_3	C_4	C_5	model constants
Rotta	$-2c_1$	0	0	0	0	$c_1 = 4.15$
LRR	$-2c_1$	0	$\frac{4}{3}c_2$	$2c_2$	$2c_2$	$c_1 = 1.8$, $c_2 = 0.6$
SSG	$-2c_1 - c_1^\star \frac{P_{ii}}{\epsilon}$	c_2	$c_3 - c_3^\star\sqrt{b_{ii}^2}$	c_4	c_5	$c_1 = 1.7$, $c_2 = 4.2$, $c_3 = 0.8$
						$c_4 = 1.25$, $c_5 = 0.40$
						$c_1^\star = 1.8$, $c_3^\star = 1.30$

Table 3.2: Model constants for three different Reynolds stress models.

The notation b_{ij}^2 is the usual abbreviation for $b_{il}b_{lj}$ and b_{ii}^2 is the trace of b_{ij}^2. Speziale et al. [155] have shown that the equilibrium structure of (3.52) in plane homogeneous turbulent flow is indistinguishable from the reduced expression:

$$\begin{aligned}\Pi_{ij}^{(f)} &= C_1\overline{\rho}\epsilon b_{ij} + C_2\overline{\rho}\epsilon(b_{ij}^2 - \frac{1}{3}b_{kk}^2\delta_{ij}) + C_3\overline{\rho}\epsilon S_{ij} \\ &+ C_4\overline{\rho}\epsilon(b_{kj}S_{ik} + b_{ik}S_{kj} - \frac{2}{3}b_{kl}S_{lk}\delta_{ij}) + C_5\overline{\rho}\epsilon(b_{ik}\Omega_{kj} + b_{kj}\Omega_{ik}). \qquad (3.53)\end{aligned}$$

If $C_1 \neq 0$ is the only non-zero constant, the linear return-to-isotropy model of Rotta is obtained [130, 138]. The model constants can be chosen in such a way that they correspond to well known turbulence models [130]. The values of the constants for the Rotta model, the model of Launder, Reece and Rodi (LRR) [90] and the model of Speziale, Sarkar and Gatski (SSG) [155] are summarised in Table (3.2).

Fluid-particle contribution We now have two additional contributions to the pressure rate of strain term: the gas-particle interaction term $\Pi_{ij}^{(\mathrm{fp})}$,

$$\Pi_{ij}^{(\mathrm{fp})} = \frac{1}{4\pi}\int_V \left\langle (\frac{\partial u_i''\mathcal{X}}{\partial x_j} + \frac{\partial u_j''\mathcal{X}}{\partial x_i})\frac{\partial \mathcal{S}_{U_k}^{(I)}}{\partial x_k}\right\rangle \frac{dV}{|\mathbf{y}-\mathbf{x}|} \qquad (3.54)$$

and the mass transfer term $\Pi_{ij}^{(m)}$:

$$\Pi_{ij}^{(m)} = \frac{1}{4\pi}\int_V \left\langle (\frac{\partial u_i''\mathcal{X}}{\partial x_j} + \frac{\partial u_j''\mathcal{X}}{\partial x_i})\frac{\partial U_{I,l}\mathcal{S}_m^{(I)}}{\partial x_l}\right\rangle \frac{dV}{|\mathbf{y}-\mathbf{x}|}. \qquad (3.55)$$

In the presence of a dispersed phase and mass transfer, the pressure strain rate can be decomposed into a particle-free part (the single phase flow turbulence model that was discussed previously) and contributions due to particle interaction and due to mass transfer:

$$\begin{aligned}\Pi_{ij} &= \Pi_{ij}^{(\mathrm{f})} + \Pi_{ij}^{(\mathrm{fp})} + \Pi_{ij}^{(m)} \\ &= \epsilon f_{ij}^{(\mathrm{f})}(\mathbf{b},\mathbf{S},\mathbf{\Omega}) + \left\langle \mathcal{S}_{u_k u_k}^{(I)}\right\rangle f_{ij}^{(\mathrm{fp})}(\mathbf{b}^{(\mathrm{fp})}) + \left\langle u_{I,k}''u_{I,k}''\mathcal{S}_m^{(I)}\right\rangle f_{ij}^{(m)}(\mathbf{b}^{(m)}). \qquad (3.56)\end{aligned}$$

Following the same procedure as described above, we propose a pressure rate of strain model of the general form

$$\Pi_{ij}^{(\mathrm{fp})} = \left\langle \mathcal{S}_{u_k u_k}^{(I)} \right\rangle f_{ij}^{(\mathrm{fp})}(\mathbf{b}^{(\mathrm{fp})}) \tag{3.57}$$

for the gradient of the source term for interface momentum transfer, and

$$\Pi_{ij}^{(m)} = \left\langle u''_{I,k} u''_{I,k} \mathcal{S}_m^{(I)} \right\rangle f_{ij}^{(m)}(\mathbf{b}^{(m)}) \tag{3.58}$$

to take into account the effect of mass transfer. In eqs. (3.57, 3.58), $f_{ij}^{(\mathrm{fp})}(\mathbf{b}^{(\mathrm{fp})})$ and $f_{ij}^{(m)}(\mathbf{b}^{(m)})$ are isotropic tensor functions, depending only on the anisotropy tensors $b_{ij}^{(\mathrm{fp})}$ and $b_{ij}^{(m)}$.

These anisotropy tensors $\mathbf{b}^{(\mathrm{fp})}$ and $\mathbf{b}^{(\mathbf{m})}$ are given by:

$$b_{ij}^{(\mathrm{fp})} = \frac{1}{2} \frac{\left\langle u''_{I,i} \mathcal{S}_{U_j}^{(I)} + u''_{I,j} \mathcal{S}_{U_i}^{(I)} \right\rangle}{\left\langle u''_{I,k} \mathcal{S}_{U_k}^{(I)} \right\rangle} - \frac{1}{3}\delta_{ij} = \frac{\left\langle \mathcal{S}_{u_i u_j} \right\rangle}{\left\langle \mathcal{S}_{u_k u_k} \right\rangle} - \frac{1}{3}\delta_{ij} \tag{3.59}$$

$$b_{ij}^{(m)} = \frac{1}{2} \frac{\left\langle u''_{I,i} u''_{I,j} \mathcal{S}_m^{(I)} + u''_{I,j} u''_{I,i} \mathcal{S}_m^{(I)} \right\rangle}{\left\langle u''_{I,k} u''_{I,k} \mathcal{S}_m^{(I)} \right\rangle} - \frac{1}{3}\delta_{ij} = \frac{\left\langle u''_{I,i} u''_{I,j} \mathcal{S}_m^{(I)} \right\rangle}{\left\langle u''_{I,k} u''_{I,k} \mathcal{S}_m^{(I)} \right\rangle} - \frac{1}{3}\delta_{ij} \tag{3.60}$$

This choice of fluid particle and mass transfer anisotropy tensor can be justified by performing an analysis analogous to that of Launder, Reece and Rodi [90]. This tedious analysis results in a model similar to the Rotta model with anisotropy tensors given by eqs. (3.59,3.60).

With the anisotropy tensor (3.59), the most general form for the contribution of interface momentum transfer to the pressure rate of strain is then found to be:

$$\mathit{\Pi}_{ij}^{(\mathrm{fp})} = -\frac{1}{2}\left\langle \mathcal{S}_{u_k u_k}^{(I)} \right\rangle \left[C_1^{(\mathrm{fp})} b_{ij}^{(\mathrm{fp})} + C_2^{(\mathrm{fp})} \left(b_{ij}^{2(\mathrm{fp})} - \frac{1}{3} b_{kk}^{2(\mathrm{fp})} \delta_{ij} \right) \right], \tag{3.61}$$

Equation (3.61) is the most general tensor satisfying equation (3.57) according to the Cayley-Hamilton theorem [130]. The factor $\frac{1}{2}\left\langle \mathcal{S}_{u_k u_k}^{(I)} \right\rangle$ in equation (3.61) specifies the time scale for the return to isotropy implied by $\mathit{\Pi}_{ij}^{(\mathrm{fp})}$, as we will see in equation (3.66). It plays the same role as the factor $\overline{\rho}\epsilon$ in equation (3.53). It is indeed the two-way coupling source term appearing in the turbulent kinetic transport equation next to $\overline{\rho}\epsilon$ (with opposite sign). Mashayek *et al.* [98, 161] proposed the form for $\mathit{\Pi}_{ij}^{(\mathrm{fp})}$ corresponding to the LRR model[2]:

$$\mathit{\Pi}_{ij}^{(\mathrm{fp})} = -C_{f3}\left\langle \mathcal{S}_{u_k u_k}^{(I)} \right\rangle b_{ij}^{(\mathrm{fp})} = -\frac{1}{2} C_1^{(\mathrm{fp})} \left\langle \mathcal{S}_{u_k u_k}^{(I)} \right\rangle b_{ij}^{(\mathrm{fp})}. \tag{3.62}$$

[2] Note that in their Eulerian-Eulerian formulation Mashayek and Taulbee do not introduce the source term $\mathcal{S}_{U_i}$ appearing in (3.2). Instead, they directly express mean source terms as functions of volume fraction, τ_{p}, and particle and fluid velocity difference by considering the drag force for a monodispersed spray.

where C_{f_3} is the model constant introduced by Mashayek *et al*. and $C_1^{(\mathrm{fp})}$ is the model constant introduced in equation (3.61).

The contribution from mass transfer can be modeled similar to the fluid particle contribution. The most general form for the mass transfer contribution is:

$$\Pi_{ij}^{(m)} = \frac{1}{2}\langle u''_{I,k} u''_{I,k} \mathcal{S}_m^{(I)} \rangle \left[C_1^{(m)} b_{ij}^{(m)} + C_2^{(m)} \left(b_{ij}^{2(m)} - \frac{1}{3} b_{kk}^{2(m)} \delta_{ij} \right) \right], \tag{3.63}$$

with $b_{ij}^{(m)}$ the normalised anisotropy tensor based on the Reynolds stress mass transfer source terms (3.60).

Note that the continuity constraints are slightly violated when mass transfer occurs, as was mentioned in section 3.4.2.

The relative importance of these extra two-way coupling terms appearing in the model for the pressure rate of strain can be seen immediately when they are compared directly with the two-way coupling source terms $\left\langle \mathcal{S}_{u_i u_j}^{(I)} \right\rangle$ that are explicitly present in the Reynolds stress equations. The source term that is explicitly present in the Reynolds stress equations is given by:

$$\left\langle \mathcal{S}_{u_i u_j}^{(I)} \right\rangle = \left\langle u''_{I,i} \mathcal{S}_{U_j}^{(I)} \right\rangle + \left\langle u''_{I,j} \mathcal{S}_{U_i}^{(I)} \right\rangle, \tag{3.64}$$

and the indirect two-way coupling source term present in the Reynolds stress equations, through the model for Π_{ij}, is given by:

$$\Pi_{ij}^{(\mathrm{fp})} = -\frac{1}{2} C_1^{(\mathrm{fp})} \left(\left\langle \mathcal{S}_{u_i u_j}^{(I)} \right\rangle - \frac{1}{3} \langle \mathcal{S}_{u_k u_k}^{(I)} \rangle \delta_{ij} \right). \tag{3.65}$$

The extra contribution due to the modification of the pressure rate of strain is of the same order of magnitude as the original ('classical') two-way coupling source term.

Evolution equation for anisotropy tensor When considering (for the sake of simplicity) a non-vaporising two phase flow, this model implies the following evolution for the fluid phase anisotropy tensor b_{ij}:

$$\begin{aligned} \frac{\mathrm{d}b_{ij}}{\mathrm{d}t} &= (2 - C_1)\, \omega b_{ij} + \omega^{(fp)} \left[\frac{\left\langle \mathcal{S}_{u_i u_j}^{(I)} \right\rangle}{\left\langle \mathcal{S}_{u_k u_k}^{(I)} \right\rangle} - \frac{\widetilde{u''_i u''_j}}{\widetilde{u''_k u''_k}} - C_{f3} b_{ij}^{(\mathrm{fp})} \right] \\ &= (2 - C_1)\, \omega b_{ij} + \omega^{(fp)} \left[b_{ij}^{(\mathrm{fp})} (1 - C_{f_3}) - b_{ij} \right], \end{aligned} \tag{3.66}$$

with

$$\omega = \frac{\epsilon}{\widetilde{k}} \qquad \text{and} \qquad \omega^{(fp)} = \frac{\left\langle \mathcal{S}_{u_k u_k}^{(I)} \right\rangle}{\overline{\rho} \widetilde{k}}. \tag{3.67}$$

The first term on the right hand side of (3.66) is the linear model of Rotta where the time scale of return to isotropy is $1/\omega$. The last term represents the effect of two-way coupling on the return to isotropy. The time scale $1/\omega^{(\mathrm{fp})}$ is based on the two-way coupling source term appearing in the turbulent kinetic energy transport equation.

Determining the model constants When extending the SSG turbulence model to dispersed two-phase flows, only two extra constants need to be evaluated. Mashayek and Taulbee [98] obtained a value of $C_{f3} = 0.5$ (or $C_1^{(\mathrm{fp})} = 1$) from their Direct Numerical Simulations. No information is available on the model constant $C_2^{(\mathrm{fp})}$. Therefore, we will now restrict to the model (3.62) proposed by Mashayek *et al*. [98], in the context of Rotta or LRR Reynolds stress models. No information in the form of detailed simulations is available at all for the mass transfer contributions to the pressure rate of strain and the coefficients $C_1^{(m)}$ and $C_2^{(m)}$ cannot be determined. To get an impression of the importance of the modification of Π_{ij} due to mass transfer, the constants are set to $C_1^{(m)} = 1$ and $C_2^{(m)} = 0$.

3.6 Scalar flux transport equation

Similar to the derivation of the transport equation for the Reynolds stresses, a transport equation for the scalar flux (also sometimes called the Reynolds flux) and scalar variance can be derived. In addition to the equation for the velocity fluctuation (3.18), the equation for the scalar fluctuation is used:

$$\begin{aligned}
&\frac{\partial}{\partial t}\left(\rho\phi''\mathcal{X}\right) + \frac{\partial}{\partial x_j}\left(\rho\phi''\widetilde{U}_j\mathcal{X}\right) + \rho u_j''\mathcal{X}\frac{\partial\widetilde{\phi}}{\partial x_j} \\
&\qquad = -\frac{\partial}{\partial x_i}\left(J_i'\mathcal{X}\right) + \left(\rho\mathcal{X}\right)\mathcal{S} - \frac{\partial}{\partial x_j}\left(\rho\phi''u_j''\mathcal{X}\right) \\
&\qquad + \mathcal{S}_\phi^{(I)} + \phi_I''\mathcal{S}_m^{(I)} - \rho\mathcal{X}\left[\frac{\partial\widetilde{\phi}}{\partial t} + \widetilde{U}_j\frac{\partial\widetilde{\phi}}{\partial x_j}\right].
\end{aligned} \tag{3.68}$$

Multiplying equation (3.68) by $u_i''\mathcal{X}$ we obtain an equation ($E_{i\phi}$). Multiplying the equation for the velocity fluctuations (3.18) by $\phi''\mathcal{X}$ we obtain an equation ($E_{\phi i}$). $\langle(E_{i\phi}) + (E_{\phi i})\rangle$ then gives the equation for the scalar flux

$$\begin{aligned}
\frac{\partial}{\partial t}\left(\overline{\rho}\widetilde{u_i''\phi''}\right) \;+\; &\frac{\partial}{\partial x_j}\left(\overline{\rho}\widetilde{u_i''\phi''}\widetilde{U}_j\right) + \overline{\rho}\widetilde{\phi''u_j''}\frac{\partial\widetilde{U}_i}{\partial x_j} + \overline{\rho}\widetilde{u_i''u_j''}\frac{\partial\widetilde{\phi}}{\partial x_j} \\
= \;& -\overline{\phi''\frac{\partial p'}{\partial x_i}} + \overline{\phi''\frac{\partial\tau_{ij}}{\partial x_j}} - \overline{u_i''\frac{\partial J_i'}{\partial x_i}} \\
-\; &\frac{\partial}{\partial x_j}\left(\overline{\rho}\widetilde{u_i''\phi''u_j''}\right) + \overline{\rho}\widetilde{u_i''S} + \left\langle\mathcal{S}_{u_i\phi}^{(I)}\right\rangle \\
+\; &2\left\langle u_{I,i}''\phi_I''\mathcal{S}_m^{(I)}\right\rangle - \left\langle u_{I,i}''\phi_I''\right\rangle\left\langle\mathcal{S}_m^{(I)}\right\rangle,
\end{aligned} \tag{3.69}$$

with

$$\left\langle \mathcal{S}^{(I)}_{u_i\phi} \right\rangle = \left\langle \phi''_I \mathcal{S}^{(I)}_{U_i} \right\rangle + \left\langle u''_{I,i} \mathcal{S}^{(I)}_{\phi} \right\rangle. \tag{3.70}$$

In these equations the fluctuations ϕ''_I and $u_{I,i}$ are defined by equation (3.11). The interface source term $\left\langle \mathcal{S}^{(I)}_{u_i\phi} \right\rangle$ reflects the modulation of the scalar flux due to interface scalar transfer (like for instance enthalpy transfer in non-isothermal flows). It contains two parts. The first contribution is the correlation between scalar fluctuations at the interface and the source term for momentum transfer; This source term is generated by scalar gradients at the surface, for instance a temperature gradient in the case of droplet heating or a concentration gradient. Similar to the assumption for the velocity fluctuations at the interface, the scalar fluctuation is given by the difference between the instantaneous scalar value at the interface (e.g. the particle surface temperature T_p or the surface vapour mass fraction $Y^{(I)}$) and the scalar mean of the fluid phase:

$$\phi''_I = \phi_\mathrm{p} - \widetilde{\phi}_\mathrm{f}. \tag{3.71}$$

The second contribution in equation (3.70) is the correlation of the velocity fluctuations at the interface and the scalar source term.

The source terms including $\mathcal{S}_m$ reflect the modulation of the scalar flux due to mass transfer (e.g. vaporising droplets). If the scalar flux and the source term for mass transfer are uncorrelated, this source term simplifies to

$$\left\langle u''_{I,i}\phi''_I \right\rangle \left\langle \mathcal{S}^{(I)}_m \right\rangle. \tag{3.72}$$

If we now introduce the scalar flux dissipation ϵ^ϕ_i as

$$\epsilon^\phi_i \equiv (\nu + I\!D) \widetilde{\frac{\partial u''_i \mathcal{X}}{\partial x_j} \frac{\partial \phi'' \mathcal{X}}{\partial x_j}} \tag{3.73}$$

and neglecting $\langle u''_i \mathcal{X} \rangle$, $\langle \phi'' \mathcal{X} \rangle$ and its divergence, the equation for the scalar flux is given by

$$\begin{aligned} \frac{\partial}{\partial t}\left(\overline{\rho}\widetilde{u''_i\phi''}\right) \; + \; & \frac{\partial}{\partial x_j}\left(\overline{\rho}\widetilde{u''_i\phi''}\widetilde{U}_j\right) \\ & = \; \frac{\partial}{\partial x_j}\left(\mathcal{T}^\phi_{ij} - \overline{\rho}\widetilde{u''_i u''_j \phi''} - \widetilde{p\phi''}\delta_{ij} + \mathcal{P}^\phi_i + \mathcal{R}^\phi_i\right) - \widetilde{\rho}\epsilon^\phi_i + \overline{\rho}\widetilde{u''_i S} \\ & + \; \left\langle \mathcal{S}^{(I)}_{u_i\phi} \right\rangle 2\left\langle u''_{I,i}\phi''_I \mathcal{S}^{(I)}_m \right\rangle - \left\langle u''_{I,i}\phi''_I \right\rangle \left\langle \mathcal{S}^{(I)}_m \right\rangle. \end{aligned} \tag{3.74}$$

The production term P^ϕ_i, defined by

$$P^\phi_i \equiv -\overline{\rho}\widetilde{\phi''u''_j}\frac{\partial \widetilde{U}_i}{\partial x_j} - \overline{\rho}\widetilde{u''_i u''_j}\frac{\partial \widetilde{\phi}}{\partial x_j}, \tag{3.75}$$

is closed in this equation. All other terms on the right hand side of equation (3.69) are unclosed and need to be modeled. The molecular transport term $\mathcal{T}_{ij}^{\phi}$ is defined as

$$\mathcal{T}_{ij} \equiv \widetilde{\rho\nu\phi''\frac{\partial u_i''}{\partial x_j}} + \widetilde{\rho\mathbb{D}u_i''\frac{\partial \phi''}{\partial x_i}} \tag{3.76}$$

and is responsible for spatial transport of the scalar flux. In high Reynolds number flows, this term is negligible and the transport of scalar flux will be due mainly to the triple correlations. The pressure scrambling term R_i^{ϕ}, defined by

$$R_i^{\phi} = \widetilde{\phi''\frac{\partial p'}{\partial x_i}} \tag{3.77}$$

is related to the pressure rate of strain term Π_{ij} in the transport equation for the Reynolds stress. This term can be decomposed into a pressure diffusion term $\widetilde{p\phi''}$ and a pressure scalar gradient term $\Pi_i^{\phi} = \widetilde{p'\frac{\partial \phi''}{\partial x_i}}$:

$$R_i^{\phi} = \Pi_i^{\phi} - \frac{\partial \widetilde{p\phi''}}{\partial x_i}, \tag{3.78}$$

The scalar flux arises in the equation for the scalar variance, which will be discussed next.

3.6.1 Scalar variance transport equation

The transport equation for the scalar variance can be derived by multiplying the equation for the scalar fluctuation by $2\phi''$ and taking the expected value of the resultant expression. This leads to:

$$\begin{aligned}\frac{\partial}{\partial t}\left(\overline{\rho}\widetilde{\phi''^2}\right) + \frac{\partial}{\partial x_j}\left(\overline{\rho}\widetilde{\phi''^2}\widetilde{U}_j\right) + 2\overline{\rho}\widetilde{\phi''u_j''}\frac{\partial \widetilde{\phi}}{\partial x_j} \\ = -2\overline{\phi''\frac{\partial J_i'}{\partial x_i}} - \frac{\partial}{\partial x_j}\left(\overline{\rho}\widetilde{\phi''\phi''u_j''}\right) + 2\overline{\rho}\widetilde{\phi''\mathcal{S}} \\ + \left\langle \mathcal{S}_{\phi\phi}^{(I)} \right\rangle + \underbrace{2\left\langle \phi_I''^2 \mathcal{S}_m^{(I)} \right\rangle - \left\langle \phi_I''^2 \right\rangle \left\langle \mathcal{S}_m^{(I)} \right\rangle}_{\mathcal{S}_{\phi\phi m}^{(I)}},\end{aligned} \tag{3.79}$$

where

$$\left\langle \mathcal{S}_{\phi\phi}^{(I)} \right\rangle \equiv 2\left\langle \phi_I'' \mathcal{S}_{\phi}^{(I)} \right\rangle. \tag{3.80}$$

Colin and Benkenida [29], following Demoulin and Borghi [39], arrive at a slightly different source term $\mathcal{S}^{(I)}_{\phi\phi m}$ in the special case when the considered scalar ϕ is the mixture fraction Z. They assume that in the equation for the scalar transport (3.3), the mixture fraction at the surface of the droplet is $Z_I = 1$, which means they start with a scalar equation where the source term is simply $\mathcal{S}^{(I)}_m$ instead of $\phi_I \mathcal{S}^{(I)}_m$. In [39], they arrive at the following expression for the effects of mass transfer in the equation for the mass fraction variance $\widetilde{Z''Z''}$:

$$\mathcal{S}^{(I)}_{\phi\phi m} = 2\overline{\rho}(\langle Z_I \mathcal{S}^{(I)}_m \rangle - \langle Z_I \rangle \langle \mathcal{S}^{(I)}_m \rangle) + \overline{\rho}(\langle Z_I \rangle^2 \langle \mathcal{S}^{(I)}_m \rangle - \langle Z_I^2 \mathcal{S}^{(I)}_m \rangle). \tag{3.81}$$

When we drop the assumption of $Z_I = 1$ and take into account the fact that the product of a scalar ϕ and a source term (which is only nonzero at the interface) will take the value at the interface, we arrive at the expression:

$$\mathcal{S}_{\phi\phi m} = \overline{\rho}(\langle Z_I Z_I \mathcal{S}^{(I)}_m \rangle - \overline{\rho}\langle Z_I \rangle \langle Z_I \mathcal{S}^{(I)}_m \rangle + \overline{\rho}(\langle Z_I \rangle^2 \langle \mathcal{S}^{(I)}_m \rangle - \langle Z_I^2 \mathcal{S}^{(I)}_m \rangle) \tag{3.82}$$

It can now easily be verified, using a Reynolds decomposition of $\left\langle Z_I Z_I \mathcal{S}^{(I)}_m \right\rangle$, that the source term (3.82) is in fact the source term $\left\langle \phi''_I \phi''_I \mathcal{S}^{(I)}_m \right\rangle$ appearing in equation (3.79). The remaining source term, $\left\langle \phi''_I \phi''_I \mathcal{S}^{(I)}_m \right\rangle - \langle \phi''_I \phi''_I \rangle \left\langle \mathcal{S}^{(I)}_m \right\rangle$, originating from the gradient of the scalar flux $\widetilde{\phi'' u''_i}$ and which takes into account the effect of fluctuations of the mass transfer source term, is not accounted for in the model of Demoulin and Borghi.

3.6.2 Scalar dissipation rate

The transport equation for the scalar dissipation rate can now be derived from the equation for the scalar fluctuations. This equation is important in the context of PDF modelling since a reduced expression for the scalar dissipation rate is used to determine the time scale of mixing in Lagrangian mixing models [55, 129]. The derivation of the transport equation for the scalar dissipation rate is analogous to the derivation of the exact transport equation for the turbulence dissipation rate. We differentiate both sides of eq. (3.68) with respect to x_i and substitute equation (3.6) for the diffusion flux. The resultant expression is then multiplied by $2\frac{\partial \phi''\mathcal{X}}{\partial x_i}$. We define $g_i \equiv \frac{\partial \phi''\mathcal{X}}{\partial x_i}$ to make the procedure more tractable. The resulting

intermediate transport equation is:

$$\begin{aligned}
&\frac{\partial \rho g_i g_i \mathcal{X}}{\partial t} + \frac{\partial \rho g_i g_i \widetilde{U_j} \mathcal{X}}{\partial x_j} + 2 g_i g_j \frac{\partial \overline{\rho} \widetilde{U_j} \mathcal{X}}{\partial x_i} + 2 g_i \phi'' \mathcal{X} \frac{\partial \mathcal{S}_m^{(I)}}{\partial x_i} \\
&\qquad = 2\Gamma g_i \frac{\partial^2 g_i \mathcal{X}}{\partial x_i^2} - 2 g_i \frac{\partial \rho u_j'' \mathcal{X}}{\partial x_i} \frac{\partial \widetilde{\phi} \mathcal{X}}{\partial x_j} - 2 g_i \rho u_j'' \mathcal{X} \frac{\partial^2 \widetilde{\phi}}{\partial x_i x_j} \\
&\qquad - 2 g_i \frac{\partial^2 \rho \phi'' \mathcal{X} u_j''}{\partial x_i \partial x_j} \\
&\qquad + 2 g_i \frac{\partial \rho \mathcal{X} \mathcal{S}}{\partial x_i} + 2 g_i \frac{\partial \mathcal{S}_\phi^{(I)}}{\partial x_i} + 2 g_i \frac{\partial \phi'' \mathcal{S}_m^{(I)}}{\partial x_i} \\
&\qquad - 2 g_i \frac{\partial}{\partial x_i} \left(\rho \mathcal{X} \left[\frac{\partial \widetilde{\phi}}{\partial t} + \widetilde{U}_j \frac{\partial \widetilde{\phi}}{\partial x_j} \right] \right).
\end{aligned} \tag{3.83}$$

We now define the scalar dissipation rate by

$$\epsilon_\phi \equiv \langle 2\Gamma g_i g_i \rangle \tag{3.84}$$

Multiplying equation (3.83) by 2Γ and Reynolds averaging yields the final form for the multiphase scalar dissipation rate transport equation:

$$\begin{aligned}
&\frac{\partial \overline{\rho} \epsilon_\phi}{\partial t} + \frac{\partial \overline{\rho} \widetilde{U}_j \epsilon_\phi}{\partial x_j} + 2 \overline{\rho} \epsilon_\phi \frac{\partial \widetilde{U}_k}{\partial x_k} \\
&\qquad = \Gamma \frac{\partial^2 \epsilon_\phi}{\partial x_j^2} - \frac{\partial \left\langle u_j'' \epsilon_\phi \right\rangle}{\partial x_j} - 4\Gamma \langle g_i g_j \rangle \frac{\partial \overline{\rho} \widetilde{U}_j}{\partial x_i} \\
&\qquad - 4\Gamma \left\langle \rho g_i \frac{\partial u_j''}{\partial x_i} \right\rangle \frac{\partial \widetilde{\phi}}{\partial x_j} - 4 \overline{\rho} \widetilde{u_j'' g_i} \Gamma \frac{\partial^2 \widetilde{\phi}}{\partial x_j \partial x_i} \\
&\qquad - 4\Gamma \left\langle g_i g_j \frac{\partial u_j''}{\partial x_i} \right\rangle + 4 \left\langle \Gamma \frac{\partial g_i}{\partial x_j} \Gamma \frac{\partial g_i}{\partial x_j} \right\rangle \\
&\qquad + \left\langle 4\Gamma g_i \frac{\partial \rho \mathcal{X} \mathcal{S}}{\partial x_i} \right\rangle + \left\langle 4\Gamma g_i \frac{\partial \mathcal{S}_\phi^{(I)}}{\partial x_i} \right\rangle + \left\langle 4\Gamma g_i g_i \mathcal{S}_m^{(I)} \right\rangle.
\end{aligned} \tag{3.85}$$

Introducing the following notations:

$\mathcal{S}_\epsilon^\phi \equiv -4\Gamma\langle g_i g_j\rangle \frac{\partial \widetilde{U}_j}{\partial x_i}$ - mean velocity gradient term
$\mathcal{G}_\epsilon^\phi \equiv -4\Gamma\Big\langle \rho g_i \frac{\partial u_j''}{\partial x_i}\Big\rangle \frac{\partial \widetilde{\phi}}{\partial x_j}$ - mean scalar gradient term
$\mathcal{C}_\epsilon^\phi \equiv -4\overline{\rho}\widetilde{u_j'' g_i}\Gamma \frac{\partial^2 \widetilde{\phi}}{\partial x_j \partial x_i}$ - mean scalar curvature
$\mathcal{V}_\epsilon^\phi \equiv 4\Gamma\Big\langle g_i g_j \frac{\partial u_j''}{\partial x_i}\Big\rangle$ - vortex stretching
$\mathcal{D}_\epsilon^\phi \equiv 4\Big\langle \Gamma \frac{\partial g_i}{\partial x_j}\Gamma\frac{\partial g_i}{\partial x_j}\Big\rangle$ - gradient dissipation
$\Big\langle \mathcal{S}_{\epsilon_\phi}^{(I)}\Big\rangle = \Big\langle 4\Gamma g_i \frac{\partial \rho \mathcal{X}\mathcal{S}}{\partial x_i}\Big\rangle$ - source term due to presence of particles
$\Big\langle \mathcal{S}_{\epsilon_m}^{(I)}\Big\rangle = \Big\langle 4\Gamma g_i g_i \mathcal{S}_m^{(I)}\Big\rangle$ - source term due to mass transfer

equation (3.86) can be written as [55]:

$$\begin{aligned}\frac{\partial \overline{\rho}\epsilon_\phi}{\partial t} + \frac{\partial \overline{\rho}\widetilde{U}_j\epsilon_\phi}{\partial x_j} + 2\overline{\rho}\epsilon_\phi\frac{\partial \widetilde{U}_k}{\partial x_k} \\ = \Gamma\frac{\partial^2\epsilon_\phi}{\partial x_j^2} - \frac{\partial\langle u_j''\epsilon_\phi\rangle}{\partial x_j} + \mathcal{S}_\epsilon^\phi + \mathcal{G}_\epsilon^\phi + \mathcal{C}_\epsilon^\phi + \mathcal{V}_\epsilon^\phi - \mathcal{D}_\epsilon^\phi \\ + \Big\langle 4\Gamma g_i \frac{\partial \rho\mathcal{X}\mathcal{S}}{\partial x_i}\Big\rangle + \Big\langle \mathcal{S}_{\epsilon_\phi}^{(I)}\Big\rangle + \langle \mathcal{S}_{\epsilon_m}^{(I)}\rangle.\end{aligned} \tag{3.86}$$

The mean scalar gradient term and the mean scalar curvature term are usually neglected under high Reynolds number assumption.

If the small scales of the scalar field are locally isotropic, then

$$4\Gamma\langle g_i g_j\rangle = \frac{2}{3}\epsilon_\phi\delta_{ij}. \tag{3.87}$$

If a steady-state problem is assumed, applying the continuity equation to the mean velocity gradient term $\mathcal{S}_\epsilon^\phi$ is found to be

$$\mathcal{S}_\epsilon^\phi = \frac{2}{3}\epsilon_\phi\langle \mathcal{S}_m^{(I)}\rangle, \tag{3.88}$$

which vanishes in flows without mass transfer between the phases.

The last two terms in equation (3.87) represent a source term from interface scalar transfer and a source term from mass transfer. Assuming vanishing correlation between fluctuating scalar dissipation rate and mass transfer source term we obtain:

$$\big\langle \mathcal{S}_{\epsilon_m}^{(I)}\big\rangle \equiv 4\big\langle \Gamma g_i g_i \mathcal{S}_m^{(I)}\big\rangle = 4\epsilon_\phi\big\langle \mathcal{S}_m^{(I)}\big\rangle. \tag{3.89}$$

Using this assumption, the source term for mass transfer in the transport equation for the scalar dissipation rate does not need any further modelling. Furthermore, the modelling of the mean velocity gradient term is similar to the mass transfer source term and they can be merged into a single source term which is $\frac{5}{3}$ times the source term (3.89).

We propose to model the source term for interface scalar transfer in a way similar to the source term appearing in the turbulence dissipation equation (3.35). We assume a form of the gradient hypothesis and propose the following model:

$$\left\langle \mathcal{S}_{\epsilon_\phi}^{(I)} \right\rangle \equiv \left\langle 4\Gamma g_i \frac{\partial \mathcal{S}_\phi^{(I)}}{\partial x_i} \right\rangle = C_{\epsilon_\phi} \frac{\epsilon_\phi}{\widetilde{\phi''\phi''}} \left\langle \mathcal{S}_\phi^{(I)} \right\rangle. \tag{3.90}$$

It should be noted that the source term for mass transfer (3.89) is significantly less complex than the source term derived by Colin and Benkenida [29]. Colin and Benkenida introduce a scalar dissipation source term of the form

$$\mathcal{S}_\epsilon^{(I)} = \frac{1}{\tau_\epsilon} \langle \phi'' \phi'' \mathcal{S}_m^{(I)} \rangle, \tag{3.91}$$

which is the source term appearing in the equation for the scalar variance, but divided by an unknown timescale τ_ϵ.

3.7 Summary and conclusions

In this chapter, the Eulerian mean transport equations describing the carrier phase of dispersed multiphase flow were presented and a modified second moment closure for the pressure rate of strain was proposed. The modified pressure rate of strain model includes the effect of the presence of particles and the effect of mass transfer on the pressure rate of strain. The extra two-way coupling source terms appearing in the model for the pressure rate of strain remain relatively simple and can be described with a model containing only two constants. When the second model constant is set to zero, the model reduces to a form similar to the Rotta model for single-phase flows, but with an anisotropy tensor based on the Reynolds stress two-way coupling source term.

Additionally, it was shown in this chapter that the source terms for mass transfer which are present *explicitly* in the transport equations for the Reynolds stresses, consist of two terms; a contribution due to the slip velocity between the phases, and a contribution due to local vaporisation fluctuations. This latter term is generally neglected in the literature [9, 60].

Furthermore, the transport equation for the scalar dissipation rate was analysed and a simple model for the effect of mass transfer was proposed.

These transport equations for turbulence will be used later in this thesis in spray flame simulations to *augment* the PDF method. The PDF method will be discussed in chapter 4.

CHAPTER 4

Turbulence modelling in dispersed two-phase flows: II

The relationship between Lagrangian models for turbulence and second moment closures for dispersed two phase flows

The analysis of the relationship between stochastic Lagrangian turbulence models and second moment closures is extended to multiphase flows with mass transfer and scalar transport. The Reynolds averaged transport equations and its Second Moment Closure model were derived in chapter 3 starting from the Eulerian multiphase Navier Stokes equations. In this chapter, a stochastic Lagrangian turbulence model is derived starting from the Lagrangian form of the multiphase Navier Stokes equations. The correspondence between the Lagrangian model and the Second Moment Closure is obtained for the pressure rate of strain Π_{ij} and the pressure scrambling term Π_{ij}^{ϕ}. The modified turbulence model for Π_{ij} predicts a faster return to isotropy in dispersed two phase flows. Lagrangian mixing models, which are related to the transport equation for the scalar dissipation rate, are shown to be affected by the mass transfer. The often used algebraic gradient diffusion models for the Reynolds stress, the triple correlations as well as the Reynolds flux are extended to multiphase flows.

4.1 Stochastic Lagrangian turbulence models

4.1.1 Introduction

In a stochastic description of turbulence, the Probability Density Function (PDF) f is considered. A general transport equation for the pdf can be derived, into which then subsequently the Navier Stokes equations can be substituted. When the density is not a constant, it is however more advantageous to consider the density weighted PDF, or Mass Density Function (MDF) $\mathcal{F}$. In multiphase flows with interphase mass transfer, the continuity equation contains a source term for mass transfer and applying the continuity equation yields a modified transport equation for the MDF. To place the derivation of the MDF in the proper context, we will first present the PDF and its general properties, then introduce the MDF and derive a transport equation into which the Navier Stokes equations are substituted.

4.1.2 Derivation of the MDF transport equation

The transport equation for the multiphase Eulerian joint velocity-composition MDF of a general state vector $\boldsymbol{\Psi}$ is derived in this section. This derivation is based on

the properties of the fine-grained PDF, which is described in detail in [130]. The description following below is an extension for multiphase flows for a general state vector and for MDFs. We consider a multiphase flow consisting of N phases $\mathrm{k} = 1..N$.In the specific case of a dispersed two phase flow, $N = 2$ and the different phases can be indicated as $\mathrm{k} = 1, 2 = \mathrm{f}, \mathrm{p}$. Phase k is completely described by the property vector $\boldsymbol{\Phi}(\boldsymbol{x}, t)$, which consists of the velocity of phase k and its composition ϕ_k: $\boldsymbol{\Phi}_\mathrm{k} = (\boldsymbol{U}_\mathrm{k}, \boldsymbol{\phi}_\mathrm{k})$. The evolution of each of the properties is described by a transport equation for $\boldsymbol{\Phi}_\mathrm{k}\mathcal{X}_\mathrm{k}$ of the form

$$\mathcal{X}_\mathrm{k}\frac{\partial\left(\boldsymbol{\Phi}_\mathrm{k}\mathcal{X}_\mathrm{k}\right)}{\partial t} + U_{\mathrm{k},j}\mathcal{X}_\mathrm{k}\frac{\partial\left(\boldsymbol{\Phi}_\mathrm{k}\mathcal{X}_\mathrm{k}\right)}{\partial x_j} = \mathcal{X}_\mathrm{k}\frac{\mathrm{D}^{|\mathrm{k}}}{\mathrm{D}t}\left(\boldsymbol{\Phi}_\mathrm{k}\mathcal{X}_\mathrm{k}\right). \tag{4.1}$$

In general, the presence of k at point $M(\boldsymbol{x}, t)$ is a random event. Moreover the flow within phase k might be turbulent. It is then of interest to consider the statistics of the values taken by $\boldsymbol{\Phi}_\mathrm{k}\mathcal{X}_\mathrm{k} = (\boldsymbol{U}_\mathrm{k}\mathcal{X}_\mathrm{k}, \boldsymbol{\phi}_\mathrm{k}\mathcal{X}_\mathrm{k})$ on the sample space $[\boldsymbol{\Psi}] = [\boldsymbol{V}, \boldsymbol{\psi}]$. For this purpose, we introduce the fine-grained pdf f_Φ. The definition of the fine-grained PDF is [128, 130]:

$$f_\Phi(\boldsymbol{\Psi}; \boldsymbol{x}, t)' = \delta\left[\boldsymbol{\Phi}(\boldsymbol{x}, t) - \boldsymbol{\Psi}\right], \tag{4.2}$$

where the state vector $\boldsymbol{\Phi}$ is defined as the sum of the state vector of each of the N phases k present,

$$\boldsymbol{\Phi} = \sum_{k=1}^{N} \boldsymbol{\Phi}_\mathrm{k}\mathcal{X}_\mathrm{k}. \tag{4.3}$$

So at each point x and time t, $f_\Phi(\boldsymbol{\Psi}; \boldsymbol{x}, t)'$ is a delta function in state space located at $\boldsymbol{\Psi} = \boldsymbol{\Phi}(\boldsymbol{x}, t)$. When taking the expected value of (4.2), we obtain

$$f_\Phi(\boldsymbol{\Psi}; \boldsymbol{x}, t) = \langle\delta\left[\boldsymbol{\Phi}(\boldsymbol{x}, t) - \boldsymbol{\Psi}\right]\rangle, \tag{4.4}$$

The conditional PDF $f_\Phi^{|\mathrm{k}}$,

$$f_\Phi^{|\mathrm{k}}(\boldsymbol{\Psi}; \boldsymbol{x}, t) = \frac{\langle\mathcal{X}_\mathrm{k}(\boldsymbol{x}, t)\,.\delta\left[\boldsymbol{\Phi}_\mathrm{k}(\boldsymbol{x}, t)\,\mathcal{X}_\mathrm{k}(\boldsymbol{x}, t) - \boldsymbol{\Psi}\right]\rangle}{\langle\mathcal{X}_\mathrm{k}(\boldsymbol{x}, t)\rangle}. \tag{4.5}$$

is only defined if the volume fraction of phase k, $\alpha_\mathrm{k}(\boldsymbol{x}, t) \neq 0$ (i.e. if the probability that phase k is present is not zero). Instead we consider the Eulerian density functions [117]:

$$f_\mathrm{k}(\boldsymbol{\Psi}; \boldsymbol{x}, t) = \langle\mathcal{X}_\mathrm{k}(\boldsymbol{x}, t)\,\delta(\boldsymbol{\Phi}_\mathrm{k}(\boldsymbol{x}, t)\,\mathcal{X}_\mathrm{k}(\boldsymbol{x}, t) - \boldsymbol{\Psi})\rangle, \tag{4.6}$$

such that $f_\mathrm{k}(\boldsymbol{\Psi}; \boldsymbol{x}, t)\,.\mathrm{d}\boldsymbol{\Psi}$ is the probability that phase k is present at $M(\boldsymbol{x}, t)$ times the conditional probability that $\boldsymbol{\Phi}_\mathrm{k}(\boldsymbol{x}, t)$ is in the interval $[\boldsymbol{\Psi}, \boldsymbol{\Psi} + \mathrm{d}\boldsymbol{\Psi}]$ (conditional

on phase k being present at $M(\boldsymbol{x},t)$). The function f_{k} is not called *probability* density function because it does not integrate to one:

$$\int_{[\boldsymbol{\Psi}]} f_{\mathrm{k}}(\boldsymbol{\Psi};\boldsymbol{x},t)\,.\mathrm{d}\boldsymbol{\Psi} = \langle \mathcal{X}_{\mathrm{k}}(\boldsymbol{x},t)\rangle = \alpha_{\mathrm{k}}(\boldsymbol{x},t)\,. \tag{4.7}$$

When the density of phase k is not constant, it is more useful to consider the mass density function (MDF) $\mathcal{F}_{\mathrm{k}}$ rather than the density function f_{k}.

$$\begin{aligned}\mathcal{F}_{\mathrm{k}}(\boldsymbol{\Psi};\boldsymbol{x},t) &= \langle \rho_{\mathrm{k}}(\boldsymbol{x},t)\,\mathcal{X}_{\mathrm{k}}(\boldsymbol{x},t)\,\delta(\boldsymbol{\Phi}_{\mathrm{k}}(\boldsymbol{x},t)\,\mathcal{X}_{\mathrm{k}}(\boldsymbol{x},t)-\boldsymbol{\Psi})\rangle\\ &= \rho_{\mathrm{k}}(\boldsymbol{\Psi})\,\langle \mathcal{X}_{\mathrm{k}}(\boldsymbol{x},t)\,\delta(\boldsymbol{\Phi}_{\mathrm{k}}(\boldsymbol{x},t)\,\mathcal{X}_{\mathrm{k}}(\boldsymbol{x},t)-\boldsymbol{\Psi})\rangle\\ &= \rho_{\mathrm{k}}(\boldsymbol{\Psi})\,f_{\mathrm{k}}(\boldsymbol{\Psi};\boldsymbol{x},t)\,.\end{aligned} \tag{4.8}$$

The MDF is defined everywhere and has the following properties:

$$\int_{[\boldsymbol{\Psi}]} \mathcal{F}_{\mathrm{k}}(\boldsymbol{\Psi};\boldsymbol{x},t)\,.\mathrm{d}\boldsymbol{\Psi} = \langle \rho_{\mathrm{k}}\mathcal{X}_{\mathrm{k}}\rangle = \alpha_{\mathrm{k}}(\boldsymbol{x},t)\,\langle \rho(\boldsymbol{x},t)\rangle_{|\mathrm{k}}, \tag{4.9}$$

$$\int_{[\boldsymbol{\Psi}]} \frac{1}{\rho_{\mathrm{k}}(\boldsymbol{\Psi})}\mathcal{F}_{\mathrm{k}}(\boldsymbol{\Psi};\boldsymbol{x},t)\,.\mathrm{d}\boldsymbol{\Psi} = \alpha_{\mathrm{k}}(\boldsymbol{x},t)\,. \tag{4.10}$$

Averages We will consider the expected value of generalised functions defined in terms of the density functions f_{k} and $\mathcal{F}_{\mathrm{k}}$:

$$\langle Q_{\mathrm{k}}\mathcal{X}_{\mathrm{k}}\rangle = \int_{[\boldsymbol{\Psi}]} \langle Q_{\mathrm{k}}|\,\boldsymbol{\Psi}\rangle_{\mathrm{k}} f_{\mathrm{k}}(\boldsymbol{\Psi})\,.\mathrm{d}\boldsymbol{\Psi}, \tag{4.11}$$

$$\langle \rho_{\mathrm{k}}Q_{\mathrm{k}}\mathcal{X}_{\mathrm{k}}\rangle = \int_{[\boldsymbol{\Psi}]} \langle Q_{\mathrm{k}}|\,\boldsymbol{\Psi}\rangle_{\mathrm{k}} \mathcal{F}_{\mathrm{k}}(\boldsymbol{\Psi})\,.\mathrm{d}\boldsymbol{\Psi}. \tag{4.12}$$

Finally it will be useful to consider the density weighted averages

$$\widetilde{Q}_{|\mathrm{k}} = \frac{\langle \rho_{\mathrm{k}}Q_{\mathrm{k}}\mathcal{X}_{\mathrm{k}}\rangle}{\langle \rho_{\mathrm{k}}\mathcal{X}_{\mathrm{k}}\rangle} = \frac{\langle \rho Q\rangle_{|\mathrm{k}}}{\langle \rho\rangle_{|\mathrm{k}}}. \tag{4.13}$$

The phasic average $\langle . \rangle_{|\mathrm{k}}$,

$$\begin{aligned}\langle Q_{\mathrm{k}}|\,\boldsymbol{\Psi};\boldsymbol{x},t\rangle_{\mathrm{k}} &= \frac{\langle Q_{\mathrm{k}}(\boldsymbol{x},t)\,\mathcal{X}_{\mathrm{k}}(\boldsymbol{x},t)\,\delta(\boldsymbol{\Phi}_{\mathrm{k}}(\boldsymbol{x},t)\,\mathcal{X}_{\mathrm{k}}(\boldsymbol{x},t)-\boldsymbol{\Psi})\rangle}{\langle \mathcal{X}_{\mathrm{k}}(\boldsymbol{x},t)\,\delta(\boldsymbol{\Phi}_{\mathrm{k}}(\boldsymbol{x},t)\,\mathcal{X}_{\mathrm{k}}(\boldsymbol{x},t)-\boldsymbol{\Psi})\rangle}\\ &= \frac{1}{f_{\mathrm{k}}(\boldsymbol{\Psi};\boldsymbol{x},t)}\langle Q_{\mathrm{k}}(\boldsymbol{x},t)\,\mathcal{X}_{\mathrm{k}}(\boldsymbol{x},t)\,\delta(\boldsymbol{\Phi}_{\mathrm{k}}(\boldsymbol{x},t)\,\mathcal{X}_{\mathrm{k}}(\boldsymbol{x},t)-\boldsymbol{\Psi})\rangle\end{aligned}$$
$$\text{if } f_{\mathrm{k}}(\boldsymbol{\Psi};\boldsymbol{x},t)>0 \text{ and equals zero otherwise.} \tag{4.14}$$

is only defined if $\alpha_{\mathrm{k}}>0$ and does not commute with time or space derivatives.

4.1.3 MDF transport equation

The transport equation of the MDF was derived previously by Naud [117] and others. Since the derivation is short and clear, it is repeated below for the sake of completeness. We are considering the function $g'_{\mathrm{k}}(\boldsymbol{\Psi};\boldsymbol{x},t)=\delta(\boldsymbol{\Phi}_{\mathrm{k}}(\boldsymbol{x},t)\,\mathcal{X}_{\mathrm{k}}(\boldsymbol{x},t)-\boldsymbol{\Psi})$. Its time and space derivatives *within* phase k are

$$\mathcal{X}_{\mathrm{k}}\frac{\partial g'_{\mathrm{k}}}{\partial t}=-\mathcal{X}_{\mathrm{k}}\frac{\partial g'_{\mathrm{k}}}{\partial \Psi_\alpha}\frac{\partial \Phi_{\mathrm{k},\alpha}\mathcal{X}_{\mathrm{k}}}{\partial t}=-\frac{\partial}{\partial \Psi_\alpha}\left[\mathcal{X}_{\mathrm{k}}\frac{\partial \Phi_{\mathrm{k},\alpha}\mathcal{X}_{\mathrm{k}}}{\partial t}g'_{\mathrm{k}}\right], \tag{4.15}$$

$$\mathcal{X}_{\mathrm{k}}\frac{\partial g'_{\mathrm{k}}}{\partial x_j}=-\mathcal{X}_{\mathrm{k}}\frac{\partial g'_{\mathrm{k}}}{\partial \Psi_\alpha}\frac{\partial \Phi_{\mathrm{k},\alpha}\mathcal{X}_{\mathrm{k}}}{\partial x_j}=-\frac{\partial}{\partial \Psi_\alpha}\left[\mathcal{X}_{\mathrm{k}}\frac{\partial \Phi_{\mathrm{k},\alpha}\mathcal{X}_{\mathrm{k}}}{\partial x_j}g'_{\mathrm{k}}\right]. \tag{4.16}$$

We can use those expressions in the following derivatives

$$\begin{aligned}\frac{\partial \rho_{\mathrm{k}}\mathcal{X}_{\mathrm{k}}g'_{\mathrm{k}}}{\partial t}&=\rho_{\mathrm{k}}\mathcal{X}_{\mathrm{k}}\frac{\partial g'_{\mathrm{k}}}{\partial t}+\frac{\partial \rho_{\mathrm{k}}\mathcal{X}_{\mathrm{k}}}{\partial t}\mathcal{X}_{\mathrm{k}}g'_{\mathrm{k}}\\&=-\frac{\partial}{\partial \Psi_\alpha}\left[\mathcal{X}_{\mathrm{k}}\frac{\partial \Phi_{\mathrm{k},\alpha}\mathcal{X}_{\mathrm{k}}}{\partial t}\rho_{\mathrm{k}}g'_{\mathrm{k}}\right]+\frac{\partial \rho_{\mathrm{k}}\mathcal{X}_{\mathrm{k}}}{\partial t}\mathcal{X}_{\mathrm{k}}g'_{\mathrm{k}},\end{aligned} \tag{4.17}$$

$$\begin{aligned}V_j\frac{\partial \rho_{\mathrm{k}}\mathcal{X}_{\mathrm{k}}g'_{\mathrm{k}}}{\partial x_j}&=\frac{\partial \rho_{\mathrm{k}}U_{\mathrm{k},j}\mathcal{X}_{\mathrm{k}}g'_{\mathrm{k}}}{\partial x_j}\\&=\rho_{\mathrm{k}}U_{\mathrm{k},j}\mathcal{X}_{\mathrm{k}}\frac{\partial g'_{\mathrm{k}}}{\partial x_j}+\frac{\partial \rho_{\mathrm{k}}U_{\mathrm{k},j}\mathcal{X}_{\mathrm{k}}}{\partial t}\mathcal{X}_{\mathrm{k}}g'_{\mathrm{k}}\\&=-\frac{\partial}{\partial \Psi_\alpha}\left[U_{\mathrm{k},j}\mathcal{X}_{\mathrm{k}}\frac{\partial \Phi_{\mathrm{k},\alpha}\mathcal{X}_{\mathrm{k}}}{\partial x_j}\rho_{\mathrm{k}}g'_{\mathrm{k}}\right]+\frac{\partial \rho_{\mathrm{k}}U_{\mathrm{k},j}\mathcal{X}_{\mathrm{k}}}{\partial x_j}\mathcal{X}_{\mathrm{k}}g'_{\mathrm{k}}.\end{aligned} \tag{4.18}$$

The expected value of the sum of (4.17) and (4.18) gives the general form for the MDF transport equation:

$$\begin{aligned}\frac{\partial \mathcal{F}_{\mathrm{k}}}{\partial t}+V_j\frac{\partial \mathcal{F}_{\mathrm{k}}}{\partial x_j}=&-\frac{\partial}{\partial \Psi_\alpha}\left[\left\langle\frac{\mathrm{D}^{|\mathrm{k}}\left(\Phi_{\mathrm{k},\alpha}\mathcal{X}_{\mathrm{k}}\right)}{\mathrm{D}t}\middle|\boldsymbol{\Psi}\right\rangle_{\mathrm{k}}\mathcal{F}_{\mathrm{k}}\right]\\&+\frac{1}{\rho_{\mathrm{k}}(\Psi)}\left\langle\frac{\partial \rho_{\mathrm{k}}\mathcal{X}_{\mathrm{k}}}{\partial t}+\frac{\partial \rho_{\mathrm{k}}U_{\mathrm{k},j}\mathcal{X}_{\mathrm{k}}}{\partial x_j}\middle|\boldsymbol{\Psi}\right\rangle_{\mathrm{k}}\mathcal{F}_{\mathrm{k}}.\end{aligned} \tag{4.19}$$

In the above expression the definition of $\mathrm{D}^{|\mathrm{k}}/\,\mathrm{D}t$ is simply the multiphase version of the substantial derivative given by equation 4.1. The second term on the right-hand side of equation (4.19) contains the continuity equation which does not equal zero in multiphase flows with interphase mass transfer.

4.1.4 Model transport equation for the MDF

Our starting point is the transport equation for the mass density function $\mathcal{F}$ (4.19). We will consider a reduced state vector $\boldsymbol{\Psi} = (\boldsymbol{U})$ with $\boldsymbol{U}$ the velocity vector. Substituting the Navier Stokes equations and considering only the continuum phase, we obtain the fluid phase velocity-MDF $\mathcal{F}_U$ [1]:

$$\frac{\partial \mathcal{F}_U}{\partial t} + V_i \frac{\partial \mathcal{F}_U}{\partial x_i} = -\frac{\partial}{\partial V_i}\left[\langle A_i | \boldsymbol{V}\rangle \mathcal{F}_U\right] - \frac{\partial}{\partial V_i}\left[\frac{1}{\rho}\left\langle \mathcal{S}_{U_i}^{(I)} \middle| \boldsymbol{V}\right\rangle \mathcal{F}_U\right] + \frac{1}{\rho}\langle \mathcal{S}_m^{(I)} | \boldsymbol{V}\rangle \mathcal{F}_U, \tag{4.20}$$

where A_i is determined by the Navier Stokes equations:

$$A_i = -\frac{1}{\rho}\frac{\partial p\mathcal{X}}{\partial x_i} + \frac{1}{\rho}\frac{\partial \tau_{ij}\mathcal{X}}{\partial x_j} + g_i\mathcal{X}. \tag{4.21}$$

We first focus on the modelling of the expected value of A_i and then use the same approach to determine the fluid-particle interaction source term and the mass transfer source term. The A_i term is decomposed into a mean and a fluctuating part, using the right-hand side of the Navier-Stokes equation:

$$\frac{\partial}{\partial V_i}\left[\langle A_i | \boldsymbol{V}\rangle \mathcal{F}_U\right] = \left(-\frac{1}{\langle \rho\mathcal{X}\rangle}\frac{\partial \langle p\mathcal{X}\rangle}{\partial x_i} + \frac{1}{\langle \rho\mathcal{X}\rangle}\frac{\partial \langle \tau_{ij}\mathcal{X}\rangle}{\partial x_j} + g_i\mathcal{X}\right)\frac{\partial \mathcal{F}_U}{\partial V_i} + \frac{\partial}{\partial V_i}\left[\frac{1}{\rho}\left\langle -\frac{\partial p'\mathcal{X}}{\partial x_i} + \frac{\partial \tau'_{ij}\mathcal{X}}{\partial x_j}\middle| \boldsymbol{V}\right\rangle \mathcal{F}_U\right], \tag{4.22}$$

The expectation of the fluctuating acceleration (conditional upon $\boldsymbol{U}(\boldsymbol{x}, t) = \boldsymbol{V}$) needs to be modeled. In a small interval of time Δt the position and velocity of the fluid particle at $x(t)$ change by

$$x_i(t + \Delta t) = x_i(t) + U_i(t)\Delta t, \tag{4.23}$$

$$U_i(t + \Delta t) = U_i(t) + \langle A_i\rangle \Delta t + \int_t^{t+\Delta t} a_i(t^{'})dt^{'}. \tag{4.24}$$

By analogy to Langevin's equation, we model the unknown acceleration $\boldsymbol{a}$ by a random contribution and a deterministic contribution [127]. For single phase flows the deterministic part is assumed to be linear in the fluctuating velocity.

For the multiphase interaction terms we assume that the deterministic part is linear in the fluctuation of the particle interaction source term $\mathcal{S}_{U_i}^{(I)}$. For vaporising

[1] all subscripts referring to the fluid phase have been left out for clarity

dispersed phase flows, we also assume that there is a contribution to the deterministic part that is linear in the fluctuation in the source term for mass vaporisation $u''_{I,i}\mathcal{S}_m^{(I)}$. The integral in equation (4.24) can then be written as:

$$\int_t^{t+\Delta t} a_i(t')dt' = G_{ij}(U_j - \widetilde{U}_j)\Delta t + B_{ij}dW_j(t) \tag{4.25}$$

$$+ G_{ij}^{(\mathrm{fp})}(\mathcal{S}_{U_j}^{(I)} - \left\langle \mathcal{S}_{U_j}^{(I)} \right\rangle)\Delta t$$

$$+ G_{ij}^{(m)}(u''_{I,j}\mathcal{S}_m^{(I)} - \left\langle u''_{I,j}\mathcal{S}_m^{(I)} \right\rangle)\Delta t, \tag{4.26}$$

with the diffusion term B_{ij} containing three contributions: a fluid phase contribution, a particle interaction contribution and a contribution due to mass transfer:

$$D_{ij} = D_{ij}^{(\mathrm{f})} + D_{ij}^{(\mathrm{fp})} + D_{ij}^{(m)}, \tag{4.27}$$

with $D_{ij} = (B \cdot B^T)_{ij}$. For single phase flows, the stochastic diffusion term $B_{ij}^{(\mathrm{f})}$ is determined based on Kolmogorov's hypothesis [84, 127], which states that in isotropic homogeneous turbulence the Lagrangian structure function:

$$D_L^{(\mathrm{f})}(s) \equiv \left\langle [U^+(t+s) - U^+(t)]^2 \right\rangle \tag{4.28}$$

for high Reynolds number turbulent flows is of the form:

$$D_L^{(\mathrm{f})}(s) = C_0 \epsilon s, \forall \tau_n \ll s \ll T_L. \tag{4.29}$$

In equation (4.28), U is a velocity component in any direction, τ_n is the Kolmogorov time scale and T_L is the integral time scale (i.e. the value of s in the inertial range). From the model Langevin equation (See e.g. [130]):

$$dU(t) = -U(t)\frac{dt}{T_L} + (\frac{2\sigma^2}{T_L})^{\frac{1}{2}}dW(t), \tag{4.30}$$

we obtain the Lagrangian structure function

$$D_L^{(\mathrm{f})}(s) = \frac{2\sigma^2}{T_L}s. \tag{4.31}$$

To be consistent with the Kolmogorov hypothesis, we demand that $\frac{2\sigma^2}{T_l} = C_0\epsilon$. The diffusion term is therefore

$$B_{ij}^{(\mathrm{f})} = \sqrt{C_0\epsilon}\delta_{ij}. \tag{4.32}$$

The Lagrangian timescale T_L can now be expressed in terms of the turbulent kinetic energy $\widetilde{k}$ and the turbulence dissipation ϵ. If we further assume that the velocity variance is that of a Gaussian distribution and therefore given by $\sigma^2 = \frac{2}{3}\widetilde{k}$, the Lagrangian timescale is:

$$T_L^{-1} = \frac{C_0\epsilon}{2\sigma^2} = \frac{3}{4}C_0\frac{\epsilon}{\widetilde{k}}. \tag{4.33}$$

Modification of the diffusion term in dispersed two phase flows We will now propose a model for the diffusion term B_{ij} in equation (4.26) to take into account the effect of the presence of the dispersed phase and interphase mass transfer. The derivation starts by a modification of the Lagrangian structure function based on the equation for turbulent kinetic energy valid for dispersed two phase flows. This modification implies a modification of the Kolmogorov hypothesis for the first order Lagrangian structure function. It is known from previous studies that indeed particle laden flows imply a modification of the theoretical results obtained by Kolmogorov, although definitive answers as to how the mechanism of turbulence modification exactly works have yet to be found [43, 44, 48, 66, 156, 160, 162].

In multiphase flows, the transport equation for the turbulent kinetic energy $\widetilde{k} = \frac{1}{2}\widetilde{u_i'' u_i''}$ (3.32) can be simplified under the assumption of homogeneous turbulence to yield

$$\frac{\partial \overline{\rho}\widetilde{k}}{\partial t} = -\overline{\rho}\epsilon + \underbrace{\frac{1}{2}\langle \mathcal{S}^{(I)}_{u_i u_i} \rangle}_{\left\langle \mathcal{S}^{(I)}_{\mathrm{k}} \right\rangle} + \underbrace{\left\langle u''_{I,i} u''_{I,i} \mathcal{S}^{(I)}_m \right\rangle - \frac{1}{2}\langle u''_{I,i} u''_{I,i} \rangle \langle \mathcal{S}^{(I)}_m \rangle}_{\left\langle \mathcal{S}^{(I)}_{\mathrm{k}m} \right\rangle}. \tag{4.34}$$

The right hand side of this equation contains the total dissipation in a turbulent multiphase flow, with a contribution from the fluid phase, the fluid particle interaction and mass transfer. The short hand notations $\left\langle \mathcal{S}^{(I)}_{\mathrm{k}} \right\rangle$ and $\left\langle \mathcal{S}^{(I)}_{\mathrm{k}m} \right\rangle$ introduced in equation (4.34) will be used from this point to indicate the two-way coupling source terms. Accordingly, the Lagrangian structure function is replaced by:

$$D_L(s) = C_0 \epsilon s - \frac{C_0^{(\mathrm{fp})}}{\overline{\rho}} \left\langle \mathcal{S}^{(I)}_{\mathrm{k}} \right\rangle s - \frac{C_0^{(m)}}{\overline{\rho}} \left\langle \mathcal{S}^{(I)}_{\mathrm{k}m} \right\rangle s \tag{4.35}$$

In this equation we have introduced different constants $C_0^{(\mathrm{fp})}$ and $C_0^{(m)}$ for the particle interaction and mass transfer to anticipate on the expected form of the modified turbulence models. The stochastic contribution to the acceleration becomes:

$$\begin{aligned} \int_t^{t+\Delta t} a_i(t')dt' &= \Big[G_{ij}(U_j - \widetilde{U}_j) + G_{ij}^{(\mathrm{fp})}(\mathcal{S}^{(I)}_{U_j} - \left\langle \mathcal{S}^{(I)}_{U_j} \right\rangle) \\ &+ G_{ij}^{(m)}(u''_{I,j}\mathcal{S}^{(I)}_m - u''_{I,j}\langle \mathcal{S}^{(I)}_m \rangle) \Big] \Delta t \\ &+ \left[C_0\epsilon - \frac{C_0^{(\mathrm{fp})}}{\overline{\rho}} \left\langle \mathcal{S}^{(I)}_{\mathrm{k}} \right\rangle - \frac{C_0^{(m)}}{\overline{\rho}} \left\langle \mathcal{S}^{(I)}_{\mathrm{k}m} \right\rangle \right]^{\frac{1}{2}} dW_i(t). \end{aligned} \tag{4.36}$$

The last term in equation (4.37) is our new model for the stochastic diffusion B_{ij}, including the effects of the presence of particles and the effect of mass transfer. It remains to determine a proper model for the drift tensors G_{ij}. When the diffusion

and the drift tensors have been determined, it is then possible to derive a mean momentum and Reynolds stress equation from them. These equations can then be compared to the Eulerian mean momentum and Reynolds stress equation that were derived by Reynolds averaging the Eulerian Navier Stokes equations.

The corresponding modeled transport equation for the MDF $\mathcal{F}_U$ can be derived [127, 172] and is given by:

$$\begin{aligned}\frac{\partial \mathcal{F}_U}{\partial t} + V_i\frac{\partial \mathcal{F}_U}{\partial x_i} &= -\left(-\frac{1}{\rho(\boldsymbol{\psi})}\frac{\partial \overline{p}}{\partial x_i} + \frac{1}{\rho(\boldsymbol{\psi})}\frac{\partial \overline{\tau_{ij}}}{\partial x_j} + g_i\right)\frac{\partial \mathcal{F}_U}{\partial V_i} \\ &- \frac{\partial}{\partial V_i}\left(\mathcal{F}_U\left[G_{il}(V_l - \widetilde{U}_l) - \frac{1}{2}C_0\epsilon\frac{\partial \ln(\mathcal{F}_U)}{\partial V_i}\right]\right) \\ &- \frac{\partial}{\partial V_i}\left(\mathcal{F}_U\left[G_{il}^{(\mathrm{fp})}(\mathcal{S}_{V_l}^{(I)} - \left\langle \mathcal{S}_{U_l}^{(I)}\right\rangle) + \frac{1}{2}\frac{C_0^{(\mathrm{fp})}}{\overline{\rho}}\left\langle \mathcal{S}_{\mathrm{k}}^{(I)}\right\rangle\frac{\partial \ln(\mathcal{F}_U)}{\partial V_i}\right]\right) \\ &- \frac{\partial}{\partial V_i}\left(\mathcal{F}_U\left[G_{il}^{(m)}(v''_{I,l}\mathcal{S}_m^{(I)} - \langle u''_{I,l}\mathcal{S}_m^{(I)}\rangle) + \frac{1}{2}\frac{C_0^{(m)}}{\overline{\rho}}\left\langle \mathcal{S}_{\mathrm{km}}^{(I)}\right\rangle\frac{\partial \ln(\mathcal{F}_U)}{\partial V_i}\right]\right).\end{aligned} \tag{4.37}$$

4.1.5 Consistency with Second Moment Closures

A modeled transport equation for the Reynolds stresses can be derived from this result by multiplying equation (4.38) by $\rho(V_j - \langle U_j\rangle)(V_k - \langle U_k\rangle)$ and integrating. The result is (with a rearrangement of indices to identify the Reynolds stresses $\widetilde{u_i''u_j''}$):

$$\begin{aligned}&\frac{\partial \overline{\rho}\widetilde{u_i''u_j''}}{\partial t} + \frac{\partial \overline{\rho}\widetilde{u_i''u_j''}\widetilde{U_k}}{\partial x_k} + \frac{\partial \widetilde{u_i''u_j''u_k''}}{\partial x_k} + \overline{\rho}\widetilde{u_j''u_k''}\frac{\partial \widetilde{U}_i}{\partial x_k} + \overline{\rho}\widetilde{u_i''u_k''}\frac{\partial \widetilde{U_j}}{\partial x_k} = \\ &\quad + G_{il}\overline{\rho}\widetilde{u_j''u_l''} + G_{jl}\overline{\rho}\widetilde{u_i''u_l''} + C_0\overline{\rho}\epsilon\delta_{ij} \\ &\quad + G_{il}^{(\mathrm{fp})}\left\langle u''_{I,j}\mathcal{S}_{U_l}^{(I)}\right\rangle + G_{jl}^{(\mathrm{fp})}\left\langle u''_{I,i}\mathcal{S}_{U_l}^{(I)}\right\rangle - C_0^{(\mathrm{fp})}\left\langle \mathcal{S}_{\mathrm{k}}^{(I)}\right\rangle\delta_{ij} \\ &\quad + G_{il}^{(m)}\langle u''_{I,j}u''_{I,l}\mathcal{S}_m^{(I)}\rangle + G_{jl}^{(m)}\langle u''_{I,i}u''_{I,l}\mathcal{S}_m^{(I)}\rangle - C_0^{(m)}\left\langle \mathcal{S}_{\mathrm{km}}^{(I)}\right\rangle\delta_{ij}.\end{aligned}$$

A model for G_{ij}, $G_{ij}^{(\mathrm{fp})}$ and $G_{ij}^{(m)}$ can now be found by comparing the above expression with the Eulerian transport equation for the Reynolds stresses (3.23) [130].

If viscous and pressure transport are neglected, then the model terms correspond to the pressure redistribution term and the dissipation. When dissipation is assumed to be isotropic we obtain the relationship:

$$\begin{aligned}\Pi_{ij} &= G_{il}\overline{\rho}\widetilde{u_j''u_l''} + G_{jl}\overline{\rho}\widetilde{u_i''u_l''} + (1 + \frac{3}{2}C_0)\overline{\rho}\epsilon\frac{2}{3}\delta_{ij} \\ &+ G_{il}^{(\mathrm{fp})}\left\langle u''_{I,j}\mathcal{S}_{U_l}^{(I)}\right\rangle + G_{jl}^{(\mathrm{fp})}\left\langle u''_{I,i}\mathcal{S}_{U_l}^{(I)}\right\rangle - \frac{3}{2}C_0^{(\mathrm{fp})}\left\langle \mathcal{S}_{\mathrm{k}}^{(I)}\right\rangle\frac{2}{3}\delta_{ij} \\ &+ G_{il}^{(m)}\left\langle u''_{I,j}u_{I,l''\mathcal{S}_m^{(I)}}\right\rangle + G_{jl}^{(m)}\langle u''_{I,i}u''_{I,l}\mathcal{S}_m^{(I)}\rangle - \frac{3}{2}C_0^{(m)}\left\langle \mathcal{S}_{\mathrm{km}}^{(I)}\right\rangle\frac{2}{3}\delta_{ij}.\end{aligned} \tag{4.38}$$

If we require $\Pi_{ii} = 0$ (redistributive) we obtain the requirement

$$\begin{aligned} &G_{il}\overline{\rho}\widetilde{u_i''u_l''} + (1 + \frac{3}{2}C_0)\overline{\rho}\epsilon + \\ &G_{il}^{(\mathrm{fp})}\left\langle u_{I,i}''\mathcal{S}_{u_l}^{(I)}\right\rangle - \frac{3}{2}C_0^{(\mathrm{fp})}\left\langle \mathcal{S}_{\mathrm{k}}^{(I)}\right\rangle + \\ &G_{il}^{(m)}\left\langle u_{I,i}''u_{I,l}''\mathcal{S}_{m}^{(I)}\right\rangle - \frac{3}{2}C_0^{(m)}\left\langle \mathcal{S}_{\mathrm{km}}^{(I)}\right\rangle = 0. \end{aligned} \tag{4.39}$$

Because we want this expression to appropriately reduce to the single phase Reynolds stress model as well as the non-vaporising Reynolds stress model, each line in equation (4.39) has to be equal to zero independently. We will now first briefly discuss the single phase flow situation and derive an expression for the drift tensor G_{ij}. The particle laden case and the vaporising particle laden case are then subsequently treated in a similar fashion.

Single phase flow The simplest choice for G_{ij} in the case of a single phase flow is

$$G_{ij} = -\frac{1}{2}(1 + \frac{3}{2}C_0)\frac{\epsilon}{\widetilde{k}}\delta_{ij}, \tag{4.40}$$

which is the Simplified Langevin Model (SLM). Substituting this into the first line (the single phase part) of equation (4.38) leads to

$$\Pi_{ij}^{(\mathrm{f})} = -\underbrace{(1 + \frac{3}{2}C_0)}_{c_1}\overline{\rho}\epsilon(\underbrace{\frac{\widetilde{u_i''u_j''}}{\widetilde{k}} - \frac{2}{3}\delta_{ij}}_{2b_{ij}}). \tag{4.41}$$

This corresponds to Rotta's model with the Rotta coefficient $c_1 = 1 + \frac{3}{2}C_0$ (see equation (3.53) and table (3.2)). A more general expression for G_{ij} can be found by assuming that G_{ij} is a general tensor function depending on n flow properties. Haworth and Pope [65] hypothesized that a sufficiently general functional form for G_{ij} is given by

$$G_{ij} = G_{ij}(\widetilde{u_k''u_l''}, \frac{\partial\widetilde{U}_p}{\partial x_q}, \epsilon). \tag{4.42}$$

The most general form of this equation that is linear in the anisotropy tensor and in the mean velocity gradients, and that satisfies the four principles of invariant modelling: dimensional consistency, coordinate system independence, Galilean invariance and rules for forming isotropic tensor functions of other tensors, is given by

$$G_{ij} = \frac{\epsilon}{\widetilde{k}}(\alpha_1\delta_{ij} + \alpha_2 b_{ij} + \alpha_3 b_{ij}^2) + H_{ijkl}\frac{\partial\widetilde{U_k}}{\partial x_l}. \tag{4.43}$$

Contribution of the fluid-particle interaction To obtain the most general model for $G_{ij}^{(\mathrm{fp})}$, it is sufficient to consider tensors of the form

$$G_{ij}^{(\mathrm{fp})} = \alpha_1^{(\mathrm{fp})}\delta_{ij} + \alpha_2^{(\mathrm{fp})} b_{ij}^{(\mathrm{fp})} + \alpha_3^{(\mathrm{fp})}(b_{ij}^{(\mathrm{fp})})^2. \tag{4.44}$$

We want to have a model for $G_{ij}^{(\mathrm{fp})}$ that corresponds to the two-way coupling part of the pressure rate of strain tensor $\Pi_{ij}^{(\mathrm{fp})}$ given by

$$\mathit{\Pi}_{ij}^{(\mathrm{fp})} = -\frac{1}{2}\langle \mathcal{S}_{u_k u_k}\rangle \left[C_1^{(\mathrm{fp})} b_{ij}^{(\mathrm{fp})} + C_2^{(\mathrm{fp})} \left(b_{ij}^{2(\mathrm{fp})} - \frac{1}{3} b_{kk}^{2(\mathrm{fp})}\delta_{ij} \right) \right]. \tag{4.45}$$

In the derivation of the Langevin model, we set $C_2^{(\mathrm{fp})} = 0$ in equation (4.45) and neglect the second and third contribution to the Langevin model in equation (4.44). We now get a fluid particle contribution similar to a Simplified Langevin Model. The fluid-particle contribution to the pressure rate of strain reduces to

$$\Pi_{ij}^{(\mathrm{fp})} \;=\; \frac{1}{2} C_1^{(\mathrm{fp})} \left(\left\langle u''_{I,i} \mathcal{S}_{U_j}^{(I)} \right\rangle + \left\langle u''_{I,j} \mathcal{S}_{U_i}^{(I)} \right\rangle - \frac{2}{3} \langle u''_{I,k} \mathcal{S}_{u_k}^{(I)} \rangle \delta_{ij} \right). \tag{4.46}$$

A model for the first contribution of the dispersed phase to G_{ij} is then:

$$G_{ij}^{(\mathrm{fp})} = -\frac{1}{2} \cdot \frac{3}{2} C_0^{(\mathrm{fp})} \delta_{ij}. \tag{4.47}$$

Substitution into equation (4.38) yields:

$$\Pi_{ij}^{(\mathrm{fp})} = -\frac{3}{2} C_0^{(\mathrm{fp})} \left(\left\langle u''_{I,i} \mathcal{S}_{U_j}^{(I)} \right\rangle + \left\langle u''_{I,j} \mathcal{S}_{U_i}^{(I)} \right\rangle - \frac{2}{3} \left\langle \mathcal{S}_{\mathrm{k}}^{(I)} \right\rangle \delta_{ij} \right), \tag{4.48}$$

which corresponds to $\Pi_{ij}^{(\mathrm{fp})}$ in the Reynolds stress model (4.45) with $C_1^{(\mathrm{fp})} = 3C_0^{(\mathrm{fp})}$ and $C_2^{(\mathrm{fp})} = 0$.

Contribution of mass transfer Similarly for the contribution of mass transfer:

$$G_{ij}^{(m)} = \alpha_1^{(m)}\delta_{ij} + \alpha_2^{(m)} b_{ij}^{(m)} + \alpha_3^{(m)}(b_{ij}^{(m)})^2. \tag{4.49}$$

A model for the mass transfer source term is obtained in a similar manner:

$$G_{ij}^{(m)} = -\frac{1}{2} \cdot \frac{3}{2} C_0^{(m)} \delta_{ij}. \tag{4.50}$$

Substitution into equation (4.38) yields:

$$\Pi_{ij}^{(m)} = -\frac{3}{2} C_0^{(m)} \left(2\langle u''_{I,i} u''_{I,j} \mathcal{S}_m^{(I)} \rangle - \frac{2}{3} \left\langle \mathcal{S}_{\mathrm{km}}^{(I)} \right\rangle \delta_{ij} \right). \tag{4.51}$$

There is now a slight inconsistency because the source term $\left\langle \mathcal{S}_{\mathrm{km}}^{(I)} \right\rangle$ contains an extra contribution due to the vaporisation fluctuations which did not appear in the model for the pressure rate of strain derived from the equation for the pressure fluctuation. This inconsistency is most likely caused by the neglect of the mean contributions in the model for the pressure rate of strain, effectively causing the pressure rate of strain to depend on the instantaneous two-way coupling terms instead of the fluctuating two-way coupling terms. Although this inconsistency deserves to be investigated (and solved), for now we will neglect it since it is most likely to play only a small contribution to the total turbulent kinetic energy budget.

4.1.6 Summary and conclusions on the Langevin model

To summarise, the complete generalised Langevin model for the equation of motion of stochastic samples of the fluid flow in a two-phase turbulent flow is:

$$dX_i(t) = U_i(t)dt, \tag{4.52}$$

$$\begin{aligned} dU_i(t) &= -\frac{1}{\rho}\frac{\partial \overline{p}}{\partial x_i}dt + g_i dt \\ &+ G_{ij}(U_j(t) - \widetilde{U_j})dt \\ &+ G_{ij}^{(\mathrm{fp})}(\mathcal{S}_{U_j}^{(I)} - \left\langle \mathcal{S}_{U_j}^{(I)} \right\rangle)dt \\ &+ G_{ij}^{(m)}(u''_{I,j}\mathcal{S}_m^{(I)} - \left\langle u''_{I,j}\mathcal{S}_m^{(I)} \right\rangle)dt \\ &+ \left[C_0\epsilon - \frac{C_0^{(\mathrm{fp})}}{\overline{\rho}}\left\langle \mathcal{S}_{\mathrm{k}}^{(I)} \right\rangle - \frac{C_0^{(m)}}{\rho}\left\langle \mathcal{S}_{\mathrm{km}}^{(I)} \right\rangle \right]^{\frac{1}{2}} dW_i(t) \\ &+ \frac{1}{\rho}\mathcal{S}_{U_i}^{(I)}dt + \frac{1}{\rho}u''_{I,i}\mathcal{S}_m^{(I)}dt, \end{aligned} \tag{4.53}$$

with G_{ij} given by:

$$\begin{aligned} G_{ij} &= \frac{\epsilon}{\widetilde{k}}(\alpha_1\delta_{ij} + \alpha_2 b_{ij} + \alpha_3 b_{ij}^2) + H_{ijkl}\frac{\partial \langle U_k \rangle}{\partial x_l}, \\ G_{ij}^{(\mathrm{fp})} &= -\frac{3}{4}C_0^{(\mathrm{fp})}\delta_{ij}, \\ G_{ij}^{(m)} &= -\frac{3}{4}C_0^{(m)}\delta_{ij}. \end{aligned} \tag{4.54}$$

The models for the fluid particle contribution and mass transfer contribution are Simplified Langevin Models, which correspond to a term similar to a Rotta term (A linear return to isotropy) in second moment closures. It is not necessary to use a SLM or a Rotta turbulence model for the continuum phase turbulence model. This model can be chosen independently.

In Monte Carlo simulations the mean velocity in a finite volume in the computational domain is obtained by averaging over the Monte Carlo particles $N_{\rm p}$ present in the cell. The calculated mean velocity will contain a statistical error which is a function of $N_{\rm p}$. When the number of particles in the cell is small, the calculated mean velocity will have a large statistical error. when this mean velocity is then used in the calculations of the individual particle evolutions, a *bias* error results, which is a deterministic error that scales with $N_{\rm p}^{-\frac{1}{2}}$ [183, 184]. To keep the bias error small, the mean velocities are obtained from the mean transport equations discussed in chapter 3 and the fluctuating quantities are obtained by solving a Langevin equation for the fluctuating velocity.

The Langevin equation for the velocity fluctuation $u_i'' = U_i - \widetilde{U}_i$ is:

$$\begin{aligned}
du_i'' &= -\left(\frac{1}{\rho}-\frac{1}{\overline{\rho}}\right)\frac{\partial \overline{p}}{\partial x_i}dt - u_j''\frac{\partial \widetilde{U}_i}{\partial x_j}dt + \frac{1}{\overline{\rho}}\frac{\partial \overline{\rho}\widetilde{u_i''u_j''}}{\partial x_j}dt \\
&+ G_{ij}u_j''dt \\
&+ (G_{ij}^{(\rm fp)}(\mathcal{S}_{U_j}^{(I)} - \left\langle \mathcal{S}_{U_j}^{(I)}\right\rangle)dt \\
&+ G_{ij}^{(m)}(u_{I,j}''\mathcal{S}_m^{(I)} - \left\langle u_{I,j}''\mathcal{S}_m^{(I)}\right\rangle)dt \\
&+ (C_0\epsilon - \frac{C_0^{(\rm fp)}}{\overline{\rho}}\left\langle \mathcal{S}_{\rm k}^{(I)}\right\rangle - \frac{C_0^{(m)}}{\overline{\rho}}\left\langle \mathcal{S}_{{\rm k}m}^{(I)}\right\rangle)^{\frac{1}{2}}dW_i(t) \\
&+ \left[\frac{1}{\rho}\mathcal{S}_{U_i}^{(I)} - \frac{1}{\overline{\rho}}\left\langle \mathcal{S}_{U_i}^{(I)}\right\rangle\right]dt + \left[\frac{1}{\rho}u_{I,i}''\mathcal{S}_m^{(I)} - \frac{1}{\overline{\rho}}\left\langle u_{I,i}''\mathcal{S}_m^{(I)}\right\rangle\right]dt. \qquad (4.55)
\end{aligned}$$

In equation (4.55), the pressure gradient is premultiplied by a factor $\frac{1}{\rho} - \frac{1}{\langle\rho\rangle}$. This factor represents the difference between the instantaneous specific volume and the mean specific volume. In an isothermal incompressible flow, the density will be constant and this term vanishes. In a spray flame however, large density variations can occur and this term may not be negligible. For now, this term will be neglected.

There are also several contributions to the Langevin model due to the presence of dispersed phase particles. The contribution to the mean drift in the third line of equation (4.55) and the contribution to the diffusion term in the fifth line of of equation result from the modification of the model for the pressure rate of strain. The two way coupling term in the last line of equation (4.55) takes into account the momentum transfer at the interface between the phases, i.e. due to the presence of dispersed phase particles interacting with fluid particles. The mean two way coupling source terms experienced by the gas phase Monte Carlo particles are known (see equation (3.14)). The instantaneous two way coupling source terms $\mathcal{S}_{U_i}^{(I)}$ and $u_{I,i}''\mathcal{S}_m^{(I)}$ seen by fluid particles are more complicated since the fluid particles are located at $x_{\rm f}$ and the dispersed phase particles are at $x_{\rm p}$. Fluid particles in the vicinity of a discrete particle will experience a force exerted by the discrete particle on the neighbouring fluid element, but fluid particles farther away will not

experience this force. The instantaneous two way coupling source term appearing in the Langevin equation is therefore non-zero only if the fluid particle shares an interface with a discrete particle. This can be modeled as a random event with a probability equal to the particle volume fraction. So when the Langevin equation is given by

$$dU_i = A_{\mathrm{f},i}dt + A_{\mathrm{p}\to\mathrm{f},i} + B_{ij}dW_j, \tag{4.56}$$

the two way coupling source term $A_{\mathrm{p}\to\mathrm{f}}$ is given by

$$A_{\mathrm{p}\to\mathrm{f},i} = \begin{cases} 0 & \text{with probability } 1-\alpha_{\mathrm{p}} \\ \frac{1}{\rho_{\mathrm{f}}}\mathcal{S}_{U_i} = \frac{1}{\rho_{\mathrm{f}}\mathcal{V}_{\mathrm{f}}}F_{\mathrm{p}\to\mathrm{f},i} & \text{with probability } \alpha_{\mathrm{p}} \end{cases} \tag{4.57}$$

where $\mathcal{V}_{\mathrm{f}}$ is the volume occupied by fluid particle f. This model was already proposed by Minier and Peirano [109]. In the case of mass transfer, other distribution algorithms for the source terms of mass transfer can be constructed, e.g. based on the saturation of the fluid phase particles [117].

4.2 Relationship with Lagrangian mixing models

In Lagrangian mixing models, scalars often evolve with a time scale based on the ratio of scalar variance and scalar dissipation rate. We want to study here the effects of the presence of particles and the effects of mass transfer on Lagrangian mixing models through the modification of the scalar dissipation rate. We will use here as an example one of the simplest models, i.e. the Interaction by Exchange with the Mean (IEM). The Lagrangian IEM model assumes a linear relaxation of a scalar towards its mean value:

$$\left\langle \Gamma\nabla^2\phi'|\psi\right\rangle = \frac{\epsilon_\phi}{2\widetilde{\phi''^2}}(\widetilde{\phi}-\psi). \tag{4.58}$$

To obtain a model for the ratio of scalar dissipation rate over scalar variance, we will analyse the simplified transport equation of the scalar dissipation rate. In the case of homogeneous nonreacting fully developed turbulence,

$$\frac{\mathrm{d}\epsilon_\phi}{\mathrm{d}t} = +\mathcal{V}_\epsilon^\phi - \mathcal{D}_\epsilon^\phi + \left\langle \mathcal{S}_{\epsilon_\phi}^{(I)}\right\rangle + \left\langle \mathcal{S}_{\epsilon_m}^{(I)}\right\rangle.$$

The vortex stretching term $\mathcal{V}_\epsilon$ is modelled as [55]

$$\begin{aligned} \mathcal{V}_\epsilon^\phi &\equiv -4\Gamma\left\langle \frac{\partial\phi''}{\partial x_j}\frac{\partial u_j''}{\partial x_i}\frac{\partial\phi''}{\partial x_i}\right\rangle \\ &\approx C_{\mathcal{V}}Re_L^{\frac{1}{2}}\frac{\epsilon}{k}\epsilon_\phi, \end{aligned} \tag{4.59}$$

and the gradient dissipation term is modelled as [55]

$$\begin{aligned}\mathcal{D}_\epsilon^\phi &\equiv 4\left\langle (\Gamma\frac{\partial^2\phi''}{\partial x_i\partial x_j})^2\right\rangle \\ &\approx C_{\mathcal{D}}Re_L^{\frac{1}{2}}\frac{\epsilon_\phi}{\widetilde{\phi''\phi''}}\epsilon_\phi,\end{aligned} \tag{4.60}$$

where the Reynolds number Re_L is defined as

$$Re_L \equiv \frac{\widetilde{k}}{\epsilon\nu}. \tag{4.61}$$

The source term accounting for the presence of the dispersed phase was already discussed when deriving the equation for the scalar dissipation rate:

$$\left\langle \mathcal{S}_{\epsilon_\phi}^{(I)}\right\rangle = C_{\epsilon_\phi}\frac{\epsilon_\phi}{\widetilde{\phi''\phi''}}\mathcal{S}_\phi^{(I)}. \tag{4.62}$$

The scalar source term $\mathcal{S}_\phi^{(I)}$ is due to diffusion at the interface:

$$\mathcal{S}_\phi^{(I)} = \left[-J_j n_j^{(I)}\right] a_I, \tag{4.63}$$

where $\boldsymbol{n}_j^{(I)}$ is the unit normal directed towards the interior of the dispersed phase, and a_I is the surface area per unit volume. When we assume a simple gradient diffusion model for the molecular flux J, such that:

$$J_j = -\Gamma\frac{\partial\phi}{\partial x_j} = -\rho\mathbb{D}\frac{\partial\phi}{\partial x_j}, \tag{4.64}$$

we can write the interface diffusion source term as:

$$\mathcal{S}_\phi^{(I)} = \left[\Gamma\frac{\partial\phi}{\partial x_j}n_j^{(I)}\right] a_I. \tag{4.65}$$

So in case of enthalpy, this represents the enthalpy gradient at the surface of a dispersed phase particle.

The source term for mass transfer was found to be:

$$\left\langle \mathcal{S}_{\epsilon_\phi}^{m}\right\rangle = 4\epsilon_\phi\langle\mathcal{S}_m^{(I)}\rangle. \tag{4.66}$$

We want to have a look at the effects of mass transfer and two-way coupling on the scalar dissipation rate, so we will not neglect these terms. In homogeneous, nonreacting fully developed turbulence, the equation for the scalar dissipation rate can be reduced to:

$$\begin{aligned}\frac{d\epsilon_\phi}{dt} &\approx \mathcal{V}_\epsilon^\phi - \mathcal{D}_\epsilon^\phi + \left\langle \mathcal{S}_{\epsilon_\phi}^{(I)}\right\rangle + \left\langle \mathcal{S}_{\epsilon_\phi}^{m}\right\rangle \\ &= Re_L^{\frac{1}{2}}\epsilon_\phi\left[C_V\frac{\epsilon}{\widetilde{k}} - \frac{\epsilon_\phi}{\widetilde{\phi''\phi''}}C_D\epsilon_\phi - \frac{\epsilon_\phi}{\widetilde{\phi''\phi''}}\frac{C_{\epsilon_\phi}}{Re_L^{\frac{1}{2}}}\left\langle \mathcal{S}_\phi^{(I)}\right\rangle - \epsilon_\phi\frac{4}{Re_L^{\frac{1}{2}}}\langle\mathcal{S}_m^{(I)}\rangle\right].\end{aligned} \tag{4.67}$$

For large Reynolds numbers, the right hand side of this expression will be large, thereby forcing the scalar dissipation rate to attain a stationary solution quickly [55]. Thus, for a fully developed scalar spectrum, the scalar mixing rate is related to the turbulent frequency by

$$\frac{\epsilon_\phi}{\widetilde{\phi''\phi''}} = C_\phi \frac{\epsilon}{\widetilde{k}} + \frac{C_{\epsilon_\phi}}{C_D} \frac{1}{\widetilde{\phi''\phi''}} \left\langle \mathcal{S}_\phi^{(I)} \right\rangle + \frac{4}{C_D} \langle \mathcal{S}_m^{(I)} \rangle, \tag{4.68}$$

with $C_\phi = \frac{C_V}{C_D}$. The analysis shows that when the Reynolds number increases, the contributions of the two way coupling source terms decrease and may be neglected in high Reynolds number flows. Mass transfer has the effect of increasing the mixing frequency; scalar mixing goes faster when there is mass transfer.

4.2.1 Pressure-scrambling term

It has already been shown by Pope [129] that a Langevin model for the rapid pressure scrambling term

$$\Pi_{ij}^{\phi} = -\left\langle \phi'' \frac{\partial p'}{\partial x_i} \right\rangle \tag{4.69}$$

is completely determined by the rapid pressure rate of strain model Π_{ij}:

$$\Pi_i^{(r)} = G_{ij} \widetilde{u_j'' \phi''}. \tag{4.70}$$

A consistent scalar-flux model will use the same expression for G_{ij} in the pressure-scrambling term as is used in the Reynolds stress model.

4.3 Gradient diffusion models

Gradient diffusion models are simple algebraic models for the Reynolds stresses and scalar fluxes. They are obtained by extreme simplification of the transport equation for the Reynolds stress or scalar flux [35, 55]. Despite their deficiencies, it is still interesting to study their extension to multiphase flows because the simplicity of the equations allows for an easy analysis of the behaviour of the Reynolds stresses. Moreover, the gradient diffusion hypothesis is often used to close specific terms in a complex differential equation like the Reynolds stress equation (3.19). The triple correlation is closed by writing down a differential equation for it and then simplifying the equation until it reduces to an algebraic expression. A similar approach can be used to obtain an algebraic closure for the scalar flux.

4.3.1 Triple velocity correlations

The triple velocity correlations $\widetilde{u_i'' u_j'' u_k''}$ appearing in the transport equation for the Reynolds stresses are often modeled using an analysis of the transport equation for the triple velocity correlations. A transport equation for the triple order correlations can be derived by multiplying the transport equation for the fluctuating velocity u_i'' by $u_j'' u_k'' \mathcal{X}$. This leads to an equation E_{ijk}. $\langle E_{ijk} + E_{jki} + E_{kij} \rangle$ then gives:

$$
\begin{aligned}
&\frac{\partial}{\partial t}\left(\overline{\rho}\widetilde{u_i'' u_j'' u_k''}\right) + \frac{\partial}{\partial x_l}\left(\overline{\rho}\widetilde{u_i'' u_j'' u_k''}\widetilde{U}_l\right) \\
&\quad + \overline{\rho}\widetilde{u_i'' u_j'' u_l''}\frac{\partial \widetilde{U}_k}{\partial x_l} + \overline{\rho}\widetilde{u_i'' u_k'' u_l''}\frac{\partial \widetilde{U}_j}{\partial x_l} + \overline{\rho}\widetilde{u_j'' u_k'' u_l''}\frac{\partial \widetilde{U}_i}{\partial x_l} \\
&\quad = -\left[\overline{u_i'' u_j''\frac{\partial p}{\partial x_k}} + \overline{u_j'' u_k''\frac{\partial p}{\partial x_i}} + \overline{u_i'' u_k''\frac{\partial p}{\partial x_j}}\right] \\
&\quad + \left[\overline{u_i'' u_j''\frac{\partial \tau_{kl}}{\partial x_l}} + \overline{u_j'' u_k''\frac{\partial \tau_{il}}{\partial x_l}} + \overline{u_k'' u_i''\frac{\partial \tau_{jl}}{\partial x_l}}\right] \\
&\quad - \frac{\partial}{\partial x_l}\left[\overline{\rho}\widetilde{u_i'' u_j'' u_k''}u_l''\right] \\
&\quad + \left\langle \mathcal{S}^{(I)}_{u_i u_j u_k} \right\rangle \\
&\quad + 3\langle u''_{I,i} u''_{I,j} u''_{I,k} \mathcal{S}^{(I)}_m \rangle - \langle u''_{I,i} u''_{I,j} u''_{I,k} \rangle \langle \mathcal{S}^{(I)}_m \rangle,
\end{aligned}
\tag{4.71}
$$

with

$$
\left\langle \mathcal{S}^{(I)}_{u_i u_j u_k} \right\rangle = \left\langle u''_{I,i} u''_{I,j} \mathcal{S}^{(I)}_{U_k} \right\rangle + \left\langle u''_{I,i} u''_{I,k} \mathcal{S}^{(I)}_{U_j} \right\rangle + \left\langle u''_{I,j} u''_{I,k} \mathcal{S}^{(I)}_{U_i} \right\rangle. \tag{4.72}
$$

The last term in eq. (4.71) arises from the gradient of the fourth order correlation and the application of the continuity equation (which contains a mass source term). The transport equation for the triple correlations derived from the pdf transport equation is obtained by multiplying eq. (4.38) by $(V_i - \langle U_i \rangle)(V_j - \langle U_j \rangle)(V_k - \langle U_k \rangle)$ and integrating. The result is

$$
\begin{aligned}
&\frac{\partial}{\partial t}\left(\overline{\rho}\widetilde{u_i'' u_j'' u_k''}\right) + \frac{\partial}{\partial x_l}\left(\overline{\rho}\widetilde{u_i'' u_j'' u_k''}\widetilde{U}_l\right) \\
&= \\
&- \frac{\partial}{\partial x_l}\left[\overline{\rho}\widetilde{u_i'' u_j'' u_k''}u_l'' - \overline{p' u_i''}\,\overline{u_j''}\delta_{kl} - \overline{p' u_i''}\,\overline{u_k''}\delta_{jl} - \overline{p' u_j''}\,\overline{u_k''}\delta_{il}\right] \\
&+ (G_{lm} - \frac{\partial \widetilde{U}_l}{\partial x_m})(\delta_{mi}\langle u_l'' u_j'' u_k'' \rangle + \delta_{mj}\langle u_l'' u_i'' u_k'' \rangle + \delta_{mk}\langle u_l'' u_i'' u_j'' \rangle) \\
&+ \left\langle \mathcal{S}^{(I)}_{u_i u_j u_k} \right\rangle \\
&+ 3\langle u''_{I,i} u''_{I,j} u''_{I,k} \mathcal{S}^{(I)}_m \rangle - \langle u''_{I,i} u''_{I,j} u''_{I,k} \rangle \langle \mathcal{S}^{(I)}_m \rangle.
\end{aligned}
\tag{4.73}
$$

For the fourth order correlation we use the Millionshchikov hypothesis [112] which relates fourth order correlations to second order correlations:

$$\left\langle u_i'' u_j'' u_k'' u_l'' \right\rangle = \left\langle u_i'' u_j'' \right\rangle \left\langle u_k'' u_l'' \right\rangle + \left\langle u_i'' u_k'' \right\rangle \left\langle u_j'' u_l'' \right\rangle + \left\langle u_i'' u_l'' \right\rangle \left\langle u_j'' u_k'' \right\rangle. \tag{4.74}$$

In order to obtain an algebraic relationship, we neglect the first two terms on the right hand side of (4.71) and substitute the Millionshchikov approximation. For the simplest stochastic model (SLM), $G_{ij} = \alpha_1 \frac{\epsilon}{\widetilde{k}} \delta_{ij}$. In general, this term is handled by introducing the tensor K_{ij}, defined to satisfy:

$$G_{ij} - \frac{\partial \widetilde{U}_i}{\partial x_j} = \alpha_1 \frac{\epsilon}{\widetilde{k}} \delta_{ij} + K_{ij}. \tag{4.75}$$

The transport equation for the triple order correlation can now be reduced to an algebraic expression:

$$\begin{aligned}
\widetilde{u_i'' u_j'' u_k''} = & - C_s \frac{\widetilde{k}}{\epsilon} \left(\widetilde{u_i'' u_l''} \frac{\partial \widetilde{u_j'' u_k''}}{\partial x_l} + \widetilde{u_j'' u_l''} \frac{\partial \widetilde{u_i'' u_k''}}{\partial x_l} + \widetilde{u_k'' u_l''} \frac{\partial \widetilde{u_i'' u_j''}}{\partial x_l} \right) \\
& - C_s \frac{\widetilde{k}}{\epsilon} \left(K_{kl} \widetilde{u_i'' u_j'' u_l''} + K_{jl} \widetilde{u_i'' u_k'' u_l''} + K_{il} \widetilde{u_j'' u_k'' u_l''} \right) \\
& + C_s \frac{\widetilde{k}}{\epsilon} \left\langle \mathcal{S}^{(I)}_{u_i u_j u_k} \right\rangle \\
& + C_s \frac{\widetilde{k}}{\epsilon} \left(3 \left\langle u_{I,i}'' u_{I,j}'' u_{I,k}'' \mathcal{S}_m^{(I)} \right\rangle - \left\langle u_{I,i}'' u_{I,j}'' u_{I,k}'' \right\rangle \left\langle \mathcal{S}_m^{(I)} \right\rangle \right),
\end{aligned} \tag{4.76}$$

with $C_s = \frac{1}{3\alpha_1}$ If we assume zero mean velocity gradients and G_{ij} given by the SLM, $K_{ij} = 0$ and equation (4.76) reduces to the two phase version of the model of Launder, Reece and Rodi [90].

$$\begin{aligned}
\widetilde{u_i'' u_j'' u_k''} = & - C_s \frac{\widetilde{k}}{\epsilon} \left(\widetilde{u_i'' u_l''} \frac{\partial \widetilde{u_j'' u_k''}}{\partial x_l} + \widetilde{u_j'' u_l''} \frac{\partial \widetilde{u_i'' u_k''}}{\partial x_l} + \widetilde{u_k'' u_l''} \frac{\partial \widetilde{u_i'' u_j''}}{\partial x_l} \right) \\
& + C_s \frac{\widetilde{k}}{\epsilon} \left\langle \mathcal{S}^{(I)}_{u_i u_j u_k} \right\rangle \\
& + C_s \frac{\widetilde{k}}{\epsilon} \left(3 \left\langle u_{I,i}'' u_{I,j}'' u_{I,k}'' \mathcal{S}_m^{(I)} \right\rangle - \left\langle u_{I,i}'' u_{I,j}'' u_{I,k}'' \right\rangle \left\langle \mathcal{S}_m^{(I)} \right\rangle \right),
\end{aligned} \tag{4.77}$$

with a model constant $C_s = 0.11$. The two phase version of the Daly-Harlow model [35] can be obtained from this already simplified expression by neglecting all gradients except the gradient of $\widetilde{u_i'' u_j''}$:

$$\begin{aligned}
\widetilde{u_i'' u_j'' u_k''} = & - C_s \frac{\widetilde{k}}{\epsilon} \widetilde{u_k'' u_l''} \frac{\partial \widetilde{u_i'' u_j''}}{\partial x_l} \\
& + C_s \frac{\widetilde{k}}{\epsilon} \left\langle \mathcal{S}^{(I)}_{u_i u_j u_k} \right\rangle \\
& + C_s \frac{\widetilde{k}}{\epsilon} \left(3 \left\langle u_{I,i}'' u_{I,j}'' u_{I,k}'' \mathcal{S}_m^{(I)} \right\rangle - \left\langle u_{I,i}'' u_{I,j}'' u_{I,k}'' \right\rangle \left\langle \mathcal{S}_m^{(I)} \right\rangle \right).
\end{aligned} \tag{4.78}$$

The best value of the model constant in single phase flow was found to be $C_s = 0.22$. The gradient of the triple velocity correlation appearing in the transport equation for the Reynolds stresses is often modeled using the Daly-Harlow approximation. In dispersed multiphase flows, this approximation needs to be extended to the multiphase Daly-Harlow approximation (4.78). More detailed numerical studies will need to be done to establish the importance of the extra terms.

The same hypothesis can be used to express the fourth order correlations appearing in the transport equation for the triple correlation $u_i'' u_j'' \phi''$, leading to the scalar multiphase version of the LRR model for the triple correlation:

$$\begin{aligned}\widetilde{u_i'' u_j'' \phi''} = & -C_s \frac{\widetilde{k}}{\epsilon} \left(\widetilde{u_i'' u_l''} \frac{\partial \widetilde{u_j'' \phi''}}{\partial x_l} + \widetilde{u_j'' u_l''} \frac{\partial \widetilde{u_i'' \phi''}}{\partial x_l} + \widetilde{\phi'' u_l''} \frac{\partial \widetilde{u_i'' u_j''}}{\partial x_l} \right) \\ & + C_s \frac{\widetilde{k}}{\epsilon} \left\langle \mathcal{S}^{(I)}_{u_i u_j \phi} \right\rangle \\ & + C_s \frac{\widetilde{k}}{\epsilon} \left(3 \left\langle u_{I,i}'' u_{I,j}'' \phi_I'' \mathcal{S}_m^{(I)} \right\rangle - \left\langle u_{I,i}'' u_{I,j}'' \phi_I'' \right\rangle \left\langle \mathcal{S}_m^{(I)} \right\rangle \right). \end{aligned} \tag{4.79}$$

4.3.2 Gradient hypothesis for diffusion flux

The modeled transport equation for the scalar flux was derived previously and is the starting point for the derivation of an algebraic model:

$$\begin{aligned}\frac{\partial}{\partial t} \left(\overline{\rho} \widetilde{u_i'' \phi''} \right) \; + \; & \frac{\partial}{\partial x_j} \left(\overline{\rho} \widetilde{u_i'' \phi''} \widetilde{U}_j \right) \\ = \; & \frac{\partial}{\partial x_j} \left(\mathcal{T}_{ij}^{\phi} - \overline{\rho} \widetilde{u_i'' u_j'' \phi''} - \widetilde{p \phi''} \delta_{ij} + \mathcal{P}_i^{\phi} + \mathcal{R}_i^{\phi} - \epsilon_i^{\phi} \right) + \overline{\rho} \widetilde{u_i'' S} + \left\langle \mathcal{S}^{(I)}_{u_i \phi} \right\rangle \\ + \; & 2 \left\langle u_{I,i}'' \phi_I'' \mathcal{S}_m^{(I)} \right\rangle - \left\langle u_{I,i}'' \phi_I'' \right\rangle \left\langle \mathcal{S}_m^{(I)} \right\rangle. \end{aligned} \tag{4.80}$$

An expression for the anisotropic rate of strain tensor $\mathcal{R}_i^{\phi}$ derived starting from a Lagrangian point of view has the form

$$\mathcal{R}_i^{\phi} = G_{ij}^{\phi} \widetilde{u_j'' \phi''}, \tag{4.81}$$

with the second order tensor G_{ij}^{ϕ} a function of the Reynolds stresses, the strain rate and the turbulence dissipation:

$$G_{ij}^{\phi} = G_{ij}^{\phi} (\widetilde{\mathbf{u}'' \mathbf{u}''}, \frac{\partial \widetilde{\mathbf{U}}}{\partial \mathbf{x}}, \epsilon). \tag{4.82}$$

At high Reynolds numbers, the molecular transport term $\mathcal{T}_{ij}^{\phi}$ will be small and for local isotropy, the scalar dissipation rate ϵ_i^{ϕ} will be zero. The scalar-flux transport

equation (3.69) thus reduces to

$$
\begin{aligned}
-K_{ij}\widetilde{u_j''\phi''} &= -\overline{\rho}\widetilde{u_i''u_j''}\frac{\partial\widetilde{\phi}}{\partial x_j} \\
&\quad + \left\langle \mathcal{S}_{u_i\phi}^{(I)} \right\rangle + 2\big\langle u_{I,i}''\phi_I''\mathcal{S}_m^{(I)}\big\rangle - \big\langle u_{I,i}''\phi_I''\big\rangle\big\langle \mathcal{S}_m^{(I)}\big\rangle. \qquad (4.83)
\end{aligned}
$$

In equation (4.83) the triple correlations were neglected as well as the transport terms and the reaction source term, and the scalar fluxes are combined using

$$
K_{ij} \equiv G_{ij}^{\phi} - \frac{\partial\widetilde{U}_i}{\partial x_j}, \qquad (4.84)
$$

The tensor K_{ij} is usually assumed to be isotropic and is modeled as:

$$
K_{ij} \approx -\mathrm{Sc}_T\frac{\epsilon}{\widetilde{k}}\delta_{ij}. \qquad (4.85)
$$

we now obtain the final form of the gradient diffusion approximation, extended for multiphase flows with mass transfer:

$$
\begin{aligned}
\widetilde{u_j''\phi''} &= \frac{1}{\mathrm{Sc}_T}\frac{\widetilde{k}}{\epsilon}\Big(-\overline{\rho}\widetilde{u_i''u_j''}\frac{\partial\widetilde{\phi}}{\partial x_j} \\
&\quad + \left\langle \mathcal{S}_{u_i\phi}^{(I)} \right\rangle + 2\big\langle u_{I,i}''\phi_I''\mathcal{S}_m^{(I)}\big\rangle - \big\langle u_{I,i}''\phi_I''\big\rangle\big\langle \mathcal{S}_m^{(I)}\big\rangle\Big). \qquad (4.86)
\end{aligned}
$$

This algebraic expression for the scalar flux reveals a number of features:

- A positive contribution of the source term $\mathcal{S}_{u_i\phi}$ will lead to an increase of the value for the scalar flux.
- A positive contribution due to the source term for mass transfer will lead to an increase of the value for the scalar flux.
- When two way coupling and mass transfer is neglected, the relationship (4.86) reduces to the gradient diffusion model described in e.g. [55, 130].

Note that this gradient diffusion model allows for a misalignment between the scalar flux and the mean scalar gradient which, although not very accurate, is an improvement over the older (single phase) gradient diffusion models of the form [35]

$$
\widetilde{u_i''\phi''} = -\frac{\nu_T}{\mathrm{Sc}_T}\frac{\partial\widetilde{\phi}}{\partial x_i}, \qquad (4.87)
$$

with ν_T the turbulent viscosity and Sc_T the turbulent Schmidt number, $\mathrm{Sc}_T \approx 0.7$ which relates Γ_T to ν_T:

$$
\Gamma_T \equiv \frac{\nu_T}{\mathrm{Sc}_T}. \qquad (4.88)
$$

Although these relationships are not actually used in the numerical simulations presented in this thesis (the scalar flux is obtained from the velocity-composition pdf), they do give a first approximation for the behaviour of the scalar flux and offer some insights that would be obtained with far more effort from the complete transport equations.

4.4 Conclusions

The relationship between Lagrangian turbulence models and second moment closures has been extended for dispersed multiphase flows with mass transfer. It has been shown that extra contributions to the model for the pressure rate of strain, due to fluid-particle interaction and to vaporisation, appear in the transport equation for the Reynolds stresses. A corresponding Lagrangian turbulence model (Langevin model) exists and a consistent model approach has been proposed. It has been shown that the presence of particles tends to accelerate the process where the fluid phase Reynolds stresses tend to 'return to isotropy'. A similar conclusion can be reached when solving the transport equation for the scalar flux. The transport equation for the scalar dissipation rate, which is the basis for Lagrangian mixing models, also contains a two way coupling source term that takes into account the effect of the presence of the particles and the effect of mass transfer on the mixing behaviour. It is shown that mixing in the continuum phase is affected by the diffusion of the scalar at the interface of the dispersed phase and by the rate of mass transfer. The conclusions are that mixing will go faster when there is mass transfer from the dispersed phase to the continuum phase (evaporation) and when the scalar gradient at the interface is positive. For temperature, this means cold solid or liquid particles in a hot environment cause faster mixing. For mixture fraction, this means that the presence of a dispersed phase is always causing faster mixing. Finally, the effects of the dispersed phase on the closure of the triple correlations is investigated and a multiphase gradient diffusion hypothesis (Daly Harlow approximation) has been derived. In future work, it will be interesting to investigate the two way coupling terms further in Direct Numerical Simulations of vaporising droplets in turbulence.

CHAPTER 5

Modelling of the dispersed phase

In this chapter the Lagrangian treatment of the dispersed phase is presented. The transport equation for the droplet mass density function $\mathcal{F}_{\mathrm{p}}$ (the MDF), which is a density weighted Droplet Density Function (f_{p}) will be discussed [85, 117, 177, 178, 189]. The transport equation for the MDF is solved using a particle method, also known as a Monte Carlo method. The Lagrangian particle equation of motion in a non-uniform flow is given by the Maxey-Riley equation [99]. Following the analysis of Hjelmfelt and Mockros [68] and Hinze [67], this equation can be reduced to a simple ordinary differential equation in the case of small heavy particles in a gaseous fluid. The equation of motion for a single particle contains the instantaneous, undisturbed velocity of the fluid at the location of the particle. This velocity is unknown in RANS and PDF approaches and needs to be modeled. The model for the velocity is a dispersion model, akin to diffusion models. To correctly model the dispersion behaviour, the continuity effect and the crossing trajectories effect need to be taken into account [33, 109, 171, 185]. The instantaneous velocity of the fluid at the location of the particle is modeled using a stochastic equation of motion for the velocity 'seen' by the particle. The coupled system of differential equations for particle location, particle velocity and particle velocity seen is a stochastic system and a weak first order stochastic integration scheme is presented to obtain the numerical solution of these properties [81, 110, 122]. The numerical scheme is extended to the general case where the mean drift velocity $\boldsymbol{U}_r$ between a discrete particle and the fluid phase is not aligned with the first coordinate axis of the reference system.

5.1 Introduction

5.2 Statistical description of the dispersed phase

In the previous chapters a multiphase description of turbulent flow was presented and the Eulerian Reynolds Averaged Navier Stokes (RANS) equations as well as the Lagrangian transport equation of the velocity-composition pdf were given. A Monte Carlo particle method to solve the transport equation for the pdf using Langevin equations was presented. In this chapter, the transport equation for the pdf of particle velocity, describing the evolution of a dispersed phase in a turbulent continuum fluid phase, is presented and the corresponding Langevin equations

are given. We will consider here a dispersed two phase flow with a fluid phase $\mathrm{k} = \mathrm{f}$ and a dispersed phase $\mathrm{k} = \mathrm{p}$.

In the statistical approach we consider a spray composed of N_p discrete (dispersed) liquid or solid particles. The particle can be described completely by the state vector. The state vector $\boldsymbol{\Phi}$ can contain any relevant property needed to describe the evolution of the dispersed phase. In turbulent spray flames, where the particles can heat up, vaporise, etc, the state vector will contain the particle position, the particle velocity, the particle diameter, the particle temperature and the velocity of the fluid phase sampled along the particle path: the velocity seen. We will come back to this property in section 5.5. The state vector in physical space then becomes $[\boldsymbol{X}, \boldsymbol{\Phi} = (\boldsymbol{X}_\mathrm{p}, \boldsymbol{U}_\mathrm{p}, d_\mathrm{p}, T_\mathrm{p}, \boldsymbol{U}_\mathrm{s}, \boldsymbol{\phi}_\mathrm{s})$. The corresponding phase space considered here is then given by $[\boldsymbol{x}, \hat{\boldsymbol{\Psi}}] = [\boldsymbol{x}, \boldsymbol{V}_\mathrm{p}, D_\mathrm{p}, \theta_\mathrm{p}, \boldsymbol{V}_\mathrm{s}, \boldsymbol{\psi}_\mathrm{s}]$, where θ_p corresponds to the possible values of droplet temperature T_p and $\boldsymbol{\psi}_\mathrm{s}$ corresponds to the possible values of composition seen $\boldsymbol{\phi}_\mathrm{s}$.

The statistical description of the flow is made in terms of the joint one-point MDF $\mathcal{F}_\mathrm{p}$ such that $\mathcal{F}_\mathrm{p}\Big(\boldsymbol{x}, \hat{\boldsymbol{\Psi}}; t\Big)\, \mathrm{d}\boldsymbol{X}\mathrm{d}\hat{\boldsymbol{\Psi}}$ is the probable mass of dispersed phase elements with position within the interval $[\boldsymbol{x}, \boldsymbol{x} + \mathrm{d}\boldsymbol{x}]$ and property $\boldsymbol{\Phi}_\mathrm{p}$ in the interval $\left[\hat{\boldsymbol{\Psi}}, \hat{\boldsymbol{\Psi}} + \mathrm{d}\hat{\boldsymbol{\Psi}}\right]$ at point $M(\boldsymbol{x}, t)$.

The ensemble of particles is enclosed in the finite volume $\mathcal{V}$. The dispersed phase is described in terms of the discrete joint mass density function of the state vector $\boldsymbol{\Phi}(t)$ (the droplet MDF):

$$\mathcal{F}_\mathrm{p}\Big(\boldsymbol{x}, \hat{\boldsymbol{\Psi}}; t\Big) = \left\langle \sum_{+ \text{ in } \mathcal{V}} m_\mathrm{p}^+(t)\, .\delta\big(\boldsymbol{X}_\mathrm{p}^+(t) - \boldsymbol{x}\big)\, .\delta\Big(\boldsymbol{\Phi}_\mathrm{p}^+(t) - \hat{\boldsymbol{\Psi}}\Big) \right\rangle. \tag{5.1}$$

$\boldsymbol{X}_\mathrm{p}^+$ is the droplet position vector, and $\boldsymbol{\Phi}_\mathrm{p}^+$ is the state vector containing the relevant properties describing the evolution of the droplet MDF. The superscript $'+'$ is used to denote discrete (dispersed phase) properties. Dispersed phase volume averages can be obtained using

$$Q_\mathrm{p}^+(t) = \frac{1}{\mathcal{V}_\mathrm{p}^+(t)} \int_{\boldsymbol{x} \in \Omega_\mathrm{p}^+(t)} Q_\mathrm{p}(\boldsymbol{x}, t)\, \mathcal{X}_\mathrm{p}(\boldsymbol{x}, t)\, .\mathrm{d}\boldsymbol{x}, \tag{5.2}$$

where $\Omega_\mathrm{p}^+(t)$ is the domain of volume $\mathcal{V}_\mathrm{p}$ occupied by droplets $+$ at time t.

The density of the dispersed phase is assumed to be constant, and the mass of a discrete spherical particle can then simply be obtained by

$$m_\mathrm{p}(D_\mathrm{p}) = \rho_\mathrm{p} \frac{\pi}{6} D_\mathrm{p}^3. \tag{5.3}$$

The effect of the composition seen by a discrete particle on the vaporisation rate of the particle has already been discussed in Chapter 2. It is possible to develop complex models for the composition seen, where molecular and turbulent mixing of

the vaporised liquid with the surrounding continuous phase is taken into account. As a model for the composition seen, we will however assume that a discrete particle sees the mean composition of the gas phase, $\phi_{\mathrm{s}} = \widetilde{\phi}_{\mathrm{f}}$. Closely related to this is the model for the temperature seen, which is taken to be the mean temperature of the gas phase, $T_{\mathrm{s}} = \widetilde{T}_{\mathrm{f}}$.

We define a conditional expectation $\langle \ | \ \rangle_{\mathrm{p}}$ such that:

$$\left\langle Q_{\mathrm{p}}^{+} \middle| \boldsymbol{x}, \hat{\boldsymbol{\Psi}}; t \right\rangle_{\mathrm{p}} \mathcal{F}_{\mathrm{p}}\left(\boldsymbol{x}, \hat{\boldsymbol{\Psi}}; t\right) = \left\langle \sum_{+ \text{ in } \mathbb{B}} Q_{\mathrm{p}}^{+}(t)\, m_{\mathrm{p}}^{+}(t)\, .\delta\big(\boldsymbol{X}_{\mathrm{p}}^{+}(t) - \boldsymbol{x}\big)\, .\delta\Big(\boldsymbol{\Phi}_{\mathrm{p}}^{+}(t) - \hat{\boldsymbol{\Psi}}\Big) \right\rangle$$

$$\text{if } \mathcal{F}_{\mathrm{p}}\left(\boldsymbol{x}, \hat{\boldsymbol{\Psi}}; t\right) > 0, \text{and equal zero otherwise.} \tag{5.4}$$

In the absence of collisions, coalescence and breakup, the droplet MDF transport equation reads [117]:

$$\begin{aligned}
\forall (\boldsymbol{x}, \boldsymbol{V}, \boldsymbol{\psi}, \hat{\boldsymbol{\varphi}}) \in [\boldsymbol{x}, \boldsymbol{V}, \boldsymbol{\psi}, \hat{\boldsymbol{\varphi}}]_{\mathbb{B}},& \\
\frac{\partial \mathcal{F}_{\mathrm{p}}}{\partial t} + V_{\mathrm{p},j} \frac{\partial \mathcal{F}_{\mathrm{p}}}{\partial x_j} =& - \frac{\partial}{\partial V_{\mathrm{p},i}} \left[\left\langle \frac{\mathrm{d}U_{\mathrm{p},i}^{+}}{\mathrm{d}t} \middle| \boldsymbol{x}, \hat{\boldsymbol{\Psi}}; t \right\rangle_{\mathrm{p}} \mathcal{F}_{\mathrm{p}} \right] \\
& - \frac{\partial}{\partial D_{\mathrm{p}}} \left[\left\langle \frac{\mathrm{d}d_{\mathrm{p}}^{+}}{\mathrm{d}t} \middle| \boldsymbol{x}, \hat{\boldsymbol{\Psi}}; t \right\rangle_{\mathrm{p}} \mathcal{F}_{\mathrm{p}} \right] - \frac{\partial}{\partial \theta_{\mathrm{p}}} \left[\left\langle \frac{\mathrm{d}T_{\mathrm{p}}^{+}}{\mathrm{d}t} \middle| \boldsymbol{x}, \hat{\boldsymbol{\Psi}}; t \right\rangle_{\mathrm{p}} \mathcal{F}_{\mathrm{p}} \right] \\
& - \frac{\partial}{\partial V_{\mathrm{s},i}} \left[\left\langle \frac{\mathrm{d}U_{\mathrm{s},i}^{+}}{\mathrm{d}t} \middle| \boldsymbol{x}, \hat{\boldsymbol{\Psi}}; t \right\rangle_{\mathrm{p}} \mathcal{F}_{\mathrm{p}} \right] - \frac{\partial}{\partial \psi_{\mathrm{s}}} \left[\left\langle \Theta_{\mathrm{s}}^{+} \middle| \boldsymbol{x}, \boldsymbol{\Psi}; t \right\rangle_{\mathrm{p}} \mathcal{F}_{\mathrm{p}} \right] \\
& + \left\langle \frac{1}{m_{\mathrm{p}}^{+}} \frac{\mathrm{d}m_{\mathrm{p}}^{+}}{\mathrm{d}t} \middle| \boldsymbol{x}, \hat{\boldsymbol{\Psi}}; t \right\rangle_{\mathrm{p}} \mathcal{F}_{\mathrm{p}},
\end{aligned} \tag{5.5}$$

The last term in (5.5) corresponds to a rescaling of $\mathcal{F}_{\mathrm{p}}$ if mass of discrete elements changes in time.

Droplet conditional averages Naud [117] showed that when the MDF $\mathcal{F}_{\mathrm{p}} = m_{\mathrm{p}} f_{\mathrm{p}}$ is considered instead of the PDF f_{p}, it is possible to directly relate the statistical moments of $\mathcal{F}_{\mathrm{p}}$ to Eulerian statistics. When the edge effect is neglected [159] and when assuming statistical homogeneity in a small domain Ω of volume $\mathcal{V}_{\Omega}$, we can write:

$$\begin{aligned}
&\forall \boldsymbol{x} \in \Omega, \\
&\langle \rho_2 Q_2 \mathcal{X}_2 \rangle = \frac{1}{\mathcal{V}_{\Omega}} \left\langle \sum_{+} m_{\mathrm{p},\Omega}^{+}(t)\, Q_{\mathrm{p},\Omega}^{+}(t) \right\rangle.
\end{aligned} \tag{5.6}$$

Note that in two phase flows the droplet MDF $\mathcal{F}_{\mathrm{p}}$ and the fluid phase MDF $\mathcal{F}_{\mathrm{f}}$ describing each of the two phases should not be considered separately. Instead,

the coupled system of MDFs should be considered as this will lead to the proper treatment of the continuity condition, imposed through the normalisation condition:

$$\sum_{\mathrm{k}} \int_{[\boldsymbol{V},\boldsymbol{\psi}]} \left[\rho_{\mathrm{k}}(\boldsymbol{\psi})\right]^{-1} \mathcal{F}_{\mathrm{k}}(\boldsymbol{V},\boldsymbol{\psi};\boldsymbol{x},t)\,.\mathrm{d}\boldsymbol{V}.\mathrm{d}\boldsymbol{\psi} = \sum_{\mathrm{k}} \alpha_{\mathrm{k}}(\boldsymbol{x},t) = 1. \tag{5.7}$$

5.3 Lagrangian modelling of the droplet MDF

In order to model and solve Eq. (5.5), a Monte Carlo method is used. A set of uniformly distributed computational droplets (each having a position, diameter, temperature, velocity and seen velocity and a composition seen) evolves according to stochastic differential equations such that the ensemble provides a numerical approximation of the modelled droplet MDF $\mathcal{F}_{\mathrm{p}}^{P}$.

In the case of a turbulent spray flame which will be considered in chapter 7, each computational droplet '$*$' has a set of properties $\{n_{\mathrm{p}}^{*}, \boldsymbol{X}_{\mathrm{p}}^{*}, D_{\mathrm{p}}^{*}, T_{\mathrm{p}}^{*}, \boldsymbol{U}_{\mathrm{p}}^{*}, \boldsymbol{U}_{\mathrm{s}}^{*}, \Theta_{\mathrm{s}}^{*}\}$, where n_{p}^{*} is a weight factor associated to the particle[1]. The superscript $*$ denotes that the quantity is a stochastic particle property. The modelled droplet MDF is defined as

$$\begin{aligned}&\mathcal{F}_{\mathrm{p}}^{P}(\boldsymbol{x}, D_{\mathrm{p}}, T_{\mathrm{p}}, \boldsymbol{V}_{\mathrm{p}}, \boldsymbol{V}_{\mathrm{s}}, \Theta_{\mathrm{s}}; t) \\ &\quad = \left\langle \sum_{*} n_{\mathrm{p}}^{*} m_{\mathrm{p}}^{*} .\delta\left(\boldsymbol{X}_{\mathrm{p}}^{*}(t) - \boldsymbol{x}\right) .\delta\left(\boldsymbol{\Phi}_{\mathrm{p}}^{*}(t) - \hat{\boldsymbol{\Psi}}_{\mathrm{p}}^{*}\right) \right\rangle,\end{aligned} \tag{5.8}$$

Unconditional droplet mean properties in a small domain Ω of volume $\mathcal{V}_{\Omega}$, are obtained as:

$$\rho_{\mathrm{p}}\langle Q_{\mathrm{p}}\rangle = \frac{1}{\mathcal{V}_{\Omega}} \left\{ \sum_{* \text{ in } \Omega} m_{\mathrm{p}}^{*} Q_{\mathrm{p}}^{*}(t) \right\}_{TA}, \tag{5.9}$$

and conditional averages are obtained as:

$$\langle Q_{\mathrm{p}}\rangle_{|\mathrm{p}} = \left\{ \sum_{* \text{ in } \Omega} m_{\mathrm{p}}^{*} Q_{\mathrm{p}}^{*}(t) \right\}_{TA} \Bigg/ \left\{ \sum_{* \text{ in } \Omega} m_{\mathrm{p}}^{*} \right\}_{TA}, \tag{5.10}$$

where $\{\ \}_{TA}$ is an averaging operator, introduced to smooth statistical fluctuations. In the case of statistically stationary flows, the conditional averages of time independent quantities Q_{p}^{*} are time independent and $\{..\}_{TA}$ can be taken as a time averaging [118].

[1] A computational droplet is not in one to one correspondence to a "real" droplet: each computational droplet is a statistical sample of the dispersed phase. The weight factors accommodate the difference between number of samples and the number of real droplets.

Model equations are now needed for each of the properties contained in the state vector $\boldsymbol{\Phi}^*$. The equations describing the droplet diameter (or, equivalently, mass) evolution $\frac{\mathrm{d}d_\mathrm{p}}{\mathrm{d}t}$ and droplet temperature evolution $\frac{\mathrm{d}T_\mathrm{p}}{\mathrm{d}t}$ was already discussed in detail in the previous chapter. In the following section, the model equation for the particle location $X_{\mathrm{p},i}$ and particle velocity $U_{\mathrm{p},i}$ will be discussed, followed by a discussion on the model equation for the velocity seen $U_{\mathrm{s},i}$ in section 5.5.

5.4 Equation of motion of a spherical particle in a turbulent fluid

The equation of motion of a spherical particle in a turbulent flow was already considered by Tchen [163]. Tchen's proposal was however based more on intuition than rigour. A more rigorous derivation of the motion of a small rigid sphere in a nonuniform flow was presented by Maxey and Riley [99] and by Gatignol [57]. They consider the exact solution of an unsteady Stokes flow disturbed by the presence of a particle. In this *creeping flow*, the Reynolds number is assumed to be small, $\mathrm{Re}_\mathrm{p} \to 0$. The final form of their equation of motion is:

$$dX_{\mathrm{p},i} = U_{\mathrm{p},i}, \tag{5.11}$$

and

$$\begin{aligned} m_\mathrm{p}\frac{dU_{\mathrm{p},i}}{dt} \;=\; & \underbrace{(m_\mathrm{p}-m_\mathrm{f})\,g_i}_{\text{gravity force}} + \underbrace{m_\mathrm{f}\frac{DU_{\mathrm{f},i}}{Dt}\Big|_{x_\mathrm{p}(t)}}_{\text{pressure gradient}} - \underbrace{6\mu_\mathrm{f}\pi d_\mathrm{p}\big(U_{\mathrm{p},i}(t)-U_{\mathrm{f},i}(x_\mathrm{p}(t),t)}_{\text{drag force}} - \underbrace{\frac{1}{6}d_\mathrm{p}^2\nabla^2 U_{\mathrm{f},i}\Big|_{x_\mathrm{p}(t)}}_{\text{Faxen force}}\big) \\ & - \underbrace{\frac{1}{2}m_\mathrm{f}\frac{d}{dt}\big(U_{\mathrm{p},i}(t)-U_{\mathrm{f},i}(x_\mathrm{p}(t),t)}_{\text{added mass}} - \underbrace{\frac{1}{10}d_\mathrm{p}^2\nabla^2 U_{\mathrm{f},i}\Big|_{x_\mathrm{p}(t)}}_{\text{Faxen force}}\big) \\ & - \underbrace{6\mu_\mathrm{f}\pi d_\mathrm{p}^2\int_0^t \frac{\frac{d}{d\tau}\left(U_{\mathrm{p},i}(\tau)-U_{\mathrm{f},i}(x_\mathrm{p}(\tau),\tau)-\frac{1}{6}d_\mathrm{p}^2\nabla^2 U_{\mathrm{f},i}\big|_{x_\mathrm{p}(\tau)}\right)}{(\pi\nu_\mathrm{f}(t-\tau))^{\frac{1}{2}}}d\tau}_{\text{history term}} + \underbrace{F_i}_{\text{other forces}} . \end{aligned} \tag{5.12}$$

In this equation, m_f is the mass of the fluid displaced by the particle and the notation $U_\mathrm{f}|_{x_\mathrm{p}(t)}$ has the meaning of the undisturbed instantaneous fluid velocity at the location of the particle. On the right-hand side of (5.13), the following terms can be distinguished:

- Body force: A buoyancy effect due to the presence of gravity.
- Pressure force: A force due to the presence of a pressure gradient.
- Drag force: The main contribution to the motion of a heavy particle is due to the drag force.

- Added mass: Added or 'virtual' mass due to the displacement effect. This term becomes important when the particle to fluid density ratio is very small, e.g. when the 'particle' is a gas bubble in a liquid fluid.
- Faxen force: A force due to non uniform flow. This term is negligible when the particle diameter is small. Two different contributions to the Faxen force can be distinguished, a Faxen contribution to the drag force an a contribution to the added mass.
- History term: The history term, also known as the Basset force represents the effect of initial and past conditions. Vojir and Michaelides [170] found that this term can be neglected when the particle to fluid density ratio $\frac{\rho_\mathrm{p}}{\rho_\mathrm{f}} > 500$.
- Other forces: Forces that do not follow from the analysis of Maxey and Riley and were not taken into account, like the Saffman force due to shear lift, Magnus effect due to particle rotation, magnetic force, etc.

This equation has also been discussed in a lot more detail in the work of Michaelides [106], where interesting analogies between the evolution of particle velocity and particle temperature are presented. Hjelmfelt *et al*. [68] analysed the equation originally proposed by Tchen [163] (no external forces, no gravity force) and considered the range of validity of the equation of motion under different approximations. They found that for high particle/fluid density ratios $\frac{\rho_\mathrm{p}}{\rho_\mathrm{f}} \gg 1$ the particle equation of motion is governed mainly by the drag term. In our approach, we will also keep the gravity force and the pressure gradient force and the final form of the equation of motion is

$$m_\mathrm{p}\frac{dU_{\mathrm{p},i}}{dt} = m_\mathrm{p}g_i - \frac{m_\mathrm{p}}{\rho_\mathrm{p}}\frac{\partial \overline{p}}{\partial x_i} + \underbrace{6\mu_\mathrm{f}\pi d_\mathrm{p}(U_{\mathrm{s},i}(t) - U_{\mathrm{p},i})}_{\boldsymbol{F}_\mathrm{drag}}, \tag{5.13}$$

where the instantaneous (undisturbed) fluid velocity at the location of the particle has been replaced by the model velocity seen $U_{\mathrm{s},i}$. Note that with 'undisturbed' it is meant undisturbed by the considered particle, but disturbed by all other particles in the flow; hence the appearance of $\overline{p} = \langle \alpha_\mathrm{f} p \rangle$ instead of $\langle p \rangle$ in equation (5.13), with α_f the volume fraction of the continuous phase.

5.4.1 Drag term

The drag force is the most dominant force acting on the particle. An exact expression can be derived for the drag force under the assumption of small Reynolds numbers, but corrections are necessary when the particle equation of motion is used in flows where $\mathrm{Re}_\mathrm{p} > 1$. The drag force can be rewritten as

$$\boldsymbol{F}_\mathrm{drag} = m_\mathrm{p}\frac{\boldsymbol{U}_\mathrm{s} - \boldsymbol{U}_\mathrm{p}}{\tau_\mathrm{p}}, \tag{5.14}$$

where $\boldsymbol{U}_\mathrm{s}$ is the velocity seen by the particle (a model for the velocity of the undisturbed instantaneous fluid flow at the position of the particle centre) and τ_p is the particle relaxation time (i.e. the timescale at which the particle velocity relaxes to the surrounding fluid velocity).

The particle Reynolds number Re_p characterises the flow around the particle:

$$\mathrm{Re}_\mathrm{p} = \frac{\rho_\mathrm{f} \left|\boldsymbol{U}_\mathrm{p} - \boldsymbol{U}_\mathrm{s}\right| d_\mathrm{p}}{\mu_\mathrm{f}}, \tag{5.15}$$

In the Stokes regime, the particle relaxation time is given by

$$\tau_\mathrm{p}^\mathrm{St} = \frac{\rho_\mathrm{p} d_\mathrm{p}^2}{18\mu_\mathrm{f}}. \tag{5.16}$$

For higher Re_p the assumption of creeping flow is not valid and the drag is not linear anymore. The particle relaxation time is then expressed as

$$\tau_\mathrm{p} = \frac{\rho_\mathrm{p}}{3\rho_\mathrm{f}} \frac{4 d_\mathrm{p}}{C_D \left|\boldsymbol{U}_\mathrm{s} - \boldsymbol{U}_\mathrm{p}\right|}, \tag{5.17}$$

where the drag coefficient C_D is given by semi-empirical correlations. A frequently used one is the Schiller-Naumann correlation for solid particles [28]:

$$C_D = \begin{cases} \dfrac{24}{\mathrm{Re}_\mathrm{p}} \left(1 + 0.15 \mathrm{Re}_\mathrm{p}^{0.687}\right) & \text{if } \mathrm{Re}_\mathrm{p} \leq 800, \\ 0.44 & \text{if } \mathrm{Re}_\mathrm{p} > 800. \end{cases} \tag{5.18}$$

Note that liquid particles will rarely approach the limit value for high Reynolds numbers due to droplet breakup, which will automatically reduce the particle diameter based Reynolds number.

A convenient way of dealing with high Reynolds number modifications is to introduce the correction factor f_1. When we introduce the notation

$$\frac{1}{\tau_\mathrm{p}} = \frac{f_1}{\tau_\mathrm{p}^\mathrm{St}}, \tag{5.19}$$

the Schiller-Naumann correlation reads:

$$f_1 = \begin{cases} 1 + 0.15 \mathrm{Re}_\mathrm{p}^{0.687} & \text{if } \mathrm{Re}_\mathrm{p} \leq 800, \\ 0.44 \dfrac{\mathrm{Re}_\mathrm{p}}{24} & \text{if } \mathrm{Re}_\mathrm{p} > 800. \end{cases} \tag{5.20}$$

Drag modification due to internal circulation Besides the high Reynolds number modification other effects may be of importance. For liquid particles where the viscosity ratio $\kappa = \frac{\mu_\mathrm{p}}{\mu_\mathrm{f}}$ is small, say $\kappa < 10$, internal circulation can reduce the drag coefficient [28, 52]. This effect will be neglected in our case because $\kappa > 10$ (for methanol droplets, $\kappa \approx 25$).

Drag modification due to vaporisation For vaporising particles, the drag coefficient is modified by the Spalding mass transfer number B_M or Spalding heat transfer number B_T, defined earlier in chapter 2. The simplest modification is due to Eisenklam [16, 47] and reads:

$$\frac{C_{D_{\text{evap}}}}{C_D} = \frac{1}{1+B_T}, \tag{5.21}$$

with C_D the drag coefficient corresponding to a nonvaporising particle, i.e. equation (5.18). Expression (5.21) is similar to the drag correction proposed by Chiang *et al*. [14, 150], who proposes

$$C_{D_{\text{evap}}}(1+B_H)^{0.32} = \frac{24}{\text{Re}_\text{p}}(1+0.2\text{Re}_\text{p}^{0.63}), \tag{5.22}$$

with

$$B_H = B_T(1-\frac{Q_l}{Q_\text{f}}). \tag{5.23}$$

In equation (5.23), Q_l is the energy spent for droplet heating and Q_f is the total heat flux obtained from the gas phase. The largest correction is obtained when the received heat goes to evaporation.

Additionally, Chiang *et al*. also suggest to correct the Nusselt and Sherwood number for vaporising droplets using the heat transfer number B_H and B_M:

$$\text{Nu}(1+B_H)^{0.700} = 2+0.454\text{Re}_\text{p}^{0.615}\text{Pr}^{0.98}, \tag{5.24}$$

$$\text{Sh}(1+B_M)^{0.557} = 2+0.390\text{Re}_\text{p}^{0.540}\text{Sc}^{0.76}, \tag{5.25}$$

leading to lower Nusselt and Sherwood numbers compared to the classical Ranz-Marshall correlations. These corrections incorporate the slower droplet vaporisation due to the finite diffusion of the fuel vapour to the environment. Similar corrections due to mass transfer have been suggested by Yuen and Chen [186].

5.4.2 Shear lift

Particles moving with a shear flow will experience a lift force perpendicular to the direction of the flow. This is illustrated in Figure (5.1) for a particle in a simple one-dimensional shear flow . The expression for the one-dimensional shear lift force on a particle was first obtained by Saffman [142] and reads:

$$F_\text{L} = 1.615\rho_\text{f}\sqrt{\nu_\text{f}}d_\text{p}^2\left(U_\text{s}-U_\text{p}\right)\left|\frac{d\widetilde{U}_\text{f}}{dy}\right|\cdot\text{sgn}\left(\frac{d\widetilde{U}_\text{f}}{dy}\right), \tag{5.26}$$

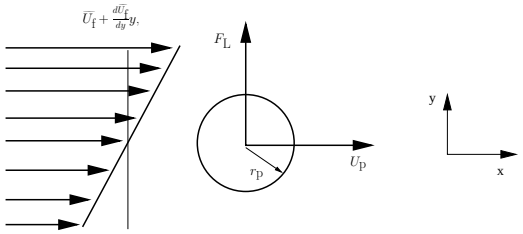

Figure 5.1: Sketch of the shear lift force on a particle.

where the instantaneous fluid velocity has again been replaced by the model velocity $U_{s,i}$. The velocity gradient at the location of the particle is obtained using the mean fluid velocity This equation can also be expressed in a more general form as [31]:

$$\mathbf{F}_L = 1.615 d_p^2 \sqrt{\mu_f \rho_f} \frac{(\boldsymbol{U}_s - \boldsymbol{U}_p) \times \omega}{|\omega|^{\frac{1}{2}}}, \tag{5.27}$$

with $\omega = \nabla \times \boldsymbol{U}_s$. The Saffman lift was derived under the assumptions that the particle Reynolds number Re_p is smaller than the shear Reynolds number Re_σ:

$$\mathrm{Re}_p \ll \sqrt{\mathrm{Re}_\sigma} = \sqrt{\frac{d_p^2}{\nu_f} \frac{d\widetilde{U}_f}{dy}} \tag{5.28}$$

An extension of the Saffman lift for particle Reynolds numbers larger than the shear Reynolds number was first proposed by McLaughlin [104]. Based on the numerical studies of Dandy and Dwyer [36], Mei [105] proposed an empirical fit to the Saffman lift:

$$\frac{F_L}{F_{L,\text{Saffman}}} = \begin{cases} (1 - 0.3314\sqrt{\beta}) e^{-0.10 \mathrm{Re}_p} + 0.3314\sqrt{\beta} & \text{if } \mathrm{Re}_p \leq 40, \\ 0.0524\sqrt{\beta \mathrm{Re}_p} & \text{if } \mathrm{Re}_p > 40 \end{cases} \tag{5.29}$$

with

$$\beta = \frac{d_p}{2\,|\boldsymbol{U}_s - \boldsymbol{U}_p|}\,|\omega|\,,\ 0.005 < \beta < 0.4. \tag{5.30}$$

The shear lift force might become very large in particle laden jets, where the shear force will cause the particles to move away from the centreline if the axial particle velocity is smaller than the axial flow velocity, and it will cause the particles to move towards the centreline if the particles move faster than the axial flow velocity. A quick analysis using equation (5.26) shows that a 100 μm particle in air moving with a slip velocity of $U_r = 10\frac{m}{s}$ in a shear flow of $\frac{dU_f}{dy} = 10,000\frac{m}{s^2}$ will experience a Saffman lift force of the order of $0.01 m_p$. A direct comparison with the gravity force $m_p g$ shows that the Saffman lift force is usually a small contribution

in particle laden jets. In particular, it was found to be small in the spray flames studied in this thesis, from which the specific values used in the above analysis were obtained. The Saffman lift is however taken into account in some numerical simulations [88] in the context of studies where particle collisions may play an important role.

5.4.3 Other forces

Other forces and corrections can also be taken into account [28, 31], but these forces are usually considered to be negligible in particle laden turbulent flows when the density ratio $\frac{\rho_p}{\rho_f} \gg 1$. No other forces are considered in this thesis.

5.5 Dispersion of particles in turbulent flow

Turbulent particle dispersion is a commonly used term to describe the transport phenomena of discrete particles which are distinguishable from the carrier phase that exhibit turbulent motion. It is the dispersed phase equivalent of turbulent diffusion in a continuum phase fluid flow. Many studies can be found in the literature devoted to Lagrangian (and Eulerian) dispersion models (e.g. [131, 146, 171] and the references therein).

After a short description of dispersion, the model for the velocity seen dispersion model will be given in the case that the mean drift velocity is aligned with the first axis of the reference coordinate system. We will call this the specific coordinate system. This model is then extended to a general coordinate system and a transformation is given that allows us to go from the specific coordinate system to the general coordinate system. A first order integration scheme can be derived in a rather straightforward manner for the equation for the velocity seen when it is given in the specific coordinate system. The numerical strategy in the general case is then to first perform an orthogonal transformation to the specific coordinate system, evolve the velocity seen over a small timestep Δt, and then transform the solution back to the generalised coordinate system.

Due to the finite particle inertia and external force fields like gravity, a fluid element and a particle element located initially at the same location will follow a different trajectory. One should therefore model the successive fluid velocities sampled or 'seen' by the dispersed phase particles as they move through the fluid. The modelling of the velocity seen by the dispersed phase particle involves two submodels where the effect of finite particle inertia and the effect of external force fields (causing the crossing trajectories effect) are modeled. These two effects will be discussed briefly before the model for the velocity seen is derived.

Inertia effect The inertia effect is due to *instantaneous* drift: the velocity difference between the particle and the surrounding fluid. We will consider an isotropic

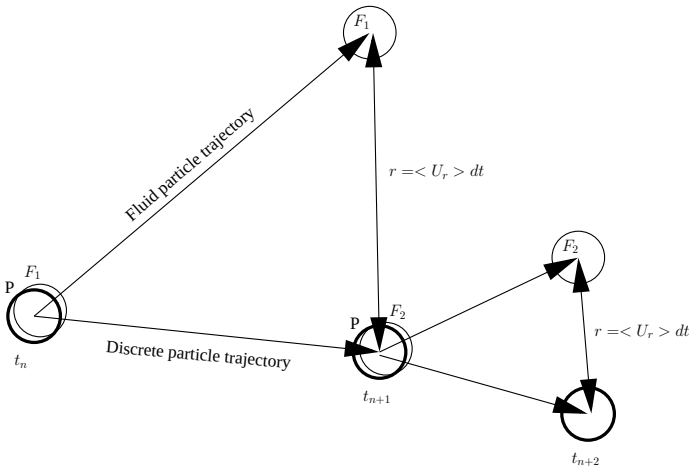

Figure 5.2: Illustration of the Crossing Trajectory Effect.

turbulent flow with zero mean drift, so no external force fields are present. In this flow a dispersed phase particle will experience ('see') small fluid phase fluctuations. Because of a difference in inertia, the dispersed phase particle is not able to respond instantaneously to the fluid phase velocity fluctuations. The particle inertia is characterised by the particle relaxation timescale τ_{p}, given by equation (5.17). Because of the inertia effect, the fluid and particle velocity correlations will be different. These correlations were already derived by Tchen [163] and revisited in Hinze [67].

In the case of dispersed phase particles with zero inertia, the particle will respond immediately to changes in the fluid phase and follow the fluid 'perfectly'. As a result, it will 'see' (experience) the fluid Lagrangian timescale, $T_L = C_L \frac{\widetilde{k}}{\epsilon}$, i.e. it will see fluctuations with an autocorrelation time T_L. When the particle inertia is large, the particle will be practically standing still with respect to the fluid phase elements and it will see an Eulerian timescale $T_E = \frac{L_E}{\sigma_{\mathrm{f}}}$, with $L_E = C_E \frac{\widetilde{k}^{\frac{3}{2}}}{\epsilon}$ and σ the fluid velocity variance. In practice, a dispersed phase particle will experience a timescale varying between the two limits T_L and T_E.

Effect of crossing trajectories The effect of a *mean* relative velocity (or drift velocity) between the discrete particle velocity and the velocity of the fluid seen, $\widetilde{U}_r = \widetilde{U}_{\mathrm{p}} - \widetilde{U}_{\mathrm{s}}$, on the velocity correlation is known as the 'crossing trajectories effect', a term introduced by Yudine [185] and later investigated by Csanady [33] and refined by Wang and Stock [171]. The effect is illustrated in Figure (5.2). When an external force, like gravity, works on a discrete particle in a turbulent fluid, a mean drift velocity occurs between the fluid and the discrete particle. A fluid and a discrete particle located at exactly the same position x_n at time t_n will follow different trajectories and after a time dt, their positions will be a distance $r = \langle U_r \rangle dt$

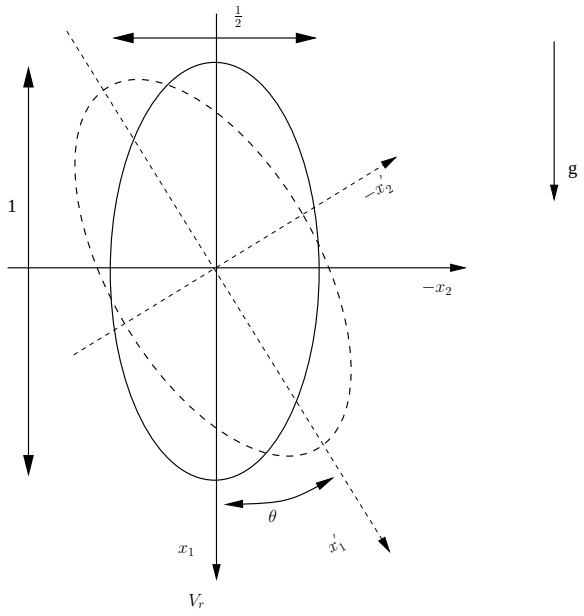

Figure 5.3: Diffusion Ellipsoid with different major axes. When the axes x' are not aligned with the mean drift, an orthogonal transformation is needed.

apart. The velocity of the fluid seen along the discrete particle trajectory from t_n to t_{n+1} will be different from the velocity of the fluid particle located at $x_n(t_n)$.

As a result, the fluid velocities 'seen' by the discrete particles are less correlated than the Lagrangian fluid velocities and the dispersion coefficient decreases.

Continuity effect In the limit as $\frac{\widetilde{U_r}}{\sqrt{\widetilde{u_\mathrm{f}''u_\mathrm{f}''}}} \to \infty$, the dispersion coefficient normal to the drift velocity $\widetilde{U_r}$ is one half that parallel to $\widetilde{U_r}$, see Figure (5.3). This effect of different dispersion behaviour in different directions is called the 'continuity effect' by Csanady [33, 171] and it is a consequence of the crossing trajectories effect.

5.5.1 Modelling dispersion

It is the purpose of a dispersion model to correctly describe the spreading of dispersed phase particles in a turbulent flow. We follow here the approach laid out by Minier and Peirano [109] and Simonin [148].

The stochastic particle position $\boldsymbol{X}_\mathrm{p}^*$ and velocity $\boldsymbol{U}_\mathrm{p}^*$ follow the simplified equations of motion (5.11) and (5.13). The velocity of the fluid at the location of the particle is then modeled by a Langevin equation, whose general form is:

$$dU_{\mathrm{s},i} = \left[A_{\mathrm{s},i}(t,\boldsymbol{Z}) + A_{\mathrm{p}\to\mathrm{s},i}(t,\boldsymbol{Z})\right] dt + B_{\mathrm{s},ij}(t,\boldsymbol{Z}) dW_j, \tag{5.31}$$

where $A_{\mathrm{s},ij}$ is the drift vector and $B_{\mathrm{s},ij}$ is the diffusion matrix. The two-way coupling term *seen* $A_{\mathrm{p}\to\mathrm{s},i}$ at the location of a discrete particle x_{p} is in principle different from the two-way coupling term appearing in the Langevin equation of the fluid phase [109].

All three terms on the right hand side of (5.31) depend on time and on a state vector which is taken to be $\boldsymbol{Z} = \boldsymbol{Z}(\boldsymbol{x}_{\mathrm{p}}, \boldsymbol{U}_{\mathrm{p}}, \boldsymbol{U}_{\mathrm{s}})$ [131]. We will first present the modelling of the drift and diffusion terms in the simplified case where the mean drift vector is aligned with the first coordinate axis.

5.5.2 Closure of the two way coupling terms

The two way coupling source term $A_{\mathrm{p}\to\mathrm{s},i}$ contains two contributions. First, a contribution due to momentum transfer, which is the usual two way coupling term. In case of vaporising particles it also contains a contribution due to mass transfer. Both source terms need to be modeled.

Momentum transfer The force exerted by one particle on the fluid is the drag force F_{drag} (with opposite sign) given in equation (5.14). The total force experienced by the fluid element surrounding a discrete particle is the sum of the individual particle forces per unit volume $\mathcal{V}_{\mathrm{f}}$. The two-way coupling term 'seen' then becomes equal to the mean two-way coupling source term $\langle \mathcal{S}_U \rangle$:

$$A^{(1)}_{\mathrm{p}\to\mathrm{s},i} = -\frac{1}{\mathcal{V}_{\mathrm{f}}} \sum_{*\in\mathcal{V}} \frac{1}{\rho_{\mathrm{f}}} F_{\mathrm{drag},i} = \frac{1}{\overline{\rho}} \Big\langle \mathcal{S}^{(I)}_{U_i} \Big\rangle. \tag{5.32}$$

In the second step we have neglected any fluctuations in the fluid phase density. The particles therefore 'see' the mean fluid phase density.

Mass transfer When there is mass transfer between the phases, the Langevin equation describing the fluid phase should contain a source term taking this mass transfer into account. And a discrete particle p will see a fluid particle which is affected by the mass transfer of the same discrete particle p.

The mass transfer from the dispersed phase to the fluid phase follows the idea of Demoulin and Borghi [38] (which was implemented by Naud [117]) that evaporated mass should be distributed to the gas phase in such a way as to feed a peak in the mass fraction pdf at saturation conditions (see also chapter 4). Out of the set of fluid particles in the neighbourhood of the discrete particle p, the fluid particle whose composition state is closest to saturation conditions is selected. This particle will get the evaporated mass until it reaches saturation conditions. If the fluid particle is not saturated after obtaining the complete evaporated mass of discrete particle p, then it will get the evaporated mass of another discrete particle until the fluid particle is saturated or until all evaporated mass has been given to the fluid phase.

This model takes into account the nonhomogeneous distribution of fuel vapour in a finite volume cell due to the finite timescale of turbulent mixing. A discrete particle is more or less immersed in its own fuel vapour and it will see fluid particles with high amounts of fuel vapour or even saturated fluid particles. We use this idea to extend the Langevin model for the velocity seen to situations where mass transfer occurs.

In the case of momentum transfer, we have assumed that particles see the mean fluid phase density. The algorithm used to distribute mass to the fluid phase particles allows to take the fluctuations in fluid phase density into account. The fluid particle density that is seen by the discrete particle is obtained from the fluid particle that received the evaporated mass of that discrete particle.

The source term added to the Langevin equation for the velocity seen,

$$A^{(2)}_{\mathrm{p}\rightarrow\mathrm{s},i} = \frac{1}{\rho_{\mathrm{f}}} U_{I,i} \mathcal{S}^{(I)}_m, \tag{5.33}$$

is implemented as a simple momentum balance of the fluid particle seen (which occupies a volume $\frac{m_{\mathrm{p}}}{\rho_{\mathrm{p}}}$ with mass $m_{\mathrm{f}} = \frac{\rho_{\mathrm{f}}}{\rho_{\mathrm{p}}} m_{\mathrm{p}}$):

$$U^{n+1}_{\mathrm{s},i} = U^n_{\mathrm{s},i} + \frac{\Delta m_{\mathrm{p}}}{m_{\mathrm{f}} + \Delta m_{\mathrm{p}}} (U^n_{\mathrm{p},i} - U^n_{\mathrm{s},i}). \tag{5.34}$$

5.5.3 Closure of drift and diffusion term

The details of how the drift and diffusion terms are obtained will now briefly be explained. A more detailed explanation is given in [109]. A modification of the diffusion term is proposed based on the presence of two way coupling and mass transfer in the evolution of the turbulent kinetic energy of the velocity fluctuation seen.

Closure of the drift term The basis for the model is the simplified Langevin model for a fluid particle. In the limit case of negligible particle inertia $\tau_{\mathrm{p}} \rightarrow 0$ and negligible mean drift velocity $U_{\mathrm{r}} \rightarrow 0$, the Langevin model for the discrete particle reduces to that of a fluid particle. The discrete particles are then ideal tracers of the fluid flow. Following the approach of Minier and Peirano [109], our starting point to create a model for the velocity of the fluid seen will be the Simplified Langevin Model discussed in Chapter 4.

In the fluid case, the drift term in the stochastic differential equation consists of the pressure gradient and a relaxation towards the mean:

$$-\frac{1}{\rho_{\mathrm{f}}} \frac{\partial \overline{p}}{\partial x_i} - \frac{U_{\mathrm{f},i} - \langle U_{\mathrm{f},i} \rangle}{T_L}. \tag{5.35}$$

To take into account the effects of crossing trajectories, an extra term containing the mean relative velocity appears in the Langevin equation for the discrete particle. The proposed drift term is then

$$A_{\mathrm{s},i} = -\frac{1}{\rho_{\mathrm{f}}}\frac{\partial \overline{p}}{\partial x_i} + \langle U_{r,i}\rangle \frac{\partial \langle U_{\mathrm{f},i}\mathcal{X}\rangle}{\partial x_j} - \frac{U_{\mathrm{s},i} - \langle U_{\mathrm{s},i}\rangle}{T_L^*}. \tag{5.36}$$

Here, T_L^* is the Lagrangian timescale of the velocity of the fluid seen. According to Csanady's analysis, the integral timescale of the velocity of the fluid seen is different from the fluid Lagrangian timescale T_L. When the mean drift is aligned with the first coordinate axis, the timescale in longitudinal direction $T_L^* = T_{L,\parallel}$ is

$$T_{L,\parallel} = \frac{T_L}{\sqrt{1 + \beta^2 \frac{\left|\overline{\boldsymbol{U}}_{\mathrm{r}}\right|^2}{\frac{2}{3}\langle u_k' u_k'\rangle}}}, \tag{5.37}$$

and in the transversal directions $T_L^* = T_{L,\perp}$:

$$T_{L,\perp} = \frac{T_L}{\sqrt{1 + 4\beta^2 \frac{\left|\overline{\boldsymbol{U}}_{\mathrm{r}}\right|^2}{\frac{2}{3}\langle u_k' u_k'\rangle}}}, \tag{5.38}$$

where $\beta = \frac{T_L}{T_E} = C_\beta$ is the ratio of the Lagrangian and Eulerian timescales of the fluid, which is a constant. The value of this constant is taken to be $C_\beta = 0.45$.

Closure of the diffusion term The modelling of the diffusion term is discussed extensively in [109]. We will follow the same step-by-step approach, but making some modifications by taking into account the two-way coupling source terms $\mathcal{S}_{U_i}^{(I)}$. In the case of stationary isotropic turbulence, with mean velocities equal to zero and vanishing pressure gradient, the stochastic differential equation for the velocity seen is given by

$$dU_{\mathrm{s},i} = -\frac{U_{\mathrm{s},i}}{T_L^*}dt + B_{\mathrm{s},ij}dW_j + \frac{1}{\rho_{\mathrm{f}}}\mathcal{S}_{U_i}^{(I)}dt + \frac{1}{\rho_{\mathrm{f}}}U_{I,i}\mathcal{S}_m^{(I)}dt. \tag{5.39}$$

Effectively, we are dealing with an equation for the velocity fluctuation seen, since the mean velocity is zero. We define the fluctuating velocity seen $\boldsymbol{u}_{\mathrm{s}}'$ as $\boldsymbol{u}_{\mathrm{s}}' = \boldsymbol{U}_{\mathrm{s}} - \langle \boldsymbol{U}_{\mathrm{f}}\rangle$. In the case considered here, there is no mean drift velocity and $\boldsymbol{u}_{\mathrm{s}}' = \boldsymbol{U}_{\mathrm{s}}$.

Using the stationarity constraint $dk_{\mathrm{s}}/dt = 0$ for the turbulent kinetic energy of the velocity seen, $k_{\mathrm{s}} = \frac{1}{2}\langle u_{\mathrm{s},i}' u_{\mathrm{s},i}'\rangle$ and by applying the stochastic calculus rule $d(U_iU_j) = U_i dU_j + U_j dU_i + D_{ij}dt$, we obtain a relationship between the diffusion term and the Lagrangian timescale:

$$B_{\mathrm{s},ij}^2 = C_0^{\mathrm{st}}\epsilon b_i - \frac{2}{3}\left\langle \frac{1}{\rho_{\mathrm{f}}}u_{\mathrm{s},i}'\mathcal{S}_{U_i}^{(I)}\right\rangle - \frac{2}{3}\left\langle \frac{1}{\rho_{\mathrm{f}}}u_{\mathrm{s},i}'U_{I,i}\mathcal{S}_m^{(I)}\right\rangle, \tag{5.40}$$

with the ratio of the fluid timescale and the seen timescale $b_i = \frac{T_\mathrm{f}}{T_i}$. C_0^{st} is the value of the proportionality constant in the stationary case, $C_0^{\mathrm{st}} = C_0 + \frac{2}{3}$ and $T_L = \frac{4}{3}\frac{k}{\epsilon}C_0^{\mathrm{st}}$. We have implicitly assumed in (5.40) that $\langle \boldsymbol{U}_\mathrm{f} \rangle = \langle \boldsymbol{U}_\mathrm{s} \rangle$.

In the case of anisotropic turbulence a weighted turbulent kinetic energy has to be introduced to compensate for the non-isotropic drift vector:

$$\mathcal{K} = \frac{3}{2}\frac{\sum_{i=1}^{3} b_i \langle u'_{\mathrm{f},i} u'_{\mathrm{f},i} \rangle}{\sum_{i=1}^{3} b_i}, \tag{5.41}$$

leading to the intermediate Langevin model

$$\begin{aligned} dU_{\mathrm{s},i} &= -\frac{3}{4}C_0^{\mathrm{st}}\frac{\epsilon}{\widetilde{k}}b_i(U_{\mathrm{s},i} - \langle U_{\mathrm{s},i}\rangle)dt + \sqrt{C_0^{\mathrm{st}}\epsilon b_i \frac{\mathcal{K}}{\widetilde{k}} - \frac{2}{3}\left\langle \frac{1}{\rho_\mathrm{f}} u'_{\mathrm{s},i}\mathcal{S}_{U_i}^{(I)} \right\rangle - \frac{2}{3}\left\langle \frac{1}{\rho_\mathrm{f}} u'_{\mathrm{s},i} U_{I,i}\mathcal{S}_m^{(I)} \right\rangle} dW_i \\ &+ \frac{1}{\rho_\mathrm{f}}\mathcal{S}_{U_i}^{(I)}dt + \frac{1}{\rho_\mathrm{f}}U_{I,i}\mathcal{S}_m^{(I)}dt. \end{aligned} \tag{5.42}$$

When considering homogeneous non-stationary turbulence, e.g. decaying turbulence, the turbulent kinetic energy of the fluid seen is expected to satisfy an equation similar to that for the turbulent kinetic energy of the fluid:

$$\frac{1}{2}\frac{d\langle u'_{\mathrm{s},i}u'_{\mathrm{s},i}\rangle}{dt} = -\epsilon + \underbrace{\left\langle u''_{I,i}\mathcal{S}_{U_i}^{(I)} \right\rangle}_{\frac{1}{2}\left\langle \mathcal{S}_{u_i u_i}^{(I)} \right\rangle} + \frac{1}{2}\langle u''_{I,i}u''_{I,i}\mathcal{S}_m^{(I)}\rangle, \tag{5.43}$$

with $\mathcal{S}_{u_i u_j}^{(I)}$ the two-way coupling source term appearing in the Eulerian transport equation for the Reynolds stresses. The final expression for the Langevin model for the velocity seen is then given by:

$$\begin{aligned} dU_{\mathrm{s},i} &= -\frac{1}{\rho_\mathrm{f}}\frac{\partial \overline{p}}{\partial x_i}dt + \langle U_{r,i}\rangle \frac{\partial \langle U_i\rangle}{\partial x_j}dt \\ &- (\frac{1}{2} + \frac{3}{4}C_0)\frac{\epsilon}{\widetilde{k}}b_i(U_{\mathrm{s},i} - \langle U_{\mathrm{s},i}\rangle)dt + \sqrt{\frac{4}{3}\epsilon\left((\frac{1}{2} + \frac{3}{4}C_0)b_i\frac{\mathcal{K}}{\widetilde{k}} - \frac{1}{2}\right)}dW_i \\ &+ \frac{1}{\rho_\mathrm{f}}\mathcal{S}_{U_i}^{(I)}dt + \frac{1}{\rho_\mathrm{f}}U_{\mathrm{s},i}^{(I)}\mathcal{S}_m^{(I)}dt. \end{aligned} \tag{5.44}$$

Note that the two way coupling source term in the diffusion term has cancelled.

5.5.4 Model equations

In an article by Minier, Peirano and Chibbaro [110], a stochastic numerical scheme is suggested to numerically integrate the coupled system of stochastic differential equations describing the evolution of a dispersed phase particle in a turbulent fluid.

The system of equations considered by Minier *et al*. are given in the general form:

$$dx_{p,i} = U_{p,i}dt \tag{5.45}$$

$$dU_{p,i} = \frac{1}{\tau_p}(U_{s,i} - U_{p,i})dt + \mathcal{A}_i dt \tag{5.46}$$

$$dU_{s,i} = G_{\mathrm{s},ij}U_{s,i}dt + C_i dt + B_{\mathrm{s},ij}dW_j(t), \tag{5.47}$$

with τ_p the characteristic particle relaxation time scale discussed in section 5.4. A_i is the acceleration containing the undisturbed fluid flow forces:

$$\mathcal{A}_i = -\frac{1}{\rho_\mathrm{f}}\frac{\partial \overline{p}}{\partial x_i} + g_i, \tag{5.48}$$

and B_{ij} is a diagonal tensor (nonzero values only on the diagonal). The description of the fluid flow in which the considered particle is immersed is assumed to be accurately described by a simplified Langevin model. One of the properties of the model should be that in the limit of zero inertia, a dispersed phase particle should follow the fluid flow and the system of equations (5.11-5.47) should reduce to the SLM describing the fluid flow. The drift term $G_{\mathrm{s},ij}$ is modeled accordingly as a diagonal tensor:

$$G_{\mathrm{s},ij} = \frac{1}{T_i}\delta_{ij}, \tag{5.49}$$

with T_i given by

$$T_i = T_\mathrm{f}\left[1 + \beta_i \frac{3}{2}\frac{|\langle \boldsymbol{U}_r\rangle|^2}{k}\right]^{\frac{1}{2}}, \tag{5.50}$$

with T_f the timescale of the fluid, defined as $T_\mathrm{f} \equiv C_\mu \frac{\widetilde{k}}{\epsilon}$. C_μ is a constant determined by the SLM, and is given here as $C_\mu^{-1} = 1 + \frac{3}{2}C_0$. β_i is a constant that depends on the direction i (according to the analysis of Csanady). The diagonal diffusion tensor B_{ij} is given by

$$B_{ij}^2 = \frac{2}{3}\epsilon\left[\left(1 + \frac{3}{2}C_0\right)b_i\frac{\mathcal{K}}{\widetilde{k}} - 1\right]\delta_{ij}, \tag{5.51}$$

and the vector C_i consists of the following terms:

$$C_i = \frac{\langle U_{\mathrm{s},i}\rangle}{T_i} - \frac{1}{\rho_\mathrm{f}}\frac{\partial \overline{p}}{\partial x_i} + (\langle U_{\mathrm{p},i}\rangle - \langle U_{\mathrm{s},i}\rangle)\frac{\partial \langle U_{\mathrm{f},i}\rangle}{\partial x_j} + \frac{1}{\rho_\mathrm{f}}\mathcal{S}_{U_i}^{(I)} + \frac{1}{\rho_\mathrm{f}}U_{I,i}\mathcal{S}_m^{(I)}. \tag{5.52}$$

It can now be easily checked that when $\tau_\mathrm{p} \to 0$, the particles behave as fluid particles and the equation for the velocity seen reduces to the SLM described in chapter 4.

5.6 Equation for the fluctuation of velocity seen

The equation for the velocity seen contains a term $G_{ij}(U_{\mathrm{s},i} - \langle U_{\mathrm{s},i}\rangle)$. A similar term occurs in the Langevin equation describing the fluid flow. It is this term that gives rise to the bias error: Due to the finite number of particles in the considered volume, the computed mean velocity seen in this volume will contain a statistical error. The feedback of this computed mean velocity seen (including the error) will then lead to a bias error [183, 184]. In single phase flow, this problem was resolved by obtaining the mean flow properties from a finite volume solver [72] and using the Langevin equation only for the fluctuating velocity. We follow here the approach of Naud [117] to obtain an equation for the fluctuating velocity seen. The starting point is the modified SLM equation (5.47) and (5.52). By subtracting the following equation from the modified SLM

$$\begin{aligned}
\frac{\partial\langle U_i\rangle_{|1}}{\partial t} + U_{\mathrm{p},j}\frac{\partial\langle U_i\rangle_{|1}}{\partial x_j} &= \frac{1}{\overline{\rho}}\left[\frac{\partial\overline{\rho}\langle U_i\rangle_{|1}}{\partial t} + \frac{\partial\overline{\rho}\langle U_i\rangle_{|1}\langle U_j\rangle_{|1}}{\partial x_j}\right] + \left(U_{\mathrm{p},j} - \langle U_j\rangle_{|1}\right)\frac{\partial\langle U_i\rangle_{|1}}{\partial x_j} - \frac{1}{\overline{\rho}}\langle U_i\rangle_{|1}\langle\mathcal{S}_m^{(I)}\rangle \\
&= \frac{1}{\overline{\rho}}\left[-\frac{\partial\overline{p}}{\partial x_i} + \frac{\partial\overline{\tau_{ij}}}{\partial x_j} + \overline{\rho}g_i - \frac{\partial}{\partial x_j}\left(\overline{\rho}\langle u_i'u_j'\rangle_{|1}\right) + \left\langle\mathcal{S}_{U_i}^{(I)}\right\rangle + \langle U_{I,i}\mathcal{S}_m^{(I)}\rangle\right] \\
&\quad + \left(U_{\mathrm{p},j} - \langle U_j\rangle_{|1}\right)\frac{\partial\langle U_i\rangle_{|1}}{\partial x_j} - \frac{1}{\overline{\rho}}\langle U_i\rangle_{|1}\langle\mathcal{S}_m^{(I)}\rangle,
\end{aligned} \tag{5.53}$$

we obtain the modeled increment for the fluctuation of the velocity seen. Neglecting the gravity and mean viscous diffusion terms we obtain the final model for the equation for the fluctuating velocity seen:

$$\begin{aligned}
du_{\mathrm{s},i}' = &-\left[\frac{1}{\rho_{\mathrm{f}}} - \frac{1}{\overline{\rho}}\right]\frac{\partial\overline{p}}{\partial x_i}dt + \frac{1}{\overline{\rho}}\frac{\partial}{\partial x_j}\left(\overline{\rho}\langle u_i'u_j'\rangle_{|1}\right)dt \\
&- \left(u_{\mathrm{p},j}' + \langle u_{\mathrm{s},j}'\rangle_{|2}\right)\frac{\partial\langle U_i\rangle_{|1}}{\partial x_j}dt + G_{\mathrm{s},ij}u_{\mathrm{s},j}'dt + B_{\mathrm{s},ij}dW_j \\
&+ \frac{1}{\rho_{\mathrm{f}}}U_{I,i}\mathcal{S}_m^{(I)}dt - \frac{1}{\overline{\rho}}\langle U_{I,i}\mathcal{S}_m^{(I)}\rangle dt + \frac{1}{\overline{\rho}}\langle U_i\rangle_{|1}\langle\mathcal{S}_m^{(I)}\rangle.
\end{aligned} \tag{5.54}$$

In equation (5.55), the source term for momentum transfer drops out of the equation because the density fluctuations are neglected. If the density fluctuations are systematically neglected, the pressure gradient can also be removed from the equation. The source term for mass transfer can still be determined by considering a momentum balance. In this way, all references to the instantaneous value for fluid density can be avoided and equation (5.55) can be solved.

5.7 Dispersion model in general coordinates

The dispersion model derived in the previous section was derived under the assumption that the mean drift velocity (the mean relative velocity $\boldsymbol{U}_r$) is aligned

with the first axis of the reference system. The Langevin model is now generalised for the case where $\boldsymbol{U}_r$ has any orientation with respect to the axis of the reference system.

Modified drift vector The modified matrix G_{ij} reads

$$G_{\mathrm{s},ij} = -\frac{1}{T_{L,\perp}}\delta_{ij} + \left[\frac{1}{T_{L,\parallel}} - \frac{1}{T_{L,\perp}}\right] r_i r_j, \tag{5.55}$$

where $\boldsymbol{r}$ is the unit vector aligned with the mean drift: $\boldsymbol{r} = \langle \boldsymbol{U}_\mathrm{r} \rangle_{|2} / |\langle \boldsymbol{U}_\mathrm{r} \rangle_{|2}|$; and where $T_{L,\parallel}$ and $T_{L,\perp}$ are the Lagrangian timescales seen in the directions parallel and perpendicular to the mean drift according to Csanady's analysis. Based on the SLM modeled Lagrangian timescale $T_L^{(\mathrm{SLM})}$, they read:

$$T_{L,\parallel} = T_L^{(\mathrm{SLM})} \,/\, H_\parallel \quad \text{and} \quad T_{L,\perp} = T_L^{(\mathrm{SLM})} \,/\, H_\perp, \tag{5.56}$$

with

$$H_\parallel = \sqrt{1 + C_\beta \xi_\mathrm{r}}, \quad H_\perp = \sqrt{1 + 4C_\beta \xi_\mathrm{r}} \quad \text{and} \quad \xi_\mathrm{r} = 3\,|\langle \boldsymbol{U}_\mathrm{r} \rangle_{|2}|^2 \Big/ \langle u_k' u_k' \rangle_{|1}. \tag{5.57}$$

Introducing the specific form of $T_L^{(\mathrm{SLM})}$, (5.55) can now be written as:

$$G_{\mathrm{s},ij} = -\frac{1}{T_L^{(\mathrm{SLM})}} H_{ij} = -\left(\frac{1}{2} + \frac{3}{4}C_0\right) \frac{2\epsilon}{\langle u_k' u_k' \rangle_{|1}} H_{ij}, \tag{5.58}$$

with

$$H_{ij} = H_\perp \delta_{ij} + \left(H_\parallel - H_\perp\right) r_i r_j. \tag{5.59}$$

Modified diffusion matrix The diffusion matrix is obtained as the solution of

$$\left(B_\mathrm{s} B_\mathrm{s}^T\right)_{ij} = D_{ij}, \tag{5.60}$$

where $B_{\mathrm{s},ij}^T$ is the transpose matrix of $B_{\mathrm{s},ij}$. The symmetric matrix D_{ij} is given as

$$D_{ij} = \epsilon \left(C_0 \lambda H_{ij} + \frac{2}{3}\left(\lambda H_{ij} - \delta_{ij}\right) \right), \tag{5.61}$$

with the factor λ specified as $\lambda = 3\,Tr(\mathbf{HR}) / \left[Tr(\mathbf{H})\,\langle u_k' u_k' \rangle_{|1}\right]$, where $Tr(\mathbf{H})$ denotes the trace of matrix H_{ij} and with $R_{ij} = \left\langle u_i' u_j' \right\rangle_{|1}$, such that in isotropic decaying turbulence, the turbulent kinetic energy of the fluid seen is given by equation (5.43)

5.8 Orthogonal transformation

The solution of the equation for the velocity seen can be obtained exactly for small timesteps when assuming constant coefficients. This solution is then used as the basis of a weak first order numerical integration scheme [110, 122]. When the equation for the velocity seen in generalised coordinates is considered, an orthogonal transformation is used to *decouple* the equations for $U_{\mathrm{s},1}$, $U_{\mathrm{s},2}$ and $U_{\mathrm{s},3}$. The exact solution of each equation can now be considered individually, which makes the analysis less complicated. In order to perform an orthogonal transformation, the eigenvalues and eigenvectors of the general system are needed. This will be discussed in the next paragraph.

Eigenvalues and Eigenvectors The eigenvalues λ_G of $G_{\mathrm{s},ij}$, given by (5.58-5.59), are found to be

$$\lambda_G = -\frac{1}{T_L^{(\mathrm{SLM})}}\left(H_{\parallel}, H_{\perp}, H_{\perp}\right) \tag{5.62}$$

and the orthogonal matrix of eigenvectors P_{ij} is given by

$$\mathbf{P} = \begin{bmatrix} +\frac{V_{rx}}{\sqrt{V_{rx}^2+V_{ry}^2+V_{rz}^2}} & -\frac{V_{ry}}{\sqrt{V_{rx}^2+V_{ry}^2}} & -\frac{V_{rx}V_{rz}}{\sqrt{V_{rx}^2+V_{ry}^2}\sqrt{V_{rx}^2+V_{ry}^2+V_{rz}^2}} \\ +\frac{V_{ry}}{\sqrt{V_{rx}^2+V_{ry}^2+V_{rz}^2}} & +\frac{V_{rx}}{\sqrt{V_{rx}^2+V_{ry}^2}} & -\frac{V_{ry}V_{rz}}{\sqrt{V_{rx}^2+V_{ry}^2}\sqrt{V_{rx}^2+V_{ry}^2+V_{rz}^2}} \\ +\frac{V_{rz}}{\sqrt{V_{rx}^2+V_{ry}^2+V_{rz}^2}} & 0 & +\frac{\sqrt{V_{rx}^2+V_{ry}^2}}{\sqrt{V_{rx}^2+V_{ry}^2+V_{rz}^2}} \end{bmatrix}. \tag{5.63}$$

With the introduction of the Euler angles

$$\begin{aligned} \cos(\theta) &= \frac{V_{rx}}{\sqrt{V_{rx}^2+V_{ry}^2}} & \sin(\theta) &= \frac{-V_{ry}}{\sqrt{V_{rx}^2+V_{ry}^2}}, \\ \cos(\psi) &= \frac{\sqrt{V_{rx}^2+V_{ry}^2}}{\sqrt{V_{rx}^2+V_{ry}^2+V_{rz}^2}} & \sin(\psi) &= \frac{-V_{rz}}{\sqrt{V_{rx}^2+V_{ry}^2+V_{rz}^2}}, \end{aligned}$$

the matrix P_{ij} can also be written as:

$$\mathbf{P} = \begin{bmatrix} & \cos(\theta)\cos(\psi) & \sin(\theta) & & \cos(\theta)\sin(\psi) \\ - & \sin(\theta)\cos(\psi) & \cos(\theta) & - & \sin(\theta)\sin(\psi) \\ - & \sin(\psi) & 0 & & \cos(\psi) \end{bmatrix}. \tag{5.64}$$

The coupled system of differential equations

$$dU_{\mathrm{s},i} = G_{\mathrm{s},ij}U_{\mathrm{s},j}dt \tag{5.65}$$

can now be decoupled by making a change of variable $\mathbf{V}_{\mathrm{s}} = \mathbf{P}^T\mathbf{U}_{\mathrm{s}}$ and solving the decoupled system

$$dV_{\mathrm{s},i} = \lambda_{\mathrm{s},ij}V_{\mathrm{s},j}dt, \tag{5.66}$$

where the matrix λ_{ij} is the eigenvalue matrix, a diagonal matrix whose diagonal entries are the eigenvalues λ_G, arranged in the same order as the corresponding eigenvectors in the eigenvector matrix P_{ij}. The solution of the original system of equations can be obtained using the back-transformation $\mathbf{U}_\mathrm{s} = \mathbf{P} \cdot \mathbf{V}_\mathrm{s}$.

Eigenvalues of diffusion matrix Since the diffusion matrix D_{ij} is a function of H_{ij}, the eigenvalues of $D_{\mathrm{s},ij}$ are closely linked to the eigenvalues of $G_{\mathrm{s},ij}$. By writing the diffusion matrix $D_{\mathrm{s},ij}$ as

$$D_{\mathrm{s},ij} = \epsilon \left((C_0 + \frac{2}{3})\lambda H_{ij} - \frac{2}{3}\delta_{ij} \right), \tag{5.67}$$

we see that the eigenvalues of D_{ij} are related to the eigenvalues of H_{ij} as:

$$\lambda_D = (C_0 + \frac{2}{3})\lambda\epsilon\lambda_H - \frac{2}{3}\epsilon, \tag{5.68}$$

and the eigenvectors of D_{ij} are the same as the eigenvectors of G_{ij}. The diffusion matrix B_{ij} can also be written as (no summation over j implied at the right hand side)

$$\begin{aligned} \left(\mathbf{B}_\mathrm{s}\mathbf{B}_\mathrm{s}^T\right)_{ij} &= \mathbf{PLP}^{-1} \\ &= (\mathbf{P}\sqrt{\mathbf{L}})(\sqrt{\mathbf{L}}^T\mathbf{P}^T) \\ &= (\mathbf{P}\sqrt{\mathbf{L}})(\mathbf{P}\sqrt{\mathbf{L}})^T, \end{aligned} \tag{5.69}$$

with L_{ij} the eigenvalue matrix and P_{ij} the corresponding orthogonalised eigenvector matrix. So B_{ij} can be written as

$$B_{ij} = P_{ij}\sqrt{l_j}, \tag{5.70}$$

with eigenvalues l_i. In the transformed equation of motion for the velocity seen, this term is premultiplied by $\mathbf{P}^T$, so the matrix B_{ij} reduces to the diagonal matrix $\sqrt{\mathbf{L}}$.

Nonhomogeneous system To solve the more general case

$$dU_{\mathrm{s},i} = G_{\mathrm{s},ij}U_{\mathrm{s},j}dt + C_i dt + B_{ij}dW_j, \tag{5.71}$$

but with the restriction that C_i is independent of the instantaneous velocity seen $U_{\mathrm{s},i}$, the same strategy can be used. Introducing the change of variable $\mathbf{U}_\mathrm{s} = \mathbf{PV}_\mathrm{s}$, with $\mathbf{P}$ still given by equation (5.63) or (5.64), we obtain

$$\begin{aligned} dV_{\mathrm{s},i} &= \lambda_{\mathrm{s},ij}V_{\mathrm{s},j}dt + P_{ij}^{-1}C_j dt + P_{ij}^{-1}P_{ij}\sqrt{l_j}dW_j \\ &= \lambda_{\mathrm{s},ij}V_{\mathrm{s},j}dt + P_{ij}^{T}C_j dt + \sqrt{l_i}dW_i, \end{aligned} \tag{5.72}$$

because P_{ij} is orthogonal. Because C_i and P_{ij} are independent of the velocity $U_{\mathrm{s},i}$, and because the diffusion matrix is reduced to a diagonal matrix, the system (5.72) is still decoupled.

5.9 Numerical integration scheme

The purpose of this section is to find the analytic solution of the general system (5.46-5.47) over small timesteps Δt. It is possible to find the solution when assuming that the values of the coefficients $\tau_{\rm p}, A_i, G_{{\rm s},ij}, C_i$ and $B_{{\rm s},ij}$ remain constant during the timestep. Since C_i given by equation (5.52) is clearly depending on the instantaneous value of the particle velocity and particle velocity seen through the two-way coupling source term, we will neglect two way coupling in the following analysis. Using the Ito formula and the Ito isometry (see appendix A), the numerical solution of equations (5.46-5.47) at timestep $n+1$ can be found in terms of the solution at timestep n as follows:

$$
\begin{aligned}
x_{{\rm p},i}^{n+1} &= x_{{\rm p},i}^{n} + AU_{{\rm p},i}^{n} + BU_{{\rm s},i}^{n} + CT_i^n C_i^n + \mathcal{A}_i \tau_{\rm p}^n (\Delta t - A) + \Omega_i^n && (5.73)\\
U_{{\rm s},i}^{n+1} &= U_{{\rm s},i}^{n} \exp(-\Delta t/T_i^n) + T_i^n C_i^n \left[1 - \exp(-\Delta t/T_i^n)\right] + \gamma_i^n && (5.74)\\
U_{{\rm p},i}^{n+1} &= U_{{\rm p},i}^{n} \exp(-\Delta t/\tau_{\rm p}^n) + D_i U_{{\rm s},i}^{n} + T_i^n C_i^n \left(E - D_i\right) + \mathcal{A}_i \tau_{\rm p}^n E + \Gamma_i^n, && (5.75)
\end{aligned}
$$

with the coefficients $A - E$ given by:

$$
\begin{aligned}
A &= \tau_{\rm p}^n \left[1 - \exp(-\Delta t/\tau_{\rm p}^n)\right] && (5.76)\\
B &= \theta_i^n \left[T_i^n \left(1 - \exp(-\Delta t/T_i^n)\right) - A\right], \text{ with } \theta_i^n = T_i^n/(T_i^n - \tau_{\rm p}^n) && (5.77)\\
C &= \Delta t - A - B && (5.78)\\
D &= \theta_i^n \left[\exp(-\Delta t/T_i^n) - \exp(-\Delta t/\tau_{\rm p}^n)\right] && (5.79)\\
E &= 1 - \exp(-\Delta t/\tau_{\rm p}^n). && (5.80)
\end{aligned}
$$

The stochastic contributions are determined by

$$
\begin{aligned}
\gamma_i^n &= P_{11}\mathcal{G}_{1,i} && (5.81)\\
\Omega_i^n &= P_{21}\mathcal{G}_{1,i} + P_{22}\mathcal{G}_{2,i} && (5.82)\\
\Gamma_i^n &= P_{31}\mathcal{G}_{1,i} + P_{32}\mathcal{G}_{2,i} + P_{33}\mathcal{G}_{3,i}, && (5.83)
\end{aligned}
$$

where $\mathcal{G}_{1,i}$, $\mathcal{G}_{2,i}$, $\mathcal{G}_{3,i}$ are independent random variables drawn from a normal distribution $\mathcal{N}(0,1)$. The coefficients P_{ij} are defined as:

$$
\begin{aligned}
P_{11} &= \sqrt{\langle (\gamma_i^n)^2 \rangle} && (5.84)\\
P_{21} &= \frac{\langle \Omega_i^n \gamma_i^n \rangle}{P_{11}}, P_{22} = \sqrt{\langle (\Omega_i^n)^2 \rangle - P_{21}^2} && (5.85)\\
P_{31} &= \frac{\langle \Gamma_i^n \gamma_i^n \rangle}{P_{11}}, P_{32} = \frac{\left(\langle \Omega_i^n \Gamma_i^n \rangle - P_{21}P_{31}\right)}{P_{22}}, P_{33} = \sqrt{\langle (\Gamma_i^n)^2 \rangle - P_{31}^2 - P_{32}^2}, && (5.86)
\end{aligned}
$$

with the covariance matrix given by:

$$
\begin{aligned}
\left\langle \gamma_i^2(t) \right\rangle &= B_i^2 \frac{T_i}{2} \left[1 - \exp(-2\Delta t/T_i)\right], \text{ where } B_i^2 = \sum_j B_{ij}^2 \\
\frac{1}{B_i^2\theta_i^2}\left\langle \Gamma_i^2(t) \right\rangle &= \frac{T_i}{2}\left[1 - \exp(-2\Delta t/T_i)\right] - \frac{2\tau_\mathrm{p} T_i}{T_i + \tau_\mathrm{p}}\left[1 - \exp(-\Delta t/T_i)\exp(-\Delta t/\tau_\mathrm{p})\right] \\
&+ \frac{\tau_\mathrm{p}}{2}\left[1 - \exp(-2\Delta t/\tau_\mathrm{p})\right] \\
\frac{1}{B_i^2\theta_i^2}\left\langle \Omega_i^2(t) \right\rangle &= (T_i - \tau_\mathrm{p})^2 \Delta t + \frac{T_i^3}{2}\left[1 - \exp(-2\Delta t/T_i)\right] + \frac{\tau_\mathrm{p}^3}{2}\left[1 - \exp(-2\Delta t/\tau_\mathrm{p})\right] \\
&- 2T_i^2(T_i - \tau_\mathrm{p})\left[1 - \exp(-\Delta t/T_i)\right] \\
&+ 2\tau_\mathrm{p}^2(T_i - \tau_\mathrm{p})\left[1 - \exp(-\Delta t/\tau_\mathrm{p})\right] \\
&- 2\frac{T_i^2\tau_\mathrm{p}^2}{T_i + \tau_\mathrm{p}}\left[1 - \exp(-\Delta t/T_i)\exp(-\Delta t/\tau_\mathrm{p})\right] \qquad (5.87) \\
\frac{1}{B_i^2\theta_i T_i}\left\langle \gamma_i(t)\Gamma_i(t) \right\rangle &= \frac{1}{2}\left[1 - \exp(-2\Delta t/T_i)\right] \\
&- \frac{\tau_\mathrm{p}}{T_i + \tau_\mathrm{p}}\left[1 - \exp(-2\Delta t/T_i)\exp(-\Delta t/\tau_\mathrm{p})\right] \\
\frac{1}{B_i^2\theta_i T_i}\left\langle \gamma_i(t)\Omega_i(t) \right\rangle &= (T_i - \tau_\mathrm{p})\left[1 - \exp(-\Delta t/T_i)\right] - \frac{T_i}{2}\left[1 - \exp(-2\Delta t/T_i)\right] \\
&+ \frac{\tau_\mathrm{p}}{T_i + \tau_\mathrm{p}}\left[1 - \exp(-\Delta t/T_i)\exp(-\Delta t/\tau_\mathrm{p})\right] \\
\frac{1}{B_i^2\theta_i^2}\left\langle \Gamma_i(t)\Omega_i(t) \right\rangle &= (T_i - \tau_\mathrm{p})T_i\left[1 - \exp(-\Delta t/T_i)\right] - \tau_\mathrm{p}\left[1 - \exp(-2\Delta t/\tau_\mathrm{p})\right] \\
&+ \frac{T_i^2}{2}\left[1 - \exp(-2\Delta t/T_i)\right] \\
&- \frac{\tau_\mathrm{p}^2}{2}\left[1 - \exp(-2\Delta t/\tau_\mathrm{p})\right] T_i\tau_\mathrm{p}\left[1 - \exp(-\Delta t/T_i)\exp(-\Delta t/\tau_\mathrm{p})\right].
\end{aligned}
$$

It is trivial to use the same numerical method for the system of equations where the fluctuating velocity seen is solved. When two-way coupling terms are present, C_i depends on the velocity seen and one of the assumptions under which the scheme was derived is violated. In the equation for the fluctuating velocity seen, the two way coupling source terms only cause a weak dependence on the fluctuating two-way coupling source term. Indeed, the instantaneous and mean two-way coupling source terms are present in equation (5.55) but they cannot be directly rewritten to yield a dependence on the fluctuating velocity seen. This issue needs to be investigated in more detail in future research.

5.10 Conclusions

In this chapter the Lagrangian treatment of the dispersed phase was discussed. First, a stochastic approach was introduced, leading to the transport equation of the Mass Density Function. The solution of the transport equation of the MDF is then obtained by means of a particle method: Lagrangian equations of motion are solved for stochastic dispersed phase samples of the MDF. In the derivation presented in this chapter, the emphasis was on the two way coupling source terms that eventually would appear in the equation for the fluctuating velocity seen. A stochastic Lagrangian dispersion model was presented, together with a weak integration scheme that is first order accurate. However, several open issues remain which were not investigated here:

- The two way coupling source terms in the equation for the fluctuating velocity seen were neglected in the numerical integration scheme. It might be possible to derive a consistent first order numerical integration scheme including the two way coupling terms. This needs to be investigated further.
- The importance of including the fluctuations of the two way coupling source term in the equation for the fluctuating velocity seen should be investigated.

CHAPTER 6

Simulation of a non-evaporating turbulent spray jet

To investigate the importance of including the two-way coupling source terms in the model for the pressure rate of strain, simulations of a turbulent polydispersed non-evaporating spray were performed. The continuum phase model consists of the Eulerian mean transport equations for momentum, Reynolds stresses and dissipation given in Chapter 3. The pressure field is obtained using a Poisson solver, which also implicitly ensures that the mean continuity equation is obeyed. The dispersed phase model consists of the Lagrangian equations of motion (5.11,5.13) and the model for the velocity fluctuation seen, eq. (5.55). These equations are discussed in chapter 5.

6.1 Configuration and boundary conditions

The configuration corresponds to the spray investigated experimentally in [53, 54]. The experiment is characterised as a constant density air jet laden with liquid particles flowing downwards, issuing from a 8 mm diameter nozzle into a cubic chamber with sides of 0.5 mm. The sides are far away from the edge of the spray and the influence of the presence of the wall on the spray behaviour can be neglected.

In this experiment, a two-component Phase Doppler anemometer (PDA) was used to simultaneously measure droplet velocities and diameters and Laser Induced Fluorescence (LIF) combined with PDA was used to extract the local value of concentration and flux per droplet size class. The estimated statistical errors for the velocity differ per size class, ranging from 0.8% for the smallest size class ($0 - 5\mu\mathrm{m}$) to 7.3% for the size class $80 - 90\mu\mathrm{m}$. This effect is mainly due to a decreasing number of samples for increasing droplet size class. Four cases were investigated experimentally with different liquid mass loadings $\phi \equiv \frac{m_\mathrm{p}}{m_\mathrm{f}}$, i.e. $\phi = 0$ (gas flow only), $\phi = 0.12$, $\phi = 0.41$ and $\phi = 0.73$. We will discuss results for the test-case with the highest mass loading only. The gas-particle interactions are the strongest for this test-case and will therefore illustrate the importance between the different two-way coupling terms more clearly. Numerical simulations of the case with mass loading $\phi = 0.41$ are presented and discussed in detail in the thesis of Naud [117].

The droplet sizes range from 1-120 $\mu\mathrm{m}$. The droplets in the smallest size class are assumed to behave as tracer particles and can be used as an estimation for the gas-phase mean and rms velocity. The inlet conditions for the simulation correspond to the measured values in the section closest to the nozzle, at x = 20 mm downstream. The inlet boundary data not available experimentally is the profile

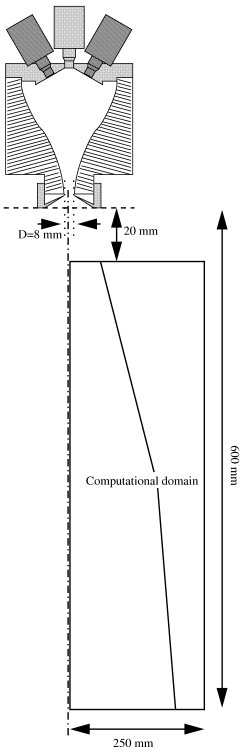

Figure 6.1: Experimental setup and computational domain.

Re	9500
ϕ	0.73
ρ_p	760 kg/m^3
domain	600×250 mm^2
grid cells	120×64 on a stretched grid

Table 6.1: Experimental and numerical conditions.

for turbulent dissipation. This profile was obtained by first estimating the dissipation profile for the unladen jet case, and then adding an extra dissipation term $\frac{1}{2}\langle \mathcal{S}_{u_k'' u_k''} \rangle$ due to two-way coupling.

A sketch of the experimental setup together with a table with some additional relevant information is shown in Figure (6.1). The Cartesian grid used for the computations consists of 120 cells in axial direction and 64 cells in the radial direction. A local time-stepping algorithm for the gas phase as well as for the dispersed phase was used to determine the time step used in each cell [114, 118]. For the dispersed phase, 5 particles per class per cell were used and 13 droplet classes were considered. An iteration averaging scheme [117] was used to reduce the statistical error, which allowed us to use this very low value for the number of particles per class per cell. Typical computation times for these simulations are less than a day and a stationary solution in an iteration averaged sense was obtained after approximately 20,000 iterations.

6.2 Results and discussion

Four simulations were performed to investigate the influence of the different two-way coupling terms:

(a) A simulation without any two-way coupling was performed as a reference.

(b) A simulation taking into account only the two-way coupling effects in the transport equation for momentum.

(c) A simulation taking into account the two-way coupling effects in the transport equation for momentum, dissipation and Reynolds stresses (called full coupling in the legend).

(d) A simulation similar to the previous simulation (full coupling), but additionally taking into account the source term appearing in the model for the pressure rate of strain.

The numerical results at four axial locations downstream of the injector will be discussed, i.e. at $x = 40$, $x = 80$, $x = 160$ and $x = 320$ mm downstream of the injector, which corresponds to 5, 10, 20 and 40 injector diameters.

6.2.1 Results for the dispersed phase

We first discuss some numerical results for the dispersed phase. In the simulation results shown, all two-way coupling source terms were taken into account (case *(d)*, including the extra source terms in the model for the pressure rate of strain). Figure (6.2) shows the mean axial velocity of the dispersed phase U_{p} for three droplet size classes at four locations downstream from the injector. The axial velocity is only slightly underpredicted, and the agreement with the experimental data is very good. The root mean square (rms) of the Reynolds stresses $\sqrt{\widetilde{u''_{\mathrm{p}}u''_{\mathrm{p}}}}$ and $\sqrt{\widetilde{v''_{\mathrm{p}}v''_{\mathrm{p}}}}$ are shown in Figures (6.3) and (6.4) respectively. The rms values of the Reynolds stresses of the dispersed phase are slightly overpredicted in the first two downstream locations. Further downstream $\sqrt{\widetilde{u''_{\mathrm{p}}u''_{\mathrm{p}}}}$ is slightly underpredicted, but we still overpredict the value of $\sqrt{\widetilde{v''_{\mathrm{p}}v''_{\mathrm{p}}}}$. However, the discrepancy is not very large and there is still a good agreement with the experimental data.

The size classes shown in the figures are the size classes $40-50\mu m$, $70-80\mu\mathrm{m}$ and $100-110\mu\mathrm{m}$. The size classes between $40-100\mu\mathrm{m}$ contribute the most to the two-way coupling source term. The larger size classes will also be less influenced by changes in the continuous phase, and the different two-way coupling models will have only a small effect on the dispersed-phase properties. The velocity of the smallest droplet size class will quickly relax to the velocity of the continuous phase

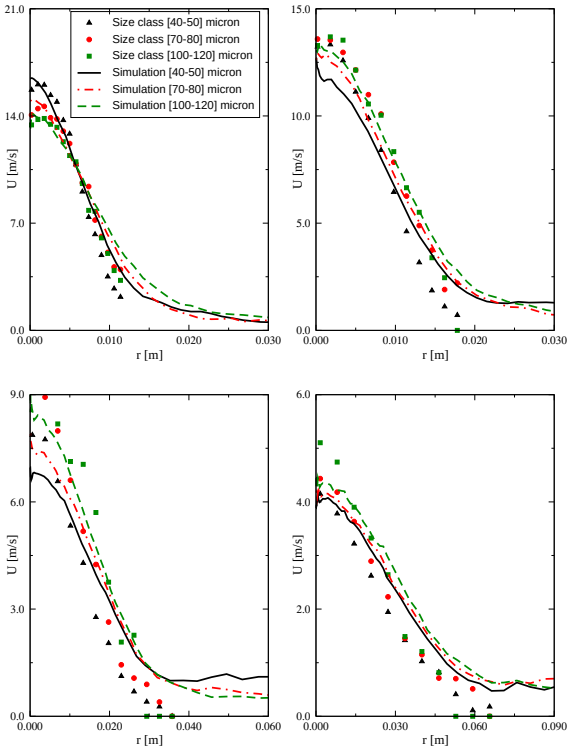

Figure 6.2: Axial velocity of the dispersed phase $\widetilde{U}_{\mathrm{p}}$ at locations $x = 40$, $x = 80$, $x = 160$, $x = 320$ mm downstream of the inlet for case *(d)*.

and the particles will then more or less follow the fluid flow. This size class will be affected the most by changes in the continuous phase, but these small particles will also have a negligible contribution to the two-way coupling source term. Since the largest droplet classes are the least affected by the surrounding gas flow, the discrepancy between the experimental and numerical results for the dispersed-phase Reynolds stresses may well be caused by modelling issues in the dispersed phase only. Since the performance analysis of the dispersion model is not the focus of this chapter, we will therefore now focus our analysis on the results of the continuous phase.

6.2.2 Results for the continuous phase

Figure (6.5) shows the axial velocity of the continuous phase for the four different simulations. For comparison, the experimental results of the single-phase test case was added to the graph as well. In the simulation without two-way coupling, the continuous phase is not influenced by the presence of the particles. This axial velocity profile quickly relaxes to the experimentally measured axial velocity profile

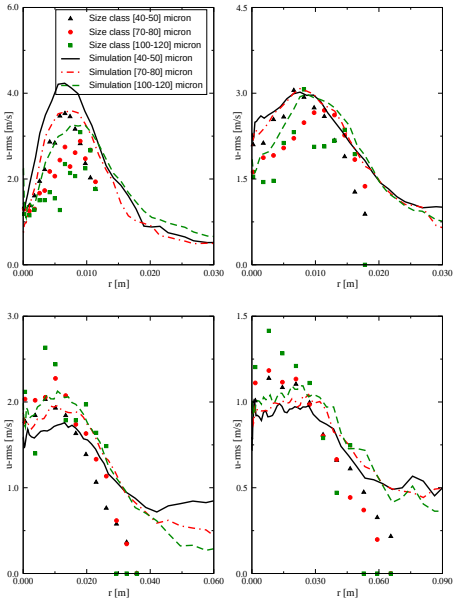

Figure 6.3: Rms of Reynolds stress $\sqrt{\widetilde{u_{\mathrm{p}}'' u_{\mathrm{p}}''}}$ at locations $x = 40$, $x = 80$, $x = 160$, $x = 320$ mm downstream of the inlet for case *(d)*.

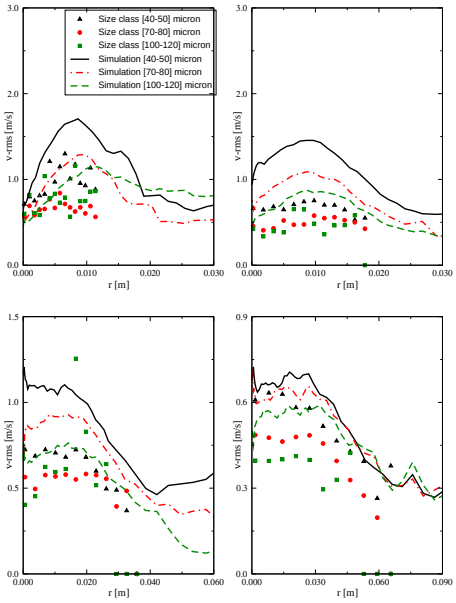

Figure 6.4: Rms of Reynolds stress $\sqrt{\widetilde{v_{\mathrm{p}}'' v_{\mathrm{p}}''}}$ at locations $x = 40$, $x = 80$, $x = 160$, $x = 320$ mm downstream of the inlet for case *(d)*.

of the single-phase flow. Only adding the two-way coupling source terms in the momentum equation is not sufficient to get a good correspondence with the measurements. When taking into account the two-way coupling source terms in the Reynolds stress equations and the dissipation equation (full coupling), the axial velocity downstream of the injector is now slightly underpredicted. When taking into account the extra particle source terms in the model for the pressure rate of strain, the prediction of the axial velocity of the gas phase improves slightly.

Larger difference can be observed in the profiles for the rms values of the normal Reynolds stresses $\sqrt{\widetilde{u''u''}}$ and $\sqrt{\widetilde{v''v''}}$, shown in Figures (6.6) and (6.7) respectively. We can again see that without two-way coupling the Reynolds stress profiles relax to the experimental values of the single-phase jet. Adding two-way coupling in the momentum equation only is not sufficient to improve the predictions of the Reynolds stresses, but full two-way coupling improves the results at all downstream locations. The performance difference between model *(c)* and model *(d)* is not clear from Figures (6.6) and (6.7), but model *(d)* tends to decrease the Reynolds stress anisotropy compared to model *(c)*. Further downstream the effect of the source term in the pressure rate of strain decreases (as the turbulence becomes more isotropic) and the difference between simulations *(c)* and *(d)* becomes smaller. For the rms values of the Reynolds stress component $\sqrt{\widetilde{v''v''}}$ shown in Figure (6.7) the experimentally measured profile at $x = 40$ mm has higher values at the symmetry axis than $\sqrt{\widetilde{u''u''}}$. When no two-way coupling effects are present, the experimental value of $\sqrt{\widetilde{v''v''}}$ is higher than that of the experiment with $\phi = 0.73$ in this figure. The two-way coupling effects cause a reduction of the rms of Reynolds stress $\sqrt{\widetilde{v''v''}}$. The simulation with no coupling also predicts higher values of $\sqrt{\widetilde{v''v''}}$ than the simulations with two-way coupling. However, models *(c)* and *(d)* underpredict the value of the Reynolds stress. This could indicate an overprediction of the magnitude of the source term for the transport equation of $\sqrt{\widetilde{v''v''}}$. Further downstream we see that both models *(c)* and *(d)* are able to capture the correct behaviour of $\sqrt{\widetilde{v''v''}}$ and there is good agreement with the experimental results. The values for the shear stress $\sqrt{\widetilde{u''v''}}$, which is shown in Figure (6.8), are overpredicted near the injector, but further downstream there is good agreement between the experimental data and the predictions from the simulations for all three two-way coupling models.

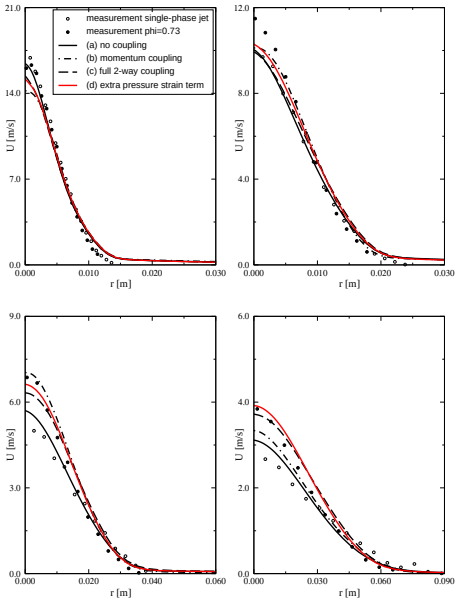

Figure 6.5: Axial velocity of the gas phase $\widetilde{U}$ at locations $x = 40$, $x = 80$, $x = 160$, $x = 320$ mm downstream of the inlet.

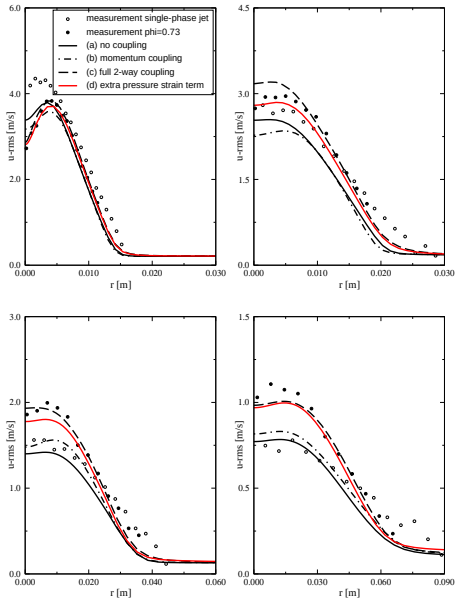

Figure 6.6: Rms of Reynolds stress $\sqrt{\widetilde{u''u''}}$ at locations $x = 40$, $x = 80$, $x = 160$, $x = 320$ mm downstream of the inlet.

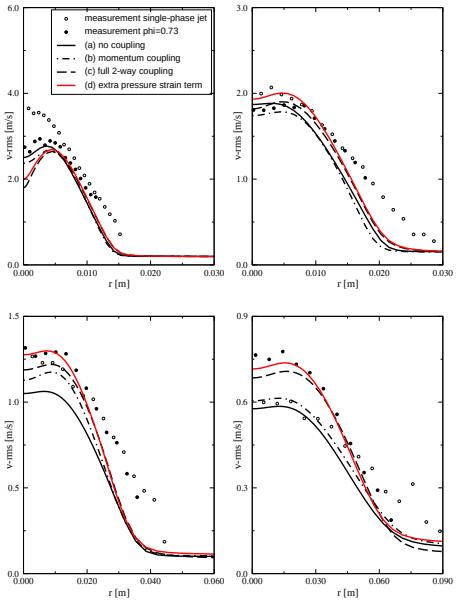

Figure 6.7: Rms of Reynolds stress $\sqrt{\widetilde{v''v''}}$ at locations $x = 40$, $x = 80$, $x = 160$, $x = 320$ mm downstream of the inlet.

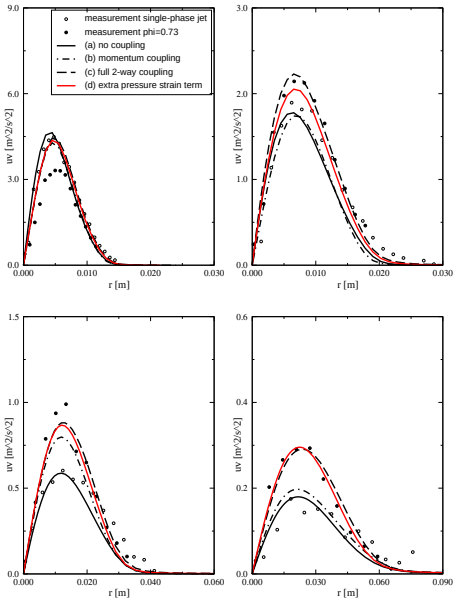

Figure 6.8: Reynolds stress $\sqrt{\widetilde{u''v''}}$ at locations $x = 40$, $x = 80$, $x = 160$, $x = 320$ mm downstream of the inlet.

6.3 Conclusions

In this chapter the dispersed phase model discussed in chapter 5 and the RANS approach for the continuous phase discussed in chapter 3 were used to obtain numerical results for a turbulent non-evaporating spray. A modified Reynolds stress model for dispersed two-phase flows was used that takes into account the modification of the pressure rate of strain due to the presence of the dispersed phase.

A simulation of a polydispersed two-phase flow was performed to investigate the importance of the different two-way coupling terms appearing in the Reynolds averaged transport equations.

For this particular test case, taking into account the particle source term in the model for the pressure rate of strain leads to a small improvement of the predictions of the gas-phase properties. The importance of this source term will however become more significant in flows with a higher fluid-particle anisotropy.

The determination of more optimal constants for the source term appearing in the model for the pressure rate of strain, is open for future research.

CHAPTER 7

Simulation of a turbulent spray flame with two-way coupling

This chapter deals with the numerical simulation of a turbulent nonpremixed methanol spray flame, with emphasis on the investigation of the importance of taking into account the different two-way coupling terms. The calculations performed are compared with each other and with an experiment described by Karpetis and Gomez [73, 74, 75]. After a short review on available spray flame experiments, the setup of the spray experiment of Karpetis will be discussed, the numerical setup is described and numerical simulations are presented.

7.1 Introduction

The numerical simulation of turbulent spray flames is still a very challenging problem, but due to the increase in computational power and the implementation of new numerical algorithms it has now become at least practically possible to numerically investigate a turbulent burning spray. Detailed DNS and LES studies of reacting dispersed two phase flows [135] have yielded many insights into flame structures and burning behaviour in spray flames, and RANS and PDF methods have advanced in the last decade towards a level that allows for accurate and detailed modelling of spray flames, taking into account many features that were not feasible in the early days of turbulent spray simulations 20 years ago.

In this study we will focus on the modelling of a spray flame using the hybrid PDF approach discussed in previous chapters. This approach has already been used for some time in the numerical modelling of single phase turbulent reacting flows [72, 113, 117, 128, 180].

Several reviews about spray combustion phenomena, including evaporation, mixing, transport and atomisation can be found in the literature [16, 49, 50, 51, 92] and the reader is referred to these papers for a more complete overview of spray combustion research prior to 1995. Some recent experimental and numerical results will be discussed now.

Successful simulations of vaporising sprays have been reported in the literature, most of them devoted to simulating the vaporising isopropyl-alcohol spray of Sommerfeld and Qiu [153]. We will refer here to the simulation results performed by [83, 152] and [141] and [12, 117] where generally a good agreement with experimental data was found in the studies.

Less numerical studies have been reported on burning sprays. This has three main reasons. First of all, the complexity of the simulation is such, that it will take a considerable amount of time to develop a computer code to solve the governing equations. Furthermore, the computational capabilities of computers only recently allows us to simulate a burning spray with enough details to be scientifically valuable. Finally, experimental data from burning sprays, suited for simulation purposes, are scarce and most often only concern a limited subset of physical properties. This last point makes the interpretation of some of the numerical results and the comparison with experimental results more difficult or questionable since too many degrees of freedom exist in setting up the numerical simulations. Even with experimental data available, caution should be applied when comparing experimental results with simulation results, since both represent a different view on physical 'reality'.

In the 1980's, simulations of turbulent reacting sprays were restricted by computational power to Locally Homogeneous Flow simulations (LHF) [49]. In LHF simulations, the gas and dispersed phase are assumed to be in dynamic and thermodynamic equilibrium, i.e. the dispersed phase acts as ideal tracer particles of the flow. No two-way coupling effects were taken into account and the only 'interaction' was the addition of fuel vapour to the gas phase. These simulations were compared to experimental data of 'ultra-dilute' sprays [147] where interaction effects were minimal. In later years, Stochastic Separated Flow (SSF) analysis was used, in which the dispersed phase was simulated using a Lagrangian approach. Two way coupling effects were taken into account in this approach. When the interaction between the dispersed phase and the fluid phase turbulence was completely ignored, the method was called Deterministic Separated Flow (DSF) analysis [50].

Recently, Ge [58] used a PDF approach to simulate the methanol spray flame of McDonell and Samuelsen [103] and the ethanol spray flame of Duwel *et al*. [45]. In his simulations flamelets based on counterflow spray diffusion flames are used. This work is closely connected to the work performed by Gutheil and Sirignano on the modelling of counterflow diffusion sprays [62, 69]. Furthermore, a modification of the Lagrangian mixing model similar to the model presented in chapter 4 of this thesis was presented and its effects on the shape of the mixture fraction pdf was investigated.

Joint PDF modelling of a turbulent spray flame was also presented by Rybakov and Maas [140].

Sadiki *et al*. [141] describe simulation results based on the testcases of Wittig *et al*. [82], which consists of a cylindrical combustor where swirled air enters the combustion chamber through a swirler and liquid dodecane is injected into the combustion chamber from axially located nozzles. The vaporising isopropyl spray of Sommerfeld [153] was also simulated in the same paper. The approach used by Sadiki *et al*. consists of an Eulerian-Lagrangian approach, where the gas

phase properties are treated in an Eulerian way by solving the RANS equations using a Finite Volume solver. The dispersed phase is solved using a Lagrangian method with the vaporisation models of Abramzon and Sirignano [1] and the non-equilibrium model of Miller *et al*. [108]. A better agreement with the experimental data of Sommerfeld was found using the latter model.

Experimental data for kerosene spray flames are also reported in the literature [46, 63, 134, 154], because of their practical application in jet engines. The modelling of this complex fuel poses an extra difficulty and is a challenge left for future research. Pichard et al. [125] have studied partially prevaporised spray flames of n-heptane using PDA to measure the droplet velocity and diameter and planar laser induced fluorescence (PLIF) to obtain information on the mean progress variable.

We will now mention some experimental studies suited for CFD modelling purposes before proceeding to the description of the experiment that is being studied in the remaining part of this chapter.

Widmann and Presser [132, 173, 174, 175] study a hollow cone turbulent methanol spray in a weakly swirling coflow. The gas phase axial, radial and tangential flow velocities were measured using a Particle Image Velocimetry (PIV) system, and the axial and radial particle velocities and the droplet diameter were measured using Phase Doppler Interferometry (PDI). It was not possible to measure the gas phase velocity in the spray region close to the injector, leaving some room for the creativity of the numericist. Near the injector the local gas phase velocities are low and the spray is injected with high velocities ($U_{\mathrm{p}} = 20\frac{m}{s}$), leading to strong two-way coupling effects near the injector. The mass flow rate in their experiments was 0.833 $\frac{g}{s}$. A kerosene spray flame was also investigated [134], and the effects of different fuels on the structure of spray flames was reported in [133]. Simulation results for the dispersed phase properties were presented by Zuo *et al*. [191] and by Giridharan *et al*. , [59]. Recently, in a short technical note about the methanol spray flame database from NIST, some simulation results for the dispersed phase are reported [132]. In another recent publication, de Jager [37] presented simulation results on the gas phase velocities (as well as dispersed phase velocities) obtained using an Eulerian-Eulerian approach, showing a disagreement between the measured and the simulated gas phase axial and radial velocity.

McDonell and Samuelsen [100, 101, 102, 103] study a methanol spray under many different conditions, including swirling and non-swirling conditions and reacting and non-reacting (but still vaporising) and with and without the presence of the dispersed phase. Phase Doppler-Interferometry (PDI) is used to measure gas phase velocities as well as dispersed phase velocities and droplet diameter. The gas phase velocities are measured by seeding the air stream with small particles. The mass flow rate in their experiments is 1.32 $\frac{g}{s}$.

Karpetis [73] and Karpetis and Gomez [74, 75] also study a methanol spray, but they do not have a swirling flow and the relative velocity between the particle

phase and the continuum phase is smaller. The two-way coupling effects are less strong, but still significant. In their experiment, they measure the droplet velocities and diameter with a PDA system. The velocities of the smallest droplets are used to represent the gas phase velocity. Additionally, they have measured the gas phase temperature using Raman spectroscopy. The experiments were done at two different mass flow rates, namely 0.085 $\frac{g}{s}$ and 0.05 $\frac{g}{s}$.

Stårner and Masri [137] on the other hand study an acetone spray flame, which has almost the same index of refraction and density as methanol. Their purpose was to investigate the effect of different vaporisation and burning properties on the flow properties of a burning spray. They have reported experimental data for the dispersed phase using a PDA setup.

In this chapter we study the importance of vaporisation modulation and particle turbulence interaction in a dilute methanol spray flame. Particularly, we will compare the simulation results with the experimental results of Karpetis [73]. This spray configuration has not been investigated numerically yet. First, the experimental testcase is presented, followed by the numerical setup of our simulations. The simulation results of the continuous phase are discussed in section 7.3 and the dispersed phase results are presented and discussed in section 7.4.

7.2 Presentation of the test case

7.2.1 Description of the experiment

A turbulent methanol spray flame under conditions similar to those measured experimentally in the experiments of Karpetis and Gomez [73, 74, 75] has been numerically simulated. This experiment will be referred to as the Karpetis spray. A sketch of the experimental configuration with the numerical domain can be found in Figure (7.1). The spray flame is of the non-premixed type. Experimental conditions for two spray flame measurements can be found in table (7.1). In table (7.1), $\dot{Q}_{\mathrm{g}}$ is the volumetric flow rate of the air and $\dot{m}_{\mathrm{p}}$ the liquid mass flow rate. The mass based equivalence ratio ϕ is defined as

$$\phi = \frac{\dot{m}_{\mathrm{p}}/\dot{m}_{\mathrm{g}}}{(\dot{m}_{\mathrm{p}}/\dot{m}_{\mathrm{g}})_{\mathrm{sto}}}, \tag{7.1}$$

where subscript sto refers to stoichiometric conditions. This nondimensional parameter is used in [75] to characterise the nondimensional flame height. The Reynolds number mentioned is based on the cold flow conditions. Re' is based on the velocity variance and the macroscopic lengthscale at cold conditions. Finally, η is the Kolmogorov length scale, which was estimated using $\eta = Re'^{-\frac{3}{4}}D$.

The spray with the highest liquid droplet mass flow rate (flame I, $\dot{m} = 0.085$ g/s) was simulated. Figure (7.1) shows the computational domain used and the location of the measurement sections. Measurements were performed at $x = 0.1D$,

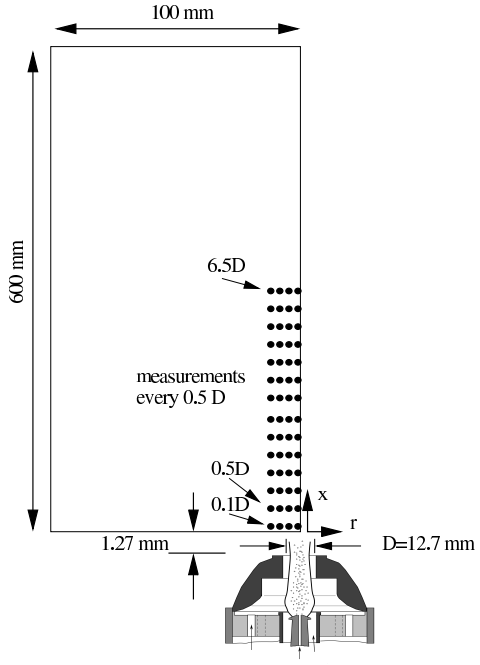

Figure 7.1: Sketch of the experimental configuration including the numerical domain used (with kind permission of A. Karpetis).

Flame	**I**
Mass flow rate gas $\dot{Q}_{\mathrm{g}}\left[\frac{1}{\mathrm{min}}\right]$	**80**
Mass flow rate liquid $\dot{m}_{\mathrm{p}}\left[\frac{g}{\mathrm{s}}\right]$	**0.085**
Equivalence ratio ϕ [-]	**0.35**
Flame length l_{flame}/D [-]	**10**
Reynolds number Re [-]	**21,000**
Reynolds number Re' [-]	**2500**
Kolmogorov scale $\eta[\mu\mathrm{m}]$	**36**

Table 7.1: Experimental conditions for one of the spray flames investigated by Karpetis and Gomez [73] (spray flame I).

$x = 0.5D$ and at every half burner diameter D ($D = 12.7$ mm) thereafter, up to $x = 6.5D$. Phase Doppler Anemometry (PDA) was used to obtain the first and second moments of gas and droplet velocities, the droplet number density N_{p} and droplet diameter d_{10}. Results for three different size classes, together with the mean results, are available. The gas velocity statistics were calculated by considering all droplets smaller than 8 μm as tracer particles of the gas flow. It is mentioned in [75] that tests where either 6 μm or 12 μm was used as an upper limit for the tracer size class yielded minimal differences in the velocity and velocity correlations attributed to the gas phase. In addition to the PDA measurements, Raman Spectroscopy was used to measure mean gas temperature T and rms of temperature fluctuations $\sqrt{\widetilde{T''T''}}$.

7.2.2 Simulation setup

Since the first measurement location is at 0.1D (1.27 mm) downstream of the injector, the inlet boundary for the computational domain starts at $x = 1.27$ mm and extends up to $x = 600$ mm. A two-dimensional cartesian grid, stretched in both axial and radial directions, is used. The total number of cells used was 170 cells in axial

direction and 80 cells in radial direction. The smallest cell size at $(x, r) = (1.27, 0.0)$ was 0.5×0.5 mm, which allowed for a sufficiently high resolution to capture the profile of the dispersed phase properties.

The spray radius at the inlet plane is $r = 3.5$ mm and the dispersed phase inlet covers only 7 cells.

The inlet profile for dissipation can be constructed by reducing the transport equation for turbulent kinetic energy to a production-dissipation balance. When two-way coupling effects are included, the equation reduces to:

$$\overline{\rho}\epsilon = \overline{\rho}\widetilde{u_i''u_j''}\frac{\partial \widetilde{U}_i}{\partial x_j} + \left\langle \mathcal{S}^{(I_\mathrm{k})}_{u_k u_k} \right\rangle + \left\langle u''_{I_\mathrm{k},k} u''_{I_\mathrm{k},k} \mathcal{S}^{(I_\mathrm{k})}_{m} \right\rangle. \tag{7.2}$$

Near the injector, the dissipation profile is then almost entirely governed by the two-way coupling term $\left\langle \mathcal{S}^{(I_\mathrm{k})}_{u_k u_k} \right\rangle$ and for the creation of an inlet profile for dissipation in dispersed two-phase flows, this source terms is the dominant term. In the discussion of the fluid phase results, the effects of the modification of the inlet conditions for turbulence dissipation will be briefly discussed.

Since mean temperature and temperature variance profiles are also available at the inlet, part of the droplets must already have evaporated. The configuration of the injector (see Figure (7.1)) makes this possible. An inlet profile for the independent scalar (mixture fraction and its variance) is needed.

The first approach was to construct the mixture fraction profile $\widetilde{Z}$ at the inlet in such a way as to match the inlet temperature profile. The temperature variance is assumed to depend only on the variance in mixture fraction, although variations in strain rate may have a significant effect on the temperature variance. A Gaussian distribution can be used to initialise the Monte Carlo particles in such a way that the mean inlet temperature and temperature variance profiles matched the measured temperature and variance. However, as will be discussed in section 7.3.1, this may not be the best choice of inlet profile. Instead, it is assumed that the carrier gas coming directly out of the injector contains already a small amount of vaporised fuel gas. The mixture fraction Z is imposed homogeneously over all the computational gas particles in the cells near the inlet. It is also assumed that some mixing has already occurred and that the mixture fraction in the outer cells is lower than the mixture fraction at the centreline.

7.2.3 Tabulated chemistry approach

A flamelet lookup table is used to obtain the thermochemical properties of the gas phase as a function of the mixture fraction Z and strain rate a, see Figure (7.2). The flamelet table was generated using the methanol mechanism of Lindstedt and Meyer [94] and the programs CHEM1D (Eindhoven university) and FLAME (Delft university). In general, the strain rate is an independent variable, but in the simulations presented here, the strain rate used was set to a constant value of $a = 100\frac{1}{s}$.

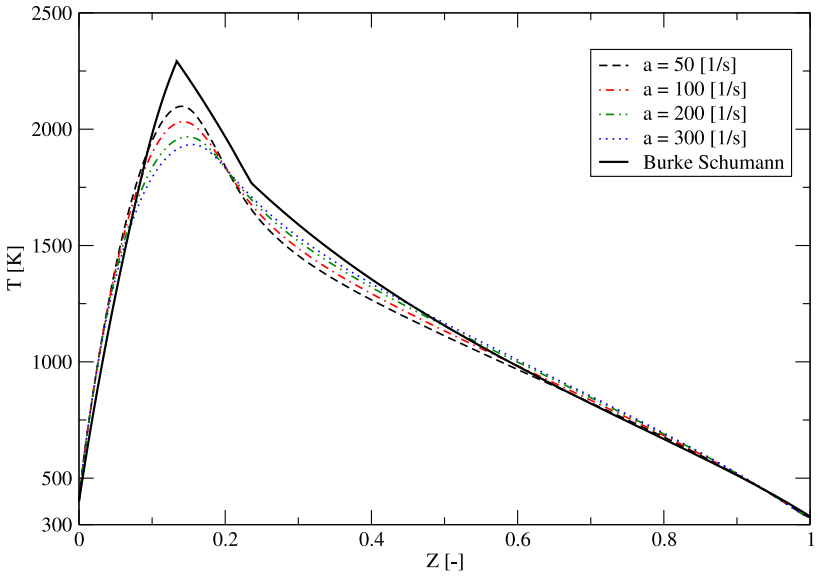

Figure 7.2: Temperature as function of mixture fraction for different strain rates. Burke-Schumann flame sheet is added for comparison.

The enthalpy of the evaporated methanol fuel entering the gas phase is assumed to correspond to the enthalpy at a wet bulb temperature of $T_{\text{wb}} = 335K$, which is slightly below the boiling temperature of liquid methanol ($T_{\text{boil}} = 338K$). Near the spray injector, droplets may have vaporised before having reached the wet-bulb temperature. However, the difference in enthalpy ($-6.26 \cdot 10^6 \frac{J}{kg}$ for methanol at 300K versus $-6.21 \cdot 10^6 \frac{J}{kg}$ for methanol at 330K) is small enough to neglect. The initial temperature of the gas phase was assumed to be $400K$ and the initial pressure 1 atm. Karpetis [73] recalls that the Raman spectrometry used to measure temperature is not accurate for low temperatures ($T_{\text{g}} < 600$K). However, the measured 400 K seems a better starting point then inlet conditions at room temperature due to the large heat release of the spray flame.

The Lagrangian mixing model used in the simulations was the Interaction by Exchange with the Mean (IEM) mixing model.

7.2.4 Dispersed phase

For the dispersed phase, experimental data on several droplet size classes were available. Data on three droplet size classes have been processed for simulation purposes, which are the size classes 20, 40 and 60 μm, with bandwidths of $\pm 2\mu$m.

The droplet size class [0-8] μm which was used to characterise the gas phase has been used to initialise the smallest droplet size class in the simulations. 9 droplet size classes were used in the simulations. The first two size classes are [0-8] and [8-15] μm, the other classes each have a bandwidth of 10 μm, starting from [15-25] and ending with [75-85] μm. The total liquid mass flux, which can usually be measured directly with a mass flow meter with high accuracy, can also be retrieved by integration of the velocity and droplet number density over the inlet area. Usually, the integrated liquid mass flux is lower than the exact liquid mass flux, because not all droplets are taken into account in the measurements. Especially with high droplet number densities, the discrepancy can be significant [174]. The small discrepancy encountered in these measurements are corrected by multiplying the volume fraction profiles for the different droplet classes in such a way, that the profile for mean inlet droplet diameter is not altered, the droplet number density profile is not increased too much and the integrated liquid mass flux matches the directly measured mass flux.

The liquid droplets have an initial temperature of $T_{\mathrm{p}} = 298$ K, which is imposed on all droplets entering the computational domain. The droplet temperature is not allowed to exceed the boiling temperature of liquid methanol. 30 computational gas-phase particles per cell were used and 5 computational liquid-phase particles per class per cell were used (which means a total of 45 computational liquid-phase particles per cell). Numerical simulations with 25 computational gas particles and 3 computational droplets per class were compared with simulations where 50 gas particles and 6 droplets per class were used. The difference between these simulations was small. Iteration averages are used to decrease statistical errors. The iteration averaging method described by Naud [117] was used. Iteration averages were obtained starting with averaging over 500 iterations and then increasing the number of iterations by 100 until iteration averaging was performed over 2000 iterations. So during the first 2600 iterations, iteration averaging was performed over 500,600,700 and 800 iterations.

A local timestepping method [114] was used for the gas phase and the liquid phase with timesteps between $\Delta t = 1.0 \cdot 10^{-3} s$ and $\Delta t = 1.0 \cdot 10^{-8} s$.

The total number of timesteps used was 20,000, which took approximately two days on a 3 GHz 64 bit single processor.

7.3 Results for the continuous phase

In this section all continuous phase results are presented. In each of the figures, the radial profiles at 4 different axial locations downstream of the injector are shown. The first radial profile shown at $0.1D$ are the imposed inlet conditions and are shown in order to get a better impression of the evolution of the flow properties. The measurements of the smallest droplet size class are used here to represent the gas phase and are indicated in the graphs by solid dots. All simulation results are

Case	Source terms	interface velocity
(a)	[-]	[-]
(b)	$\mathcal{S}_{U_i}, \mathcal{S}_{u_i u_j}, \mathcal{S}_\epsilon$ $\mathcal{S}_m, U_{\mathrm{p},i}\mathcal{S}_m, u_i'' u_j'' \mathcal{S}_m, \mathcal{S}_{\epsilon_m}$	Crowe
(c)	$\mathcal{S}_{U_i}, \mathcal{S}_{u_i u_j}, \mathcal{S}_\epsilon$ $\mathcal{S}_m, U_{\mathrm{p},i}\mathcal{S}_m, u_i'' u_j'' \mathcal{S}_m, \mathcal{S}_{\epsilon_m}$	Ahmadi *et al*.
(d)	$\mathcal{S}_{U_i}, \mathcal{S}_{u_i u_j}, \mathcal{S}_\epsilon, \Pi_{ij}^{(\mathrm{fp})}$ $\mathcal{S}_m, U_{\mathrm{p},i}\mathcal{S}_m, u_i'' u_j'' \mathcal{S}_m, \mathcal{S}_{\epsilon_m}, \Pi_{ij}^{(m)}$	Crowe

Table 7.2: The source terms that are taken into account in the different simulations.

depicted by lines. The effects of two-way coupling on the continuous phase results is shown first. Each plot contains four lines representing different settings for the two-way coupling models. The solid line represents the simulation results without any two-way coupling (case (a)). The dashed line represents the simulation results with two-way coupling in the momentum equation, the Reynolds stress equation and the equation for turbulence dissipation (case (b) and case (c)), for both the presence of the particles as mass transfer source terms. The difference between models (b) and (c) is that in model (b), the two-way coupling source terms $\langle \mathcal{S}_{u_i u_j} \rangle$ are evaluated according to the analysis of Ahmadi *et al*. , explained in section 3.4.1, and in model (c), the velocity of the fluid at the interface is determined using the analysis of Crowe, which was explained in the same section.

The correction to the pressure rate of strain presented in chapter 3 is included in case (d). The conditions for the different cases are presented in table (7.3). For all cases, the inlet profile for turbulence dissipation was modified by the presence of the liquid phase using equation (7.2). For the case without two-way coupling, this was not possible as the increase in turbulence dissipation leads to Reynolds stress values close to zero, causing numerical stability issues to occur. Therefore the inlet profile for dissipation was not altered due to two-way coupling in case (a).

When the source terms for mass transfers are used, the pressure correction algorithm (PISO) [121] is modified by these source terms to correctly take into account the momentum transfer due to vaporisation.

In Figure (7.3), the radial profiles of axial velocity $\widetilde{U}_\mathrm{f}$ are shown. The velocity profiles have a typical bell-shape with a centreline velocity that is decreasing with axial distance from the injector. Close to the injector there is a marked depression near the centreline. This depression slowly diminishes further downstream and it has disappeared completely at $x = 2D$. The computed axial velocity profiles all show a reasonable agreement with the experimentally measured values. The axial velocity at the symmetry axis is however overpredicted by all simulations that include two-way coupling. The axial velocity of the liquid phase is lower than the axial velocity of the gas phase, so including the source terms $\mathcal{S}_{U_i}^{(I)}$ will lead

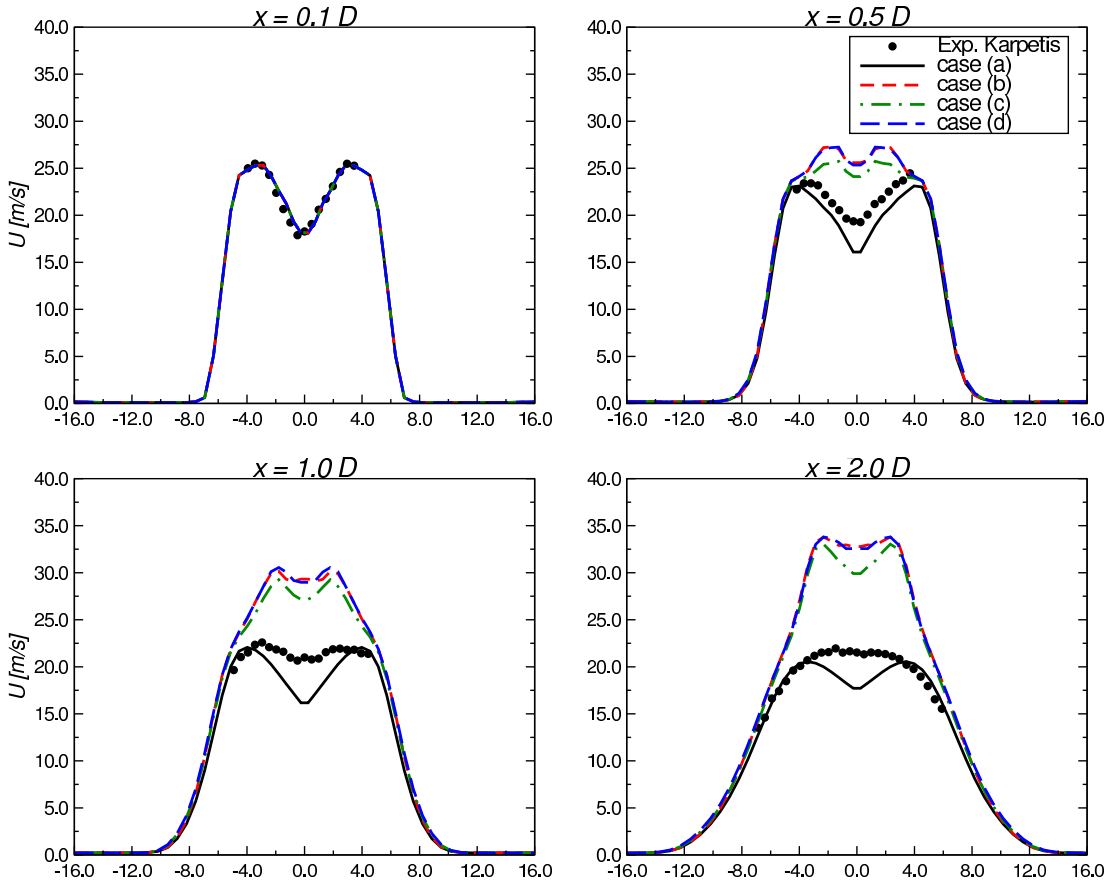

Figure 7.3: Radial profiles of mean gas phase axial velocity $\widetilde{U}_{\mathrm{f}}(r)$. Symbols: experimental data of smallest droplets. Lines: simulation data.

to a lower value of axial velocity (and will in fact *underpredict* the axial velocity) at the centreline, where the highest droplet number density occurs. This effect is (over)compensated by the source term for mass transfer through the modification of the pressure and by satisfying the continuity equation (the pressure correction algorithm). A correction factor to the drag coefficient in case of vaporising droplets was proposed by Chiang [14] and discussed in section 5.4.1, together with corrections for the Nusselt and Sherwood number. The correction to the drag coefficient is implemented by using the Schiller-Naumann correlations on the right hand side of eq. (5.22) and the Ranz-Marshall correlations for the Nusselt and Sherwood numbers are replaced by eq. (5.24, 5.25). The simulation results for the axial velocity of the gas phase including these correction factors are shown in Figure (7.4). The numerical results show a significant improvement of the predictions of the axial velocity when compared to the results shown in Figure (7.3). The axial velocity is much lower and shows a good agreement with the experimentally measured

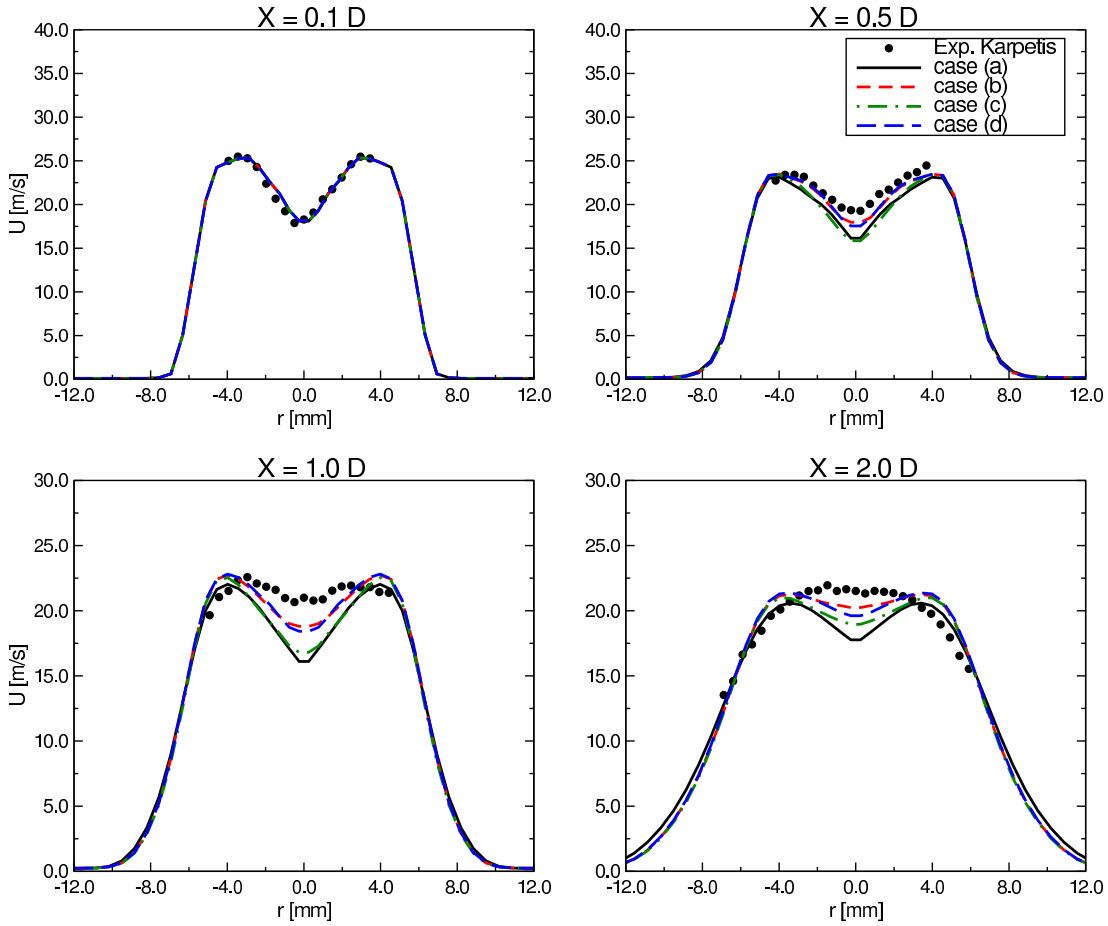

Figure 7.4: Radial profiles of mean gas phase axial velocity $\widetilde{U}_{\mathrm{f}}(r)$. Symbols: experimental data of smallest droplets. Lines: simulation data.

axial velocity profiles at all downstream axial locations. The two way coupling source terms $\mathcal{S}_{U_i}$ and $U_{\mathrm{p},i}\mathcal{S}_m$ in the momentum equation and $\mathcal{S}_m$ in the pressure correction equation balance each other and the net effect is very small compared to case (a), where no two way coupling source terms were taken into account. A small improvement can be observed when two way coupling is taken into account.

From this point on, the simulation results *including* the correction factors of Chiang will be shown and discussed.

Figure (7.5) shows the gas phase radial velocity $\widetilde{V}_{\mathrm{f}}$. The radial velocity shows a steep linear increase with radial distance from the centreline. Further downstream, the linear increase slowly weakens. The experimentally observed values for the radial velocity remain much higher than the numerical results and especially downstream of the injector the discrepancy between numerical and experimental results remains large. From the numerical simulations it is clear that the details of the two-way coupling terms have little to no effect on the mean axial and

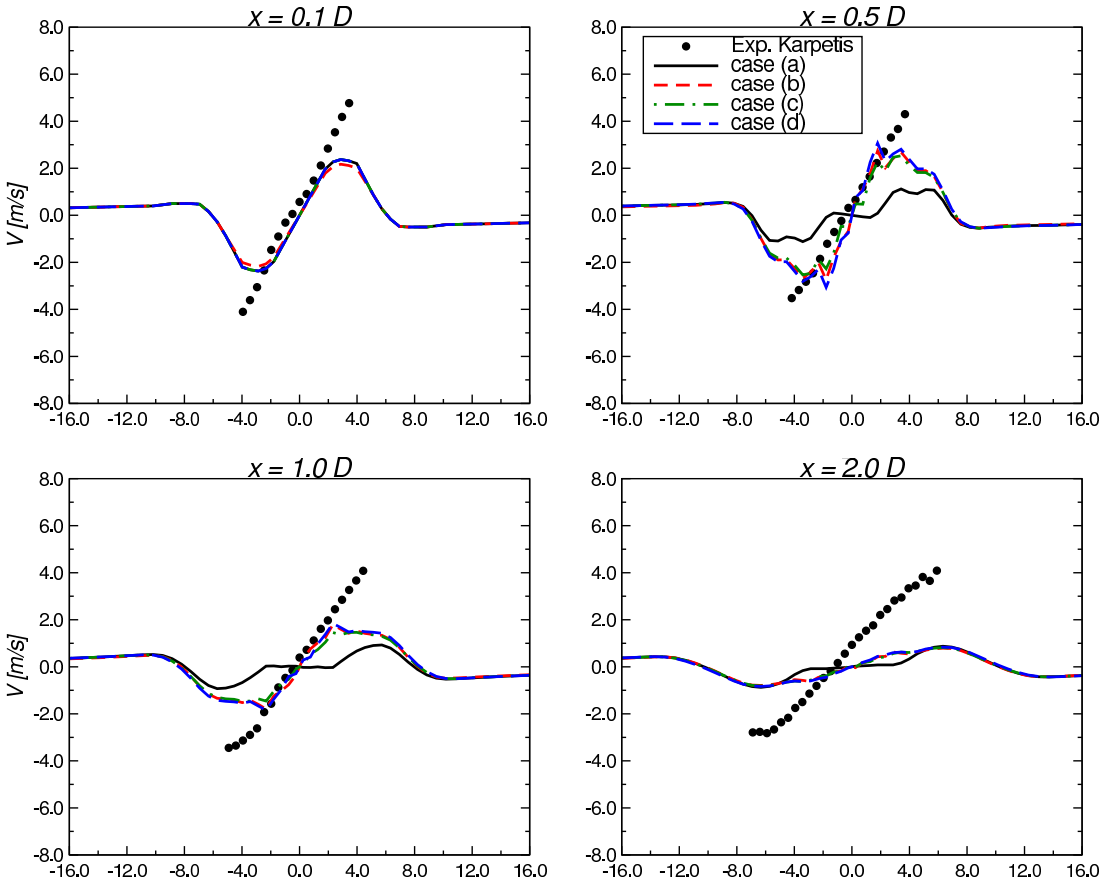

Figure 7.5: Radial profiles of mean gas phase radial velocity $\widetilde{V}_{\mathrm{f}}(r)$. Symbols: experimental data of smallest droplets. Lines: simulation data.

radial velocity profile. A different explanation for the bad predictions of the radial velocity has to be found.

Radial gas phase velocity results: analysis of the suitability of vaporising droplets as tracer particles. The simulated results for radial velocity profiles shown in Figure (7.5) do not agree well with the experimentally measured values. In the experiment, the radial velocity shows a linear behaviour with a very steep slope. This radial velocity is more typical for ballistic particles than for a gaseous flow. The radial velocity of the continuum phase is able to follow the experimentally observed velocity profile close to the centreline but drops to much lower values for larger radial distances.

An explanation for this discrepancy is that the droplet size class used to represent the gas phase (the [0-8] μm droplets) is not a good indicator for the radial velocity of the actual gas phase away from the centreline. Figure (7.6) shows a

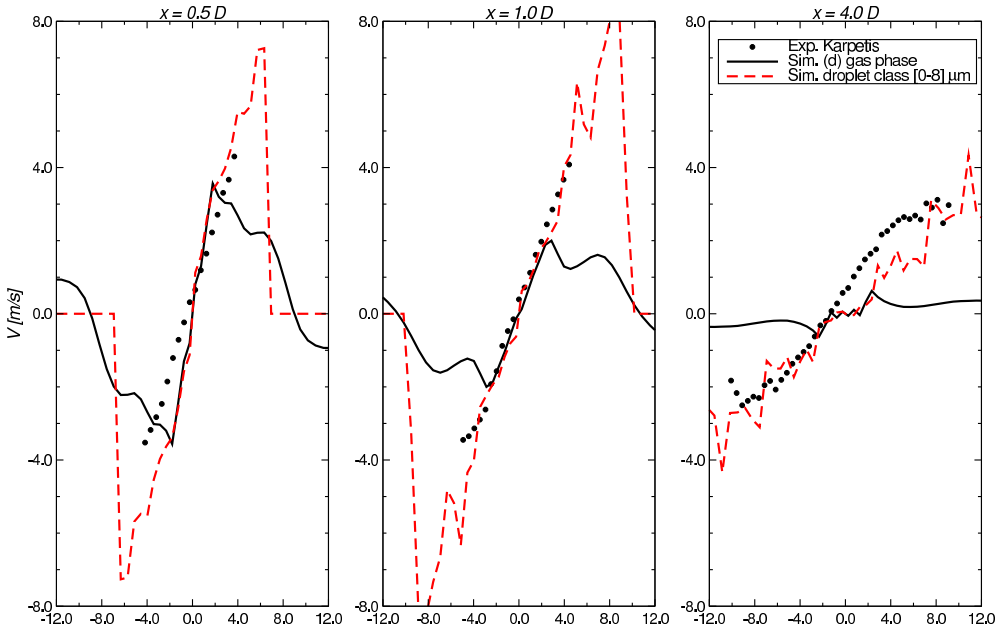

Figure 7.6: Radial profiles of mean gas phase radial velocity $\widetilde{V}_{\mathrm{f}}(r)$. Symbols: experimental data. Lines: simulation data.

comparison between the measured radial velocity of the gas phase, the simulated radial velocity of the gas phase and the simulated radial velocity of the droplets in the size class [0-8] μm. The figure clearly shows that the computed radial velocity of the smallest droplets agrees very well with the experimentally observed values of radial velocity. Note that the experimentally measured values are in fact the measured radial velocities of the smallest droplets.

An explanation for this is as follows: a tracer liquid particle originally situated in the spray region will have a large positive radial velocity and it will therefore move away from the centreline. A fluid particle situated outside of the spray region has a much lower radial velocity. However, the velocity of this fluid particle cannot be measured since the flow surrounding the spray region does not contain any particles. The velocity measurements near the edge of the spray are biased due to the conditional measuring of tracer particles coming from the spray region.

Another explanation for the discrepancy is that vaporising particles do not have time to relax to the gas phase as their vaporisation time is shorter than their relaxation time.

A criterion for the suitability as tracer particles of vaporising droplets is that the droplet lifetime should be larger than the droplet relaxation time: $\frac{t_{\mathrm{p}}}{\tau_{\mathrm{p}}} > 1$. A simple analysis shows that the following criterion has to be fulfilled by the tracer

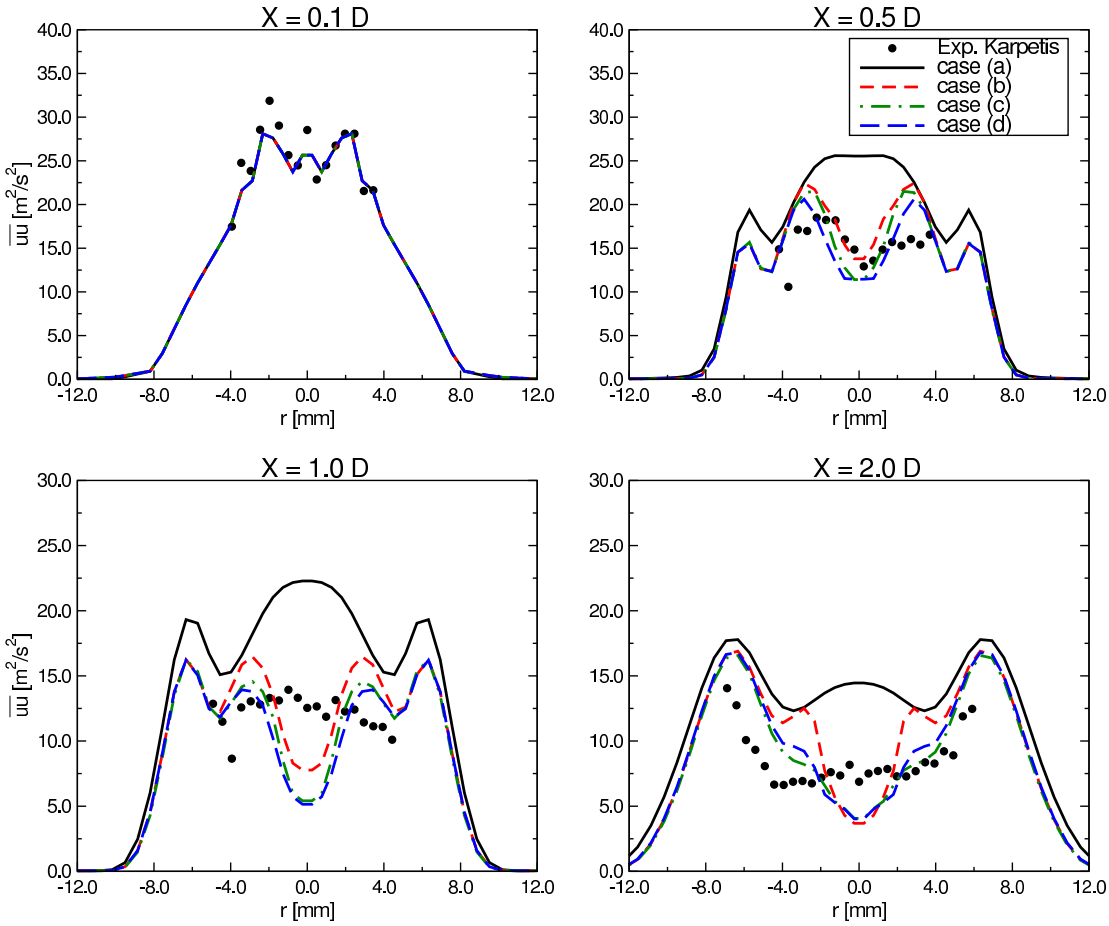

Figure 7.7: Radial profiles of gas phase axial Reynolds stress $\widetilde{u''_{\mathrm{f}}u''_{\mathrm{f}}}(r)$. Symbols: experimental data of smallest droplets. Lines: simulation data.

particles:

$$\frac{t_{\mathrm{p}}}{\tau_{\mathrm{p}}} = 8\frac{\mathrm{Sc}}{\mathrm{Sh}}\ln(1+B_M)^{-1} > 1. \tag{7.3}$$

The main factor determining the suitability as tracer particles is the Spalding mass transfer rate (or actually the temperature, since temperature will determine B_M as well as the actual value of the Schmidt number $\mathrm{Sc}(T)$).

Reynolds stresses of the gas phase Figures (7.7)-(7.9) show the Reynolds stress components $\widetilde{u''u''}$, $\widetilde{v''v''}$ and $\widetilde{u''v''}$. Compared to the simulations without two-way coupling the Reynolds stress profile shows a large depression at the centreline, followed by a pronounced peak at the location of the spray edge. The peaks are less pronounced further downstream of the injector. Close to the injector, the peak values lie above the predictions without two-way coupling and the depression is

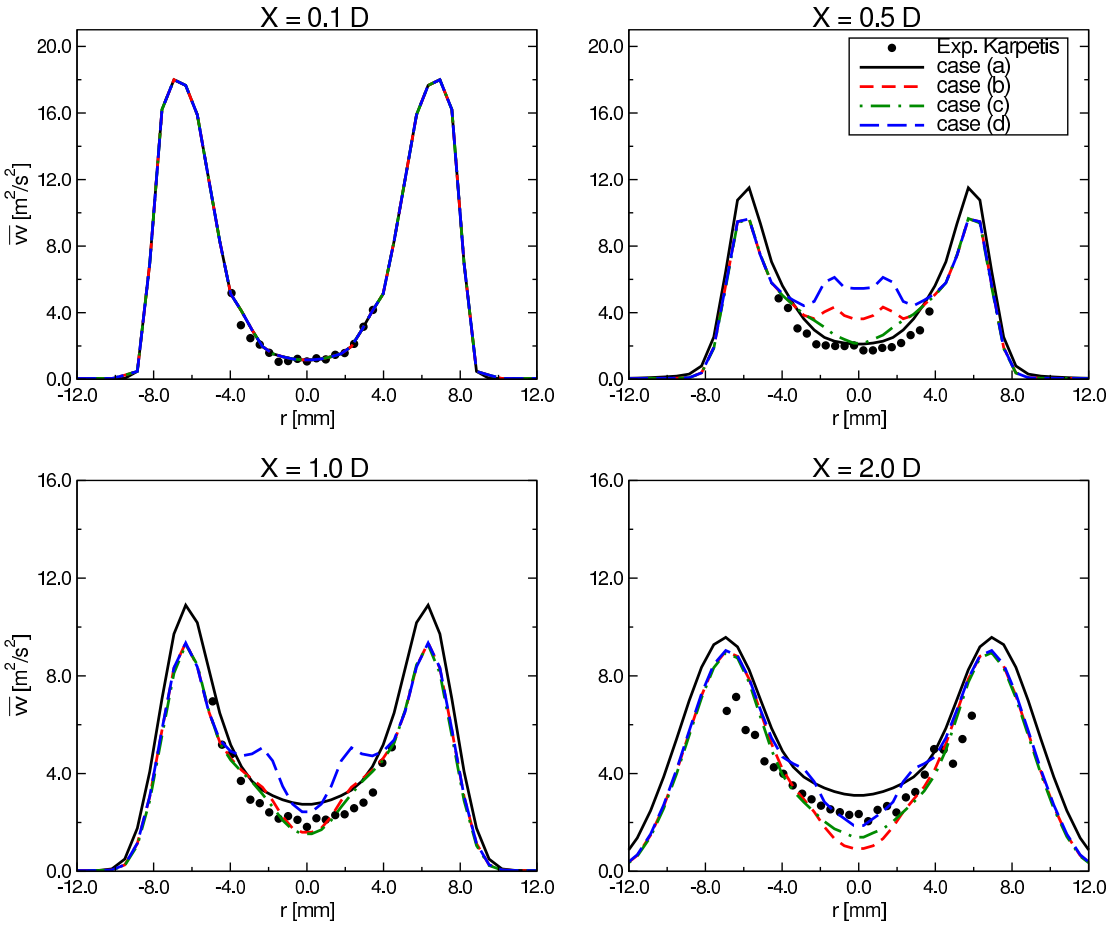

Figure 7.8: Radial profiles of gas phase radial Reynolds stress $\widetilde{v_{\mathrm{f}}'' v_{\mathrm{f}}''}(r)$. Symbols: experimental data of smallest droplets. Lines: simulation data.

lower than the prediction without two-way coupling. Further downstream, the peak values decrease more rapidly than the minimum values and at 4D downstream of the injector, the Reynolds stress predictions with two-way coupling are lower than the predictions without two-way coupling. The 'full' two-way coupling case where the modification of the pressure rate of strain is also taken into account shows smaller, less pronounced peak values and slightly lower minimum values for the axial component $\widetilde{u''u''}$, but the radial component $\widetilde{v''v''}$ is larger. When the mass source terms are also taken into account, all radial profiles predict higher values for the Reynolds stresses. Vaporisation clearly enhances turbulence in these simulations. In all simulations, the constant value of $C_{\epsilon 3} = 1.80$ was used in the model constant for the two-way coupling source term in the transport equation for the turbulence dissipation. Using a lower value for $C_{\epsilon 3}$ does increase the value of the Reynolds stresses near the centreline, but this is the case for the axial Reynolds stress $\widetilde{u''u''}$ as well as the radial Reynolds stress $\widetilde{v''v''}$. The radial Reynolds stresses

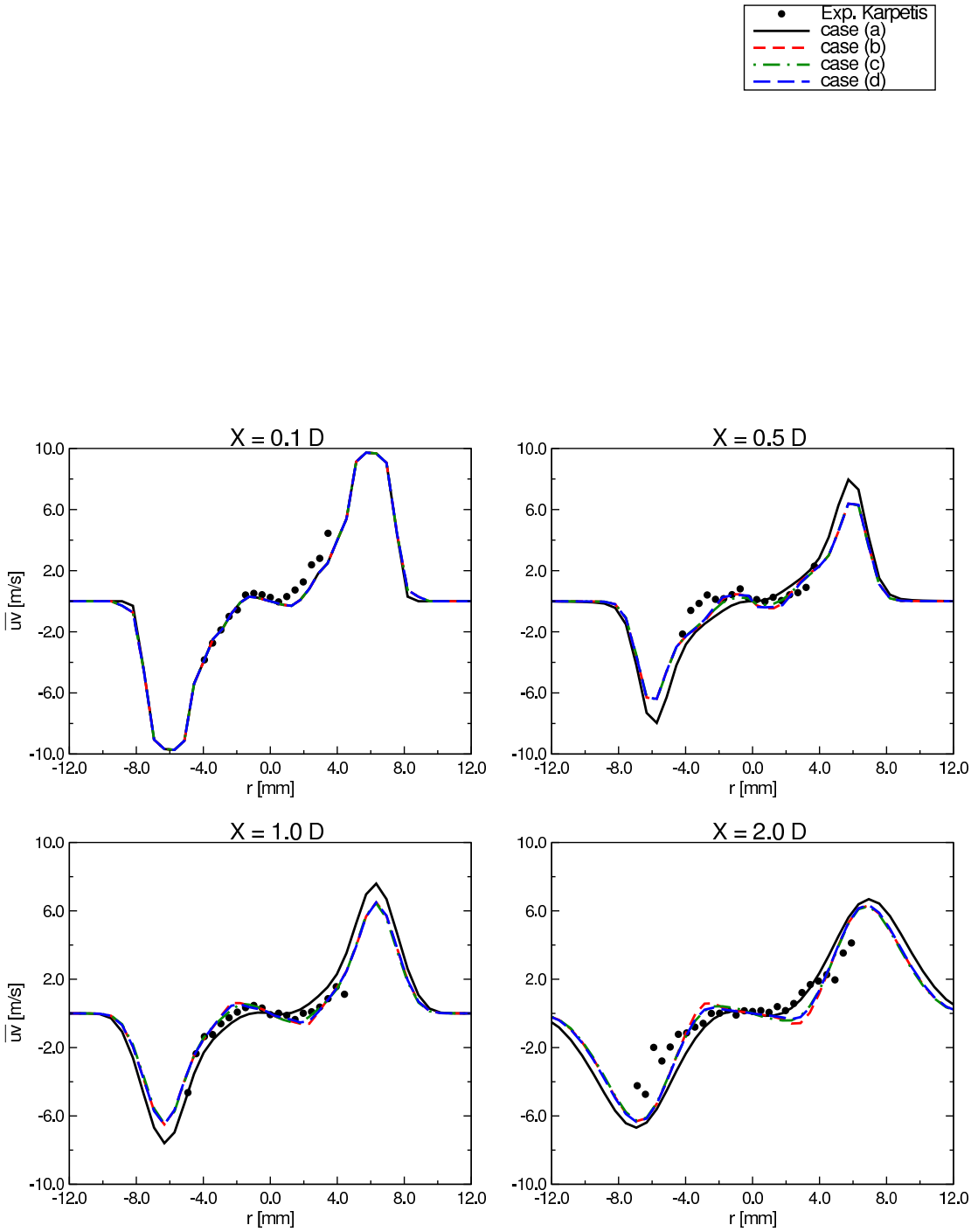

Figure 7.9: Radial profiles of gas phase shear stress $\widetilde{u_{\mathrm{f}}'' v_{\mathrm{f}}''}(r)$. Symbols: experimental data of smallest droplets. Lines: simulation data.

are strongly overpredicted for smaller values of the model constant and the overall performance does not improve. The vaporisation fluctuations, present in the

Reynolds stress equations, have a large influence on the numerical results. Neglecting the terms $\left\langle u''_{I,i}u''_{I,j}\mathcal{S}_m^{(I)}\right\rangle - \widetilde{u''_i u''_j}\left\langle \mathcal{S}_m^{(I)}\right\rangle$ and keeping only $\left\langle u''_{I,i}u''_{I,j}\mathcal{S}_m^{(I)}\right\rangle$ (so we neglect fluctuations in the source term for mass transfer), results in much higher values of the Reynolds stresses. This effect can be seen for the axial Reynolds stresses in Figure (7.10). Case (a) and case (b) are as before, but the dash-dotted line is now a simulation similar to case (b) but neglecting the vaporisation fluctuations in the Reynolds stress equations.

In chapter 3, an exact model taking into account the effect of mass transfer on the turbulence dissipation was introduced. Case (d) has been replaced in Figure (7.10) by a simulation similar to case (b), but instead of using the exact source term for mass transfer in the equation for turbulence dissipation, a model source term is used. So in the equation for the turbulence dissipation, the exact source term

$$\left\langle \mathcal{S}_{\epsilon_m}^{(I)}\right\rangle = \epsilon\left\langle \mathcal{S}_m^{(I)}\right\rangle. \tag{7.4}$$

is replaced by a source term similar to what is used to take into account the effect of the presence of particles:

$$\left\langle \mathcal{S}_{\epsilon_m}^{(I)}\right\rangle = C_{\epsilon_3}\frac{\epsilon}{\widetilde{u''_k u''_k}}\left\langle u''_{I,i}u''_{I,j}\mathcal{S}_m^{(I)}\right\rangle. \tag{7.5}$$

In equation (7.5), the same modelling constant C_{ϵ_3} that was used to evaluate $\left\langle \mathcal{S}_\epsilon^{(I)}\right\rangle$ is being used. It is clear from Figure (7.10) that neglecting the fluctuations in the vaporisation rate leads to an overestimation of the Reynolds stresses near the centreline starting immediately after the injector and continuing throughout the domain. Since this source term represents in a way the effect of fluctuations of the vaporisation rate, it can be concluded that vaporisation fluctuation are not negligible and may even be important in turbulent spray flames. In order to obtain the 'exact' model (7.4) -exact in the sense that no extra modelling constant is introduced- it is assumed that the gradients of the Reynolds stresses and vaporisation are uncorrelated. We immediately obtain the final 'exact' model when fluctuations in the vaporisation rate are neglected and therefore the 'exact' model may not perform very well. When model equation (7.5) is used instead of (7.4), the long-dashed lines in Figure (7.10) are obtained. The difference between the two models is not very large and diminishes further downstream. Still, it seems that the model based on the classical approach performs slightly better than the exact model derived in this thesis. However, since the exact model knows no model constants and because the use of a gradient hypothesis to obtain equation (7.5) is not entirely justifyable, it makes more sense to keep using equation (7.4) in favour of equation (7.5).

7.3.1 Temperature profiles

Figure (7.11) shows the radial profiles of mean temperature. In the experiment, a peak temperature of approximately 1650 K was measured at the centreline of the

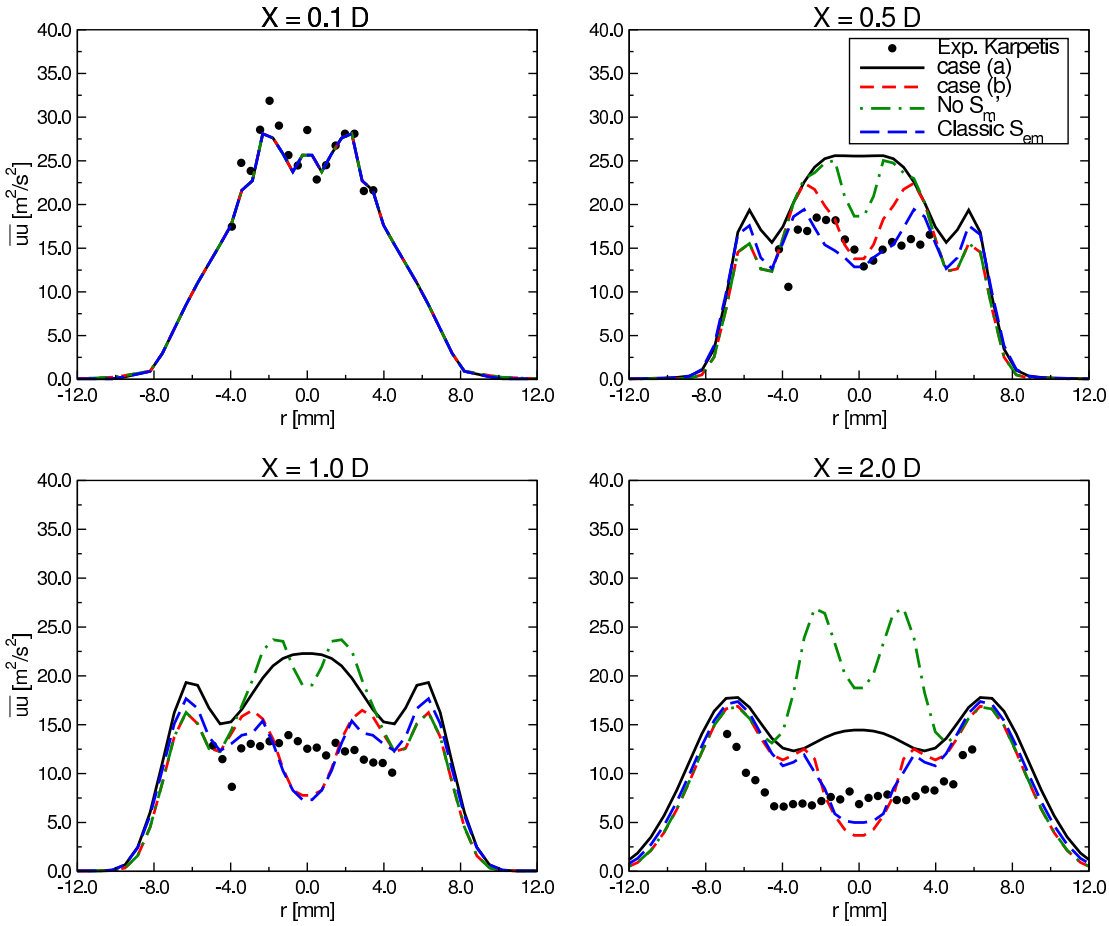

Figure 7.10: Radial profiles of gas phase axial Reynolds stress $\widetilde{u_f'' u_f''}(r)$. Symbols: experimental data of smallest droplets. Lines: simulation data.

spray flame. In the simulations, the same peak temperature is predicted but at a small distance from the centreline. Due to the evaporative cooling and the abundance of fuel vapour, the temperature in the core of the spray drops to around 1000 K. This is precisely what is described by the group combustion regimes of Chiu [22]. The rms of temperature fluctuations in Figure (7.12) show a large underprediction of the temperature fluctuations. This can be caused by the way the fuel vapour is distributed to the gas phase. Instead of distributing the fuel vapour homogeneously over all gas particles in a finite volume cell, the fuel vapour is distributed in such a way that it feeds a peak in the pdf of mixture fraction at saturation conditions. Figures (7.11)-(7.12) also show the mean temperature and the rms of temperature fluctuations for a simulation with homogeneous fuel vapour distribution. The results show no improvement in T as well as $\sqrt{T''T''}$.

The variance of mixture fraction is influenced by the choice of Lagrangian mixing model. For the IEM model, it has been shown that extra source terms taking

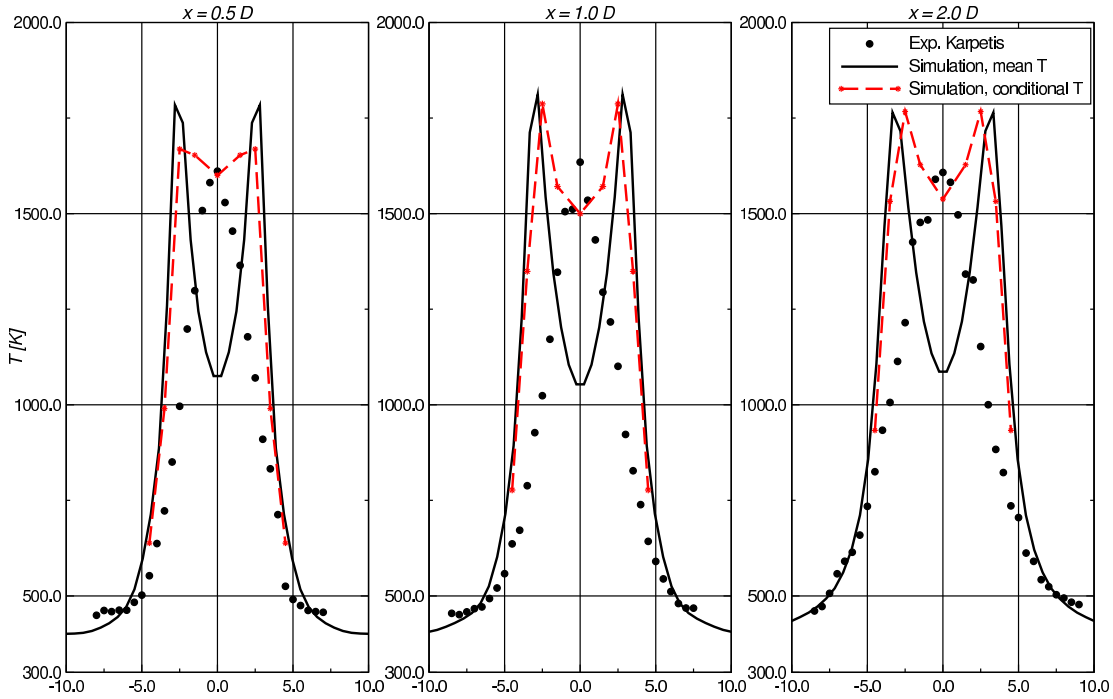

Figure 7.11: Radial profiles of mean temperature. Symbols: experimental data. Solid line: simulation data for mean temperature. broken line: simulation data for conditional mean temperature $\langle T|Z \leq c_z \rangle$.

into account the presence of (vaporising) particles appear in the mixing model. The dominant effect however is the two-way coupling source terms arising in the transport equation for turbulence dissipation, directly influencing the mixing time scale. The general effect of two-way coupling is a faster return to the mean, therefore decreasing the mixture fraction variance.

It is interesting that the mean temperature in the Karpetis has its peak temperature at the centreline, whereas the numerical simulations show a decrease in temperature at the centreline. The decrease in temperature at the centreline can be explained by two mechanisms. First of all, the droplet vaporisation process extracts heat from the gas phase, which is expressed in equation (3.69) by the particle source term at the right-hand side. Secondly, the fuel vapour entering the gas phase will increase the local mixture fraction to a value far above the stoichiometric value near the injector. The temperature drops due to oxygen deprivation and fuel saturation. The measured mean temperature does not show these two mechanisms, although the correct maximum temperature as well as the broadness of the temperature profile is measured correctly. The magnitude of the temperature

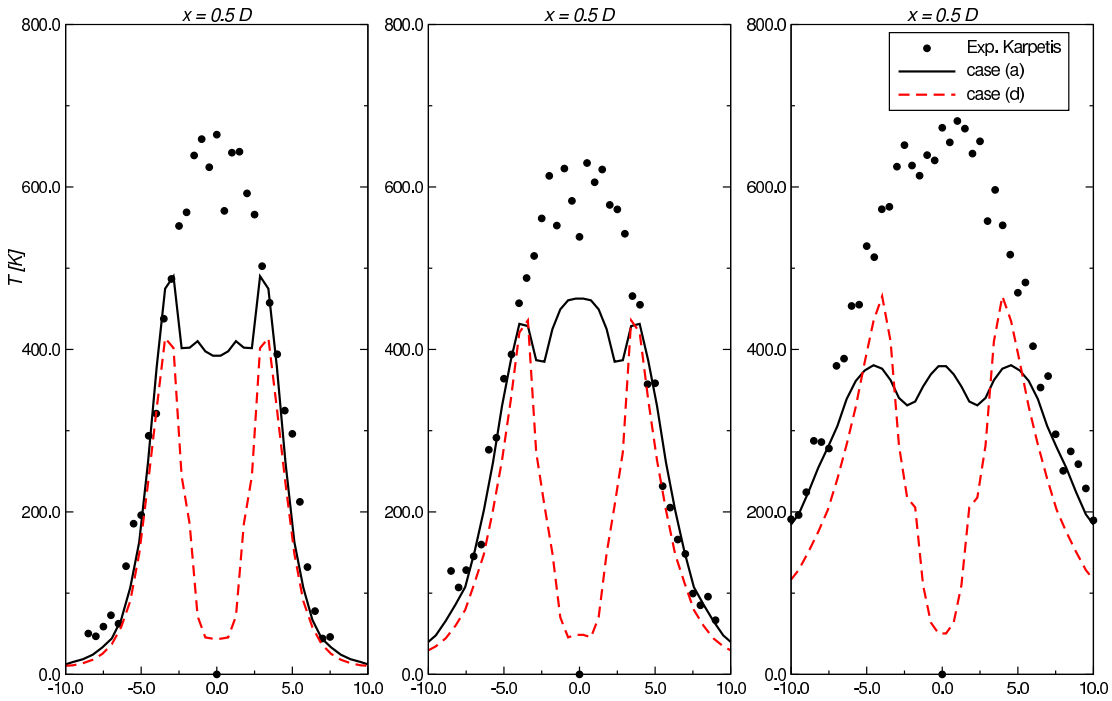

Figure 7.12: Radial profiles of gas phase rms of temperature $\sqrt{T''T''(r)}$. Symbols: experimental data. Lines: simulation data.

fluctuations is also remarkable, and Karpetis and Gomez attribute this behaviour to two reasons:

1. turbulent mixing, which generally leads to non-Gaussian, bi-modal pdf's in the temperature field [10], automatically leading to a large variance.

2. intermittency behaviour due to the presence of particles, which is a common phenomenon in spray flames.

Karpetis and Gomez do remark that the Raman thermometry measures temperature only if the probe is not disturbed by the presence of droplets. It is a form of conditional averaging, conditional on the absence of particles. Because the vapour from liquid particles does not mix instantaneously, the fuel vapour concentration in the neighbourhood of a particles is higher and the temperature in a region with vaporising droplets is lower. It is possible, and Karpetis and Gomez certainly make this clear in their paper, that this conditional averaging can have a significant influence on the measured temperature. Gas samples in the high temperature region of the pdf of temperature were systematically taken, and samples containing liquid particles, and therefore (with high probability) in a high mixture fraction, low

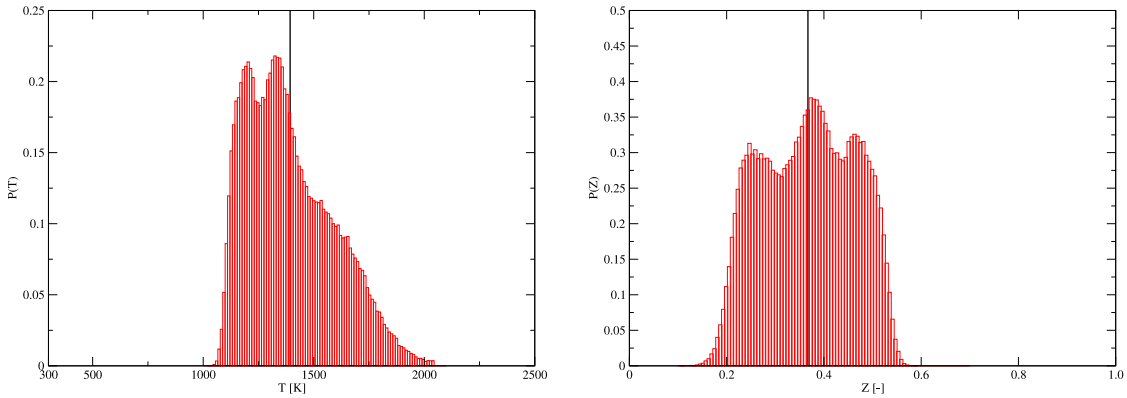

Figure 7.13: Conditional averaged pdfs of temperature (left) and mixture fraction (right)

temperature part of the pdf, were rejected. This conclusion was partly based on the measurements of the emissions of CH* radicals, which can be considered an indicator for the presence of a flame sheet. The CH* emissions at the centreline are practically zero, indicating that the probability of presence of a flame is low at the centreline.

Figure (7.13) shows the pdf of temperature and mixture fraction at the centreline at $x = 0.5D$ downstream of the injector. The mixture fraction pdf shows that there is a peak near the saturation conditions. The vapour distribution algorithm [117] feeds the peak at saturation in the mixture fraction pdf. Fluid particles receive fuel vapour according to their saturation rate: the fluid particle closest to saturation receives fuel vapour first until it reaches saturation, then the next fluid particle that is closest to saturation, etc. In this algorithm an artificial correlation between fluid and dispersed phase particles is created. Computational gas particles which already have some fuel vapour can be seen as 'close' to a liquid fuel particle, thus receiving more vapour.

Karpetis and Gomez report a 90% rejection rate when taking temperature samples, due to the presence of liquid particles disturbing the measurements. We could try to mimic the experimental conditions of Karpetis computing a conditional mean temperature, conditional on the absence of liquid particles. A computational gas particle which has a fuel vapour mass fraction close to saturation conditions indicates the presence of a liquid particle. We will therefore reject the 90% of the weighted computational gas particles with the highest mass fraction. The resulting conditional mean temperature profile at $x = 0.5D$ downstream of the injector is shown in Figure (7.11). Indeed, the temperature at the centreline rises significantly when conditional samples are taken and even in this rather crude approach used here, there is a significant improvement of the numerical results towards the experimentally measured temperature profiles and the explanation of conditional

sampling seems plausible. In this light, it is also interesting to know that temperature measurements in other spray flames, e.g. McDonell and Samuelsen [103], do show temperature profiles with a local minimum at the centreline.

The problems associated with the measurement of temperature profiles in a spray flame make it difficult to draw solid conclusions for this test case. However, the discussion of Karpetis and Gomez, as well as measured temperature profiles in other spray flame experiments, lead to the conclusion that the most probable profile for the (unconditional) mean temperature is the profile obtained with the simulations, with a local minimum temperature on the symmetry axis.

7.4 Results of the dispersed phase

In this section, the results of the dispersed phase simulations will be discussed and compared with experimental data. Data for three different size classes are available for the velocity and velocity fluctuations. The size class that was used to represent the gas phase velocities is also plotted in the figures presented in this section, as well as the simulation results for this size class. The simulations presented here are the simulations for the full two-way coupling case (d), where the source terms for exerted particle forces and vaporisation are taken into account, as well as the modification of the pressure rate of strain.

Figure (7.14) shows the measured axial velocity of the dispersed phase for the droplet size classes [0-8], [18-22] and [58-62] μm (black dots) as well as the simulation results for the droplet size classes [0-8], [15-25] and [55-65] μm (lines). In the previous section, the emphasis has been on assessing the importance of different contributions of particle interaction. Here, the results of the full two-way coupling simulations are shown and no comparison is made between different two-way coupling models. Although the behaviour of the smallest droplet size classes may be influenced by the different two-way coupling terms, the larger size classes are mainly influenced by the dispersion model (in our case: the model for for the fluctuating velocity seen u'_{s}). It can be seen that there is a good agreement with the experimental data close to the injector at $x = 0.5D$, but further downstream the velocity profiles are broader then in the experiment, which is due to a higher spreading of the spray. The radial velocity profiles shown in Figure (7.15) are in good agreement with the experimental data at all downstream locations, although the numerical results are a little bit more 'noisy' further downstream. Most droplets have already vaporised between 2-4 injector diameters downstream of the injector and long time statistics are needed to obtain smooth mean velocity profiles in this region.

Figures (7.16) and (7.17) show the radial profiles of the Reynolds stresses $\widetilde{u''_{\mathrm{p}}u''_{\mathrm{p}}}(r)$ and $\widetilde{v''_{\mathrm{p}}v''_{\mathrm{p}}}(r)$. It is interesting to see that near the centreline the Reynolds stresses of the dispersed phase are reduced significantly in the numerical simulations, whereas the experimental data does not show such strong decrease in turbulence

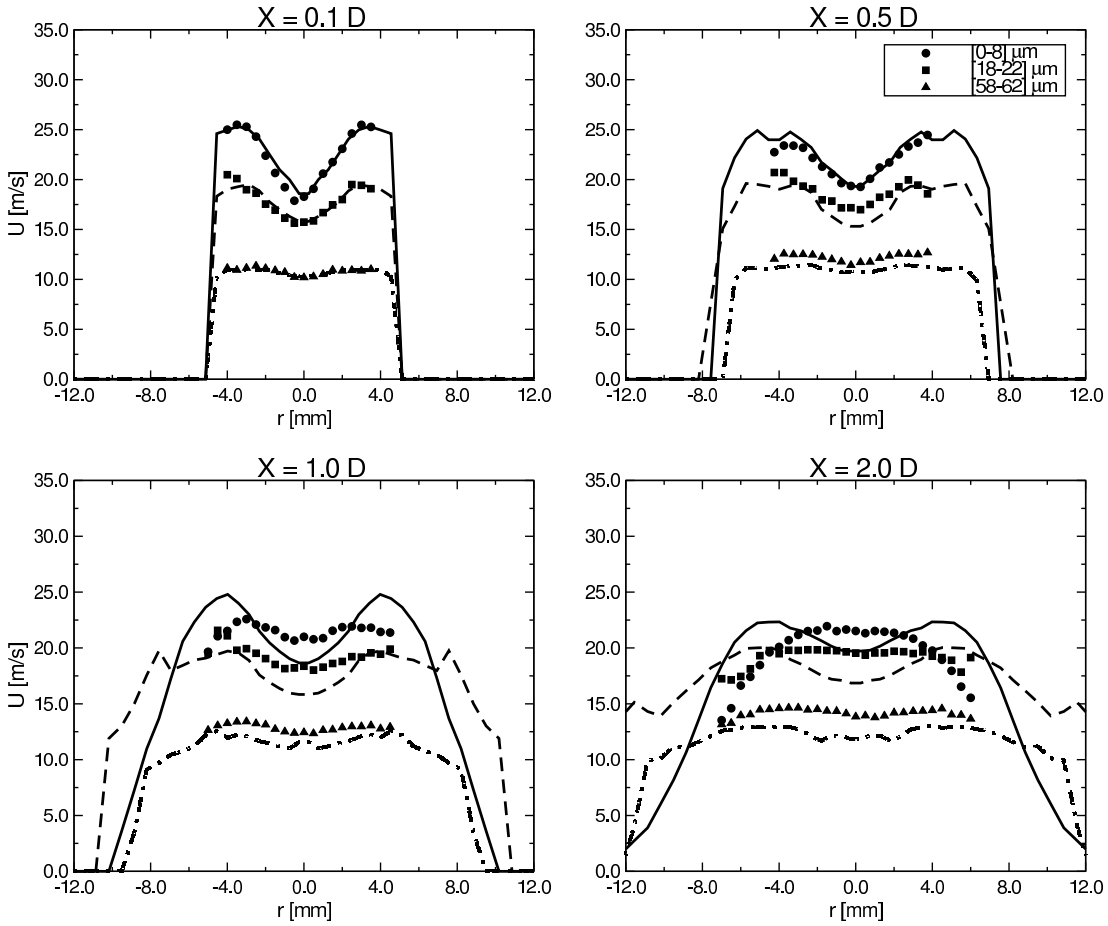

Figure 7.14: Radial profiles of mean droplet axial velocity $\widetilde{U}_{\mathrm{p}}$ for three different size classes. Symbols: experimental data. Lines: simulation data.

levels near the symmetry axis. This could be due to the omission of the two-way coupling terms in the model for the fluctuating velocity seen or it might be due to too strong turbulence dissipation levels.

Figures (7.18) and (7.19) show the radial profiles of the arithmetic mean diameter $d_{10}(r)$ and the droplet number density $N_{\mathrm{p}}(r)$ at several axial distances downstream of the injector. Simulations with several droplet vaporisation models (discussed in chapter 2) showed only small differences between the results. Only the results for the vaporisation model of Miller *et al*. [108] and the classical rapid mixing model are shown here for case (d). There is a good agreement for the droplet number density at all axial locations downstream of the injector. The width of the spray is a little larger in the experiment, which is caused by the grid resolution near the injector. An even smaller grid will correct this.

The droplet diameter is however overpredicted near the centreline. In the experiment, the droplet size remains at an almost constant level of $30\mu\mathrm{m}$, whereas

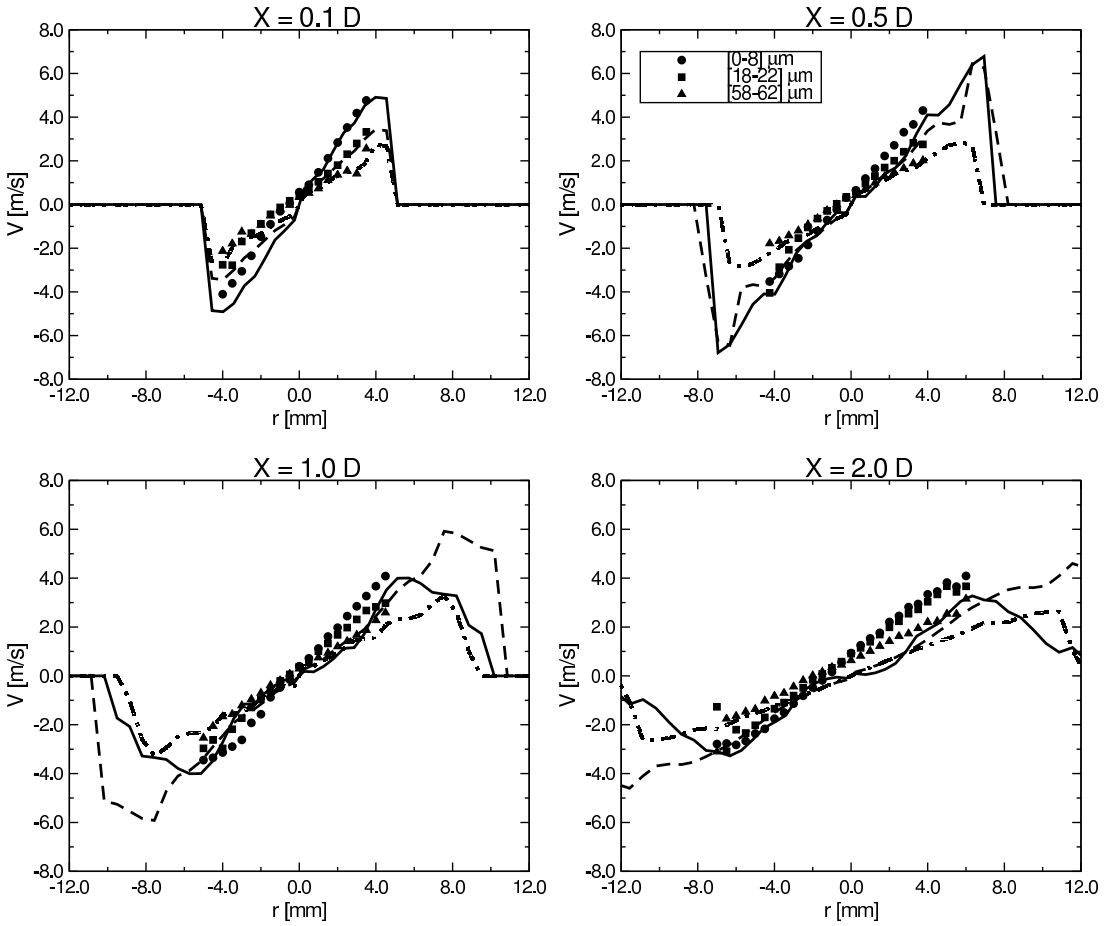

Figure 7.15: Radial profiles of mean droplet radial velocity $\widetilde{V}_{\mathrm{p}}$ for three different size classes. Symbols: experimental data. Lines: simulation data.

in the simulations, the droplet diameter rises immediately after the injector to a value of $40\mu\mathrm{m}$. The droplet diameter then remains at this level throughout the spray region.

A possible explanation is that the droplet size distribution used in the simulations does not match the size distribution in the experiments, i.e. in the experiment there were more large droplets. Another explanation is that in the smaller droplet size classes, some droplets vaporise so fast that they vaporise completely from their current sizeclass in a single timestep and skip the lower size classes. The lower size class is under-represented and the droplet diameter rises.

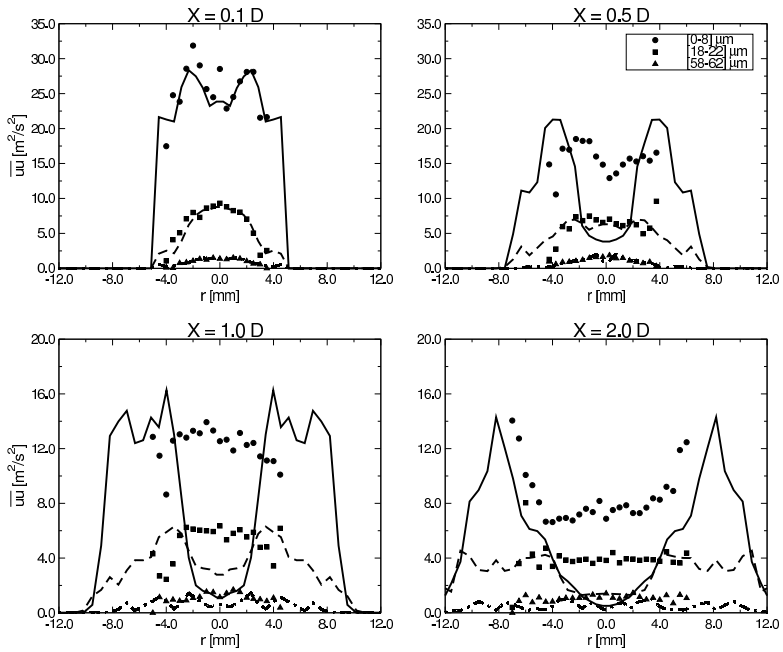

Figure 7.16: Radial profiles of droplet normal stress $\widetilde{u_\mathrm{p}'' u_\mathrm{p}''}$ for three different size classes. Symbols: experimental data. Lines: simulation data.

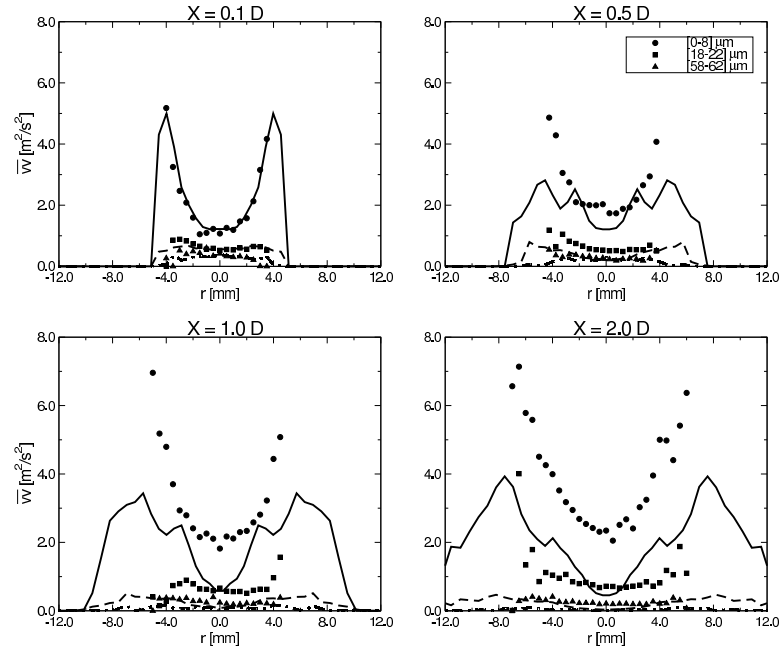

Figure 7.17: Radial profiles of droplet normal stress $\widetilde{v_\mathrm{p}'' v_\mathrm{p}''}$ for three different size classes. Symbols: experimental data. Lines: simulation data.

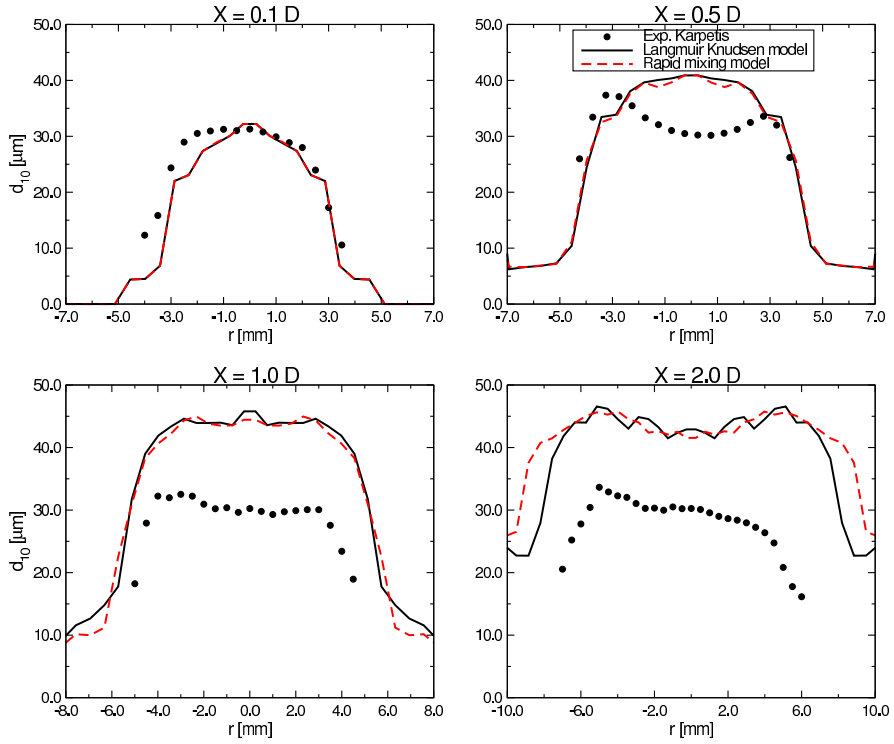

Figure 7.18: Radial profiles of the droplet mean diameter d_{10}. Symbols: experimental data. Lines: simulation data.

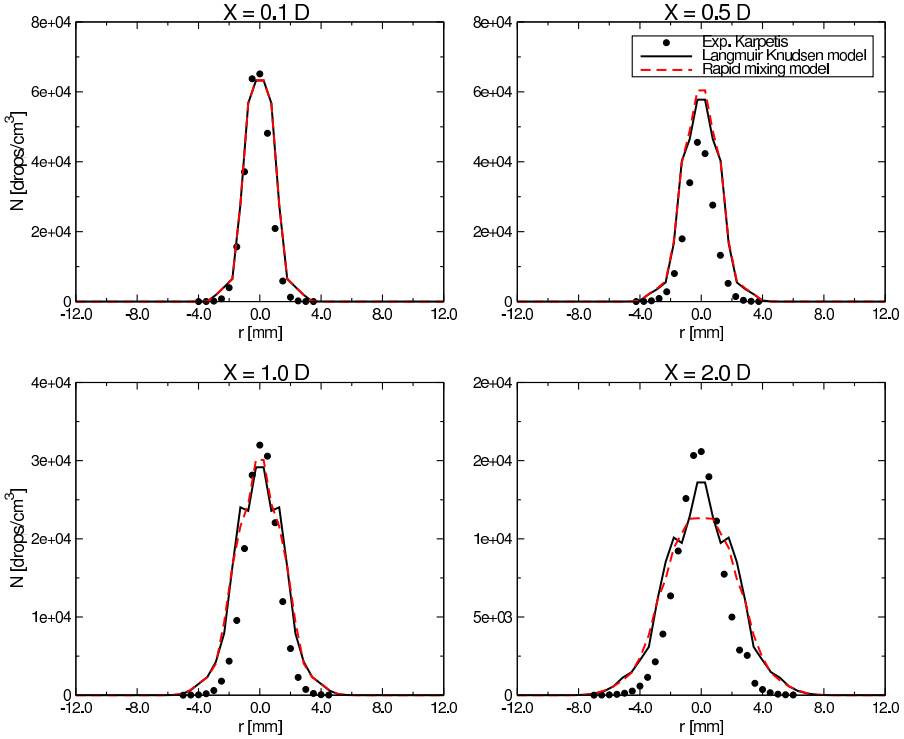

Figure 7.19: Radial profiles of the droplet number density $N_\mathrm{p}\,\frac{[\mathrm{droplets}]}{\mathrm{cm}^3}$. Symbols: experimental data. Lines: simulation data.

7.5 Turbulence modulation by Kolmogorov lengthscale sized particles

The Kolmogorov lengthscale was estimated in [75] to be $\eta \approx 30\mu\mathrm{m}$. The mean arithmetic droplet diameter near the spray injector is also around $d_{10} \approx 30\mu\mathrm{m}$. It can be expected that droplets with a lengthscale smaller than the Kolmogorov lengthscale have different effects on turbulence than droplets with a lengthscale that is larger than the Kolmogorov lengthscale. Analytical studies by Druzhinin and Elghobashi [43, 44] have indeed shown that in isotropic turbulence, the particle turbulence modulation depends on the particle size with respect to the Kolmogorov length scale η. Their studies show that when the particles are smaller than the Kolmogorov lengthscale, $d_\mathrm{p} < \eta$, the particles will increase the turbulent kinetic energy and the turbulence dissipation rate of the continuum phase. For particle sizes of the order of the Kolmogorov lengthscale $d_\mathrm{p} \approx \eta$, the turbulent kinetic energy decreases. A quick investigation of the transport equations of turbulent kinetic energy and dissipation rate equation (3.32) and (3.35) shows that the source term due to the presence of particles can have a positive or a negative sign, depending on the slip velocity $|\boldsymbol{U}_s - \boldsymbol{U}_\mathrm{p}|$ between the particle and the fluid. No mechanism is present that takes into account the particle diameter with respect to the Kolmogorov lengthscale. In fact, in the derivation of the particle equation of motion the assumption is made that the particle diameter is smaller than the Kolmogorov lengthscale [67] and no such mechanism can be present. A more general particle-turbulence interaction theory is needed to capture the effect mentioned by Druhzinin, Elghobashi and others, but this falls outside the scope of this thesis.

In this context it is worthwhile to mention that the effects of vaporisation on the turbulence dissipation is very clear in that it will always increase dissipation.

7.6 Conclusions and recommendations

The simulation results for this spray flame are encouraging. There was a good agreement with the experimental data for most of the measured properties. The disagreement with the mean temperature and temperature variance was extensively discussed in section 7.3.1 and can be attributed to either conditional measuring (as was also suggested by Karpetis) or to a vaporisation interaction effect that has not been taken into account in the simulations presented in this chapter. In our model as presented in chapter 5 the influence of the surroundings of the droplet is determined by the velocity seen, composition seen and the temperature seen. Fluctuations in the velocity are included in the model, but fluctuations in the composition and temperature have been neglected. In chapter 2 the group combustion concept predicted a lower vaporisation rate. Less fuel enters the gas phase and the gas mixture will generally be more lean. This could result in higher temperatures.

Karpetis already showed that mass transfer is a dominant effect in the spray flame [75]. Indeed, only when the two-way coupling effects due to mass transfer are taken into account through the incorporation of all effects of $\mathcal{S}_m^{(I)}$ in the simulations it is possible to realise such strong axial and radial velocities that they are comparable to the measured values. Moreover, the corrections of found by Chiang for the Nusselt and Sherwood number as well as the corrections to the drag coefficient due to mass transfer are extremely important and crucial to obtain good predictions in this mass transfer dominated spray flame.

Still, there is plenty of room for improvement and the following points deserve to be considered in future work:

1. Karpetis and Gomez [73] mention that intermittency is a common phenomena in turbulent spray flames. To properly take intermittency into account the turbulence dissipation (or equivalently turbulence frequency) has to be considered as a fluctuating variable and the velocity-frequency-composition PDF should therefore be considered.

2. The present model uses the fluctuating velocity seen and a mean temperature seen. Generalisation to a fluctuating temperature seen is possible using the information in the continuum phase pdf.

3. The flamelet approach used here is based on only a single strainrate, $a = 100\frac{1}{s}$. A lookup table in which the strain rate is a second independent variable (together with mixture fraction) can be created. The strain rate experienced by flamelets in turbulent flow can be calculated from the turbulence frequency using relationships given in [123]. This will have an effect on the simulation results for the gas phase temperature near the injector, since there the strain rate will have the largest variations.

4. Related to the previous item, a lookup table based on a single phase flamelet approach can be replaced by a spray flamelet approach. The work of Gutheil [61, 62] may be of use in further developments in this direction.

5. Since the correction factors due to vaporisation had such an impact on the performance of the numerical simulations, a correction factor to the drag coefficient proposed by Chiu [21] for *interacting* particles in a turbulent flow might be considered to see if this leads to further improvements.

6. The experimental data used in this chapter also has room for improvement. The velocity profiles at the first measurement plane at $x = 1.27$ mm downstream of the injector are discontinued at $r = 4$ mm and one needs to speculate on the possible continuation of the data for $r > 4$ mm. An experiment with more complete radial profiles would leave less to the creativity of the modeller. The study of an additional, but similar experiment like the methanol spray of Mcdonell and Samuelsen [103] will be very useful.

CHAPTER 8

Concluding remarks

In this thesis, a hybrid Finite Volume - Monte Carlo method has been proposed to compute turbulent reacting dispersed two phase flows. Some progress in the development of turbulence modelling of two phase flows has been made, but many aspects still remain to be investigated. In this last chapter we review some interesting achievements and mention some open problems.

The Eulerian mean transport equations were derived and a modification of the model for the pressure rate of strain - a classical turbulence closure problem - has been proposed. This modification takes into account the **effect of the presence of particles** and the effect of **mass transfer** (vaporisation) on the **pressure rate of strain**. The model has been derived in such a way that it is easy to incorporate in existing codes since no additional information is needed to evaluate the extra two-way coupling terms with respect to the original 'classical' two-way coupling terms. Simulation results have shown that this term is **not negligible** in turbulent non-vaporising sprays as well as in turbulent spray flames and can give small improvements of the predictions of turbulence quantities.

The consistency between the Lagrangian turbulence model and second moment closures was investigated and the Langevin model has been extended to take into account the modification of the turbulent flow by the presence of particles as well as by mass transfer due to vaporisation. The **extension of the Langevin model** to take into account these two-way coupling effects implies a modification of the result of Kolmogorov for the first order Lagrangian structure function. The extension of the model allows to use the modifications to the pressure rate of strain in PDF simulations. The practical implementation of this model poses some difficulties since additional information is needed to distribute the two-way coupling source terms over the computational fluid particles. In this sense, more information is embedded in the Langevin model than is present in the Eulerian transport equations.

The influence of **vaporisation fluctuations** on the Reynolds stresses was taken into account and this turned out to have a noticeable influence on the predictions of the Reynolds stresses in the karpetis spray flame.

A model that takes into account the modification of the **turbulence dissipation due to vaporisation** was proposed. The attractive feature of this model is that no modelling constant is introduced and it is in that sense more 'exact' than other models that were proposed in the literature. Small differences between the models were found in favour of the classical model, but a more thorough study needs to be performed in order to assess its general performance.

Additionally, it was shown how the closure of the **triple correlations**, either by the Daly Harlow (gradient diffusion) approximation or by a model that is tensorially invariant, can be extended to multiphase flow problems including mass transfer. It still remains to be investigated how influential these modifications are but since the details of the model for the triple correlations in single phase flows are generally not very important, it can safely be assumed that two-way coupling modifications to the triple correlations are negligible.

Micro-mixing models are also affected by the presence of vaporising particles, but this also remains a theoretical observation in this thesis.

The details of the droplet vaporisation models studied in the beginning of the thesis do not seem to play a dominant role in turbulent spray flames. Many effects like Saffman lift, radiation and internal circulation can be neglected. However, **vaporisation corrections to the drag coefficient** and also the Nusselt and Sherwood number are important and necessary in order to obtain a good agreement with experimental data.

A very challenging topic to pursue in future work is the extension of the dispersion model based on a Generalised Langevin Model instead of the Simplified Langevin Model.

In a more theoretical approach towards the problems encountered in particle turbulence interaction one might consider **reviewing** the **Kolmogorov theories** and extend the results found in this thesis for the first order Lagrangian structure function to higher order structure functions and the turbulence energy spectra. These theoretical exercises might be important in the derivation of Large Eddy models for multiphase flows and give more insight in the numerical results of Direct Numerical Simulations.

It has been reported in the literature that in turbulent spray flames, **intermittency** might play an important role. Another improvement therefore is to extend the pdf method to a **velocity-composition-frequency pdf** and investigate the influence of the two-way coupling terms on the equation for the turbulence frequency.

As to the aspect of **group combustion** an important remark needs to be made. In the literature, two (often implicit) definitions of group combustion exist. In one definition, group combustion is presented according to the original idea of Chiu [23] that in non-dilute droplet clouds vaporised fuel gas will quench the chemical reactions, causing the droplet cloud to have a colder centre with vaporising droplets. In this sense, group combustion is completely understood since it is due to the enthalpy drop and the excess fuel vapour (or mixture fraction) that this phenomena occurs.

A different view on group combustion which was also developed by Chiu [18] is that in dense sprays, the presence of neighbouring droplets will influence droplet vaporisation, as well as droplet drag, etc. The classical vaporisation laws for isolated droplets are not valid anymore. In this sense, group combustion can

actually be seen as a hydrodynamic interaction problem and a one-point pdf approach is insufficient to describe this. Spray flames with such dense regions will most likely also have non-negligible collision and coalescence rates and this has to be incorporated simultaneously in numerical simulations. Proper experimental data of denser sprays are needed to evaluate the performance of the derived models in such cases.

Some restrictions of the model presented in this thesis are that it is in the first place suited mainly for steady state spray flames. Variable time stepping and smoothing by time averaging are important to obtain accurate iteration averaged mean turbulence quantities from the model. We also have to adhere to the limitations of the second moment closure model and we have limited ourselves to certain classes of flame structures by using the flamelet approach.

In this light, the use of pdf methods in combination with large eddy simulations (and considering filtered density functions) is an interesting topic to pursue in future research. Closure problems will remain, but they will be of a different nature than the closure problems discussed in this thesis.

Many challenges still lie ahead of us.

APPENDIX A

Ito calculus

A.1 Analytical expression for U_s

Integration schemes for stochastic differential equations follow a slightly different procedure compared to standard Riemann integration [81] because the stochastic nature of the equations violates local integrability. An important result from stochastic calculus is the *Ito theorem*, saying that if X_t is an Ito process given by

$$dX_t = Udt + VdB_t \tag{A.1}$$

and $g \in C^2([0,\infty) \times R)$, then

$$Y_t = g(t, X_t) \tag{A.2}$$

is again an Ito process and

$$dY_t = \frac{\partial g}{\partial t}dt + \frac{\partial g}{\partial x}dX_t + \frac{\partial^2 g}{\partial x^2}(dX_t)^2. \tag{A.3}$$

With the above Ito formula, we can evaluate $d(\exp(-\frac{t}{T_i})U_{s,i})$ (note that we assume that $G_{ij} = \frac{1}{T_i}\delta_{ij}$) as in equation (5.49):

$$d(\exp(-\frac{t}{T_i})U_{s,i}) = -\frac{1}{T_i}\exp(-\frac{t}{T_i})U_{s,i}dt + \exp(-\frac{t}{T_i})dU_{s,i}. \tag{A.4}$$

If the stochastic equation for the velocity seen is multiplied by $\exp(-\frac{t}{T_i})$ and if we substitute (A.4) into the result, we obtain

$$d(\exp(-\frac{t}{T_i})U_{s,i}) = \exp(-\frac{t}{T_i})C_i dt + \exp(-\frac{t}{T_i})\sum_j \sigma_{ij}dW_j(t). \tag{A.5}$$

We now take the integral of this expression:

$$\int_{t_0}^{t} d(\exp(-\frac{t}{T_i})U_{s,i})) = \int_{t_0}^{t}\exp(-\frac{s}{T_i})C_i ds + \int_{t_0}^{t}\exp(-\frac{s}{T_i})\sum_j \sigma_{ij}dW_j(s). \tag{A.6}$$

and we obtain:

$$\begin{aligned}\exp(-\frac{t}{T_i})U_{s,i}(t) - \exp(-\frac{t_0}{T_i})U_{s,i}(t_0) &= -T_iC_i\left[\exp(-\frac{t}{T_i}) - \exp(-\frac{t_0}{T_i})\right] \\ &+ \int_{t_0}^{t}\exp(-\frac{s}{T_i})\sum_j \sigma_{ij}dW_j(s),\end{aligned} \tag{A.7}$$

which leads to the final analytical expression for the velocity seen:

$$\begin{aligned} U_{s,i}(t) &= U_{s,i}(t_0)\exp(\frac{\Delta t}{T_i}) - T_i C_i \left[1 - \exp(\frac{\Delta t}{T_i})\right] \\ &+ \exp(\frac{t}{T_i}) \int_{t_0}^{t} \exp(-\frac{s}{T_i}) \sum_j \sigma_{ij} dW_j(s), \end{aligned} \tag{A.8}$$

A.2 Evaluation of the covariance matrix

Using the Ito isometry [120], we obtain the following equality for the second order moments:

$$\begin{aligned} \left\langle \left(\sum_j g_j(t) \int_{t_0}^{t} f_j(s) dW(s) \right)^2 \right\rangle &= \sum_j g_j^2(t) \int_{t_0}^{t} f_j^2(s) ds \\ &+ 2 \sum_{j<k} g_j(t) g_k(t) \int_{t_0}^{t} f_j(s) f_k(s) ds. \end{aligned} \tag{A.9}$$

In the general case where we have a full matrix B_{ij} and G_{ij}, the second term on the right hand side will give a nonzero contribution. Since we will only solve the orthogonally transformed equation, B_{ij} and G_{ij} are diagonal and we will not have these terms. We can now evaluate the variance of the stochastic part of equation (A.8), which will be needed to evaluate the stochastic contributions of the exact solution of the stochastic system of equations:

$$\gamma_i(t) = \sum_j \sigma_{ij} \int_{t_0}^{t} \exp(\frac{1}{T_i}(t-s)) dW_j(s), \tag{A.10}$$

which results in:

$$\left\langle \gamma_i^2(t) \right\rangle = \sum_j \sigma_{ij}^2 \frac{-T_i}{2} \left[1 - \exp(2\frac{\Delta t}{T_i})\right]. \tag{A.11}$$

Similar expressions can be found for the other variances and covariances.

BIBLIOGRAPHY

[1] B. Abramzon and W.A. Sirignano. Droplet vaporization model for spray combustion calculations. *Int. J. Heat Mass Transfer*, 32(9):1605–1618, 1989.

[2] G. Ahmadi, J. Cao, L. Schneider, and A. Sadiki. A thermodynamical formulation for chemically active multiphase turbulent flows. *International Journal of Engineering Science*, 44:699–720, 2006.

[3] K. Annamalai and W. Ryan. Interactive processs in gasification and combustion. part I:liquid drop arrays and clouds. *Progress in Energy and Combustion Science*, 18:221–295, 1992.

[4] N.A. Beishuizen, D. Roekaerts, and B. Naud. Evaluation of a modified Reynolds stress model for turbulent dispersed two-phase flows including two-way coupling. *Flow, Turbulence and Combustion*, 79(3):321–341, 2007.

[5] J. Bellan and K. Harstad. Analysis of the convective evaporation of nondilute clusters of drops. *International Journal of Heat and Mass Transfer*, 30:125–136, 1987.

[6] J. Bellan and K. Harstad. The details of the convective evaporation of dense and dilute clusters of drops. *International Journal of Heat and Mass Transfer*, 30:1083–1093, 1987.

[7] J. Bellan and K. Harstad. The dynamics of dense and dilute clusters of drops evaporating in large, coherent vortices. *23rd Symposium (International) on Combustion*, pages 1375–1381, 1990.

[8] J. Bellan and M. Summerfield. Theoretical examination of assumptions commonly used for the gas phase surrounding a burning droplet. *Combustion and Flame*, 33:107–122, 1978.

[9] A. Berlemont, M.S. Grancher, and G. Gouesbet. Heat and mass transfer coupling between vaporizing droplets and turbulence using a Lagrangian approach. *International Journal of Heat and Mass Transfer*, 38:3023–3034, 1995.

[10] R.W. Bilger. Turbulent diffusion flames. *Ann. Rev. Fluid Mech.*, 21:101–135, 1989.

[11] R.P. Borghi. The links between turbulent combustion and spray combustion and their modelling. *Proceedings 8th int. symp. on transport phenomena in combustion (ISTP-VIII) San Francisco 16-20 July 1995*, pages 1–18, 1996.

[12] X.Q. Chen and J.C.F. Pereira. Computation of turbulent evaporating sprays with well-specified measurements: a sensitivity study on droplet properties. *International Journal of Heat and Mass Transfer*, 39(3):441–454, 1996.

[13] X.Q. Chen and J.C.F. Pereira. Numerical study of the effects of gas temperature fluctuation on a turbulent evaporating spray. *Atomization and Sprays*, 8:63–82, 1998.

[14] C.H. Chiang, M.S. Raju, and W.A. Sirignano. Numerical analysis of convecting, vaporizing fuel droplet with variable properties. *International Journal of Heat and Mass Transfer*, 35:1307–1324, 1992.

[15] C.H. Chiang and W.A. Sirignano. Interacting, convecting, vaporizing fuel droplets with variable properties. *International Journal of Heat and Mass Transfer*, 36:875–886, 1993.

[16] N.A. Chigier. The atomization and burning of liquid fuel sprays. *Progress in Energy and Combustion Science*, 2:97–114, 1976.

[17] H.H. Chiu. Droplet vaporization law in non-dilute sprays. aerothermodynamics in combustors. *IUTAM Symposium Taipei*, 1991.

[18] H.H. Chiu. Advances and challenges in droplet and spray combustion. i. toward a unified theory of droplet aerothermochemistry. *Prog. Energy Combust. Science*, 26:381–416, 2000.

[19] H.H. Chiu and N. Chigier. *Mechanics and combustion of droplets and sprays*. Begell house, 1995.

[20] H.H. Chiu and L.H. Hu. Dynamics of ignition transcience and gasification partition of a droplet. *27th Symposium (International) on Combustion*, pages 1889–1896, 1998.

[21] H.H. Chiu and J.S. Huang. Multiple-state phenomena and hysteress of a combusting isolated droplet. *Atomization and Sprays*, 6:1–26, 1996.

[22] H.H. Chiu, H.Y. Kim, and E.J. Croke. Internal group combustion of liquid droplets. *19th Symposium (International) on Combustion*, pages 971–980, 1982.

[23] H.H. Chiu and T.M. Liu. Group combustion of liquid droplets. *Combustion Science and Technology*, 17:127–142, 1977.

[24] H.H. Chiu and S.P. Su. Theory of droplets ii: states, structures, and laws of interacting droplets. *Atomization and sprays*, 7:1–32, 1997.

[25] S.Y. Cho, M.Y. Choi, and F.L. Dryer. Extinction of a free methanol droplet in microgravity. *23rd Symposium (International) on Combustion*, pages 1611–1617, 1990.

[26] P.Y. Chou. On velociy correlations and the solutions of the equations of turbulent fluctuation. *Quarterly of Applied Mathematics*, 3:38–54, 1945.

[27] M. Chrigui, A. Sadiki, and G. Ahmadi. Study of interaction in spray between evaporating droplets and turbulence using second order turbulence RANS modeling and a lagrangian approach. *Progress in Computational Fluid Dynamics*, 4:162–174, 2004.

[28] R. Clift, J.R. Grace, and M.E. Weber. *Bubbles, drops and particles*. Dover books, 1978.

[29] O. Colin and A. Benkenida. A new scalar fluctuation model to predict mixing in evaporating two-phase flows. *Combustion and Flame*, 134:207–227, 2003.

[30] S.M. Correa and M. Sichel. The group combustion of a spherical cloud of monodisperse fuel droplets. *19th Symposium (International) on Combustion*, pages 981–991, 1982.

[31] C. Crowe, M. Sommerfeld, and Y. Tsuji. *Multiphase flows with droplets and particles*. CRC press, 1998.

[32] C.T. Crowe. On models for turbulence modulation in fluid-particle flows. *International Journal of Multiphase Flow*, 26:719–727, 2000.

[33] G.T. Csanady. Turbulent diffusion of heavy particles in the atmosphere. *Journal of the Atmospheric Sciences*, 20:201–208, 1963.

[34] A. Cuoci, M. Mehl, G. Buzzi-Ferraris, T. Faravelli, D. Manca, and E. Ranzi. Autoignition and burning rates of fuel droplets under microgravity. *Combustion and Flame*, 143:211–226, 2005.

[35] B.J. Daly and F.H. Harlow. Transport equations in turbulence. *Physics of Fluids*, 13:2634–2649, 1970.

[36] D.S. Dandy and H.A. Dwyer. A sphere in shear flow at finite Reynold snumber: effect of particle lift, drag and heat transfer. *Journal of Fluid Mechanics*, 216:381, 1990.

[37] B. de Jager. *Combustion and noise phenomena in turbulent alkane flames*. PhD thesis, University of Twente, Enschede, 2007.

[38] F.X. Demoulin and R. Borghi. Assumed PDF modeling of turbulent spray combustion. *Combustion Science and Technology*, 158:249–271, 2000.

[39] F.X. Demoulin and R. Borghi. Modeling of turbulent spray combustion with application to diesel like experiment. *Combustion and Flame*, 129:281–293, 2002.

[40] V. Devarakonda and A.K. Ray. Effect of inter-particle interactions on evaporation of droplets in a linear array. *Aerosol Science*, 34:837–857, 2003.

[41] D.L. Dietrich, P.M. Struik, M. Ikegami, and G. Xu. Single droplet combustion of decane in microgravity: experiments and numerical modelling. *Combustion Theory and Modelling*, 9:569–585, 2005.

[42] D.A. Drew. Mathematical modeling of two-phase flow. *Annual review of fluid mechanics*, 15:261–291, 1983.

[43] O.A. Druzhinin. The influence of particle inertia on the two-way coupling and modification of isotropic turbulence by microparticles. *Physics of Fluids*, 13(12):3738–3755, 2001.

[44] O.A. Druzhinin and S. Elghobashi. On the decay rate of isotropic turbulence laden with microparticles. *Physics of Fluids*, 11(3):602–610, 1999.

[45] I. Düwel, H.-W. Ge, H. Kronemayer, R. Dibble, E. Gutheil, C. Schulz, and J. Wolfrum. Experimental and numerical characterization of a turbulent spray flame. *Proceedings of the Combustion Institute,*, 31:2247–2255, 2006.

[46] C.F. Edwards and R.C. Rudoff. Structure of a swirl-stabilized spray flame by imaging, laser doppler velocimetry and phase doppler anemometry. *23rd Symposium (International) on Combustion*, pages 1353–1359, 1990.

[47] P. Eisenklam, S.A. Arunachalam, and J.A. Weston. Evaporation rates and drag resistance of burning drops. *11th Symposium (International) on Combustion*, page 715, 1967.

[48] S. Elghobashi and G.C. Truesdell. On the two-way interaction between homogeneous turbulence and dispersed solid particles I: turbulence modification. *Phys. Fluids A*, 5:1790–1801, 1993.

[49] G.M. Faeth. Evaporation and combustion of sprays. *Progress in Energy and Combustion Science*, 9:1–76, 1983.

[50] G.M. Faeth. Mixing, transport and combustion in sprays. *Progress in Energy and Combustion Science*, 13:293–345, 1987.

[51] G.M. Faeth. Spray combustion phenomena. *26th Symposium (Internatonal) on Combustion*, pages 1593–1612, 1996.

[52] Z.G. Feng and E.E. Michaelides. Heat and mass transfer coefficients of viscous spheres. *International Journal of Heat and Mass Transfer*, 44:4445–4454, 2001.

[53] V. Ferrand, R. Bazile, and J. Boree. Measurements of concentration per size class in a dense polydispersed jet using planar laser-induced fluorescence and phase Doppler techniques. *Experiments in Fluids*, 31:597–607, 2001.

[54] V. Ferrand, R. Bazile, J. Boree, and G. Charnay. Gas-droplet turbulent velocity correlations and two-phase interaction in an axisymmetric jet laden with partly responsive droplets. *International Journal of Multiphase Flow*, 29:195–217, 2003.

[55] R.O. Fox. *Computational models for turbulent reacting flows*. Cambridge University Press, 2003.

[56] C.W. Gardiner. *Handbook of stochastic methods for physics, chemistry and the natural sciences*. Springer Verlag, Berlin, 1990.

[57] R. Gatignol. The Faxén formulae for a rigid particle in an unsteady non-uniform Stokes flow. *Journal de Mécanique théorique et appliquée*, 1:143–160, 1983.

[58] H.W. Ge. *Probability density modeling of turbulent non-reactive and reactive spray flows*. PhD thesis, University of Heidelberg, 2006.

[59] M.G. Giridharan, D.S. Crocker, J. Widmann, and C. Presser. Issues related to spray combustion modeling validation. *AIAA 39th aerospace sciences meeting & exhibit*, pages AIAA 2001–0363, 2001.

[60] G. Gouesbet and A. Berlemont. Eulerian and Lagrangian approaches for predicting the behaviour of discrete particles in turbulent flows. *Progress in Energy and Combustion Science*, 25:133–159, 1999.

[61] E. Gutheil. Structure and extinction of laminar ethanol-air spray flames. *Combustion Theory and Modelling*, 5:131–145, 2001.

[62] E. Gutheil and W.A. Sirignano. Counterflow spray combustion modeling with detailed transport and detailed chemistry. *Combustion and Flame*, 113:92–105, 1998.

[63] R. Hadef and B. Lenze. Measurements of droplet characteristics in a swirl stabilized spray flame. *Experimental thermal and fluid science*, 2005.

[64] K. Hanjalic and B.E. Launder. A Reynolds stress model of turbulence and its applications to thin shear flows. *Journal of Fluid Mechanics*, 52:609–638, 1972.

[65] D.C. Haworth and S.B. Pope. A generalized Langevin model for turbulent flows. *Physics of Fluids*, 29:1026–1044, 1986.

[66] G. Hetsroni. Particles-turbulence interaction. *International Journal of Multiphase Flow*, 15(5):735–746, 1989.

[67] J. O. Hinze. *Turbulence, 2nd edition*. McGraw-Hill, 1975.

[68] A.T. Hjelmfelt and L.F. Mockros. Motion of discrete particles in a turbulent fluid. *Appl. Sci. Res.*, 16:149–161, 1966.

[69] C. Hollmann and E. Gutheil. Flamelet modeling of turbulent spray diffusion flames based on a laminar spray flame library. *Combustion Science and Technology*, 135:175–192, 1998.

[70] R.T. Imaoka and W.A. Sirignano. A generalised analysis for liquid-fuel vaporisation and burning. *International Journal of Heat and Mass Transfer*, 48:4342–4353, 2005.

[71] R.T. Imaoka and W.A. Sirignano. Vaporisation and combustion in three-dimensional droplet arrays. *Proceedings of the Combustion Institute*, 30:1981–1989, 2005.

[72] P. Jenny, S.B. Pope, M. Muradoğlu, and D.A. Caughey. A hybrid algorithm for the joint PDF equation of turbulent reactive flows. *Journal of Computational Physics*, 166:218–252, 2001.

[73] A.N. Karpetis. *Self-similarity, momentum scaling and Reynolds stress in non-premixed turbulent spray flames*. PhD thesis, Yale University, 1998.

[74] A.N. Karpetis and A. Gomez. An experimental investigation of non-premixed turbulent spray flames and their self similar behavior. *27th Symposium (International) on Combustion*, pages 2001–2008, 1998.

[75] A.N. Karpetis and A. Gomez. An experimental study of well-defined turbulent nonpremixed spray flames. *Combustion and Flame*, 121:1–23, 2000.

[76] I. Kataoka. Local instant formulation of two-phase flow. *International Journal of Multiphase Flow*, 12:745–758, 1986.

[77] A. Kazakov, J. Conley, and F.L. Dryer. Detailed modeling of an isolated, ethanol droplet combustion under microgravity conditions. *Combustion and Flame*, 134:301–314, 2003.

[78] R.J. Kee, J.F. Grcar, M.D. Smooke, and J.A. Miller. *A FORTRAN program for modeling steady laminar one-dimensional premixed flames*. Sandia National Laboratories, 1997.

[79] R.J. Kee, F.M. Rupley, and J.A. Miller. *CHEMKIN-II: a FORTRAN chemical kinetics package for the analysis of gas-phase chemical kinetics*. Sandia national laboratories, 1997.

[80] R.J. Kee, F.M. Rupley, and J.A. Miller. *The CHEMKIN thermodynamic data base*. Sandia National Laboratories, 1997.

[81] P.E. Kloeden and E. Platen. *Numerical solution of stochastic differential equations*. Springer, 1992.

[82] G. Klose, R. Schmehl, R. Meier, G. Meier, R. Koch, and S. Wittig. Evaluation of advanced two-phase flow and combustion models for predicting low emission combustors. *Proceedings of ASME Turbo Expo 2000*, may 8-11, 2000.

[83] D.I. Kolaitis and M.A. Founti. A comparative study of numerical models for eulerianlagrangian simulations of turbulent evaporating sprays. *International Journal of Heat and Fluid Flow*, 27:424–435, 2006.

[84] A.N. Kolmogorov. The local structure of turbulence in incompressible viscous fluid for very large Reynolds numbers. *Proc. R. Soc. London Ser. A*, 434:9–13, 1991.

[85] K.K. Kuo. *Principles of combustion*. J. Wiley and sons, 1986.

[86] M. Labowski. The effect of nearest neighbor interactions on the evaporation rate of cloud particles. *Chemical Engineering Science*, 31:803–813, 1976.

[87] M. Labowski. Comments arising from 'effect of multiple particle interactions on burning droplets' by marberry et al. *Combustion and Flame*, 65:367–369, 1986.

[88] S. Lain and J.A. Garcia. Study of four-way coupling on turbulent particle-laden jet flows. *Chemical Engineering Science*, 61:6775–6785, 2006.

[89] S. Lain and M. Sommerfeld. Turbulence modulation in dispersed two-phase flow laden with solids from a Lagrangian perspective. *International Journal of Heat and Fluid Flow*, 24:616–625, 2003.

[90] B.E. Launder, G.J. Reece, and W. Rodi. Progress in the development of a Reynolds-stress turbulence closure. *Journal of Fluid Mechanics*, 68:537–566, 1975.

[91] C. K. Law and W. A. Sirignano. Unsteady droplet combustion with droplet heating - II: conduction limit. *Combustion and Flame*, 28:175–186, 1977.

[92] C.K. Law. Recent advances in droplet vaporization and combustion. *Progress in Energy and Combustion Science*, 8:171–201, 1982.

[93] C.K. Law. Alcohol droplet vaporization in humid air. *International Journal of Heat and Mass Transfer*, 30:1435–1443, 1987.

[94] R.P. Lindstedt and M.P. Meyer. A dimensionally reduced reaction mechanism for methanol oxidation. *Proceedings of the combustion institute*, 29:1395–1402, 2002.

[95] J.L. Lumley. Computational modeling of turbulent flows. *Advances in Applied Mechanics*, 18:123–176, 1978.

[96] M. Marberry, A.K. Ray, and K. Leung. Effect of multiple particle interactions on burning droplets. *Combustion and Flame*, 57:237–245, 1984.

[97] A.J. Marchese and F.L Dryer. The effect of liquid mass transport on the combustion and extinction of bicomponent droplets of methanol and water. *Combustion and Flame*, 105:104–122, 1996.

[98] F. Mashayek and D.B. Taulbee. Turbulent gas-solid flows part I: direct simulations and Reynolds stress closures. *Numerical Heat Transfer B*, 41:1–29, 2002.

[99] M.R. Maxey and J.J. Riley. Equation of motion for a small rigid sphere in a nonuniform flow. *Physics of Fluids*, 26:883–889, 1983.

[100] V.G. McDonell, M. Adachi, and G.S. Samuelsen. Structure of reacting and non-reacting swirling air assisted sprays. *Combustion Science and Technology*, 82:225–248, 1992.

[101] V.G. McDonell, M. Adachi, and G.S. Samuelsen. Structure of reacting and non-reacting, non-swirling, air assisted sprays, part I: gas-phase properties. *Atomization and Sprays*, 3(4):389–410, 1993.

[102] V.G. McDonell, M. Adachi, and G.S. Samuelsen. Structure of reacting and non-reacting, non-swirling, air assisted sprays, part II: drop behavior. *Atomization and Sprays*, 3(4):411–436, 1993.

[103] V.G. McDonell and G..S. Samuelsen. An experimental database for the computational fluid dynamics of reacting and nonreacting methanol sprays. *Journal of Fluids Engineering*, 117:145–153, 1995.

[104] J.B. McLaughlin. Inertial migration of a small sphere in linear shear flows. *Journal of Fluid Mechanics*, 224:261, 1991.

[105] R. Mei. An approximate expression for the shear lift on a spherical particle at finite Reynolds number. *International Journal of Multiphase Flow*, 18:145, 1992.

[106] E.E. Michaelides. Hydrodynamic force and heat/mass transfer from particles, bubbles, and drops - the Freeman scholar lecture. *Journal of Fluids Engineering*, 125:209–238, 2003.

[107] M. Mikami, H. Kato, J. Sato, and M. Kono. Interactive combustion of two droplets in microgravity. *25th Symposium (International) on Combustion*, pages 431–438, 1994.

[108] R.S. Miller, K. Harstad, and J. Bellan. Evaluation of equilibrium and non-equilibrium evaporation models for many-droplet gas-liquid flow simulations. *International Journal of Multiphase Flow*, 24:1025–1055, 1998.

[109] J.P. Minier and E. Peirano. The PDF approach to turbulent polydispersed two-phase flows. *Physics Reports*, 352:1–214, 2001.

[110] J.P. Minier, E. Peirano, and S. Chibbaro. Weak first- and second-order numerical schemes for stochastic differential equations appearing in Lagrangian two-phase flow modeling. *Monte Carlo methods and appl.*, 9(2):93–133, 2003.

[111] K. Miyasaka and C.K. Law. Combustion of strongly interacting linear droplet arrays. *18th Symposium (International) on Combustion*, pages 283–292, 1981.

[112] A.S. Monin and A.M. Yaglom. *Statistical fluid mechanics vol. II*. MIT Press, 1975.

[113] M. Muradoğlu, P. Jenny, S.B. Pope, and D.A. Caughey. A consistent hybrid finite volume-particle method for the PDF equations of turbulent reacting flows. *Journal of Computational Physics*, 154:342–371, 1999.

[114] M. Muradoğlu and S.B. Pope. A local time-stepping algorithm for solving the probability density function turbulence model equations. *AIAA Journal*, 40:1755–1763, 2002.

[115] H. Nagata, I. Kudo, and K. Ito. Interactive combustion of two-dimensionally arranged quasi-droplet clusters under microgravity. *Combustion and Flame*, 129:392–400, 2002.

[116] D. Naot, A. Shavit, and M. Wolfshtein. Two-point correlation model and the redistribution of Reynolds stresses. *Physics of Fluids*, 16:738–743, 1973.

[117] B. Naud. *PDF Modeling of turbulent sprays and flames using a particle stochastic approach*. PhD thesis, Delft University of Technology, 2003.

[118] B. Naud, C. Jiménez, and D. Roekaerts. Velocity-position error for tracer particles in stochastic Lagrangian modelling of polydispersed sprays based on the seen velocity. In *5th International Conference on Multiphase Flow, ICMF'04*, 2004.

[119] K. Okai, O. Moriue, M. Araki, M. Tsue, and M. Kono. Pressure effects on combustion of methanol and methanol/dodecanol single droplets and droplet pairs in microgravity. *Combustion and Flame*, 121:501–512, 2000.

[120] B. Oksendal. *Stochastic differential equations, 6th edition*. Springer, 2003.

[121] S.V. Patankar. *Numerical heat transfer and fluid flow*. Taylor and Francis, 1980.

[122] E. Peirano, S. Chibbaro, J. Pozorski, and J.-P. Minier. Mean-field/PDF numerical approach for polydispersed turbulent two-phase flows. *Progress in Energy and Combustion Science*, 32(3):1–57, 2006.

[123] N. Peters. *Turbulent combustion*. Cambridge University Press, 2000.

[124] C. Pichard, C. Chauveau, and I. Gökalp. Experimental characterisation of the atomisation and combustion of partially prevaporised and premixed sprays. *Proceedings of the European Combustion Meeting*, 2003.

[125] C. Pichard, Y. Michou, C. Chauveau, and I. Gökalp. Average droplet vaporization rates in partially prevaporized turbulent spray flames. *29th Symposium (International) on Combustion*, 29:527–533, 2002.

[126] B.E. Poling, J.M. Prausnitz, and J.P. o'Connell. *The properties of gases and liquids*. McGraw-Hill, 2001.

[127] S.B. Pope. A Lagrangian two-time probability density function equation for inhomogeneous turbulent flows. *Physics of Fluids*, 26(12):3448–3450, 1983.

[128] S.B. Pope. PDF methods for turbulent reacting flows. *Prog. Energy Combust. Sci.*, 11:119–192, 1985.

[129] S.B. Pope. On the relationship between stochastic Lagrangian models of turbulence and second-moment closures. *Physics of Fluids*, 6(2):973–985, 1994.

[130] S.B. Pope. *Turbulent Flows*. Cambridge University Press, 2000.

[131] J. Pozorski and J.-P. Minier. On the Lagrangian turbulent dispersion models based on the Langevin equation. *International Journal of Multiphase Flow*, 24:913–945, 1998.

[132] C. Presser. Application of a benchmark experimental database for multiphase combustion modeling. *Journal of propulsion and power*, 22:1145–1149, 2006.

[133] C. Presser, A.K. Gupta, C.T. Avedisian, and H.G. Semerjian. Fuel property effects on the structure of spray flames. *23rd Symposium (International) on Combustion*, pages 1361–1367, 1990.

[134] C. Presser, A.K. Gupta, and H.G. Semerjian. Aerodynamic characteristics of swirling spray flames: Pressure jet atomizer. *Combustion and Flame*, 92:25–44, 1993.

[135] J. Réveillon and L. Vervisch. Analysis of weakly turbulent diluted-spray flames and spray combustion regimes. *Journal of Fluid Mechanics*, 537:317–347, 2005.

[136] H. Risken. *The Fokker Planck equation: methods of solution and applications*. Springer Verlag, Berlin, 1989.

[137] S.S. Stårner, J. Gounder, and A.R. Masri. Effects of turbulence and carrier fluid on simple, turbulent spray jet flames. *Combustion and Flame*, 143:420–432, 2005.

[138] J. C. Rotta. Statistische Theorie nicht-homogener Turbulenz. *Z. Phys.*, 129:547–572, 1951.

[139] S. Russo and A. Gomez. The extinction behavior of small interacting droplets in a cross-flow. *Combustion and Flame*, 130:215–224, 2002.

[140] A. Rybakov and U. Maas. Joint PDF modeling of a turbulent spray flame. In *11th SIAM conference on computational combustion, Granada, Spain*, 2006.

[141] A. Sadiki, M. Chrigui, J. Janicka, and M.R. Maneshkarimi. Modeling and simulation of effects of turbulence on vaporisation, mixing and combustion of liquid-fuel sprays. *Flow, Turbulence and Combustion*, 75:105–130, 2005.

[142] P.G. Saffman. The lift on a small sphere in a slow shear flow. *Journal of Fluid Mechanics*, 22:385–400, 1965.

[143] S.S. Sahzin, P.A. Krutiskii, W.A. Abdelghaffar, S.V. Mikhalovski, S.T. Meikle, and M.R. Heikal. Transient heating of diesel fuel droplets. *International Journal of Heat and Mass Transfer*, 47:3327–3340, 2004.

[144] J.J. Sangiovanni. Burning times of linear fuel droplet arrays: a comparison of experiment and theory. *Combustion and Flame*, 47:15–30, 1982.

[145] S.S. Sazhin. Advanced models of fuel droplet heating and evaporation. *Progress in Energy and Combustion Science*, 32:162–214, 2006.

[146] J.S. Shirolkar, C.F.M. Coimbra, and M.Q. McQuay. Fundamental aspects of modeling turbulent particle dispersion in dilute flows. *Progress in Energy and Combustion Science*, 22:363–399, 1996.

[147] J.S. Shuen, A.S.P. Solomon, and G.M. Faeth. Drop-turbulence interactions in a diffusion flame. *AIAA Journal*, 24:101–108, 1986.

[148] O. Simonin, E. Deutsch, and J.P. Minier. Eulerian prediction of the fluid/particle correlated motion in turbulent two-phase flows. *Applied scientific research*, 51:275–283, 1993.

[149] W.A. Sirignano. Fuel droplet vaporization and spray combustion theory. *Progress in Energy and Combustion Science*, 9:291–322, 1983.

[150] W.A. Sirignano. *Fluid Dynamics and Transport of Droplets and Sprays*. Cambridge University Press, 1999.

[151] G.F. Smith. On isotropic functions of symmetric tensors, skew-symmetric tensors and vectors. *Intl. J. Engng Sci.*, 9:899–916, 1971.

[152] M. Sommerfeld. Analysis of isothermal and evaporating turbulent sprays by phase-doppler anemometry and numerical calculations. *International Journal of Heat and Fluid Flow*, 19:173–186, 1998.

[153] M. Sommerfeld and H.H. Qiu. Experimental studies of spray evaporation in turbulent flow. *Int. J. of Heat and Fluid Flow*, 19:10–22, 1998.

[154] R.J. Sornek, R. Dobashi, and T. Hirano. Effects of turbulence on vaporization, mixing and combustion of liquid-fuel sprays. *Combustion and Flame*, 120:479–491, 2000.

[155] C.G. Speziale, S. Sarkar, and T.B. Gatski. Modelling the pressure-strain correlation of turbulence: an invariant dynamical systems approach. *Journal of Fluid Mechanics*, 227:245–272, 1991.

[156] K.D. Squires and J.K.. Eaton. Measurements of particle dispersion obtained from direct numerical simulations of isotropic turbulence. *Journal of Fluid Mechanics*, 226:1–35, 1991.

[157] S. Stauch, S. Lipp, and U. Maas. Detailed numerical simulations of the autoignition of single n-heptane droplets in air. *Combustion and Flame*, 145(3):533–542, 2006.

[158] D. Stoyan and H. Stoyan. *Fractals, random shapes and point fields*. J. Wiley & Sons, 1994.

[159] S. Subramaniam. Eulerian and Lagrangian statistical representations of multiphase flow. *4th international conference on multiphase flow*, 2001.

[160] S. Sundaram and L.R. Collins. A numerical study of the modulation of isotropic turbulence by suspended particles. *Journal of Fluid Mechanics*, 379:105–143, 1999.

[161] D.B. Taulbee, F. Mashayek, and C. Barré. Simulation and Reynolds stress modeling of particle-laden turbulent shear flows. *International Journal of Heat and Fluid Flow*, 20:368–373, 1999.

[162] A.M.Al Taweel and J. Landau. Turbulence modulation in two-phase jets. *International Journal of Multiphase Flow*, 3:341–351, 1977.

[163] C.M. Tchen. Mean value and correlation problems connected with the motion of small particles suspended in a turbulent fluid. *PhD thesis, Delft University of Technology*, 1947.

[164] G. Temple. *Cartesian Tensors*. John Wiley & Sons, 1960.

[165] J.M. Tishkoff. A model for the effect of droplet interactions on vaporization. *International Journal of Heat and Mass Transfer*, 22:1407–1415, 1978.

[166] S. Ulzama and E. Specht. An analytical study of droplet combustion under microgravity: quasi-steady transient approach. *Proceedings of the combustion institute*, 31:2301–2308, 2006.

[167] A. Umemura. Interactive droplet vaporization and combustion: approach from asymptotics. *Progress in Energy and Combustion Science*, 20:325–372, 1994.

[168] A. Umemura, S. Ogawa, and N. Oshima. Analysis of the interaction between two burning droplets. *Combustion and Flame*, 41:45–55, 1981.

[169] A. Umemura, S. Ogawa, and N. Oshima. Analysis of the interaction between two burning droplets with different sizes. *Combustion and Flame*, 43:111–119, 1981.

[170] D.J. Vojir and E.E. Michaelides. The effect of the history term on the motion of rigid spheres in a viscous fluid flow. *International Journal of Multiphase Flow*, 20:547–556, 1994.

[171] L-P. Wang and D.E. Stock. Dispersion of heavy particles by turbulent motion. *Journal of the Atmospheric Sciences*, 50(13):1897–1913, 1993.

[172] N. Wax. *Noise and stochastic processes*. Dover, 1954.

[173] J.F. Widmann, S.R. Charagundla, C. Presser, and A. Heckert. Benchmark experimental database for multiphase combustion model input and validation: baseline case. Technical report, NIST Internal Report 6561, 1999.

[174] J.F. Widmann and C. Presser. A benchmark experimental database for multiphase combustion model input and validation. *Combustion and Flame*, 129:47–86, 2002.

[175] J.F. Widmann and C. Presser. Erratum to "a benchmark experimental database for multiphase combustion model input and validation" combustion and flame 129:47-86(2002). *Combustion and Flame*, 130:386–390, 2002.

[176] D.C. Wilcox. *Turbulence modeling for CFD*. Griffin Printing, Glendale, 1993.

[177] F.A. Williams. Spray combustion and atomization. *Physics of Fluids*, 1:541–545, 1958.

[178] F.A. Williams. *Combustion Theory, Second Edition*. Benjamin/Cummings Publishing Company, 1985.

[179] S.C. Wong and A.R. Lin. Internal temperature distributions of droplets vaporizing in high-temperature convective flows. *Journal of Fluid Mechanics*, 237:671–687, 1992.

[180] H. Wouters. *PDF Lagrangian models for turbulent reacting flows*. PhD thesis, Delft University of Technology, 1998.

[181] T.Y. Xiong, C.K. Law, and K. Miyasaka. Interactive vaporizatin and combustion of binary droplet systems. *20th Symposium (International) on Combustion*, pages 1781–1787, 1984.

[182] G. Xu, M. Ikegami, S. Honma, K. Ikeda, X. Ma, H. Nagaishi, D.L. Dietrich, and P.M. Struk. Inverse influence of initial diameter on droplet burning rate in cold and hot ambiences: a thermal action of flame in balance with heat loss. *International Journal of Heat and Mass Transfer*, 46:1155–1169, 2003.

[183] J. Xu and S.B. Pope. Sources of bias in particle-mesh methods for PDF models for turbulent flows. Technical report, Cornell University, Ithaca, NY, 1997.

[184] J. Xu and S.B. Pope. Assessment of numerical accuracy of PDF/Monte Carlo methods for turbulent reacting flows. *Journal of Computational Physics*, 152:192–230, 1999.

[185] M.I. Yudine. Physical consideration on heavy-particle dispersion. *Advances in Geophysics*, 6:185–191, 1959.

[186] M.C. Yuen and L.W. Chen. On drag of evaporating liquid droplets. *Combustion Science and Technology*, 14:147–154, 1976.

[187] B.L . Zhang and F.A. Williams. Effects of the Lewis number of water vapor on the combustion and extinction of methanol drops. *Combustion and Flame*, 112:113–120, 1998.

[188] B.L. Zhang, J.M. Card, and F.A. Williams. Application of rate-ratio asymptotics to the prediction of extinction for methanol droplet combustion. *Combustion and Flame*, 105:267–290, 1996.

[189] M. Zhu, K.N.C Bray, O. Rumberg, and B. Rogg. PDF transport equations for two-phase reactive flows and sprays. *Combustion and Flame*, 122:327–338, 2000.

[190] F.C. Zhuang, B. Yang, J. Zhou, and H. Yang. Unsteady combustion and vaporization of a spherical fuel droplet group. *21st Symposium (International) on Combustion*, pages 647–653, 1986.

[191] B. Zuo, D.L. Black, and D.S. Crocker. Fuel atomization and drop breakup models for advanced combustion CFD codes. *38th AIAA/ASME/SAE/ASEE Joint Propulsion Conference & Exhibit*, pages 1–11, 7-10 July 2002.

Acknowledgement

Het onderzoek beschreven in dit proefschrift is onderdeel van het FOM programma 'gedispergeerde meerfasenstromingen' en werd financieel mogelijk gemaakt door de Stichting STW, waarvoor mijn hartelijke dank.

Er zijn verschillende personen die ik wil bedanken wiens hulp en steun tijdens mijn promotietraject van onschatbare waarde is gebleken. Ten eerste wil ik natuurlijk Dirk Roekaerts bedanken. Zijn grondige manier van corrigeren zowel als zijn suggesties voor verbetering hebben veel bijgedragen aan de kwaliteit van dit proefschrift. For the same reason I would like to thank Bertrand Naud who, despite that he was in Spain (first in Saragossa, later in Madrid), helped in many ways. I was always welcome with my questions and you always took the time to explain complicated matters to me, to point out errors in the code that I wrote and you suggested improvements on how to express myself in writing. De derde persoon die ik wil bedanken is Erwin de Beus. Zijn kennis en vaardigheden maakten het mogelijk om de vele berekeningen die nodig waren (vaak) probleemloos uit te voeren op het computercluster.

Nijso Beishuizen
September 2007

About the author

— Nijso Arie Beishuizen —

September 8, 1977	Born in Assen, the Netherlands.
Sep. 1989 – May 1996	Secondary school at Dr. Nassau College, Assen, the Netherlands
Sep. 1996 – May 2003	Aerospace Engineering at Delft University of Technology, the Netherlands
Jan. 2002 – May 2003	Graduation project under supervision of Dr. M.I. Gerritsma, titled "A posteriori error estimation for the Least Squares Spectral Element Method", at the department of Aerodynamics
May 2003 – May 2007	Ph.D. research at the Multiscale Physics group at Applied Physics, Delft University of Technology, under the supervision of prof. Dirk Roekaerts.
Sep. 2007 – Sep. 2008	Post-doc at the group of Thermal Engineering, University of Twente